SARS-CoV-2 Orf6 requires the Nup98/Rae1 complex to inhibit host nuclear transport

by

Nicole Danielle Love

A thesis submitted in partial fulfillment of the requirements for the degree of

Master of Science

Department of Cell Biology
University of Alberta

Abstract

The nucleus is a hallmark organelle of eukaryotes. It separates the genetic material from the rest of the cytoplasm using a selectively permeable double phospholipid bilayer called the nuclear envelope (NE). The NE contains numerous pores with embedded macromolecular structures called nuclear pore complexes (NPCs), which are formed from ~30 different proteins called nucleoporins (Nups). In conjunction with soluble nuclear transport factors, cellular proteins and RNAs are able to move through the NPC. Although humans and the budding yeast *Saccharomyces cerevisiae* have been separated by approximately a billion years of evolution, both organisms contain a striking conservation in overall NPC structure and function, with many Nups, transport factors, and transport pathways functionally conserved. Of interest, the human Nup98/Rae1 complex is related to the *S. cerevisiae* Nup116/Gle2 complex, and both have been shown to have important functions in transport across the NPC.

Many viruses, including the SARS-CoV-2 virus, have been shown to target host NPCs in order to create an environment conducive for viral replication. Numerous viral proteins, one of which is the SARS-CoV-2 Orf6 protein, achieve this by binding to the Nup98/Rae1 complex to inhibit the bidirectional nuclear transport of host proteins and RNAs. The viral proteins that interact with the Nup98/Rae1 complex contain a common motif, termed a Nup98/Rae1 interaction motif.

Interestingly, residues within the human Nup98/Rae1 complex that form major interactions with the Nup98/Rae1 interaction motif of Orf6 are conserved in the *S. cerevisiae* Nup116/Gle2 complex. On the basis of this similarity, we hypothesized that

the SARS-CoV-2 Orf6 protein interacts with the Nup116/Gle2 complex and would inhibit the bidirectional nuclear transport of conserved nuclear import and export pathways in yeast. We show here that Orf6 can be expressed and localizes to the NE of *S. cerevisiae,* potentially to a subset of NPCs. However, we observed no detectable inhibition of two protein import pathways or bulk mRNA export defects associated with Orf6 expression. Thus, the consequences of Orf6 association at the yeast NE remain to be determined.

Although Orf6 has been shown to target the mammalian Nup98/Rae1 complex, how Orf6 inhibits the nuclear transport of host proteins and RNAs remains unclear. To further investigate the functional relationship between Orf6 and the Nup98/Rae1 complex, the Orf6-mediated block of nuclear transport was examined in Vero cells depleted of either Nup98 or Rae1. We show that depletion of Rae1 abolishes the Orf6-mediated block of both STAT1 nuclear import and poly-A RNA nuclear export. Similarly, depletion of Nup98 also suppresses Orf6-mediated inhibition of STAT1 nuclear import. Collectively, these studies suggest Orf6 requires the Nup98/Rae1 complex to function, and further points to an important role for Rae1 in facilitating the block of nuclear transport caused by Orf6 expression. Since the Nup98/Rae1 complex is commonly targeted by viral proteins to cause a dysregulated immune response, understanding how Orf6 inhibits nuclear transport by targeting Nup98 or Rae1 could provide important insights into therapeutic treatments for viral infection, and may also further elucidate the roles of Nup98 and Rae1 in nuclear transport.

Preface

A version of Chapter IV of this thesis is included within an in-progress manuscript. T. Makio is the first author, and was responsible for data generation and analysis, concept formation, and manuscript composition. I was responsible for concept formation and data collection and analysis. K. Zhang was responsible for concept formation and data collection and analysis. I have indicated specific data contributions in the corresponding figures. R. Wozniak is the supervisory author. R. Wozniak and B. Fontoura contributed to concept formation, manuscript composition, and data analysis.

Acknowledgements

I would like to express my sincerest gratitude to the many individuals who have extended their support and valuable assistance throughout my graduate studies, allowing for the completion of this degree. Firstly, I extend my deepest thanks and appreciation to Dr. Richard Wozniak for granting me the opportunity to study as a member of the Wozniak laboratory. Under your supervision I have grown both personally and professionally, and I feel extremely fortunate to have been able to learn under your support and guidance. Your passion and enthusiasm for excellence in science and research is admirable, and I thank you for always challenging me to think deeper, to question harder, and to be both curious and cautious about what remains unknown, encouraging me to think critically and to remain inquisitive in all areas of my academic endeavours.

To the members of the Wozniak laboratory that I have had the great pleasure of researching with; Dr. Chris Ptak, Dr. Tadashi Makio, Dr. Natasha Saik, and Saif Rehman, your encouragement, insights, and thoughtful feedback has greatly enhanced my knowledge and has significantly contributed to any success that I have had throughout my graduate studies. In particular, I would like to extend my upmost appreciation and a heartfelt thank you to Dr. Chris Ptak and to Dr. Tadashi Makio for providing consistent support and encouragement throughout my studies, for taking the time to teach me experimental techniques, and for enriching my learning experience with countless conversations addressing my questions and assisting with the interpretation of perplexing experimental results. Chris, thank you for being an incredible educator throughout my graduate studies and for always being good for a much-needed laugh. Tadashi, thank you for your superb mentorship during both my undergraduate and graduate research studies, and thank you for allowing me to contribute to the project that you spearheaded.

To the members of my supervisory committee, Dr. Ben Montpetit and Dr. Tom Hobman, thank you for your support and assistance throughout my graduate studies. The input and feedback provided throughout my master's degree have been incredibly valuable to both my research project and to my professional development.

I would also like to acknowledge the generosity of the Li Ka Shing Institute of Virology, the Faculty of Graduate Studies and Research, and Alberta Innovates for the funding that I have received in the form of scholarships during my graduate studies. I feel very honored and fortunate to have been considered worthy of receiving these awards. This funding, in conjunction with the support provided by Dr. Wozniak and the Canadian Institutes of Health Research, has ultimately made this research possible.

Finally, to my loving family and friends; the unwavering support and the endless encouragement you have given to me throughout my studies has been instrumental to the completion of my master's degree. To my mom, thank you for always believing in my dreams and my capabilities, and for encouraging me to explore all of my interests and to pursue all of my goals. To my dad, thank you for endlessly supporting my passions, for providing for me, and for encouraging me in all of my life's adventures. Without both of your love, support, and reassurance I would not be the person I am today. To my grandma and grandad, thank you for always lovingly checking in on me, for helping to teach me the value of hard work, and for reminding me that it is also just as important to take a moment to refuel and recharge. To my mémère, thank you for your genuine interest in my research, for our Sunday phone calls, for your abundance of love, care, and support, and for cheering me on during every step of my life's journey. To Michael, thank you for being a genuine, consistent, and an incredibly supportive presence in my life. Without your care packages, your fierce encouragement, and your constant reminders to keep focused on the bigger picture, this would have been a much more challenging endeavour. To Mark, thank you for being both a rock and a calming force in my life; your reassurance, care, and love have helped alleviate many stressors during this journey, and I will always be thankful for your support and encouragement in my life. The encouragement and love I have been given from all of you during this journey is truly immeasurable to me, and I am incredibly fortunate and grateful for all of the support that I have received throughout this endeavour.

Table of Contents

List of Tables

List of Figures

List of Symbols, Abbreviations and Nomenclature

ADP: Adenosine diphosphate
ATP: Adenosine triphosphate
cNLS: Classical NLS
CRM1: Chromosomal maintenance 1
DAPI: 4',6-diamidino-2-phenylindole
DMEM: Dubelcco's modified Eagle's media
dsRNA: Doubled stranded RNA
E: Envelope protein
ER: Endoplasmic reticulum
FBS: Fetal bovine serum
FG: Phenylalanine-glycine
FISH: Fluorescence in situ hybridization
GDP: Guanosine diphosphate
GTP: Guanosine triphosphate
GFP: Green fluorescent protein
GLEBS: Gle2 binding sequence
GLFG: Glycine-leucine-phenylalanine-glycine
GSP1: Genetic suppressor of Prp20-1
GTP: Guanosine triphosphate
HBV: Hepatitis B virus
HIV-1: Human immunodeficiency virus 1
HSV-1: Herpes simplex virus 1
IF: Immunofluorescence
IFN-α: Interferon alpha
IFN-β: Interferon beta
IgG: Immunoglobulin G
INM: Inner nuclear membrane
IRF3: Interferon regulatory factor 3
IRF7: Interferon regulatory factor 7
ISG: Interferon stimulated gene
ISGF3: Interferon-stimulated gene factor 3
ISRE: Interferon stimulation response element
Kap(s): Karyopherin(s) (a.k.a. importins and exportins)
LB: Luria Broth
M: Membrane protein
mCh: mCherry, monomeric cherry
min: Minute
mRNP: Messenger ribonucleoprotein particle
N: Nucleocapsid protein
NE: Nuclear envelope
NES: Nuclear export signal
NLS: Nuclear localization signal
NPC(s): Nuclear pore complex(es)
NTF(s): Nuclear transport factor(s)

Nup(s): Nucleoporin(s)
NXF1: nuclear RNA export factor 1
NXT1: NTF2-related export protein 1
OD: Optical density
ONM: outer nuclear membrane
PAMP: Pathogen associated molecular pattern
PBS: Phosphate buffered saline
PCR: Polymerase chain reaction
PRR: Pattern recognition receptor
RanGAP: Ran GTPase-activating protein
RanGEF: Ran guanine nucleotide exchange factor
RCC1: Regulator of chromosome condensation 1
RdRp: RNA dependent RNA polymerase
RRE: Rev response element
RT: Room temperature
S: Spike protein
s: second
ssRNA: Single stranded RNA
SARS-CoV-1: Severe acute respiratory syndrome coronavirus 1
SARS-CoV-2: Severe acute respiratory syndrome coronavirus 2
SDS-PAGE: Sodium dodecyl sulfate polyacrylamide gel electrophoresis
shRNA: Short hairpin RNA
STAT1: Signal transducer and activator of transcription 1
STAT2: Signal transducer and activator of transcription 2
VSV: Vesicular Stomatitis virus
XPO1: Exportin 1
YPD: Yeast extract peptone dextrose media
ZIKV: Zika virus

Å: angstrom
C°: degrees Celsius
kDa: kilodalton
L: liter
mL: milliliter
mM: millimolar
g: gram
µg: microgram
µm: micron/micrometre
µL: microliter

Chapter I

Introduction

1.1 Nuclear envelope.

The defining feature of eukaryotes is that they possess membrane bound organelles, allowing for the compartmentalization of different cellular processes. This compartmentalization of function in eukaryotes allows for the spatial separation of cellular activities, which then decreases the interference between different cellular factors, ultimately increasing the overall efficiency of eukaryotic cellular processes and pathways (Diekmann and Pereira-Leal, 2013). This cellular compartmentalization is what has allowed for increased organizational complexity within eukaryotes and has facilitated the generation of multicellularity (Ispolatov *et al*., 2011; King *et al*., 2004).

The nucleus is a hallmark organelle of eukaryotes. It surrounds the genetic material in a selectively permeable double phospholipid bilayer which is referred to as the nuclear envelope (NE) (Hetzer, 2010). The NE separates the contents of the nucleus, termed the nucleoplasm, from the rest of the cytoplasm, and disruptions to this barrier have been shown to cause severe cellular disfunction leading to disorders such as muscular dystrophy, lipodystrophy, premature aging syndrome, cardiomyopathy, peripheral neuropathy, and progressive high-frequency hearing loss (Bonne *et al*., 1999; Speckman *et al*., 2000; Sandre-Giovannoli *et al*., 2002; Eriksson *et al*., 2003; De Vose *et al*., 2011; Worman and Segil, 2013; Sakuma and D'Aangelo, 2017).

The double membrane NE is composed of both an inner nuclear membrane (INM) and an outer nuclear membrane (ONM), which is contiguous with the endoplasmic reticulum (ER) (Hetzer, 2010; Katta *et al*., 2013). Despite the lipid contiguity between the NE and the ER, the protein composition of both the INM and the ONM are discrete and differ from the protein composition of the ER (Hetzer *et al*.,

2007). The ONM provides an impenetrable barrier for large molecules and most small molecules, and the INM is enriched in proteins that are required for maintaining nuclear structure, chromosome organization, and transcriptional regulation, among others (Somech *et al*., 2005; Stancheva and Schirmer, 2014). Numerous diseases such as, but not limited to, Emery-Dreifuss Muscular Dystrophy, Greenberg skeletal dysplasia, Hutchinson-Gilford Progeria Syndrome (HGPS), and Autosomal Dominant Leukodystrophy, have been associated with mutations in NE components and are collectively referred to as nuclear envelopathies (Katta *et al*., 2013; Janin *et al*., 2017).

The presence of a highly organized NE that separates the nucleoplasmic and cytoplasmic contents while still maintaining a permeable barrier for the selective movement of cellular cargo, has allowed for a highly complex system of gene expression and regulation within eukaryotes (Stancheva and Schirmer, 2014). For instance, the complex interactions between NE components and chromatin leads to genome reorganization and thus helps to regulate expression of eukaryotic genes (Van de Vosse *et al*., 2011; Zuleger *et al*., 2013), the spatial separation of transcription from translation allows for a series of splicing and processing events leading to a more diverse proteome within eukaryotes (Nilsen and Graveley, 2010), and the regulatable separation of cytoplasmic transcription factors from the nucleoplasm allows for the inducible expression of genes needed during periods of cellular invasion by foreign pathogens (Maciejowski and Hatch, 2020; Selezneva *et al*., 2022). Fundamental to eukaryotic gene expression though, is the transport of both cellular protein and RNA across the NE, and this occurs in perforated areas of the INM and OMN where macromolecular structures embed and form aqueous channels, allowing for the

selective movement of cellular cargo into and out of the nucleus (Knockenhauer and Schwartz, 2016).

1.2 Nuclear pore complex.

Embedded within nuclear pores is an extensive macromolecular structure called the nuclear pore complex (NPC). The NPC is responsible for the selective movement of cellular cargo across the NE, however, these dynamic structures also participate in diverse roles outside of nuclear transport, including chromatin organization, gene expression, and cell cycle regulation (Beck and Hurt, 2016).

The NPC is composed of multiple different copies of approximately 30 different proteins, termed nucleoporins or Nup(s), which arrange to form an 8-fold rotational symmetry within the nuclear pore (Beck and Hurt, 2016). Interestingly, NPCs retain a high level of conservation across eukaryotes, with striking similarities in both the overall structure and composition of NPCs, and a substantial conservation of many individual Nups (Cronshaw *et al*., 2002; Neumann *et al*., 2010). Since the NPC is essential for eukaryotic cell function, it is not surprising that this complex has retained high levels of conservation over evolution. However, despite the overall conservation in structure, there is evidence to suggest that not all NPCs contain the same Nup composition (Lapetina *et al*., 2017). Differences within the stoichiometry of various Nups between different cell types suggests that cells can use a combination of distinct Nups to assemble NPCs with diverse properties and specialized functions (Raices and D'Angelo, 2012). Nonetheless, regardless of these differences, NPCs across eukaryotes retain a similar basic structure and transport function.

1.2.1 Nuclear pore complex structure.

The NPC is an impressively large structure. It has a molecular mass of approximately 110 MDa in humans and 55 MDa in yeast with an inner channel diameter of approximately 425 Å (Lin and Hoelz, 2019). This channel selectively inhibits macromolecules from moving across the NE, however, molecules that are smaller than ~5 nm in diameter or ~40 kDa in mass can freely diffuse throughout the NPC (Knockenhauer and Schwartz, 2016). As previously mentioned, NPC structure, function, and composition are well conserved across eukaryotes, and to highlight this, a schematic depiction of a human NPC compared to a yeast NPC is presented in (Figure 1.1), which illustrates the conservation between the key structural components of the NPC and the various Nups that comprise them (Neumann *et al*., 2010; Beck and Hurt, 2016).

The NPC is composed of distinct substructures. The major substructures of the NPC include the inner ring which spans the length of the fused inner and outer nuclear membrane, the cytoplasmic and nucleoplasmic rings which are anchored to the inner ring on their respective sides of the NE, along with the cytoplasmic filaments and the nuclear basket which are peripheral substructures that branch out from the cytoplasmic and nucleoplasmic rings, respectively (von Appen and Beck, 2016). Nups can be classified into several broad groups as well, based upon their location and function within the NPC. Generally, these groups include pore membrane Nups, core scaffold Nups, cytoplasmic filament and nuclear basket Nups, as well as FG-repeat Nups (Lin and Holtz, 2019).

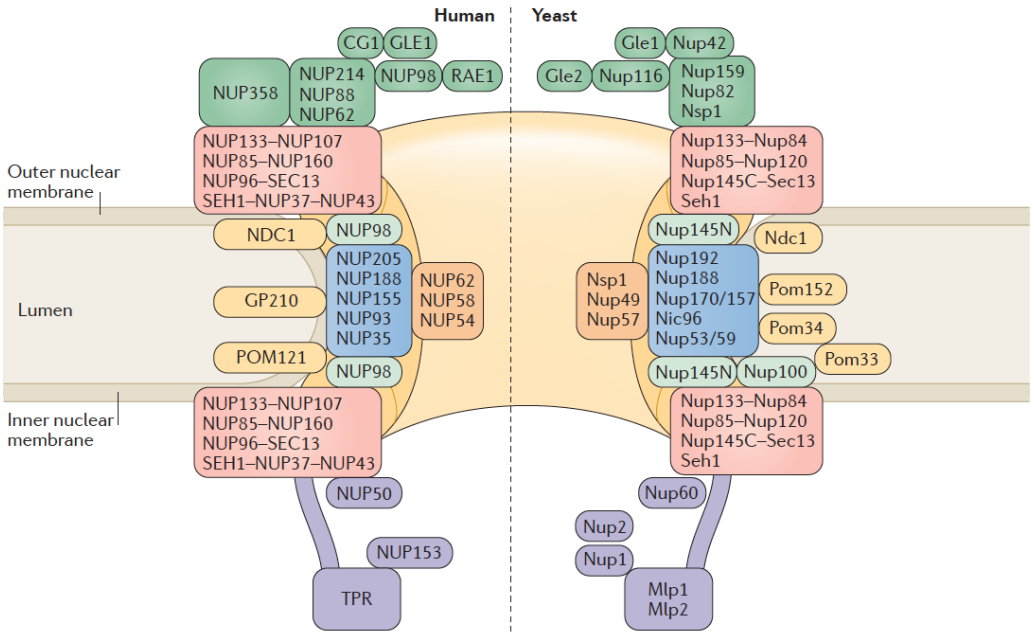

Figure 1.1 Diagram of the conservation between human and *S. cerevisiae* NPCs.

Diagram of an NPC shown in a cut-away view displaying half of an NPC embedded within the NE (which is shown in beige). Conserved Nups from both humans and yeast and are mirrored against each other according to their approximate positions within the NPC and are color-coded according to their subcomplex. Color labels are as follows: yellow = pore membrane Nups; red = Y-complex Nups; blue = interior ring complex Nups; orange = central FG-repeat Nups (list does not include all FG-repeat Nups); green = cytoplasmic filament Nups; purple = nuclear basket Nups. Adapted from Beck and Hurt, 2016. Reproduced with permission from Springer Nature. Original publication DOI: 10.1038/nrm.2016.147.

Pore membrane Nups are transmembrane proteins that reside within the NE. They facilitate NPC assembly and act as anchors for the stability of NPC within the pore (Stavru *et al*., 2006). The core scaffold Nups form the characteristic three-ringed structure of the NPC and are suggested to help stabilize the membrane curvature of the nuclear pore. Scaffold Nups are enriched in α-helical repeats and β-propeller domains allowing for extensive protein-protein interactions which form a complex interconnected network that coat the pore membrane (Alber *et al*., 2007). They form the basic structural framework of the NPC and are essential for NPC assembly and anchorage at the pore (Dultz and Ellenberg, 2010). Scaffold Nups arrange into two subcomplexes, namely, the Y-complex (also called the Nup107-Nup160 complex) and the inner ring complex (also called the Nup93 complex), which are collectively formed by approximately 15-20 different Nups (Anderson *et al*., 2013; Beck and Hurt, 2016). Cytoplasmic filament and nuclear basket Nups help to establish nuclear transport by providing docking sites for various nuclear transport factors and the small GTPase Ran (which will be described later in further detail) (Bley *et al*., 2022). Lastly, FG-repeat Nups, which have domains enriched in phenylalanine (F) and glycine (G) amino acid residues, line the central transport channel of the NPC and ultimately establish the permeability barrier of the NPC (Beck and Hurt, 2016).

1.2.2 FG-repeat nucleoporins.

FG-repeat Nups are characterized as having domains of extensive FG, FXFG, or GLFG repeats (Terry and Wente, 2009). These FG-repeat domains are largely unstructured and are suggested to form a mesh-like network within the

central channel of the NPC (Stelter *et al*., 2011). Several FG-repeat Nups can be found located symmetrically throughout the central channel of the NPC, as is the case for human Nup62 (yeast Nsp1), Nup58 (yeast Nup49), and Nup54 (yeast Nup57). Other FG-repeat Nups have been suggested to be asymmetrically located towards the either cytoplasmic or nucleoplasmic faces of the NPC (Terry and Wente, 2009), although, the exact positioning of these other FG-repeat Nups is much less well understood (Beck and Hurt, 2016). Regardless, it is thought that the disordered FG-repeat domains of the various FG-repeat Nups extend both into the central channel of the NPC and protrude into the cytoplasm and nucleoplasm as well, ultimately forming a selectively permeable barrier which facilitates the transport of molecules into and out of the nucleus (Alber *et al*., 2007; Beck and Hurt, 2016).

1.2.3 GLFG-repeat nucleoporins; human Nup98 and *S. cerevisiae* Nup116.

An interesting class of FG-repeat Nups are the GLFG-repeat Nups. In vertebrates, Nup98 is the only GLFG containing Nup found within the NPC and has been shown to be critical for the nuclear transport of various classes of cellular cargo (Powers *et al*., 1997; Wu *et al*., 2001). Furthermore, Nup98 deletion has been shown to be lethal in mouse models, suggesting that this GLFG-repeat Nup is required for proper cellular function (Wu *et al*., 2001). Nup98 has been suggested to localize to both the cytoplasmic and nucleoplasmic faces of the central channel of the NPC (Rout *et al*., 2000; Griffis *et al*., 2003), and has been shown to have important roles in many cellular processes including, but not limited to, gene expression (Light *et al*., 2003; Capitanio *et al*., 2018), cell cycle regulation (Laurell

et al., 2011), and nuclear transport of both protein and mRNA (Powers *et al*., 1997; Wu *et al*., 2001; Oka *et al*., 2010).

There are three Nup98 counterparts within yeast, and these include Nup100, Nup116, and Nup145N (Cronshaw *et al*., 2002). Single deletion of these genes in the budding yeast *Saccharomyces cerevisiae* have been shown to cause varying effects, with the *Δnup116* gene deletion causing the most dramatic growth rate defects when compared to either *Δnup100* or *Δnup145N* deletion mutants (Wente and Blobel, 1994). Notably, *Δnup116* cells show a temperature sensitive growth defect, only growing at the permissive temperature of 23°C but not at 37°C (Wente and Blobel, 1994). Knockout of Nup100 does not seem to affect the NE structure or transport function of the NPC (Wente *et al*., 1992), however, the knockout of either Nup145N or Nup116 results in abnormal aberrations to the NE, which have been referred to as nuclear herniations (Wente and Blobel, 1993; Wente and Blobel, 1994). Further investigation has revealed that Nup145N knockout does not cause significant nuclear transport defects, however, the knockout of Nup116 leads to significant impairments in nucleocytoplasmic transport (Wente and Blobel, 1994). Genetic interaction studies between these three yeast proteins have shown that the double deletion of both *Δnup100 and Δnup145N* do not cause lethal growth defects in cells, however there is a lethal phenotype associated with the double deletion of *Δnup116* and either *Δnup100* or *Δnup145N* (Wente and Blobel, 1994), ultimately suggesting that there may be functional redundancy between these three Nups. Although, taken together, these reports suggest an important role for Nup116 within *S. cerevisiae* NPCs.

Both human Nup98 and yeast Nup116 are the only nucleoporins within each respective species that contain a Gle2 binding sequence, termed a GLEBS motif (Bailer *et al*., 1998; Griffis *et al*., 2003). This GLEBS motif is both necessary and sufficient to allow for human Rae1 to bind Nup98 (Ren *et al*., 2010) and for *S. cerevisiae* Gle2 to bind Nup116 (Bailer *et al*., 1998). When bound, human Nup98/Rae1 and *S. cerevisiae* Nup116/Gle2 form complexes that have suggested functions in mRNA export from the nucleus (Murphey *et al*., 1996; Ren *et al*., 2010; Iwamoto *et al*., 2010). Since Nup98 and Nup116 are the only Nups that contain a GLEBS motif required for complex formation with nucleoporins Rae1 and Gle2 respectively, it is likely that their incorporation into the NE is required for the stable association of either Rae1 or Gle2 at the NPC of both humans and yeast.

1.3 Nucleocytoplasmic transport.

The NPC maintains selective permeability between the cytoplasm and nucleoplasm by acting as both a barrier and binding partner to various cellular molecules. The NPC allows for the selective movement of an assortment of cargo across the NE, including both protein and RNA. The NPC can accommodate the movement of molecules up to 39 nm in diameter, although, it has been shown that molecules larger than this can be remodeled in order to transverse through the channel (Mehlin *et al*., 1992; Wente and Rout, 2010).

Previous reports have indicated that the NPC restricts the free movement of molecules that are larger than ~5 nm in diameter or ~40 kDa in mass, however, small molecules, ions, and metabolites are able to freely diffuse throughout the

central channel (Knockenhauer and Schwartz, 2016). Molecules that are larger than this size must overcome the energetic barrier posed by the FG-repeat Nups that line the central channel of the NPC, in order to be transported across the NE (Ghavami *et al*., 2016). One way this can be overcome is through interactions with soluble nuclear transport factors (NTFs), which are cellular proteins that facilitate the movement of cargo through the NPC (Macara, 2001; Wente and Rout, 2010). This process of cargo trafficking must be highly regulated so that the intended cargo is transported to the appropriate cellular location.

1.3.1 NLS and NES containing cargo.

Proteins that are destined for transport into and out of the nucleus contain specific sequences and structures that signal for cellular transport machinery to bind and subsequently facilitate translocation through the NPC (Lu *et al*., 2021). These sequences are referred to as either nuclear localization sequences (NLS) or nuclear export sequences (NES) and mediate the targeting of these proteins to their correct cellular location either inside or outside of the nucleus, respectively.

An NLS is generally a short peptide motif that signals for nuclear import and can be located at almost anywhere within the protein sequence (Kosugi *et al*., 2008; Lu *et al*., 2021). Arguably, the most well studied NLS is the classical nuclear localization sequence (cNLS), for which two consensus sequences have been well characterized. The first is a monopartite cNLS which contains a cluster of 4-8 basic amino acid residues, and the second is a bipartite cNLS that contains two clusters of 2-3 basic amino acid residues that are separated by a 9-12 residue linker sequence (Lange *et al*., 2007; Kosugi *et al*., 2009; Lu *et al*., 2021).

There are many other types of NLS that do not contain a cNLS, and these are broadly referred to as non-classical nuclear localization sequences (ncNLS) (Chook and Blobel, 2001). Among this class of NLS, the non-classical PY-NLS has been best studied. The PY-NLS is characterized by 20-30 amino acid residues that assume a disordered structure and contain an N-terminal hydrophobic or basic motif, followed by a C-terminal R/K/H$(X)_{2-5}$PY motif, where X_{2-5} is any sequence of 2–5 residues (Lu *et al*., 2021; Lee *et al*., 2006). Other types of ncNLS have been studied also, but their consensus sequences are much less well characterized. This is, in part, due to the large sequence diversity amongst proteins targeted for nuclear import (Lee *et al*., 2006). Despite significant effort from the scientific community, only a subset of proteins have a defined NLS. Furthermore, there are many proteins that contain a NLS sequence that do not match a known consensus sequence, and there are also proteins that are not targeted for nuclear import which contain sequences that do match a consensus NLS (Kosugi *et al*., 2008). Therefore, it remains extremely difficult to predict nuclear localization sequences in candidate import substrates without significant investigation (Lee *et al.,* 2006).

If a protein is required to be exported from the nucleus, an NES signals for its transport across the NE and into the cytoplasm (Kosugi *et al*., 2008). An NES is characterized broadly as a peptide sequence that is 8-15 residues long and loosely conforms to the consensus sequence Φ1-$X_{2,3}$-Φ2-$X_{2,3}$-Φ3-X-Φ4, where Φ*n* represents leucine, valine, isoleucine, phenylalanine, or methionine, and X is any amino acid residue (Xu *et al*., 2012). However, like mentioned above for NLS sequences, this NES consensus sequence is not present in all proteins targeted for

nuclear export, and additionally, this sequence can also be found in proteins which are not exported from the nucleus (Kosugi *et al*., 2008; Xu *et al*., 2012). Therefore, further investigation is required to fully elucidate the complexities of both nuclear import and nuclear export sequences in eukaryotes.

1.3.2 Nuclear transport factors.

Nuclear transport factors (NTFs) facilitate the movement of protein and RNA cargo across the NE. A large family of NTFs in eukaryotes are referred to as karyopherins, however, karyopherins can also be referred to as importins or exportins depending on their respective transport function (Chook and Blobel, 2001). The mechanism of nuclear transport is well conserved from yeast to humans. Many human karyopherins have yeast counterparts and many nuclear transport pathways are also well conserved (Wozniak *et al*., 1998; Chook and Blobel, 2001; Quan *et al*., 2008; Aitchison and Rout, 2012).

β-karyopherins are a major class of NTFs in humans and yeast. Humans have 20 karyopherin-β genes whereas *S. cerevisiae* contain 14 (Kimura and Imamoto, 2014). In humans, 11 β-karyopherins are suggested to be importins that function to shuttle molecules into the nucleus, 7 are exportins that shuttle molecules out of the nucleus, and 2 are bidirectional nuclear transport factors (Kimura and Imamoto, 2014; Oldrini *et al*., 2017). Although there has been much effort into the study of NTFs in eukaryotes, a unified naming scheme has not been developed. Therefore, in these studies, I will refer to human karyopherins as importins and exportins and I will refer to the yeast counterparts as karyopherins or "Kaps", when applicable.

Human importin-β molecules, and the yeast karyopherin-β counterparts, bind to their cargo mainly through specific interactions with an NLS. Human importin-β1 and the yeast karyopherin-95 (Kap95) counterpart, are the exception to this rule, requiring an additional adaptor protein (see below) to bind NLS containing cargo (Wozniak *et al*., 1998; Aitchison and Rout, 2012; Kimura and Imamoto, 2014). Although it has been proposed that both human importin-β's and yeast karyopherin-β's can interact with unique cargo, there are also instances where a single cargo can be imported into the nucleus by multiple different karyopherin-β's. This strongly implies there is a functional redundancy between different karyopherin-β transport factors, such that these NTFs can compensate for one another and can bind to cellular cargo with varying degrees of promiscuity (Aitchison and Rout, 2012; Leslie *et al*., 2014).

The karyopherin-α family of proteins are also an important class of NTFs and are responsible for recognizing cNLS containing cargo within the cytoplasm. Humans produce 7 importin-α molecules (importin-α1 to -α7) whereas yeast encode for only one karyopherin-α called Kap60 (Aitchison and Rout, 2012; Kimura and Imamoto, 2014). Importin-α's and Kap60 are the adaptor molecules that connect either importin-β1 or Kap95 to cNLS containing cargo. In this manner, a trimeric complex is formed which includes importin-α/β1, or Kap60/95, in complex with a cNLS cargo. Importin-β1 and Kap95 are then ultimately responsible for facilitating import of the trimeric complex through the NPC (Wente and Rout, 2010; Kimura and Imamoto, 2014). As previously mentioned, importin-β1 and Kap95 are the only importin-β's in humans and yeast that require the use of an

adaptor molecule to facilitate an interaction with a cellular cargo, as all other importin-β's (and their respective yeast counterparts) bind directly to cargo to facilitate their translocation through the NPC (Kimura and Imamoto, 2014).

For nuclear protein export, the majority of cargo proteins associate with the nuclear transport factor CRM1, which is also known as Exportin 1 (XPO1) (Thakar *et al*., 2013). In *S. cerevisiae*, CRM1 is also the name associated with this export factor. CRM1-mediated nuclear export has been shown to be conserved in both humans and yeast, and CRM1 has been suggested to be responsible for the export of cargo containing a leucine-rich NES (Wozniak *et al*., 1998; Nguyen *et al*., 2012). In yeast, CRM1 has been shown to be an essential gene and is required for the export of both protein and ribosomal RNA (Toda *et al*., 1992; Stade *et al*., 1997, Ho *et al*., 2000). In humans, CRM1 has been suggested the be the major export factor for the transport of cellular proteins out of the nucleus but it has also been shown to export a subset of cellular RNAs, including ribosomal RNA and various other cellular mRNAs (Hutten and Kehlenback, 2007; Carmody and Wente, 2009).

The bulk of mammalian mRNA export is facilitated by the nuclear transport factor NXF1 (also known as TAP) and NXT1 (also known as p15), which together, form an NXF1:NXT1 dimer. The binding of the NXF1:NXT1 dimer to mRNA is facilitated by cellular adaptor proteins which increases the affinity of NXF1:NXT1 to their cargo mRNA (Smulevitch *et al*., 2005; Delaleau and Borden, 2015). The yeast Mex67 protein is related to the human NXF1 protein, and the yeast Mtr2 protein is related to human NXT1. The Mex67:Mtr2 dimer has also been shown to be essential for the nuclear export of mRNA in yeast, and interestingly, human

NXF1:NXT1 can functionally replace yeast Mex67:Mtr2, suggesting that these export factors have a conserved role in both humans and *S. cerevisiae* (Katahira *et al*., 1999).

Ultimately, the role of NTFs is to shuttle cellular cargo through the NPC. As mentioned previously, the energetic barrier posed by the FG-Nups that line the central channel of the NPC must be overcome to allow for the transport of energetically unfavorable cargo across the NE (Ghavami *et al*., 2016). This energetic barrier is largely overcome by the interactions made between NTFs and the FG-Nups within the central channel of the NPC, allowing for the facilitated nuclear transport of cargo proteins that are larger than ~5 nm in diameter (Ghavami *et al*., 2016). Compared to other cytoplasmic proteins NTFs have a higher surface hydrophobicity, and structural analysis has indicated that hydrophobic side chains of FG-Nups can interact with the hydrophobic pockets on the surface of NTFs (Bayliss *et al*., 2000; Ribbeck *et al*., 2002). NTFs have been suggested to travel across the NPC through these transient and low-affinity contacts with the numerous FG-repeat domains present within the central channel of the NPC, allowing for the shuttling of cellular cargo across the NE (Tetenbaum-Novatt *et al*., 2012). Interestingly, cargo that is normally blocked from nuclear import can transverse through the NPC without the use of an NTF by modifying the surface of the protein with hydrophobic residues (Naim *et al*., 2009). Ultimately, this suggests that a certain level of surface hydrophobicity is required for cargo to be transported though the NPC, however, a unified model for how NTF-cargo complexes mechanistically transverse across the NPC remains controversial.

1.3.3 Directionality of transport.

Movement of NTF-cargo complexes though the meshwork of FG-repeat Nups is suggested to be a passive process, however, the last part of the nuclear transport process does require energy expenditure (Macara, 2001). Directionality of transport ultimately depends on a nucleocytoplasmic gradient of the small GTPase Ran, which is found in either a GTP or GDP bound form (Cavazza and Vernos, 2016). The basic process of nuclear transport is conserved between humans and *S. cerevisiae*, however for simplicity, the mechanism of nuclear transport will be described below mainly referring to human nuclear transport proteins. Additionally, a simplified schematic of nuclear import and export is depicted in (Figure 1.2), illustrating the basic process of nuclear transport across the NE, which will be further elaborated on in the next sections.

To maintain a gradient of RanGTP across the NE, the Ran guanine nucleotide exchange factor (RanGEF), which is called RCC1, is physically tethered to chromatin in order to restrict its localization to within the nucleoplasm (Nemergut *et al*., 2001). In the cytoplasm, the Ran GTPase-activating protein (RanGAP) is physically tethered to the cytoplasmic filament nucleoporin, Nup358, ultimately restricting the hydrolysis of RanGTP to within the cytoplasm (Mahajan *et al*., 1997). Of note, the *S. cerevisiae,* RanGAP (Rna1p) is largely a cytoplasmic protein that not tethered to the NPC, potentially owing to a lack of a Nup358 counterpart in *S. cerevisiae* (Traglia *et al*., 1996; Beck and Hurt, 2016). Regardless, by spatially separating the localization of RanGEF and RanGAP across the NE, a nucleocytoplasmic gradient of RanGTP is established, where levels of RanGTP are

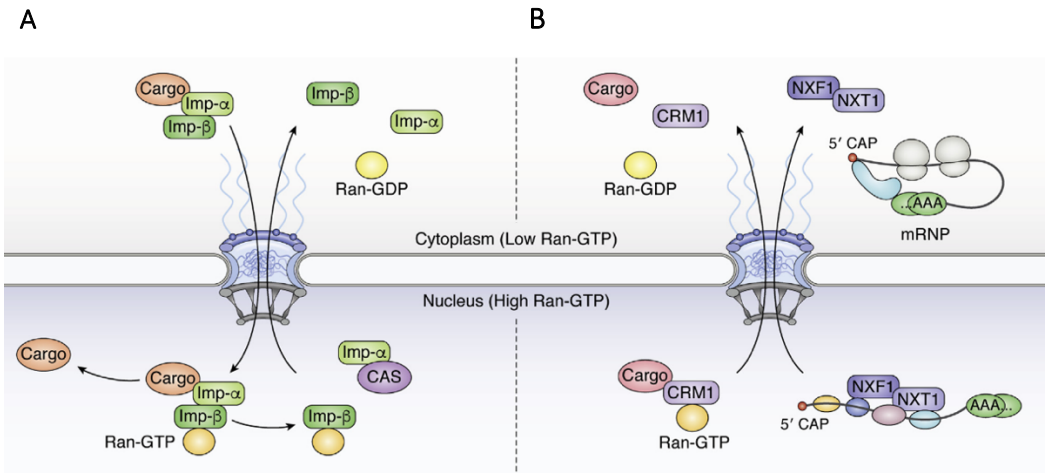

Figure 1.2 Schematic representation of the nuclear import and export cycle. **(A)** In the classical nuclear import pathway, a cargo containing a cNLS is recognized by nuclear import factor importin-α (imp-α), followed by the binding of importin-β1 (imp-β1), which docks and facilitates movement of the imp-α/β1-cargo complex through weak and transient interactions with the FG-repeat Nups that line the central channel of the NPC. Once in the nucleus, the binding of Ran-GTP to importin-β1 causes the disassembly of the import complex and release of the cargo into the nucleoplasm. Importin-β1 bound to Ran-GTP is transported back to the cytoplasm, where the hydrolysis of RanGTP leads to dissociation of importin-β1 and RanGDP. Importin-α is recycled back into the cytoplasm by its nuclear export factor, CAS. **(B)** For nuclear export, a cargo with an NES is typically bound by the export factor CRM1 which is complexed to RanGTP. CRM1 then docks the cargo complex at the nucleoplasmic face of the NPC and facilitates transport through the central channel. Upon entry into the cytoplasm RanGTP is hydrolysed, and this promotes dissociation of the export complex. CRM1 also mediates the export of a subset of cellular RNAs in a similar RanGTP dependent manner, using additional adaptor proteins to facilitate CRM1 binding to RNA (not depicted above). The export of the bulk of cellular mRNA requires the nuclear transport factors NXF1/NXT1 which dock and facilitate movement of the mRNA particle through the NPC. Export of mRNA differs from protein export because mRNAs are bound by many additional adaptor molecules and form large messenger ribonucleoprotein (mRNP) complexes. NXF1:NXT1 nuclear export is RanGTP independent, instead, RNA cargo are released into the cytoplasm in an ATP-dependent manner via the DEAD-box helicase DDX19. During export into the cytoplasm, the mRNP undergoes remodeling events facilitated by DDX19, where transport factors and adaptor molecules are removed from the mRNP complexes allowing for subsequent translation of the mRNA within the cytoplasm. Reprinted from Shen *et al*., 2021. Original publication DOI: 10.1016/j.jbc.2021.100856. This is an open access article under the CC BY-NC-ND license (http://creativecommons.org/licenses/by-nc-nd/4.0/).

substantially higher in the nucleus than within the cytoplasm (Görlich *et al*., 1996).

During nuclear import, importin molecules bind to their NLS containing cargo within the cytoplasm and subsequently facilitate their nuclear import through weak and transient interactions with the FG-Nups that line the central channel of the NPC (Tetenbaum-Novatt *et al*., 2012). Once in the nucleoplasm, the binding of RanGTP to the importin reduces the affinity of the importin for its cargo, which ultimately leads to the release of the NLS containing cargo into the nucleoplasm. The newly bound importin-RanGTP complex is then recycled back into the cytoplasm where upon exit from the NPC RanGTP hydrolysis is triggered by RanGAP, leading to the dissociation of the importin-RanGDP complex and allowing for another cycle of nuclear import to begin (Lui and Haung, 2009).

During nuclear export, an exportin in complex with RanGTP binds to nucleoplasmic cargo containing an NES and facilitates its docking and translocation through the central channel of the NPC. Upon entry into the cytoplasm, RanGTP hydrolysis is induced by RanGAP, causing a complete dissociation of the exportin, its cargo, and RanGDP into the cytoplasm. The exportin is then recycled back into the nucleus where it can participate another round of nuclear export (Lui and Haung, 2009).

During the nuclear import and export cycles RanGDP is released into the cytoplasm. For its import back into the nucleus RanGDP complexes with its nuclear transport factor, NTF2, which facilitates its transport through the NPC. Inside of the nucleoplasm RanGDP interacts with the RanGEF, RCC1, for exchange of GDP

with GTP, replenishing the RanGTP gradient across the NE and ultimately allowing for further cycles of nucleocytoplasmic transport to occur (Weis, 2003).

While protein import and export depend on an established RanGTP gradient, the nuclear export of the bulk of cellular mRNA do not require a Ran gradient. As mentioned previously, the NXF1:NXT1 dimer is the major transport factor responsible for the nuclear export of most cellular mRNA (Smulevitch *et al*., 2005; Delaleau and Borden, 2015). NXF1:NXT1 interact with mRNA, along with various other adaptor molecules, to facilitate the movement of these large complexes through the meshwork of FG-Nups within the central channel of the NPC. On the cytoplasmic face of the NPC interacting with Nup214, is an ATP-dependent DEAD-box helicase (human DDX19, yeast Dbp5) which is responsible for remodeling the NXF1:NXT1:mRNP complex as it emerges from the pore. This ultimately releases the transport factors from the transcript and ensures correct directionality of transport (Napetschnig *et al*., 2009; Montpetit *et al*., 2011). Undeniably, mRNA export is much more complex than the simplified explanation given above, as RNA export requires the addition of a variety of different adaptor proteins for the export of these large cellular cargo (Xie and Ren., 2019).

1.4 Nuclear import.

There are multiple different nuclear transport pathways that use a variety different transport factors to accomplish nuclear import, and these pathways and factors are largely conserved from humans to yeast (Wozniak *et al*., 1998; Stewart, 2007). The nuclear transport pathway that has been best characterized in

eukaryotes is the classical nuclear import pathway, which facilitates the nuclear import of protein cargo containing a cNLS (Figure 1.2A) (Lange *et al*., 2020).

1.4.1 Classical nuclear import.

The classical nuclear import pathway requires coordinated functions between the importin-α molecules which bind to cellular cargo, and the importin-β1 molecules that enable docking and movement through the NPC. In *S. cerevisiae* the Kap60/95 nuclear transport factors function comparatively, but without the use of multiple karyopherin-α molecules (Aitchison and Rout, 2012; Lu *et al*., 2021).

Cytoplasmic cargo containing a cNLS are first recognized in the cytoplasm by an importin-α molecule, or in the case of *S. cerevisiae*, Kap60 is responsible for binding cNLS containing cargo (Aitchison and Rout, 2012). In humans, some cNLS cargo proteins are preferentially transported into the nucleus by specific importin-α transporters, however, others can be recognized by multiple different importin-α's (Wirthmuller *et al*., 2013; Pumroy and Cingolani, 2015). At their N-terminus importin-α molecules, and Kap60, contain an importin-β1 binding (IBB) domain, which is then followed by 10 Armadillo (ARM) repeats, and a C-terminal domain that interacts with the nuclear export factor, CAS (which is called Cse1 in *S. cerevisiae*) (Herold *et al*., 1998; Cingolani *et al*., 1999; Macara, 2001; Lu *et al*., 2021).

The ARM repeats of importin-α's and Kap60 function to recognize and bind protein cargo containing a cNLS (Cingolani *et al*., 1999). The binding of cargo leads to a conformational change in importin-α (or Kap60) exposing its IBB

domain, triggering binding of importin-β1 (or Kap95) and leading to the formation of an importin-α/β1-cargo complex (Lott and Cingolani, 2011). Importin-β1 then directs the trimeric cargo-importin-α/β1 complex to the NPC. Both importin-α and importin-β1 have been suggested to contribute to the translocation of the trimeric complex across the NE, however, it is thought that importin-β1 forms the major interactions with the various FG-repeat Nups that line the central channel of the NPC (Ogawa *et al*., 2012; Lu *et al*., 2021).

Once in the nucleus, RanGTP binding to importin-β1 leads to a conformational change in importin-β1, causing release of the IBB domain of importin-α. The RanGTP-importin-β1 complex is then recycled back across the NE where the hydrolysis of RanGTP triggered by RanGAP (Rna1p in *S. cerevisiae*) allows for the release of importin-β1 back into the cytoplasm. Within the nucleus, nucleoporin Nup50 (Nup2 in *S. cerevisiae*) helps catalyze the cNLS cargo dissociation from importin-α, and importin-α is then exported from the nucleus in conjugation with its nuclear export factor, CAS bound to RanGTP (Cse1 in *S. cerevisiae*) (Macara, 2001; Stewart, 2007; Lange *et al*., 2020). Upon export at the cytoplasmic face of the NPC, hydrolysis of Ran-GTP allows for the complete dissociation of the importin-α, CAS, RanGDP complex within the cytoplasm. RanGDP is then recycled back into the nucleoplasm by its nuclear import factor NTF2 (Nft2p in *S. cerevisiae*), and CAS readily crosses back through the NPC on its own (Corbett and Silver, 1996; Ribbeck *et al*., 1998; Kutay *et al*., 1997; Macara, 2001; Lu *et al*., 2021).

1.4.2 Nup98 and Nup116 in protein import.

Nup98 is an FG-repeat Nup that contains FG, FXFG, and GLFG repeat domains, and localizes to both the nuclear and cytoplasmic faces of the central channel of the NPC (Radu *et al*., 1995; Griffis *et al*., 2003). Nup98 is a distinct FG-repeat Nup because it is the only GLFG-repeat containing Nup in mammalian cells (Iwamoto *et al*., 2010). Nup98 has been suggested to act as a docking site for NTFs at the central channel of the NPC, due to its unique GLFG-repeat domains (Radu *et al*., 1995; Lau and Webber, 2020). Importin-β1 has been shown to physically interact with Nup98, and Nup98 has also been shown to help facilitate the dissociation of cargo from importin-β2 at the nucleoplasmic face of the NPC, suggesting that Nup98 may play an important role in specific nuclear transport pathways (Moroinau *et al*., 1997; Fontoura *et al*., 2000). Indeed, the knockout of Nup98 in embryonic murine cells has been shown to inhibit the nuclear transport of cargo proteins imported by the importin-α/β1 pathway, as well as the importin-β2 pathway (Wu *et al*., 2001). However, Nup98 knockout does not seem to affect the importin-β3 nuclear import pathway, suggesting that Nup98 is not required for the nuclear import of proteins transported by this NTF (Wu *et al*., 2001). Together, this suggests that Nup98 may have specific functions in various nuclear import pathways, and that Nup98 is likely required for the proper nuclear import of various importin-α/β1 and importin-β2 cargo proteins.

Nup116 in *S. cerevisiae* has also been shown to have an essential role in mediating protein import. It has been previously mentioned that the knockout of Nup116 in yeast leads to a temperature sensitive phenotype, with extensive NE

aberrations and a block of nucleocytoplasmic transport at 37ºC (Wente and Blobel, 1993). Further analysis has revealed that deletion of the GLFG-repeat domain of Nup116 also leads to a temperature sensitive phenotype, and at a semi-permissive growth temperature, cells lacking the Nup116 GLFG region have impaired import capacity (Iovine *et al*., 1995). Additionally, Nup116 has been shown to interact with Kap95 suggesting a role for Nup116 in cNLS mediated protein import (Iovine *et al*., 1995; Allen *et al*., 2001). Interestingly, there are multiple GLFG-repeat nucleoporins within *S. cerevisiae,* including Nup49, Nup57, Nup100, and Nup145N, however, the GLFG-repeat regions of these nucleoporins do not seem to be required for proper NPC function (Wente *et al*., 1992; Wente and Blobel, 1994; Iovine *et al*., 1995). Collectively, this suggests that Nup116 is a unique GLFG-repeat nucleoporin within *S. cerevisiae* and is required for proper nuclear import.

1.5 Nuclear export.

As mentioned previously, the major nuclear transport factor that facilitates protein export from the nucleus in both humans and *S. cerevisiae* is CRM1 (Nguyen *et al*., 2012). CRM1 has also been shown to be involved in the export of ribosomal RNAs as well as various mRNAs, however unlike in protein export, CRM1 must use an adaptor protein to facilitate its binding to target RNA (Carmody and Wente, 2009; Delaleau and Borden, 2015). The NXF1:NXT1 heterodimer is the main nuclear export factor responsible for facilitating the nuclear export of the bulk of cellular mRNA in a complex process involving the use of many additional adaptor

molecules, which will be further described below (Carmody and Wente, 2009; Rodríguez-Navarro and Hurt, 2011).

1.5.1 mRNA export.

Messenger RNA export is a highly regulated process and is necessary for both gene expression and for the regulation of physiological responses within eukaryotic cells. Like protein import, mRNA processing and export pathways are well conserved between humans and *S. cerevisiae* (Serpeloni *et al*., 2011; Sen *et al*., 2019).

There are several main processing events that occur during the formation of the mature mRNA transcript. When a newly formed RNA transcript is around 20-30 nucleotides in length, a 7′-methalguanosine cap is added to its 5′-end, and adaptor molecules of the cap binding complex, CBP20 (Cbc2p in *S. cerevisiae*) and CBP80 (Sto1p in *S. cerevisiae*) bind to the 5′-cap to protect the RNA from exonuclease degradation (Carmody and Wente, 2011; Sen *et al*., 2019). Next, if a transcript undergoes splicing, a set of adaptor molecules are deposited at the site of exon fusion, which is collectively referred to as the exon-junction complex (Carmody and Wente, 2011). Both capping and splicing are important for the recruitment of the highly conserved transcription-export complex, termed the TREX complex, which links transcription with mRNA export. The TREX complex is composed of an RNA helicase UAP56 (Sub2 in *S. cerevisiae*), the RNA binding adaptor protein ALY (Yra1 in *S. cerevisiae*), and the THO complex, which in itself, is composed of multiple proteins that are conserved between *S. cerevisiae* and humans. The THO complex associates with the nascent mRNA during transcription

and recruits the other members of the TREX complex to the transcript. The final pre-mRNA processing event occurs when the 3′-end of the transcript is cleaved and polyadenylated (Carmody and Wente, 2011; Serpeloni *et al*., 2011; Aitchison and Rout, 2011). Together with all its adaptor proteins, the mRNA is referred to as an mRNP (messenger ribonucleoprotein) and requires the use of nuclear export factors to facilitate its transport through the NPC and into the cytoplasm (Hieronymus and Silver, 2004).

The bulk of mRNA export in cells is accomplished by the NXF1:NXT1 heterodimer (Mex67:Mtr2 heterodimer in *S. cerevisiae*), which is recruited to the mRNP particle through the TREX component ALY (*S. cerevisiae.* Yra1). The NXF1:NXT1 dimer then recruits the mRNP to the nucleoplasmic face of the NPC, where it facilitates docking and transport across the NPC through interactions with the FG-Nups lining the central channel (Carmody and Wente, 2011). Directionality of mRNP transport is dependent on the cytoplasmic localization of the DDX19 helicase (Dbp5 in *S. cerevisiae*), which is a member of the DEAD-box family of proteins. DEAD-box helicases are characterized as having both RNA-dependant ATPase and ATP-dependent RNA unwinding activities, and the DEAD-box helicase DDX19 has been suggested to have important roles in remodeling the mRNP particle as it exits the NPC (von Moeller *et al*., 2009). DDX19 is part of the mRNA export platform that also contains Gle1, Nup42, Nup214, Nup98, and Rae1 (Gle1, Nup42, Nup159, Nup116, and Gle2 in *S. cerevisiae*), which is located on the cytoplasmic face of the NPC (Xie and Ren, 2019). When the mRNP particle emerges, it associates with DDX19 and the nucleoporin Gle1. Gle1 ultimately

stimulates the ATPase activity of DDX19, converting it from an ATP to an ADP bound state. This has been suggested to induce a conformational change in DDX19 that allows it to remove a subset of proteins from the mRNP complex as it emerges from the cytoplasmic face of the NPC, including the NXF1:NXT1 transport factors (von Moeller *et al*., 2009; Carmody and Wente, 2011). This then ultimately allows for release of the mRNP particle into the cytoplasm, where it can then be targeted by translation machinery.

Unlike NXF1:NXT1 mediated nuclear export, CRM1 nuclear export is dependent on a RanGTP gradient in both humans and *S. cerevisiae*. In the nucleus CRM1 is bound to RanGTP, and since CRM1 it is not an RNA binding protein itself, it requires an adaptor protein to associate with its target RNA. There have been several adaptor proteins identified in various RNAs exported by CRM1, but this has not been extensively characterised (Carmody and Wente, 2011). However, once bound to an RNA, CRM1 facilitates the docking and transport of the RNA complex through the NPC, where the hydrolysis of RanGTP triggered by RanGAP on the cytoplasmic face of the NPC dissociates CRM1 from the exporting RNA complex (Hutton and Kehlenback, 2007; Carmody and Wente, 2011).

1.5.2 Nup98 and Nup116 in nuclear export.

Regardless of the pathway of nuclear export, the weak and transient interactions facilitated by the various NTFs and the FG-Nups that line the central channel of the NPC are crucial for the transport of cargo across the NE.

Among the many functions of Nup98, this GLFG repeat Nup has also been suggested to facilitate the nuclear export of RNA. As previously mentioned, human

Nup98, and *S. cerevisiae* Nup116, are the only Nups in each species to contain a Gle2 binding sequence, also termed a GLEBS motif (Bailer *et al*., 1998; Griffis *et al*., 2003). Rae1, and its yeast counterpart Gle2, have been shown to bind to the GLEBS motif of Nup98 and Nup116 respectively, and this GLEBS motif has been shown to be both necessary and sufficient for either Rae1 or Gle2 binding (Bailer *et al*., 1998; Ren *et al*., 2010).

Rae1 and Gle2 are both Nups that are suggested to shuttle between the nucleoplasm and cytoplasm in a RanGTP-independent manner (Pritchard *et al*., 1999). Both human Rae1 and *S. cerevisiae* Gle2 have been suggested to function in facilitating RNA export from the nucleus through their interactions with the GLEBS motif of either Nup98 or Nup116 (Murphy *et al*., 1996; Pritchard *et al*., 1999; Ren *et al*., 2010). Various mutations in yeast Nup116 and Gle2 have been shown to cause poly-A RNA export defects, however, protein import is not noticeably affected in Gle2 mutants (Wente and Blobel, 1993; Murphy *et al*., 1996). Deletion of the GLEBS motif in Nup116 has been shown to cause temperature sensitive growth defects and NE herniations that can be overcome by the insertion of the Nup116 GLEBS motif into Nup100, which is a paralogue of Nup116 that does not contain an endogenous GLEBS motif (Bailer *et al*., 1998). Together, this suggests that targeting of Gle2 to the NE is dependent on the GLEBS motif of Nup116, and that the binding of Gle2 to the NPC is required for proper NPC function in *S. cerevisiae.*

In mammalian systems, the binding of human Rae1 to Nup98 is suggested to create a hydrophobic mRNA binding pocket capable of interacting with single

stranded RNA's (Ren *et al*., 2010), however, the precise function of Rae1 in mammalian RNA export remains to be determined (Xie and Ren, 2019). For example, the Nup98/Rae1 complex has been shown to be upregulated during viral infection, and the targeting of this complex by viral proteins has been shown to block the export of host RNA from the nucleus (Faria *et al*., 2005; Quan *et al*., 2014; Addetia *et al*., 2021). This would suggest that Rae1 and Nup98 have important functions in RNA export, however, the depletion of Rae1 does not seem to cause noticeable RNA export defects on its own (Rajani *et al*., 2012, Makio *et al.,* in preparation). Therefore, the specific mechanism as to how Rae1 functions in RNA export requires further investigation.

Besides its binding to Rae1, Nup98 has also been shown to physically interact with the nuclear export factor NXF1 (Belvins *et al*., 2003). Both Rae1 and Nup98 can interact with NXF1 individually, but they can also form a ternary complex consisting of a Nup98-Rae1-NXF1 trimer. However, when Nup98 and Rae1 are in a complex, Rae1 no longer interacts directly with NXF1, suggesting a possible mechanism whereby Rae1 may function to deliver NXF1 to Nup98. Moreover, NXF1 has been shown to have a strong preference for binding to GLFG repeats, suggesting that Nup98 likely plays an important role in the export of RNA facilitated by the NXF1 nuclear transport factor (Belvins *et al*., 2003). Nup98 has also been suggested to facilitate the docking of mRNP complexes near the DDX19 DEAD-box helicase to allow for remodeling of the mRNP complex as it emerges from the cytoplasmic face of the NPC, further suggesting a role for Nup98 in NXF1-mediated mRNA export (Xie and Ren, 2019). Coimmunoprecipitation studies from

S. cerevisiae whole cell lysates have also revealed that Nup116 and Mex67 (the NXF1 counterpart) physically interact, and further analysis has confirmed the direct interactions between the GLFG regions of Nup116 and the Mex67 transport factor (Strawn *et al*., 2001). Together, these results suggest that both Nup98 and Nup116 play important roles in mRNA export through the interactions made between the NXF1 or Mex67 export factors and the GLFG repeats of either Nup98 or Nup116, respectively.

Not only has Nup98 been shown to bind to the NXF1 export factor, Nup98 has also been shown to interact with CRM1, the export factor responsible for facilitating both the nuclear export of the majority of nucleoplasmic cargo proteins containing an NES, and the export of a variety of cellular RNAs (Ho *et al*., 2000; Hutten and Kehlenback, 2007; Carmody and Wente, 2009). Previous investigations have shown that Nup98 interacts with CRM1 in a RanGTP dependent manner, and that the GLFG-repeat domains of Nup98 are sufficient for binding to CRM1, suggesting that Nup98 has functions in CRM1 mediated export (Oka *et al*., 2009). Furthermore, Nup98 fusion proteins found in various human leukemias have been shown to inhibit the export of various CRM1 cargo, further suggesting a role for Nup98 in CRM1-mediated nuclear export (Takeda *et al*., 2009). In *S. cerevisiae*, Nup116 has been shown to also interact with CRM1 (Allen *et al*., 2001), however, the deletion of the GLFG-repeat domains of Nup116 does not lead to noticeable RNA export defects (Terry and Wente, 2007). Since *S. cerevisiae* expresses multiple Nups containing GLFG-repeat domains, this may indicate a functional

redundancy between the various GLFG containing Nups of *S. cerevisiae* in facilitating CRM1-mediated nuclear export.

Taken together, these reports ultimately suggest an important role for both human Nup98 and *S. cerevisiae* Nup116, in various nuclear export pathways.

1.6 Nuclear transport during viral infection.

The regulation of nucleocytoplasmic transport is critical for maintaining the proper functioning of eukaryotic cells. The controlled movement of both RNA and protein across the NE allows for a complex system of gene regulation and expression, which is critical for maintaining cellular homeostasis. Equally as critical, the regulation of nucleocytoplasmic transport during viral infection allows for the inducible expression of a subset of cellular genes required for an effective host antiviral response, which is necessary to inhibit viral propagation. Unsurprisingly, to combat these antiviral defenses, many viruses have evolved mechanisms to inhibit antiviral signalling pathways and to hijack host machinery in order to create an environment conducive for viral replication (Tessier *et al*., 2019; Shen *et al*., 2021).

1.6.1 Cellular response to viral infection: the type-1 interferon pathway.

Upon viral invasion, cells must employ a strategic and regulated response to effectively combat viral infection. The first line of host defence against viruses is the innate immune response, which is a complex network of signal transduction pathways that coordinate a cellular response against foreign pathogens. The innate immune response is an evolutionarily conserved response across vertebrates, highlighting the importance of this complex system amongst higher eukaryotes

(Romo *et al*., 2016; Shen *et al*., 2021). In particular, the type-1 interferon (IFN) response is an effective and robust first line of defence against many pathogens, including viruses. Type-1 IFN production and release from infected cells is critical for the coordination of an antiviral immune response and for the suppression of viral replication during the early stages of infection (Huang *et al*., 2019; Shen *et al*., 2021). Critical to the regulation of these processes is the nuclear import of various transcription factors, and the nuclear export of various cellular RNAs whose expression are required for an effective antiviral defence. A schematic of the type-1 IFN response can be referred to in (Figure 1.3), indicating the major signaling cascades and the major transcription factors activated during a typical antiviral response, which is described in further detail below.

Cells of the innate immune system use pattern recognition receptors (PRRs) to identify foreign invaders. Interactions between a PRR and a pathogen associated molecular pattern (PAMP), which are molecular motifs conserved within specific classes of pathogens, triggers the innate immune response. The PRR's in vertebrates function to detect PAMPs which are present in both the extracellular and intracellular environments (Tompson *et al*., 2011; Shen *et al*., 2021). Toll-like receptors (TLRs) are the most extensively studied PRR's. They are transmembrane proteins that localize on the plasma membrane and within endosomal vesicles and are responsible for sensing a large variety of PAMPs including components of viral particles and viral nucleic acids. Within the cytoplasm, another class of PRR called retinoic acid-inducible gene I-like receptors (RLRs) recognize and respond to viral cytoplasmic RNA. The two main RLRs are RIG-1 and MDA-5. RIG-1 recognizes

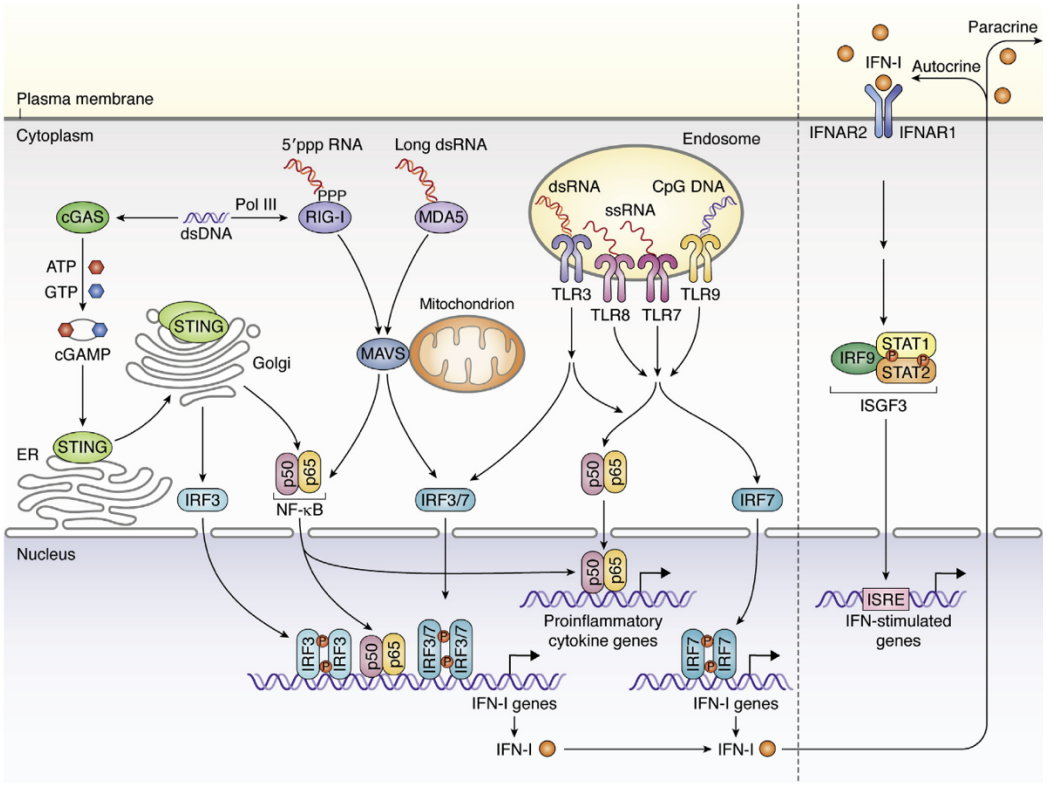

Figure 1.3 Activation of the type-1 IFN response initiated by host pattern recognition receptors.
Host cell PRRs initiate distinct signaling cascades that lead to the activation and nuclear translocation of transcription factors, which include IFN-regulatory factor 3 (IRF3), IRF7, and NF-κB. Once in the nucleus, these transcription factors then stimulate the expression of specific genes, including type-1 interferons (IFN-1) and proinflammatory cytokine genes. Once produced, type-1 IFNs are then secreted from cells, and can either bind to the infected cell or a neighboring cell through the type-1 interferon receptors (IFNAR) that reside on the surface of the plasma membrane. This initiates an antiviral signaling cascade, leading to the phosphorylation of transcription factors STAT1 and STAT2 with subsequent association of IRF9. This complex is referred to as IFN-stimulated gene factor 3 (ISGF3) and is imported into the nucleus where it can bind to ISRE containing promoters found within IFN-stimulated genes (ISGs). The expression of ISGs are required for an effective cellular antiviral response. Reprinted from Shen *et al.*, 2021. Original publication DOI: 10.1016/j.jbc.2021.100856. This is an open access article under the CC BY-NC-ND license (http://creativecommons.org/licenses/by-nc-nd/4.0/).

5′-triphosphorylated uncapped single stranded RNA (ssRNA) which is common in many viral genomes, and short double stranded RNA (dsRNA) which is a common by-product of viral replication. MDA-5, on the other hand, recognizes long dsRNA that is not usually present in uninfected cells (Tompson *et al*., 2011; Shen *et al*., 2021). Additionally, other cytoplasmic PRRs like the cyclic GMP-AMP synthase (cGAS) can recognize various forms of cytosolic DNA, including the DNA derived from DNA virus replication, the DNA derived from reverse transcription of retroviral genomes, as well as the presence of cytoplasmic chromosomal DNA that can result from viral infection (Shen *et al*., 2021; Zhou *et al*., 2021).

Ultimately, the recognition of viral PAMPs by these various PRRs leads to a downstream activation and nuclear translocation of multiple cellular transcription factors necessary for the expression of genes required to induce an antiviral cellular response. TLR activation leads to the downstream activation of NF-κB (which consists of the proteins p65 and p50), interferon regulatory factor 3 (IRF3), and interferon regulatory factor 7 (IRF7). PAMP recognition by RIG-1 or MDA5 leads to the stimulation of the mitochondrial antiviral signalling protein (MAVS) which induces the activation of NF-κB, IRF3, and IRF7 as well, and activation of the cGAS pathway by cytoplasmic DNA leads to the activation of NF-κB and IRF3 (Ren *et al*., 2020; Shen *et al*., 2021). The activation of these transcription factors triggers their nuclear import, where inside of the nucleus, NF-κB, IRF3, and IRF7 function to activate transcription of proinflammatory genes and type-1 IFN's. IFN-α and IFN-β, the major type-1 interferons, are transcribed within the nucleus upon the nuclear localization of NF-κB, IRF3, and IRF7, and their mRNA is suggested

to be exported from the nucleus by the CRM1-mediated nuclear export pathway (Kimura *et al*., 2004; Burke *et al*., 2021).

Once produced, type-1 IFNs are excreted from cells where they then bind to the type-1 IFN receptors that reside on the surface of the cell that produced them, or on the surface of neighboring cells. Regardless, the binding of type-1 IFNs trigger a signalling cascade that leads to the phosphorylation of the STAT (Signal Transducers and Activators of Transcription) proteins (Darnell *et al*., 1994; Shen *et al*., 2021). Upon phosphorylation, STAT1 molecules can either form a homodimer with itself, or they can form a heterodimer with STAT2 which then further recruits the IRF9 protein. Together, this complex is referred to as the interferon stimulated gene factor 3 (ISGF3) complex, which is then targeted for nuclear import. Once in the nucleoplasm the ISGF3 complex can then bind to DNA containing an interferon stimulated response element (ISRE) which is located within the promoter regions of IFN-stimulated genes (ISGs) (Fu *et al*., 1990; Shen *et al*., 2021). Ultimately, the STAT1-induced activation of ISGs is required for the expression of antiviral proteins which are required to fight viral infection (Schoggins, 2014).

Not surprisingly, the nuclear import of all the transcription factors mentioned above require the use of nuclear transport factors to mediate their nuclear import, however, they must first be post-translationally modified to facilitate their localization to within the nucleus. NF-κB is typically associated in the cytoplasm bound to inhibitor of κB (IκB) proteins. Activation of NF-κB occurs when IκB proteins are phosphorylated and degraded after PAMP recognition by cellular PRRs. The dissociation of IκB from the NF-κB molecules reveals its NLS, and NF-

κB can then be imported into the nucleus using either importin-α3 or importin-α4, in complex with importin-β1 (Biancalana *et al*., 2021; Shen *et al*., 2021). IRF3 nuclear retention, rather than its localization, is stimulated by its phosphorylation (Kumar *et al*., 2000). IRF3 contains both an NES and bi-partite cNLS, however, its nuclear export is more rapid than its import and therefore localizes mainly within the cytoplasm under normal cellular conditions. When IRF3 is phosphorylated and imported into the nucleus, its phosphorylation stimulates its association with other nuclear proteins, leading to a retention of IRF3 in the nucleus during viral infection (Kumar *et al*., 2000). IRF3 has been shown to be imported into the nucleus using either importin-α3 or importin-α4, in complex with importin-β1 (Zhu *et al*., 2015; Shen *et al*., 2021). The STAT molecules are activated through phosphorylation allowing for STAT1:STAT1 or STAT1:STAT2 dimerization. During dimerization, STAT1 undergoes a conformational change that exposes a dimer specific NLS allowing for the binding of importin-α5 with subsequent importin-β1 association and transport into the nucleus (Nardozzi *et al*., 2010; Shen *et al*., 2021).

Since the nuclear import of transcription factors, and the nuclear export of both ISGs and type-1 IFN RNA are crucial for the activation of an effective antiviral response, it is not surprising that many viruses have evolved mechanisms to target the nucleocytoplasmic transport of these innate immune molecules.

1.6.2 Viral interactions with the Nup98/Rae1 complex inhibit host nuclear transport during infection.

Critical to the viral life cycle is its ability to both inhibit host cellular processes and to usurp host cellular machinery. Not only have viruses evolved

mechanisms to inhibit the nucleocytoplasmic transport of host proteins and RNAs required for an effective immune response, but they have also evolved mechanisms to disrupt host nuclear transport pathways and NPC functions to promote viral replication. Viruses such as Adenovirus, HSV-1, Influenza A, HIV-1, and HBV all have a nuclear stage in their viral replication cycle and require both the host NPC, and components of the host cellular transport machinery to allow for import into the nucleus (Wu *et al*., 2007; Fay and Panté, 2015; Shen *et al*., 2021). Also important to many viruses, is the inhibition of the nuclear transport of host factors which are required to prevent viral replication. Therefore, many viruses have evolved mechanisms to target host NPCs and transport pathways to block the bidirectional nuclear transport of host protein and RNA required to inhibit viral propagation (Fontoura *et al*., 2005).

Among the many host factors targeted by viral proteins, the Nup98/Rae1 complex has been shown to be a common target of viral interference (Yarbrough *et al*., 2014; Li *et al*., 2022). Both Nup98 and Rae1 expression are induced by interferons, and together, the Nup98/Rae1 complex has been referred to as an interferon inducible mRNA export complex (Ennigna *et al*., 2005; Faria *et al*., 2005; Gordon *et al*., 2020). The Nup98/Rae1 complex can bind to ssRNA through the hydrophobic binding groove formed by Rae1 binding to the GLEBS motif of Nup98, however, the precise role of Rae1 in mRNA export remains largely unknown (Ren *et al*., 2010; Xie and Ren, 2019). Regardless, the Nup98/Rae1 complex has been shown to be a target of many viruses to inhibit the nuclear

transport of host proteins and RNAs that are necessary to induce an effective antiviral response (Li *et al*., 2022).

The vesicular stomatitis virus (VSV) is a negative sense RNA virus, and its matrix (M) protein has been shown to target the Nup98/Rae1 complex to inhibit the export of host mRNA (von Kobbe *et al*., 2000; Faria *et al*., 2005). *In vitro* binding experiments have shown that the VSV M protein can independently interact with both the GLEBS domain of Nup98, along with Rae1, and the overexpression of either Rae1 or Nup98 have been shown to significantly suppress the VSV M-mediated block of poly-A RNA export (Enninga *et al*., 2002; Faria *et al*., 2005). Structural analysis of the VSV M protein in complex with Nup98/Rae1 has shown that the M protein inserts itself into the hydrophobic binding pocket of the Nup98/Rae1 complex. By inserting into this groove, the VSV M protein is suggested to compete for binding with host mRNA, as the Nup98/Rae1 complex can no longer interact with ssRNAs when bound to the VSV M protein (Quan *et al*., 2014). A methionine (M51) residue within the M protein makes extensive interactions with Rae1 residues that are within the hydrophobic Nup98/Rae1 binding groove, and mutation of this single methionine residue (M51R) inhibits the M protein from interacting with the Nup98/Rae1 complex. Additionally, cells expressing the mutant M (M51R) protein no longer show RNA export defects, suggesting that the M51 residue is critical for M protein function (Petersen *et al*., 2000; von Rajani *et al*., 2012; Quan *et al*., 2014).

Herpesviruses are large DNA viruses and have also been shown to interfere with host nuclear transport by targeting the Nup98/Rae1 complex. Instead of blocking the nuclear export of the bulk of cellular mRNA, Kaposi's sarcoma

associated herpesvirus (KSHV) accessory protein Orf10 blocks a subset of host mRNA through its interactions with Nup98/Rae1 (Gong *et al*., 2016). *In vitro* binding experiments show that Orf10 interacts individually with Rae1 and can only interact with Nup98 when Rae1 is present, suggesting that Orf10 binds the Nup98/Rae1 complex through its interactions with Rae1. Furthermore, the RNA export defects associated with Orf10 can be suppressed by Rae1 overexpression, suggesting an important role for Rae1 in Orf10 function (Gong *et al*., 2016). Like the VSV M protein, the KSHV Orf10 protein inserts into the hydrophobic pocket formed between the Nup98/Rae1 complex, and also has a critical methionine (M413) residue that makes major interactions with residues on Rae1 that are located within the hydrophobic pocket of Nup98/Rae1. Additionally, mutation of the M413 residue (M413A) significantly reduces the binding of KSHV Orf10 with the Nup98/Rae1 complex (Feng *et al*., 2020).

The SARS-CoV-1 virus is a positive sense RNA virus that has also been shown to inhibit nuclear transport using its accessory protein Orf6. Previously, it was suggested that Orf6 localizes to the ER/Golgi membrane and inhibits the nuclear import of the transcription factor STAT1 by binding to importin-α2. By binding importin-α2 Orf6 is suggested to create a conformational change in importin-α2, which allows for binding to importin-β1, ultimately sequestering both importin-α2 and importin-β1 to the ER/Golgi membrane (Frieman *et al*., 2007). It was proposed that by blocking the interaction of importin-β1 with other nuclear transport factors, importin-β1 can no longer facilitate the import of other importin-α bound cargo and therefore leads to the inhibition of the nuclear import of STAT1 and the downstream

expression of ISGs. When mutations are made in the C-terminus of Orf6, Orf6 can no longer bind importin-α2 and the Orf6-mediated inhibition of STAT1 nuclear import is suppressed (Frieman *et al*., 2007). Recently, the SARS-CoV-1 Orf6 protein has also been shown to interact with the Nup98/Rae1 complex. The crystal structure of the C-terminal tail of Orf6 in complex with Nup98/Rae1 has been determined and shows that Orf6 also interacts within the hydrophobic binding pocket formed by the Nup98/Rae1 complex. Orf6 binding to the Nup98/Rae1 complex decreases the ability of Nup98/Rae1 to bind ssRNA, and mutation of a critical methionine residue in SARS-CoV-1 Orf6 (M58R) disrupts its ability to bind to the Nup98/Rae1 complex (Li *et al*., 2022). Taken together, this suggests that SARS-CoV-1 Orf6 may also function to inhibit innate immune signalling by targeting the Nup98/Rae1 complex to interfere with host nuclear transport.

Interestingly, the VSV M, KSHV Orf10, and SARS-CoV-1 Orf6 proteins, all contain critical methionine residues that are important for interacting with several key residues of Rae1 that are buried within the hydrophobic pocket formed by the Nup98/Rae1 complex. Further investigation has revealed that all three viral proteins share a common motif, which is characterized by a central critical methionine residue that is surrounded by several acidic amino acid residues. This motif has been termed a Nup98/Rae1 interaction motif, and all three viral proteins use this motif to interact within the same site of the Nup98/Rae1 complex. Together, this suggests a common strategy for which different viruses have evolved to target the Nup98/Rae1 complex to interfere various aspects of host nuclear transport and inhibit the activation of an innate immune response (Gordan *et al*., 2020; Li *et al*., 2022).

1.7 SARS-CoV-2 virus.

Most epidemics over the past decade have been caused by RNA viruses, and among those, single stranded RNA viruses have been a major focus of concern (Heaton, 2019). Owing to their RNA genome and lack of a high-fidelity proof-reading polymerase, most RNA viruses are prone to rapid mutation. Thus, the incredible evolvability of RNA viruses has contributed to their great success as infectious agents. Moreover, the rapid mutation rate of these viruses has aided their ability to frequently cross species barriers, to evolve into new serotypes, and to develop resistance against both drug and vaccine therapies, making infections caused by RNA viruses difficult to both contain and to treat (Carrasco-Hernandez *et al*., 2017).

Among the RNA viruses, coronaviruses are a large family of enveloped, positive sense ssRNA viruses that can infect many animals and humans and have the capacity to cause serious disease. Of note, three highly pathogenic human coronaviruses have caused epidemics over the past two decades; starting with the emergence of the SARS-CoV-1 epidemic in 2002, followed by the MERS-CoV epidemic in 2012, and as of December 2019 the SARS-CoV-2 virus has swiftly traveled the globe leading to the current COVID-19 pandemic (Zhu *et al*., 2020).

1.7.1 SARS-CoV-2 viral particle and genomic organization.

As mentioned above, the SARS-CoV-2 virus is the etiological agent of the COVID-19 pandemic and has caused detrimental medical and socioeconomical impacts since its emergence in late 2019. SARS-CoV-2 is part of the *Coronaviridae* family of viruses and possesses a large non-segmented single-stranded positive

sense RNA genome (Pal *et al*., 2020). The structure of the SARS-CoV-2 viral particle is composed of a host derived double-phospholipid bilayer with imbedded viral envelope (E), membrane (M), and spike (S) proteins. The viral nucleocapsid (N) protein coats the viral RNA genome that is packaged within the viral particle (Figure 1.4B). The viral RNA genome is approximately 29.8 kB in length and contains 13 recognized open reading frames (ORF) (Malone *et al*., 2022). ORF1a and ORF1b together encode for 16 non-structural proteins that are required for viral replication, 4 separate ORFs encode for the viral S, E, M, and N structural proteins, and the rest of the ORFs encode for the viral accessory proteins (Figure 1.4A) which are not required for replication but enhance viral pathogenicity during infection (Malone *et al*., 2022).

SARS-CoV-2 has a virion size ranging from approximately 70 to 90 nm in diameter and enters host cells through interactions with its S protein and host ACE2 receptors which are found on a wide range of different cell types (Kumar *et al*., 2020). The S protein is composed of two subunits: S1 and S2. The S1 subunit facilitates the binding of the viral particle to the ACE2 receptor on the host cell surface, which triggers cleavage by the host cell protease TMPRSS2. This then allows for fusion of the cellular and viral membranes, which is a process facilitated by the S2 subunit of the S protein (Hoffmann *et al*., 2020). Once fused, the viral particle is internalized and the viral positive sense RNA genome which is 5′capped and 3′polyaddenylated is then released into the cytoplasm, where it can then be directly translated by host cell ribosomes. ORF1a within the genomic RNA is first translated into polyprotein 1a (pp1a), and a -1 ribosomal frameshift just upstream of the ORF1a termination codon

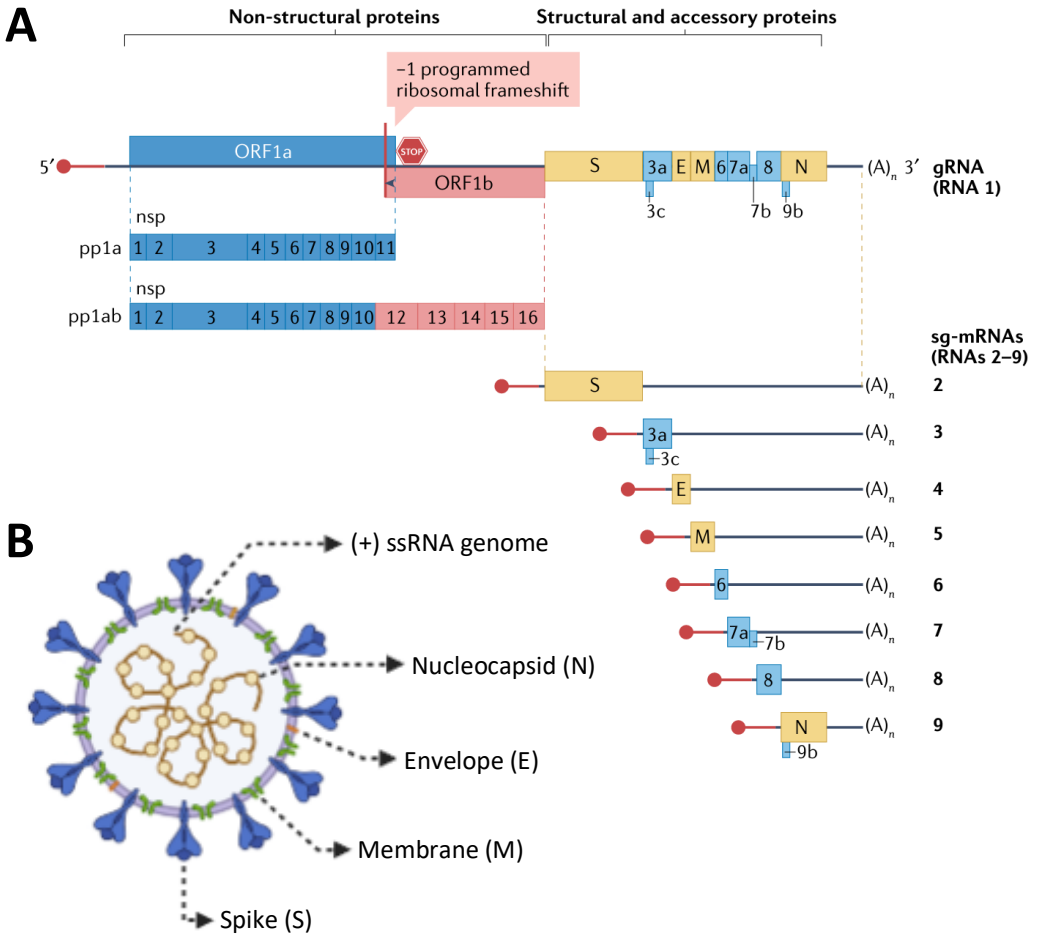

Figure 1.4 Schematic depictions of SARS-CoV-2 genomic organization and viral particle structure.
(A) SARS-CoV-2 genome organization. The SARS-CoV-2 genomic RNA (gRNA) has a 5′ cap (red circle) followed by a leader sequence (red line), and a 3′ poly-A tail. ORF1a and ORF1ab at the 5′-end of the genome encode for polyproteins pp1a and pp1ab, which are cleaved into 16 individual non-structural proteins (nsp1–nsp16). The 3′ end of the genome encodes viral structural and accessory proteins. Structural and accessory proteins are expressed from a set of subgenomic mRNAs (sg-mRNAs), which also contain a 5′ cap, followed by a leader sequence, and a poly-A tail. Adapted from Malone *et al*., 2022. Reproduced with permission from Springer Nature. Original publication DOI: 10.1038/s41580-021-00432-z. **(B)** Structure of SARS-CoV-2 viral particle. SARS-CoV-2 has several surface viral proteins. The spike protein (S) mediates interaction with the host cell surface receptor ACE2, and the viral membrane (M) and envelope (E) proteins are embedded in host-derived phospholipid bilayer which encapsulates the viral positive sense ssRNA coated with nucleocapsid (N) protein. This schematic was created with BioRender.com.

allows for the translation of ORF1a and ORF1b generating polyprotein 1ab (pp1ab) (Figure 1.4A). Cleavage events mediated by viral proteases that are encoded within ORF1a and ORF1b allow for the cleavage of pp1a and pp1ab into the 16 individual non-structural proteins required to mediate viral replication (Malone *et al*., 2022).

The viral RNA-dependent RNA polymerase (RdRp) uses the viral genomic RNA as a template to produce a full-length negative sense RNA genome, and a subset of negative sense subgenomic RNAs. These subgenomic RNAs are derived from the viral genomic RNA downstream of ORF1a and ORF1b, and are produced in a process referred to as discontinuous transcription (Sawicki *et al*., 2007). The full-length negative sense RNA then acts as a template to produce new viral positive sense genomic RNA, which can then be further used to generate more viral protein, to serve as a template for more minus strand synthesis, or it can be packaged into assembling virions. The negative sense subgenomic RNAs are used as a template to synthesize subgenomic mRNA which encode for the viral structural and accessory proteins (Figure 1.4A) (Malone *et al*., 2022).

SARS-CoV-2 structural proteins S, E, and M are translated in the ER and are retained within the ER–Golgi intermediate compartment (ERGIC) membrane. Virion assembly begins with the coating of viral genomic RNA with N protein, which then traffics and buds into ERGIC membranes, thereby acquiring a host derived lipid bilayer that contains the viral S, E, and M structural proteins. Assembled virions are then exported from cells by exocytosis, where they can then bind and infect neighboring cells (Hartenian *et al*., 2020; Malone *et al*., 2022).

1.7.2 SARS-CoV-2 accessory protein Orf6.

Deficiency of the innate immune response upon viral infection has been considered a hallmark of the COVID-19 disease contributing to both viral pathogenicity and progression. Although significant effort has been put into investigating the SARS-CoV-2 virus, the exact mechanisms of viral evasion from innate immune detection remain to be fully elucidated (Min *et al*., 2021). The SARS-CoV-2 Orf6 protein is an accessory protein encoded by the viral ORF6 subgenomic mRNA. As an accessory protein, Orf6 is not required for viral replication, however, Orf6 contributes to disease pathology and viral propagation by being a potent inhibitor of the type-1 IFN response (Xie *et al*., 2020; Lei *et al*., 2020).

The SARS-CoV-2 Orf6 protein is 61 amino acid residues in length and is considered to be a moderately disordered protein (Giri *et al*., 2021). SARS-CoV-2 Orf6 is suggested to be related to the 63 amino acid residue Orf6 protein of the SARS-CoV-1 virus. These SARS-CoV Orf6 proteins contain a 68.85% sequence similarity, and both have been shown to target type-1 IFN production, although, SARS-CoV-2 has been suggested to antagonize antiviral innate immunity more efficiently than the SARS-CoV-1 Orf6 protein (Giri *et al*., 2021; Kimura *et al*., 2021; Gao *et al*., 2022). The N-terminal amino acid residues of Orf6 are suggested to form an α-helical structure that has membrane binding capacity, and the C-terminus of Orf6 is suggested to contain an intrinsically disordered region (Zhou *et al*., 2010; Riojas *et al*., 2020; Giri *et al*., 2021). The C-terminal region of the Orf6 protein contains molecular recognition features (MoRFs) which are defined as

intrinsic disorder-based protein-protein interaction sites that are commonly utilized by proteins for interactions with specific interacting partners (Giri *et al*., 2021). This would suggest that the C-terminal domain of Orf6 is important for its interactions with other proteins.

1.7.3 SARS-CoV-2 Orf6 interacts with the Nup98/Rae1 complex.

Indeed, the C-terminus of SARS-CoV-2 Orf6 is suggested to form interactions with the mammalian Nup98/Rae1 complex (Gordon *et al*., 2020; Miorin *et al*., 2020; Li *et al*., 2022). Early in the pandemic, a high confidence interaction was found between the Orf6 protein and the Nup98/Rae1 complex suggesting a role for Orf6 in inhibiting host nucleocytoplasmic transport. Sequencing analysis revealed that, similar to the VSV M, KSHV Orf10, and the SARS-CoV-1 Orf6 proteins, the SARS-CoV-2 Orf6 protein also contains a Nup98/Rae1 interaction motif. This motif spans residues 56-61 at the C-terminal end of Orf6 and contains a central methionine residue surrounded by several acidic amino acid residues (Gordon *et al*., 2020). Structural analysis of the SARS-CoV-2 Orf6 C-terminal domain in complex with Nup98/Rae1 indicate that Orf6 inserts into the hydrophobic groove formed by Rae1 binding to the GLEBS motif of Nup98. The central methionine residue (M58) within the Nup98/Rae1 interaction motif of Orf6 makes extensive interactions with Rae1 residues that are buried within the hydrophobic pocket. Notably, Orf6 M58 interacts with residues F257, W300, D301, K302, and R305 within Rae1 (Li *et al*., 2022). Physical interactions between Nup98, Rae1 and Orf6 are drastically reduced when the M58 residue is mutated, suggesting that this methionine residue is critical for Orf6 interactions

with the Nup98/Rae1 complex (Miorin *et al*., 2020; Gao *et al*., 2022). Furthermore, mutation of Rae1 (R305G) also results in loss of binding of Orf6 to Rae1, further supporting the critical interactions made between the M58 residue of Orf6 and residues of Rae1 that are buried within the hydrophobic pocket of the Nup98/Rae1 complex (Hall *et al*., 2022).

1.7.4 SARS-CoV-2 Orf6 functions in innate immune evasion by targeting the Nup98/Rae1 complex.

Mentioned previously, the SARS-CoV-2 Orf6 protein is a potent inhibitor of the type-1 IFN response. Acting both upstream and downstream of type-1 IFN production, Orf6 has been shown to inhibit the nuclear transport of both protein and RNA required for an effective antiviral response. Through interactions with the Nup98/Rae1 complex, Orf6 inhibits both the nuclear import of transcription factors required for the expression of type-1 IFNs and ISGs, and also inhibits the export of various cellular RNAs (Miorin *et al*., 2020; Xie *et al*., 2020; Addetia *et al*., 2021; Hall *et al*., 2022; Makio *et al.,* in preparation).

Orf6 has been shown to inhibit the nuclear import of a variety of host factors. Upon detection of viral invasion, the IRF3 transcription factor is typically activated by phosphorylation and transported into the nucleus, however, Orf6 expression inhibits the nuclear import of IRF3 without affecting its activation (Xia *et al*., 2020). The STAT1 signalling pathway activated by type-1 IFNs is also affected by the expression of Orf6, as Orf6 again inhibits the nuclear import of STAT1 without affecting its phosphorylation (Miorin *et al*., 2020; Xia *et al*., 2020). Furthermore, Orf6 has also been shown to physically interact with several nuclear

import factors, including importin-α1 and importin-α5 (Miorin *et al*., 2020; Addetia *et al*., 2021; Miyamoto *et al*., 2022), although, these immunoprecipitation experiments do not differentiate if the interactions are direct or indirect due to Orf6 association with the Nup98/Rae1 complex. However, further experiments have shown that purified recombinant importin-α1 can bind recombinant GST-GFP-Orf6, suggesting that the interactions between Orf6 and importin-α1 are likely direct interactions (Miyamoto *et al*., 2022). Direct binding between recombinant importin-α5 and GST-GFP-Orf6 is less clear however, as there is only faint detection of importin-α5 after pull-down with Orf6 (Miyamoto *et al*., 2022).

Interestingly, in Orf6 expressing cells, importin-α1, importin-α3, importin-α4, importin-α6, and importin-α8 are all mainly localized to within the cytoplasm, however, the localization of importin-α5 and importin-α7 remains mainly nuclear, suggesting that Orf6 has distinct effects on different importin-α subtypes. *In vitro* binding experiments with immobilized GST-GFP-Orf6, reveals that recombinant GST-GFP-Orf6 binds to recombinant Flag-importin-α5 to a lesser extent than it binds recombinant Flag-importin-α1. This suggests that Orf6 may inhibit the movement of importin-α1 across the NPC by direct binding to importin-α1 and, therefore, restricts the transport of its cargo (Miyamoto *et al*., 2022). On the other hand, Orf6 strongly inhibits the importin-α5 cargo protein STAT1 without strongly binding to importin-α5, suggesting that Orf6 acts more specifically to inhibit STAT1 nuclear import. Indeed, it has been shown that Orf6 can bind to STAT1 independent of importin-α5. A purified recombinant Flag-STAT1 protein was shown to bind to recombinant GST-GFP-Orf6 protein immobilized on glutathione-

Sepharose beads, suggesting that Orf6 may function to inhibit STAT1 nuclear import through interactions with the STAT1 protein itself, rather than with its nuclear transport factor importin-α5 (Miyamoto *et al*., 2022). Furthermore, Orf6 has also been shown to decrease the nuclear import of the transcription factor NF-κB which is transported into the nucleus by either importin-α3/β1 or importin-α4/β1 (Shen *et al*., 2021), however, Orf6 inhibits STAT1 nuclear accumulation to a much greater extent (Miyamoto *et al*., 2022). Since the Orf6 protein differentially affects the nuclear import of these transcription factors, this may suggest a mechanism whereby Orf6 can specifically inhibit the nuclear import of some proteins (such as STAT1), while also partially impairing nuclear import of other cargo targeted by the importin-α/β1 nuclear import pathway.

In addition to targeting protein import, Orf6 has also been shown to inhibit host RNA export through its interactions with the Nup98/Rae1 complex (Addetia *et al*., 2021; Hall *et al*., 2022; Savellini *et al*., 2022; Makio *et al*., in preparation). SARS-CoV-2 infected cells have been shown to have an accumulation of poly-A RNA within the nucleus, and expression of Orf6 has revealed similar poly-A RNA export defects (Addetia *et al*., 2021). This suggests that the Orf6 protein is involved in the block of nuclear export caused by the SARS-CoV-2 virus, however, Orf6 is not the only SARS-CoV-2 protein that has been shown to cause RNA export defects (Zhang *et al*., 2021). Regardless, RNA sequencing analysis of nuclear and cytoplasmic fractions of mRNA species in control and Orf6 expressing cells have indicated that Orf6 expression inhibits the nuclear export of a subset of host mRNAs, as some RNA species are enriched within the nucleus when Orf6 is

expressed, while others are not (Hall *et al*., 2021). This suggests that the mRNA export defects caused by Orf6 are likely specific, rather than causing a block to the bulk of mRNA export. Notably, the nuclear export of IFN-β mRNA has been shown to be inhibited by the expression of Orf6 (Savellini *et al*., 2022), suggesting that Orf6 plays important roles in dampening innate immune activity by inhibiting the expression of the IFN molecules needed to signal for an appropriate antiviral response.

Although the mechanism of Orf6 function largely remains to be elucidated, Orf6 has been shown to be a potent inhibitor of the type-1 IFN response through its interactions with the Nup98/Rae1 complex. As mentioned previously, mutations of the M58 residue of the Orf6 protein have been shown to impair its interactions with the Nup98/Rae1 complex, and by interfering with the interaction of Orf6 with the Nup98/Rae1 complex, Orf6 function is also perturbed. Orf6 M58R mutations have been shown to abolish the nuclear transport defects caused by Orf6 expression, as the nuclear import of STAT1 (Miorin *et al*., 2020), the nuclear export of poly-A mRNA (Addetia *et al*., 2021), and the nuclear export of IFN-β mRNA (Savellini *et al*., 2022) are all restored in cells expressing the mutant Orf6 protein. Together, these results show that Orf6 is an important virulence factor that inhibits the host innate immune response by targeting the Nup98/Rae1 complex to perturb host nuclear transport.

Since Orf6 is a potent inhibitor of the innate immune response, it may provide an interesting target for therapeutic intervention. However, the molecular mechanisms underlying Orf6 function remain poorly understood. Therefore, to

further elucidate the mechanism of Orf6 function, the studies in this thesis aim to focus on the functional role of the Nup98/Rae1 complex on the Orf6-mediated block of bidirectional nuclear transport. Using *S. cerevisiae* as a model organism, we first focused on attempting to elucidate specific nuclear import and export pathways impaired by the SARS-CoV-2 Orf6 protein. Additionally, using a mammalian model system, the function of Orf6 was investigated during either Nup98 or Rae1 depletion to determine the requirement of Nup98 or Rae1 on the Orf6-mediated block of nuclear transport. The work described in this thesis provide further insights into the molecular mechanisms of Orf6 function and provide additional support that the Nup98/Rae1 complex is an attractive target for viruses to interfere with host bidirectional nuclear transport in order to inhibit an antiviral innate immune response during the onset of infection.

Chapter II

Experimental procedures

2.1 Antibodies.

Table 2.1 Antibodies

Antibody	Dilution used in WB	Dilution used in IF	Type	Source/Reference
α-GFP	1:10,000	N/A	Rabbit polyclonal	Wozniak Lab
α-HA	1:10,000	N/A	Mouse monoclonal	Santa Cruz (Cat No. sc-7392)
α-GSP1	1:10,000	N/A	Rabbit polyclonal	Wozniak Lab
α-V5	1:5000	N/A	Mouse monoclonal	Abcam (Cat No. ab27671)
α-Nup98	1:10,000	1:1000	Rabbit polyclonal	Mitchell *et al*., 2010
α-Nup96	1:2000	1:100	Rat monoclonal	EMD Milipore (Cat No. MABE1039)
α-Nup358	1:10,000	1:1000	Rabbit polyclonal	Fontoura *et al*., 2001
α-Rae1	1:5000	1:1000	Mouse monoclonal	Santa Cruz (Cat No.sc-393252)
α-Tubulin	1:10,000	N/A	Mouse monoclonal	Sigma-Aldrich (Cat No. T6074)
α-mAb414	N/A	1:1000	Mouse monoclonal	Abcam (Cat No. ab24609)
α-panSTAT1	1:10,000	N/A	Rabbit monoclonal	Cell Signaling (Cat No. 14994)
α-(pY701)STAT1	1:10,000	1:1000	Rabbit monoclonal	Cell Signaling (Cat No. 9167)
α-Flag	N/A	1:1000	Mouse monoclonal	Sigma-Aldrich (Cat No. F1804)
HRP-conjugated Goat α-mouse IgG,	1:10,000	N/A	Secondary HRP conjugated	BioRad (Cat No. 170-6516)
HRP-conjugated Goat α-rabbit IgG,	1:10,000	N/A	Secondary HRP conjugated	BioRad (Cat No. 170-6515)
HRP-conjugated Goat α-Rat IgG,	1:5000	N/A	Secondary HRP conjugated	Jackson ImmunoResearch (No. 712055150)
Alexa488-conjugated donkey α-rabbit IgG	N/A	1:1000	Secondary Alexa Flour conjugated	Life Technologies (Cat No. A21206)
Alexa488-conjugated donkey α-mouse IgG	N/A	1:1000	Secondary Alexa Flour conjugated	Life Technologies (Cat No. A21202)
Alexa594-conjugated goat α-rabbit IgG	N/A	1:1000	Secondary Alexa Flour conjugated	Life Technologies (Cat No. A11012)
Alexa647-conjugated goat α-rabbit IgG	N/A	1:1000	Secondary Alexa Flour conjugated	Life Technologies (Cat No. A21246)
Alexa594-conjugated donkey α-rat IgG	N/A	1:1000	Secondary Alexa Flour conjugated	Jackson ImmunoResearch (No. 712585153)

2.2 Yeast strains and media.

Yeast strains were grown in either YPD (consisting of 1% yeast extract, 2% bactopeptone, and 2% glucose), or synthetic minimal media lacking methionine (per l L: 1.7 g yeast nitrogen base, 5 g ammonium acetate, 1.7 g amino acid dropout powder and 2% glucose), as indicated. Yeast strains were grown overnight at room temperature (RT) under agitation on a platform shaker. The next day, yeast strains were diluted to an OD_{600} of 0.1 and grown for three generations at 30°C, unless otherwise indicated. All yeast strains used in this thesis are listed in Table 2.2.

Table 2.2 Yeast strains

Strain Name	Genotype	Base Strain	Source
Wildtype	MAT**α** *leu2Δ0 lys2Δ0 ura3Δ0 his3Δ1*	BY4742	Brachmann *et al*.,1998
GFP-Orf6	MAT**α** *his3Δ1:: NOP1pr-GFP-ORF6-ADH1term-HPH$_R$*	BY4742	This study
GFP-Orf6 /Nup116mCh	MAT**α** *his3Δ1:: NOP1pr-GFP-ORF6-ADH1term-HPH$_R$ NUP116-mCh-NAT$_R$*	BY4742	This study
GFP-Orf6 /Gle2-mCh	MAT**α** *his3Δ1:: NOP1pr-GFP-ORF6-ADH1term-HPH$_R$ GLE2-mCh-NAT$_R$*	BY4742	This study
GFP-Orf6 /P$_{MET3}$-HA-Nup116	MAT**α** *his3Δ1:: NOP1pr-GFP-ORF6-ADH1term-HPH$_R$ KAN$_R$-MET3pr-3xHA-NUP116*	BY4742	This study
GFP-Orf6 /P$_{MET3}$-HA-Gle2	MAT**α** *his3Δ1:: NOP1pr-GFP-ORF6-ADH1term-HPH$_R$ KAN$_R$-MET3pr-3xHA-GLE2*	BY4742	This study
Wildtype /cNLS-GFP	MAT**α** *leu2Δ0 lys2Δ0 ura3Δ0 his3Δ1 pRS315-NLS^{SV40}-2xGFP*	BY4742	This study
Wildtype /pho4NLS-GFP	MAT**α** *leu2Δ0 lys2Δ0 ura3Δ0 his3Δ1 pRS315-NLS^{Pho4}-3xGFP*	BY4742	This study
GFP-Orf6 /cNLS-GFP	MAT**α** *his3Δ1:: NOP1pr-GFP-ORF6-ADH1term-HPH$_R$ pRS315-NLS^{SV40}-2xGFP*	BY4742	This study
GFP-Orf6 /pho4NLS-GFP	MAT**α** *his3Δ1:: NOP1pr-GFP-ORF6-ADH1term-HPH$_R$ pRS315-NLS^{Pho4}-3xGFP*	BY4742	This study

2.3 Yeast expression constructs.

All of the yeast expression plasmids used in this study are listed in Table 2.3. Plasmids constructed for these studies were made by restriction digestion of polymerase chain reaction (PCR) products, or by direct digestion of DNA from a previously constructed plasmid, with subsequent ligation into the indicated plasmid backbone as described in further detail below. PCR primers used in these studies are listed in Table 2.4.

PCR was carried out using Phusion High-Fidelity DNA Polymerase (Thermo Fisher Scientific Cat No. F530) following the manufacturer's protocol. PCR products were purified with the QIAquick PCR Purification kit (QIAGEN, Cat No. 28106) and digested with appropriate restriction endonuclease (New England BioLabs), as per manufacturer's protocol. Digested DNA was purified using the QIAquick Gel Extraction kit (QIAGEN, Cat No. 28706) and ligated into the indicated vectors using T4 DNA Ligase (New England BioLabs, Cat No. M022) as per manufacture's protocol. Sub-cloning Efficiency DH5α Competent Cells (Thermo Fisher Scientific, Cat No. 18265017) were transformed with ligated plasmids using a previously described heat shock method (Froger and Hall; 2007) and the transformed bacteria were plated into Luria Broth (LB) agar plates (per 1 L: 10 g tryptone, 5 g yeast extract, 5 g NaCl, 15 g bacto-agar) containing the appropriate selection antibiotic. Plasmids were isolated from overnight cultures of DH5α cells using a Plasmid Miniprep Kit (QIAGEN, Cat No. 27106).

The *pRS315-NOP1pr-GFP-ORF6-ADH1term-HPH$_R$* plasmid was constructed by cloning 5 separate DNA fragments into a pRS315 backbone

plasmid (Sikorski and Hieter, 1989). The NOP1 promoter sequence (*NOP1pr*) was amplified by PCR using BY4742 genomic DNA as a template with Sac1-Nop1pr-S/Not1-Nop1pr-AS primers, to generate a NOP1 promoter sequence (530 bp of the 5' UTR of *NOP1*) flanked by Sac1 and Not1 restriction enzyme sites. The ADH1 terminator sequence (*ADH1term*) was amplified by PCR using BY4742 genomic DNA as a template, with EcoR1-ADH1t-S/ADH1t-Sal1-AS primers to generate an ADH1 terminator sequence (350bp of the 3'UTR of *ADH1)* flanked by EcoR1 and Sal1 restriction enzyme sites. The GFP sequence was amplified by PCR using the *pRS315.SMT3pr-GFP-Smt3* plasmid (Table 2.3) with Not1-GFP-S/GFP-Spe1-AS primers to generate a GFP sequence flanked by Not1 and Spe1 restriction enzyme sites. The Orf6 sequence was amplified using the plasmid *pCI-Neo-3xFLAG-ORF6* (Table 2.3) with Spe1-linker-Orf6-S/Orf6-stop-EcoR1-AS primers to generate an Orf6 sequence flanked by Spe1 and EcoR1 restriction enzyme sites. The HPH resistance cassette (HPH_R) was obtained by directly removing the DNA cassette from an already available *pRS315-SMT3pr-*His_8*-SMT3-HPH* plasmid (Table 2.3) using restriction enzymes Sal1 and Apa1. The *pRS315-NOP1pr-GFP-ORF6-ADH1term-*HPH_R plasmid was then constructed in a 4-step process as follows; 1) insertion of the NOP1 promoter (*NOP1pr*) bound by Sac1/Not1 restriction enzyme sites 2) insertion the HPH resistance cassette (HPH_R) bound by Sal1/Apa1 restriction sites, 3) insertion of both *ORF6* bound by Spe1/EcoR1 restriction sites and the ADH1 terminator (*ADH1term*) bound by EcoR1/Sal1 restriction sites, and 4) the insertion of a *GFP* sequence bound by Not1 and Spe1 restriction sites.

To generate PCR products for transformation, plasmid DNA (listed in Table 2.3) was amplified using Phusion High-Fidelity DNA Polymerase (Thermo Fisher Scientific Cat No. F530) following the manufacturer's protocol. For constructing yeast strains with constitutive expression of the GFP-Orf6 protein, the *NOP1pr-GFP-Orf6-ADH1term-HPH$_R$* cassette was amplified by PCR using the *pRS315-NOP1pr-GFP-ORF6-ADH1term-HPH* plasmid and primers (his3Δ1-int-pRS315-S and his3Δ1-int-pRS315-AS) that anneal to the regions just outside of the pRS315 multiple cloning site. The resultant PCR product contains 60 bp flanking sequences homologous to genomic regions in the *his3Δ1* locus of BY4742. During transformation, the amplified cassette was then integrated into the *his3Δ1* locus of BY4742 *S. cerevisiae* by homologous recombination. For the genomic integration of the *KAN$_R$-MET3pr-HA* construct, the *pFA6a-kanMX6-P$_{MET3}$-HA* (pTM1046) plasmid and PCR primers (Met3p-HA-Nup116-S and AS, or Met3p-HA-Gle2-S and AS) were used for amplification. The resultant PCR product contains 40 bp flanking sequences which are homologous to the regions immediately upstream and downstream of the start codon of either *NUP116* or *GLE2,* for the targeted integration of the *KAN$_R$-MET3pr-HA* construct. For the genomic integration of the *mCherry-NAT$_R$* construct, the *pGEM-4Z-mCherry-NAT* plasmid and PCR primers (Nup116-mCherry-S and AS, or Gle2-mCherry-S and AS) were used for amplification. The resultant PCR product contains 60 bp franking sequences which are homologous to regions immediately upstream and downstream of the stop codon of either *NUP116* or *GLE2,* for subsequent targeted integration of the *mCherry-NAT$_R$* construct.

Table 2.3 Plasmids

Plasmid	Utilization	Source
pRS315	-backbone for integration of *NOP1pr-GFP-ORF6-ADH1term-HPH$_R$* insert	Sikorski and Hieter, 1989
pRS315-NOP1pr-GFP-ORF6-ADH1term-HPH	-template for the integration of *NOP1pr-GFP-ORF6-ADH1term-HPH$_R$* into the *his3Δ1 locus of BY4742*	These studies
pRS315-SMT3pr-His$_8$-SMT3-HPH	-template for the addition of the HPH sequence into *pRS315-NOP1pr-GFP-ORF6-ADH1term-HPH$_R$* plasmid	Gift from Dr. Chris Ptak University of Alberta
pRS315.SMT3pr-GFP-Smt3	-template for the amplification of the GFP sequence to construct the *pRS315-NOP1pr-GFP-ORF6-ADH1term-HPH$_R$* plasmid	Gift from Dr. Chris Ptak University of Alberta
pCI-Neo-3xFLAG-ORF6	-template for the amplification of the *ORF6* sequence to construct the *pRS315-NOP1pr-GFP-ORF6-ADH1term-HPH$_R$* plasmid	Gift from Dr. Beatriz Fontoura Miorin *et al*., 2020
pGEM-4Z-mCherry-NAT	-template for the integration of the *mCherry-NAT$_R$* sequence at the 3' end of *NUP116 or GLE2*	Cairo *et al*., 2013
pFA6a-kanMX6-P$_{MET3}$-HA (pTM1046)	-template for the integration of the *KAN$_R$-MET3pr-3xHA* sequence at the 5' end of *NUP116 or GLE2*	Makio *et al*., 2009
pRS316-NLS^{Pho4}- 3xGFP	-used for the exogenous expression of the pho4-NLS-GFP reporter protein	Kaffman *et al*., 1998
pRS315-NLS^{SV40}-2xGFP	-used for the exogenous expression of the cNLS-GFP reporter protein	Stade *et al.,* 1997

Table 2.4 Primer Sequences

Primer Name	Primer sequence (5' to 3')
Not1-GFP-S:	CGAGCGCGGCCGCATGGCTAGCAAAGGAGAAGAAC
GFP-Spe1-AS:	CGAGCACTAGTTTTGTAGAGCTCATCCAT
Sac1-Nop1pr-S	GCAGCGAGCTCGCAGAGATTTTTTTCAAAACATC
Not1-Nop1pr-AS	GCAGCGCGGCCGCTACTGTTTTAGTTGATTTGAG
EcoR1-ADH1t-S	CGAGCGAATTCGCTTTGGACTTCTTCGCCAG
ADH1t-Sal1-AS	CGAGCGTCGACGCCGGTAGAGGTGTGGTC
Spe1-Linker-Orf6-S	CGAGCACTAGTGGTGGAAGCGGGGGCAGTGGCGGA AGTGGGGGCAGCGGAGGGAGTATGTTTCATCTCGTT GACTTTC

Orf6-Stop-EcoR1	CGAGCGAATTCTTAATCAATCTCCATTGGTTGC
his3Δ1-int-pRS315-S	ATGACAGAGCAGAAAGCCCTAGTAAAGCGTATTACA AATGAAACCAAGATTCAGATTGCGCGACTCACTATA GGGCGAATTG
his3Δ1-int-pRS315-AS	CTACATAAGAACACCTTTGGTGGAGGGAACATCGTT GGTACCATTGGGCGAGGTGGCTTCCACTAAAGGGAA CAAAAGCTG
Nup116-mCherry-S	GCTATGATGCAGACAGTGGTACATACGTGTTTATCG TAAACCACGCTGCAGAGCAGACCGGCGGTGGCGGTG GCGGTGAAGCTCAAAAACTTAAT
Nup116-mCherry-AS	GGTTAATTACACTAAATGCATTACAAATTTGTATTTG ATTCTATATATAGTTTCGTTATATAATAACGCTGACG GTATCGATAAGCTT
Gle2-mCherry-S	CCAAACGTCATTAGGCTACATGCCACAACTGATGAA GAGGTTAAAGAGAAAAAGAAAAGGGGCGGTGGCGG TGGCGGTGAAGCTCAAAAACTTAAT
Gle2-mCherry-AS	GCAAATATAAAAAATTACAAAAGTAATGTGGTTGC GCACGGAAGCTATCCGAAGAACGAATTGCTGACGG TATCGATAAGCTT
Met3p-HA-Nup116-S	GGCACCATTCAGCTTCGAAGATTTCTTTTTTAAAAC ATTATTGAATTCGAGCTCGTTTAAAC
Met3p-HA-Nup116-AS	GTTGTTGCGCTGGGGAATGCGCCACGGCTAACTCC AAACATGCACTGAGCAGCGTAATCTG
Met3p-HA-Gle2-S	CAATAAAATAAAGAAATACGTAAGAAGAGGAAAA GTGGGGAACTGAATTCGAGCTCGTTTAAAC
Met3p-HA-Gle2-AS	GTTCCCAAAGCTGAGGTTGTATTTGATCGATTAAA AAAAGACATGCACTGAGCAGCGTAATCTG

2.4 Yeast transformations.

Yeast cells were transformed with either plasmids (listed in Table 2.3) or PCR products (described above) in order to express exogenous gene products. Transformations were performed using a previously described lithium acetate/polyethylene glycol method (Gietz and Woods, 2002). Briefly, cells were washed and resuspended in 50 µL of transformation buffer (10 mM Tris-HCL pH 8.0, 1 mM EDTA/NaOH pH 8.0, 100 mM LiOAc), and either 5 µL of plasmid DNA or 10 µL of linear PCR amplified DNA was added to the cells. 10 µL of salmon sperm carrier DNA (Invitrogen Cat No. 15632011) was then added to the cell slurry, and cells were then thoroughly resuspended in a 6-fold volume of PEG transformation buffer (100 mM LiOAc, 10 mM Tris-HCL pH 8.0, 1 mM

EDTA/NaOH pH 8.0, 40% PEG) and incubated at 30°C for 1 hour (h). Cells were then placed in a 42°C water bath for 15 minutes (min), pelleted, and resuspended in YPD for overnight incubation at RT while under agitation. The following day, cells were pelleted and plated onto either minimal media agar plates lacking an amino acid or onto YPD agar plates supplemented with drug (i.e., kanamycin, nourseothricin, or hygromycin) and grown at 30°C for selection of viable transformants.

Confirmation of protein fusions was confirmed by western blot analysis or by sequencing analysis using the Molecular Biology Facility (MBSU) DNA sequencing service at the University of Alberta. Strains bearing multiple gene modifications were either subjected to two rounds of transformation or were derived by crossing relevant strains followed by sporulation, dissection, and selection.

2.5 Yeast plating assays.

To test growth rate of various strains used in this study, indicated strains were grown overnight at RT under agitation in YPD, diluted to an OD_{600} of 0.1 in fresh media the following morning, and were then grown for approximately three generations at 30°C. Cells were then diluted to an OD_{600} of 0.5 and were spotted as 10-fold serial dilutions onto YPD agar plates for incubation at either 30°C or 37°C for two days prior to imaging.

2.6 Western blotting.

2.6.1 Preparation of whole cell lysates.

To collect whole cell lysates, cells grown in the appropriate medium at 30°C to at least mid-log phase, were measured using a spectrophotometer (Biochrom Ultrospec 2100 pro). Volumes of cell culture equivalent to an OD_{600} of 1, which is approximately $1.5x10^7$ cells (Yap and Trau, 2019), were collected, pelleted, and resuspended in 50 µL SDS-PAGE sample buffer (1% SDS, 5% glycerol, 100 mM DTT, 0.001% bromophenol blue, 100 mM Tris-HCl, pH 6.8). Samples were then heated at 80°C for 10 min and were subjected to sonication (Branson Sonifier 250). 10 µL of these cell samples were then used for downstream analysis (described below).

2.6.2 SDS-PAGE and western blot analysis.

Protein samples were resolved by SDS-PAGE using 8% acrylamide gels and separated proteins were then transferred to nitrocellulose membranes using a wet transfer system (BioRad). Following transfer, membranes were incubated with a blocking buffer containing a 5% non-fat skim milk powder (Carnation) resuspended in PBS-T (0.1% Tween-20, 137 mM NaCl, 2.7 mM KCl, 4.3 mM Na_2HPO_4, 1.4 mM KH_2O_4, pH 7.4) for at least 1 h at RT before incubation in fresh blocking buffer containing the indicated primary antibody. The membrane was then incubated overnight at 4°C with gentle shaking. Primary antibodies and dilutions used are listed in Table 2.1. Membranes were then washed with PBS-T for 15 min three times, followed by a 1 h incubation at RT in fresh blocking buffer supplemented with a corresponding HRP-conjugated secondary antibody (Table

2.1). Membranes were then washed three times for 15 min with PBS-T and proteins were visualized by chemiluminescence (Amersham RPN2106) using an ImageQuant LAS 4000 (Cytiva) imaging system. All western blot images were rendered using ImageJ software (NIH; Schneider *et al*., 2012).

2.7 Epifluorescence microscopy analysis.

2.7.1 Sample preparation.

All strains used for live cell imaging were grown to mid-log phase at 30°C in the required growth media. 1 mL of cell culture was pelleted, washed once with 1 mL of dH_2O, and resuspended in a small volume of synthetic complete media. 2 µL of this cell suspension was then spotted onto either a bare glass microscope slide, or a microscope slide containing an agarose pad, and cells were then imaged at RT.

2.7.2 Image acquisition and processing.

Epifluorescence images were acquired on a DeltaVision Elite imaging system (Cytiva) equipped with a Plan Apo N 60x/1.42 NA oil objective (Olympus). Images were collected as 20 x 0.24 µm z-stacks. Images were deconvolved using a deconvolution module of the SoftWoRx software (Cytiva) under a "conservative" setting. All deconvolved images were further rendered using ImageJ FIJI software (NIH; Schindelin *et al*., 2012).

2.8 Methionine-induced repression of MET3 promoter-controlled genes.

For depletion of either Nup116 or Gle2, both genes were placed under the control of the regulatable *MET3* promoter (P_{MET3}-HA-Nup116 or P_{MET3}-HA-Gle2).

GFP-Orf6/P_{MET3}-HA-Nup116 and GFP-Orf6/P_{MET3}-HA-Gle2 strains were grown overnight at RT in minimal media lacking methionine. The following morning, 1 OD_{600} equivalent of cells were diluted into 30 mL of fresh minimal media lacking methionine, or fresh minimal media supplemented with excess methionine (200 µg/mL) and grown for 8 h at 30°C. Cellular depletion of both Nup116 and Gle2 protein levels was confirmed by western blot analysis.

2.9 Nuclear import assay.

The nuclear import assay was performed with slight modifications from a previously established protocol (Shulga *et al*., 1996). Wildtype and GFP-Orf6 expressing *S. cerevisiae* transformed with a plasmid to express various NLS reporter proteins (*pRS316-NLS^{Pho4}-3xGFP* or *pRS315-NLS^{SV40}-2xGFP*) were grown to early mid-log phase in synthetic complete media (i.e. synthetic minimal media supplemented with all amino acids) containing 2% glucose at 30°C. Cells were collected by centrifugation and the cell pellet was resuspended in 1 mL of 10 mM sodium azide and 10 mM 2-deoxyglucose in glucose free synthetic complete media. Cells were incubated for 45 min at 30°C on a rotating shaker, to allow for nucleocytoplasmic equilibration of the NLS-GFP signal. 2 µL of cells were spotted onto a glass slide and imaged by epifluorescence microscopy to assess the NLS-GFP signal after sodium azide/2-deoxyglucose treatment in order to confirm nucleocytoplasmic equilibration of the NLS-GFP signal. To assess nuclear import of the NLS-GFP reporter, 2 µL of cells were spotted onto an agarose pad containing 2% glucose and images of the same field of cells were captured by epifluorescence

microscopy exactly one min after spotting onto glucose containing media (denoted as the “0 min” timepoint in Figure 3.5) which continued every min for 15 min.

Quantification of the nuclear import of the NLS-GFP reporter protein was conducted as follows. Cells were followed throughout 15 min after removal of sodium azide/2-deoxyglucose and addition of glucose, to determine the relative rate of import of the various reporter proteins in either WT or GFP-Orf6 expressing cells. A cell was scored as having nuclear accumulation of the reporter protein, only if the nuclear signal was brighter than the surrounding cytoplasmic signal and if the cell had a clear nuclear/cytoplasmic boundary visible. Consistent scoring required that the focus be adjusted onto the plane of the nuclei of each cell. Scoring was conducted blind to control for experimenter bias. The number of cells with nuclear accumulation of the NLS-GFP reporter protein at each time point is presented as an average percent of cells counted throughout two rounds of each time course.

2.10 Fluorescence *in situ* hybridization (FISH).

This experiment was very kindly performed and analyzed by Dr. Rima Sandhu from Dr. Ben Montpetit’s laboratory (University of California, Davis). FISH analysis was performed as previously described in (Lari *et al*., 2019).

2.11 Immortalized mammalian cell lines and growth media.

The African Green Monkey Vero E6 cells (ATCC) used in these studies were a generous gift from Dr. Tom Hobman (Department of Cell Biology, University of Alberta). Cells were cultured in Dubelcco’s modified Eagle’s media

(DMEM) (Gibco) supplemented with 10% fetal bovine serum (FBS) (Gibco) and 1% penicillin-streptomycin solution (Gibco). Adherent cells lines were kept at 25-90% confluence. All cell lines were maintained in a humid 37ºC incubator with 5% CO_2. Trypsin-EDTA 0.05% (Gibco) was used to detach adherent cells for sub-culturing when required. Cell lines were preserved by freezing in Recovery Cell Culture Freezing Medium (Thermo Fisher Scientific) at -80ºC. Cells were grown for no longer than 12 passages before being discarded and replaced.

2.12 Mammalian expression plasmids.

2.12.1 Plasmids and purification.

The *Tet-pLKO-puro-shNup98-14* (pTM1448) plasmid used for the integration of the shRNA construct targeted against Nup98 in Vero cells, was a gift from Dr. Tadashi Makio (Department of Cell Biology, University of Alberta). The *pCI-neo-3xFlag-Orf6* plasmid was generously gifted by Dr. Beatriz Fontoura's laboratory (Miorin *et al*., 2020) and used for the expression of Flag-Orf6 in Vero cells. The *pLenti-zeo-Nup96(mut)-V5* plasmid (pTM1618) was kindly constructed and gifted by Dr. Tadashi Makio (Department of Cell Biology, University of Alberta) and used for the integration and expression of an shNup98 RNA resistant Nup96-V5 construct (referred to as Nup96-V5 in these studies). The *Tet-pLKO-puro-shRae1-24* (pTM1484) plasmid used for the integration of the shRNA construct targeted against Rae1 in Vero cells was constructed and used in experiments performed by Dr. Tadashi Makio (Department of Cell Biology, University of Alberta). The *Tet-pLKO-puro-SH002* (pTM1356) plasmid used for

the integration of a shRNA construct targeted against a non-mammalian control (referred to as shScramble in these studies) was also a generous gift from Dr. Tadashi Makio (Department of Cell Biology, University of Alberta). Plasmids were amplified in Sub-cloning Efficiency DH5α Competent Cells (Thermo Fisher Scientific, Cat No. 18265017). The bacteria were transformed with plasmids using a previously described heat shock method (Froger and Hall; 2007) and the transformed bacteria were plated onto Luria Broth (LB) agar plates containing the appropriate antibiotic for selection. Plasmids were isolated from overnight cultures of DH5α cells using an EndoFree Plasmid Midiprep Kit (QIAGEN, Cat No. 12143).

2.12.2 Transfection of plasmids into mammalian cells.

Plasmid transfection was performed using Lipofectamine 3000 (Life Technologies) following the manufacturer's protocol. Per well, 0.5 µg of *pCI-neo-3xFlag-Orf6* (Miorin *et al*., 2020), 1 µg P3000 and 1.5 µL Lipofectamine 3000 were mixed with optiMEM media (Life Technology) to a final volume of 50 µL. The plasmid solution was incubated at room temperature for 20 min in a biosafety cabinet. After the 20 min incubation, the mixture was then added directly to cell culture adhered to the bottom of a 24-well plate and incubated at 37°C for 6 h. Cells were then subjected to a heparin wash to remove all uninternalized plasmid. Briefly, culture media was aspirated, cells were washed once with cold PBS (137 mM NaCl, 2.7 mM KCL, 4.3 mM Na_2HPO_4 pH 7.5), cells were then washed with a cold PBS-Heparin solution (137 mM NaCl, 2.7 mM KCL, 4.3 mM Na_2HPO_4 pH 7.5, 50 µg/mL heparin sulfate), and washed twice

more with cold PBS before being replaced with fresh culture media. Cells were then incubated at 37ºC until being processed for downstream experiments.

2.13 Production of lentiviruses and stable cell lines.

2.13.1 Production of lentivirus in HEK293T cells.

Lentiviral pseudo-particles were produced in HEK293T cells as previously described by (Schoggins *et al*., 2011). The plasmid Tet-pLKO-puro (Addgene #21915; Wiederschain *et al*., 2009) was used as a backbone plasmid to construct the lentiviral transfer plasmids for the doxycycline-dependent shRNA (Tet-shRNA) constructs. The annealed oligonucleotides coding for the shRNA sequences (listed in Table 2.5) were inserted into the backbone plasmid at the Age1/EcoR1 restriction sites. For producing lentiviral pseudo-particles, HEK293T cells were transfected using Lipofectamine 3000 (Life Technologies) and a mixture of psPAX2 (Addgene #12260; a gift from Didier Trono), pMD2.G (Addgene #12259; a gift from Didier Trono) and the lentiviral transfer plasmid containing one of the Tet-shRNA constructs, or the Nup96-V5 construct.

The supernatant containing lentiviral particles was harvested at 24 h and 48 h following transfection, combined, and cellular debris was removed by centrifugation at 500 g for 5 min. Lentiviral pseudo-particles present in the collected supernatants were concentrated using Lenti-X Concentrator following the manufacture's protocol (Clontech, Cat No. 631231). Concentrated supernatants were then aliquoted and stored at -80ºC.

Table 2.5 Oligonucleotides coding for shRNA sequences	
Primer Name	**Primer Sequence (5' to 3')**
SH002-F	CCGGCAACAAGATGAAGAGCACCAACTCGAGTTGGTGCTCTTCATCTTGTTGTTTTT
SH002-R	AATTAAAAACAACAAGATGAAGAGCACCAACTCGAGTTGGTGCTCTTCATCTTGTTG
shRae1-24-F	CCGGCGATGTCATTGTTCAGCAGCTCTCGAGAGCTGCTGAACAATGACATCGTTTTTT
shRae1-24-R	AATTAAAAAACGATGTCATTGTTCAGCAGCTCTCGAGAGCTGCTGAACAATGACATCG
shNup98-14-F	CCGGCCCTTGCAGATGGCTCTTAATCTCGAGATTAAGAGCCATCTGCAAGGGTTTTT
shNup98-14-R	AATTAAAAACCCTTGCAGATGGCTCTTAATCTCGAGATTAAGAGCCATCTGCAAGGG

2.13.2 Reverse transduction of lentiviral pseudo-particles.

Lentiviral transduction for establishing cell lines harboring the Tet-shRNA constructs, or the Nup96-V5 construct was performed using a reverse transduction method. Detached Vero cells (5 x 10^4 cells) were mixed with the concentrated lentivirus suspension (0-10 µL) and 8 µg/mL hexadimethrine bromide (Sigma-Aldrich) in a total volume of 200 µL and were then seeded in a 24-well plate. After 6 h of incubation at 37°C and 5% CO_2, 1 mL of fresh culture media was supplemented to each well.

2.13.3 Production of stable cell lines.

At 48 h post transfection, the cells were subjected to drug selection with either 5 µg/mL puromycin or 300 µg/mL of zeocin. The selection media was changed every 2 days until the negative control samples (transduced without lentivirus) did not contain any viable cells. Single cell clones were isolated using a previously established protocol (Ryan, J. A., Corning Incorporated, Life Sciences). Briefly, 100

μL of culture media was added to all wells in a 96-well plate, except for well A1 (top left well). Detached cells (4 x 10^3 cells) in a volume of 200 μL was then added to well A1, and 100 μL of this cell suspension was serially transferred from wells B1 to H1, making 1:2 dilutions down the length of the entire first column of wells. Using an 8-channel micropipette, 100 μL of fresh culture media was added to wells A1-H1 (the entire first column), the cell slurry was gently resuspended, and 100 μL from each well of the first column was transferred to the second column (A2-H2). This process was repeated until 1:2 dilutions were made down the entire length of the plate. Each well was then supplemented with an additional 100 μL of fresh culture media and incubated at 37°C. Cells were visualized each day to determine the wells which contained a single colony of growth, and these wells were subjected to further expansion. Throughout this time of selection, culture media in the 96-well plate was replaced every 3 days.

The successful transduction of the Tet-shRNA constructs and knock-down of the target genes was confirmed by western blot and immunofluorescence microscopy analysis after doxycycline treatment. The successful transduction and isolation of the single cell Nup96-V5 expressing clones was also confirmed by western blot and immunofluorescence microscopy analysis.

To note, the Vero cells containing the doxycycline inducible shNup98, shRae1, and shScramble constructs used in these studies, are polyclonal populations of cells and the integration of these constructs was selected for using puromycin. The Vero cells integrated with the shNup98 resistant Nup96-V5 construct used in these

studies were selected for using zeocin and have undergone single cell isolation to generate monoclonal populations of cells.

2.14 Treatment conditions.

2.14.1 Doxycycline treatment for induction of shRNA expression.

Cells containing the various Tet-shRNA constructs were subjected to treatment with doxycycline to induce the expression of the respective shRNA construct. Cells were treated with a final concentration of 100 ng/mL of doxycycline (Sigma-Aldrich) for the times indicated in each experiment.

2.14.2 Interferon treatment for induction of STAT1 nuclear import.

When required, Vero cells integrated with the various Tet-shRNA constructs were treated with a final concentration of 10 U/μL of IFN-α1 (Sigma-Aldrich), to induce the activation of STAT1 for 40 min before processing for downstream experiments.

2.15 Growth and cell viability assays.

To examine cell growth, the appropriate Tet-shRNA Vero cell line was seeded as two sets of triplicates, in 4 separate 6-well plates (4×10^4 cells per well). Per 6-well plate, one triplicate was grown in culture media containing doxycycline and the other set was grown without doxycycline for either 24 h, 48 h, 72h and 96h. At either 24 h, 48 h, 72 h, and 96 h of growth, cells were trypsinized and treated with 3.7% formaldehyde, and cells were counted. A sample of cells at the 0 h time point was also fixed with 3.7% formaldehyde, to confirm cells were seeded at ~4 x

10^4 cells per well. Cell number was counted manually using a hemocytometer and an inverted light microscope, in order to calculate cell growth throughout 96 h of doxycycline treatment.

The cell viability assay was performed using a Cell Cytotoxicity Assay Kit as per manufacturer's protocol (Abcam, Cat No. ab112119). Briefly, cells were seeded (1 x 10^3 cells per well) in triplicate in 5 separate columns of a 96-well plate and incubated for 96 h. Triplicates were supplemented with doxycycline for either 0 h, 24 h, 48 h, 72 h or 96 h, and after a total 96 h of growth, cell viability was assessed using the Cell Cytotoxicity Assay Kit (Abcam, Cat No. ab112119). Assay solution (resazurin solution) was added to each well at 1/5 the volume of the culture media and cells were incubated for 1 h at 37°C. Fluorescence signals produced from each well were measured using a CLARIOstar microplate reader (BMG Labtech). The fluorescence produced from shNup98 cells was normalized against the fluorescence produced from the scramble control cells at each time of doxycycline treatment indicated, and the results were plotted as the population of viable shNup98 cells relative to the population of viable scramble control cells.

2.16 Western blotting.

2.16.1 Preparation of mammalian whole cell lysates.

Cells were lysed in SDS-PAGE sample buffer (1% SDS, 5% glycerol, 100 mM DTT, 0.001% bromophenol blue, 100 mM Tris-HCl, pH 6.8) containing 1 mM PMSF, 1:1000 Benzonase Nuclease (MilliporeSigma Cat No. E1014), and, if needed, 1:100 phosphatase inhibitor cocktail (Cell Signaling Cat No. 5870). The

samples were briefly sonicated (Branson Sonifer 250) and boiled at 65°C for 10 min. If protein samples needed to be quantified before being separated by SDS-PAGE, cells were lysed in RIPA buffer (150 mM NaCl, 1% IGEPAL Ca-630, 0.5% DOC, 1% SDS, 50 mM Tris-HCl pH 7.4) containing 1 mM PMSF and 1:1000 Benzonase Nuclease, and subjected to quantification using a BCA Protein Assay Kit (Thermo Fisher Scientific, Cat no. 23225) as per manufacture's protocol. The protein concentrations of the samples were adjusted using RIPA buffer, they were then mixed in a 3:1 ratio with 4xSDS-PAGE sample buffer (8% SDS, 40% glycerol, 100 mM DTT, 0.001% bromophenol blue, 250 mM Tris-HCl, pH 6.8), and were then boiled for 10 min at 65°C before being resolved by SDS-PAGE.

2.16.2 SDS-PAGE and western blot analysis.

SDS-PAGE and western blot analysis were carried out as previously described in section 2.6.2. All primary and secondary antibodies used for western blot analysis in mammalian cells are listed in Table 2.1.

2.17 Immunofluorescence microscopy.

2.17.1 Sample preparation.

Cells were seeded in 24-well plates containing 12 mm round glass coverslips (Thermo Fisher). The samples were fixed with 3.75% formaldehyde in PBS at room temperature for 10 min and were then washed twice with 1 mL PBS. Cells were permeabilized with 0.5 mL of 0.5% Triton X-100 in PBS for 10 min, washed with 1 mL of PBS-T and blocked with 0.5 mL of PBS-T + 1% BSA at room temperature for 20 min. The samples were incubated with primary antibodies

(1:1000 dilution, except for anti-Nup96 which was used in a 1:100, Table 2.1) in PBS-T + 1% BSA at 4°C overnight. After washes (3 x 5 min) with 1 mL of PBS-T + 0.1% BSA, the samples were incubated with the corresponding secondary antibody (1:1000 dilution, Table 2.1) in PBS-T + 1% BSA at RT for 1 h. Samples were then washed with PBS-T (3 x 5 min) and the coverslips containing the cell samples were finally mounted on DAPI-fluoromountG (Southern Biotech) before being visualized.

2.17.2 Image acquisition, processing, and quantification.

A series of z-stack images of fixed samples were acquired using the DeltaVision Elite imaging system (Cytiva) equipped with a PlanApo N 60x/1.42 NA oil objective (Olympus) at 0.24μm intervals along the z axis. Images were deconvolved with the deconvolution module of the SoftWoRx software (Cytiva) under a "conservative" setting. Deconvolved images were further rendered using ImageJ FIJI software (NIH; Schindelin *et al*., 2012).

The quantification of the signal intensity of Flag-Orf6 was performed using ImageJ FIJI software. For each cell, a single slice containing the equatorial section of the nucleus was used for analysis. The integral signal intensities in the defined regions of the cytoplasm and the nuclear periphery (the regions within two pixels of the cytoplasmic and the nucleoplasmic sides of the NE) were divided by the area of the indicated regions to yield the normalized signal intensities of the regions of interest. The normalized signal intensity of Flag-Orf6 at the NE was then plotted against the normalized signal intensity of Flag-Orf6 within the cytoplasm.

Quantification of the signal intensity of STAT1 was measured using ImageJ FIJI software. For each cell, a 20 x 20-pixel box was created within the nucleus and the cytoplasm and the raw signal intensity of the STAT1 signal was measured. A 20 x 20-pixel box was also created in a region without any cells and the raw signal intensity was measured, which was used as a background signal intensity. After the background signal was subtracted from both the nuclear (N) and the cytoplasmic (C) signals (background correction), the N/C ratio of STAT1 was calculated as the ratio between the normalized signal intensities within the nucleus and within the cytoplasm.

Quantification of Nup96 foci was performed on Imaris software (Oxford instruments) using a spot detection function with a minimum dimeter threshold set at 0.2 μm. The spot quality threshold value was adjusted for each image, to generate a threshold value that optimally fit each data set, which was suggested by the Imaris Reference Manual (Bitplane Scientific Solutions).

2.18 Fluorescence *in situ* hybridization.

2.18.1 Sample preparation.

The fluorescence in situ hybridisation (FISH) experiment was performed essentially as described by (Faria *et al*., 2005). The cells were seeded in 24-well plates containing 12 mm round coverslips (Thermo Fisher). Samples were fixed with 3.75% formaldehyde in PBS at RT for 10 min and washed twice briefly with PBS. The cells were permeabilized with PBS + 0.2% Triton X-100 at RT for 10 min and incubated with primary antibodies (1:1000 dilution) in PBS + 0.2% Triton

X-100 + 1:100 RNasein Ribonuclease inhibitor (Invitrogen) for 1 h. After washes (3 x 5 min) with PBS, the cells were fixed with 3.75% formaldehyde in PBS at RT for 10 min and then washed twice with PBS. The samples were then incubated with prehybridization buffer (15% formamide in 1xSSC) for 20 min at RT. Hybridization of the oligo-dT probe was performed by incubation of the sample with hybridization buffer (15% formamide, 10% dextran sulfate, 0.2 μg/μL tRNA, 2 mM VRC, Texas Red-Oligo dT_{50} in 1xSSC) at 37°C overnight. In the morning, cells were washed (2 x 30 min) with prehybridization buffer at 37°C, followed by two brief washes with PBS. Following this, cells were incubated with secondary antibodies (1:1000 dilution) in PBS at RT for 1 h, then washed with PBS. The coverslips containing the cell samples were mounted on DAPI-fluoromountG (Soughern Biotech) before visualization.

If FISH analysis was performed without the use of antibodies, the protocol above was modified by excluding the primary and secondary antibody incubations. Briefly, after permeabilization, cells were incubated in pre-hybridization buffer (2 x 30 min), with subsequent incubation in hybridization buffer overnight. The next day, cells were washed with prehybridization buffer (2 x 30 min), washed briefly with PBS twice, and mounted on DAPI-fluoromountG.

2.18.2 Image acquisition, processing, and quantification.

A series of z-stack images of fixed samples were acquired using the DeltaVision Elite imaging system (Cyitvia) and were subjected to deconvolution as described previously in section 2.17.2. Deconvolved images were further rendered using ImageJ FIJI software (NIH; Schindelin *et al*., 2012).

Quantification of the signal intensity of poly-A RNA was measured using ImageJ FIJI software. For each cell, a 20 x 20-pixel box was created within the nucleus and the cytoplasm, and the raw signal intensity of the poly-A RNA signal was measured. A 20 x 20-pixel box was also created in a region without any cells and the raw signal intensity was measured, which was used as a background signal intensity. After the background signal was subtracted from both the nuclear (N) and the cytoplasmic (C) signals (background correction) the N/C ratio of the poly-A RNA signal was calculated as the ratio between the normalized signal intensities within the nucleus and within the cytoplasm.

***All ImageJ macros and python scripts used for the generation of the various presented images, graphs, and for the statistical analysis of the quantification studies, are listed within the appendix. These macros and scripts were generously written and provided by Dr. Tadashi Makio (Department of Cell Biology, University of Alberta).

Chapter III

Using *S. cerevisiae* as a model organism to study SARS-CoV-2 Orf6 function

3.1 Overview.

There are many benefits to using yeast as a model organism; they are single cell eukaryotes, they are inexpensive, genetic manipulation and cultivation is easy, and they have a quick generation time allowing for much more rapid experimentation when compared to mammalian model systems (Pesic, 2021). Due to a surprising genetic similarity between yeast and humans, along with a remarkable conservation of many important cellular pathways, *S. cerevisiae* has been used extensively as a model organism to study various aspects of human biology and disease (Mager and Winderickx; 2005; Karathia *et al*., 2011; Kachroo *et al*., 2022). Residues within the human Nup98/Rae1 complex, which are critical for forming interactions with the SARS-CoV-2 Orf6 protein (Li *et al*., 2022), are conserved within the *S. cerevisiae* Nup116/Gle2 complex (Ren *et al*., 2010; Quan *et al*., 2014). This suggested to us that Orf6 would also likely interact with the Nup116/Gle2 complex at NPCs in yeast. Moreover, the overall conservation between *S. cerevisiae* and human NPCs, along with the striking similarity between the molecular mechanisms of nuclear transport between yeast and humans, suggested that *S. cerevisiae* may be a useful alternative model organism to study the nuclear transport defects caused by the SARS-CoV-2 Orf6 protein (Cronshaw *et al*., 2002; Aitchison and Rout, 2012; Ptak and Wozniak, 2014).

3.2 Results

3.2.1 SARS-CoV-2 Orf6 can be constitutively expressed in *S. cerevisiae.*

Due to the considerable sequence similarity found between the *S. cerevisiae* Nup116/Gle2 complex when compared to the human Nup98/Rae1 complex (Ren *et al*., 2010) and because of the many advantages of utilizing yeast as a model organism (Pesic, 2021), we used *S. cerevisiae* to study the nuclear transport defects caused by the production of the SARS-CoV-2 Orf6 protein. The expression and localization of Orf6 within *S. cerevisiae* was first examined to assess if *S. cerevisiae* could be a potential candidate to study Orf6 function. To investigate if the SARS-CoV-2 Orf6 protein could be expressed in yeast, a DNA open reading frame encoding GFP-tagged Orf6 under the control of the constitutively active yeast NOP1 promoter was integrated into the *his3Δ1* locus of *S. cerevisiae* (strain BY4742). Western blot analysis of whole cell lysates from both wild type (WT) and GFP-Orf6 expressing cells show that *S. cerevisiae* can express the GFP-Orf6 protein (Figure 3.1A). Next, to assess if the constitutive expression of GFP-Orf6 caused growth rate defects, both WT and GFP-Orf6 expressing cells were spotted as 10-fold serial dilutions on YPD plates and were grown at either 30°C or 37°C for two days. Results indicate that the consistent expression of GFP-Orf6 in *S. cerevisiae* does not lead to any noticeable growth rate defects, as both WT and GFP-Orf6 expressing cells show similar rates of growth when incubated at either 30°C or 37°C (Figure 3.1B).

WT and GFP-Orf6 expressing cells were also examined by fluorescent microscopy analysis to assess the localization of GFP-Orf6 in *S. cerevisiae*, and results show that GFP-Orf6 localizes in a radial fashion as punctate foci in yeast

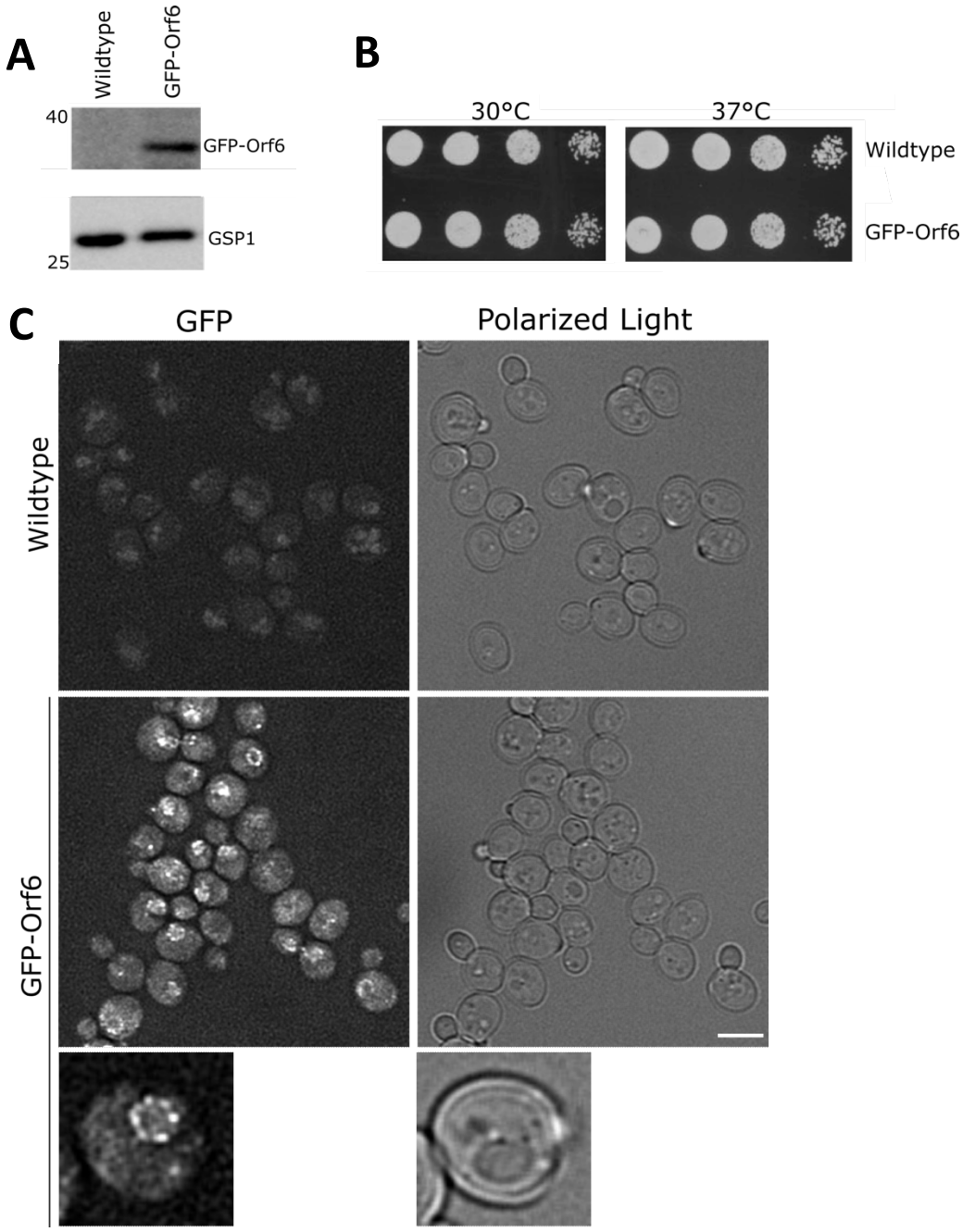

Figure 3.1 SARS-CoV-2 Orf6 can be constitutively expressed in *S. cerevisiae.* **(A)** Wildtype and GFP-Orf6 expressing cells were grown to mid log phase, whole cell extracts were prepared, and analyzed by western blotting using anti-GFP and anti-GSP1 (load control) antibodies as indicated to the right. Molecular mass markers (shown in kDa) are depicted on the left. **(B)** Wildtype and GFP-Orf6 expressing cells were spotted as 10-fold serial dilutions onto YPD plates and incubated at the indicated temperatures for 2 days to assess growth defects associated with GFP-Orf6 expression. **(C)** Wildtype and GFP-Orf6 expressing cells were grown to mid log phase in YPD and the localization of GFP-Orf6 was assessed by fluorescence microscopy analysis. Scale bar represents 5 μm.

(Figure 3.1C), which is reminiscent of NPC staining within the NE. Furthermore, the overall cellular morphology does not seem to be affected by Orf6 expression, as the polarized light images of both WT and GFP-Orf6 expressing *S. cerevisiae* show cells with comparable size and shape (Figure 3.1C). Collectively, these results suggest that the SARS-CoV-2 Orf6 protein can be constitutively expressed and localizes to the NE within *S. cerevisiae* without affecting cell growth or morphology.

3.2.2 Orf6 partially co-localizes with Nup116 and Gle2 at the nuclear envelope of *S. cerevisiae.*

Since the SARS-CoV-2 Orf6 protein has been shown to co-localize with Nup98 at the NPCs of mammalian cells (Miorin *et al*., 2020), we wanted to investigate if Orf6 localizes at NPCs in *S. cerevisiae*. To assess this, GFP-Orf6 expressing cells were subject to targeted integration with an mCherry (mCh) construct to tag the C-terminus of either Nup116 or Gle2, in order to visualize co-localization between GFP-Orf6 and either Nup116-mCherry or Gle2-mCherry. Western blot analysis of whole cell lysates of WT, GFP-Orf6, GFP-Orf6/Nup116-mCh, and GFP-Orf6/Gle2-mCh strains confirm expression of GFP-Orf6 in all three GFP-Orf6 expressing strains (Figure 3.2A). However, GFP-Orf6 expression seems to be slightly reduced within the GFP-Orf6/Gle2-mCh expressing strain when compared to both the GFP-Orf6 and GFP-Orf6/Nup116-mCh strains (Figure 3.2A). Cell growth of WT, GFP-Orf6, GFP-Orf6/Nup116-mCh, and GFP-Orf6/Gle2-mCh strains was also assessed to evaluate potential growth rate changes caused by the introduction of an mCherry tag at the C-terminus of either Nup116 or Gle2 in GFP-

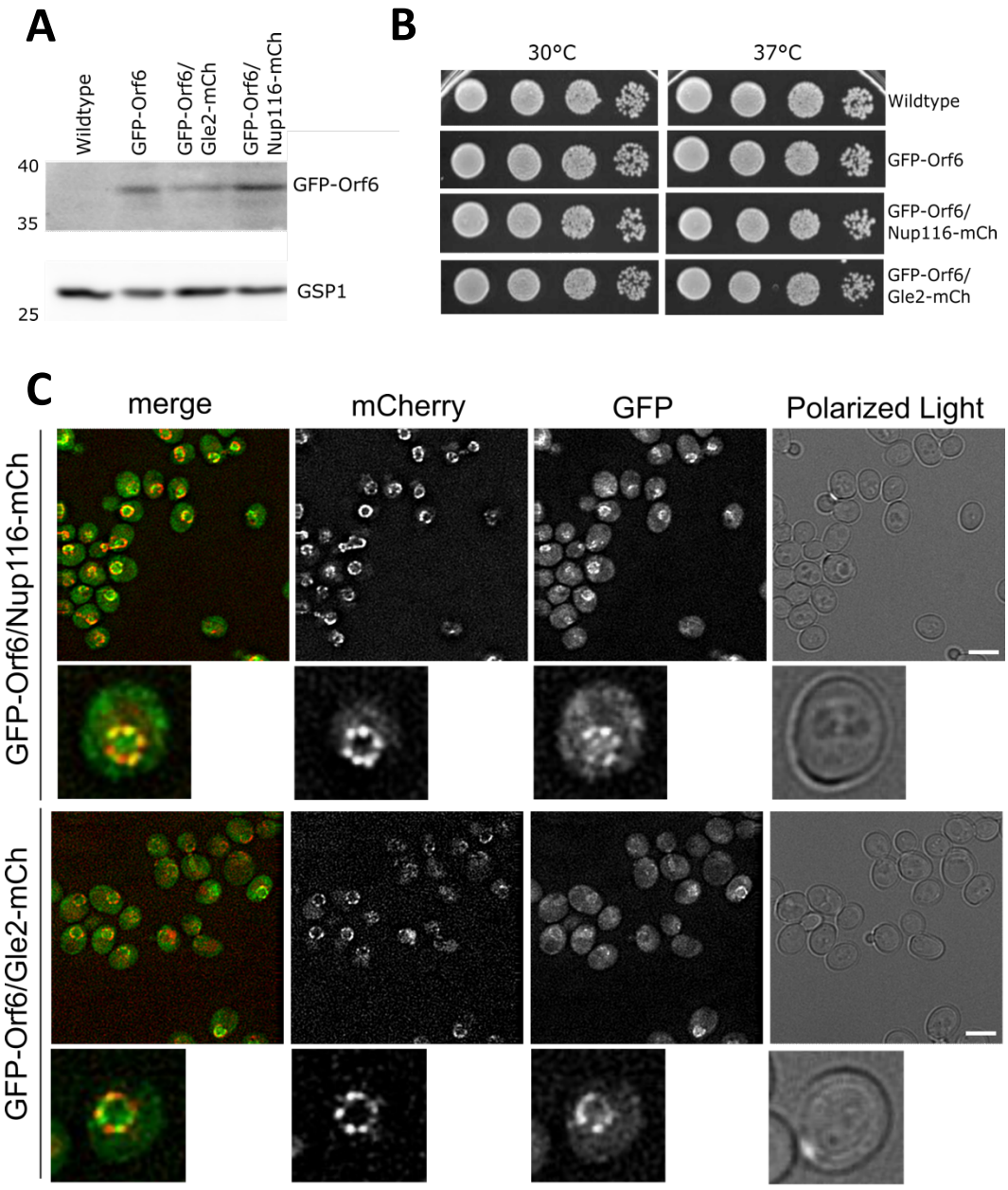

Figure 3.2 Orf6 partially co-localizes with Nup116 and Gle2 at the nuclear envelope.

(A) Wildtype, GFP-Orf6, GFP-Orf6/Nup116-mCh, and GPF-Orf6/Gle2-mCh strains were grown to mid log phase, whole cell extracts were prepared, and analyzed by western blotting using anti-GFP and anti-GSP1 (load control) antibodies as indicated to the right. Molecular mass markers (shown in kDa) are depicted on the left. **(B)** Wildtype, GFP-Orf6, GFP-Orf6/Nup116-mCh, and GPF-Orf6/Gle2-mCh strains were spotted as 10-fold serial dilutions onto YPD plates and incubated at the indicated temperatures for 2 days. **(C)** Wildtype, GFP-Orf6, GFP-Orf6/Nup116-mCh, and GPF-Orf6/Gle2-mCh strains were grown to mid log phase in YPD and were assessed by fluorescence microscopy. Scale bars represent 5 μm.

Orf6 expressing cells (Figure 3.2B). Results indicate that there are no striking growth defects associated with these strains when grown at either 30°C or 37°C for two days, as all three GFP-Orf6 expressing strains show similar growth rates to WT *S. cerevisiae* (Figure 3.2B).

GFP-Orf6/Nup116-mCh and GFP-Orf6/Gle2-mCh strains were further characterized by fluorescent microscopy analysis to determine co-localization between GFP-Orf6 and either Nup116-mCh or Gle2-mCh (Figure 3.2C). These results show that both Nup116-mCh and Gle2-mCh localize in punctate foci similar to the staining pattern of GFP-Orf6, however, there is only partial co-localization detected between the GFP-Orf6 foci and either Nup116-mCh or Gle2-mCh foci (Figure 3.2C). GFP-Orf6 levels seem to be higher in Nup116-mCh expressing strains when compared to Gle2-mCh expressing strains, as there are more cells with visible GFP-Orf6 foci detected in the GFP-Orf6/Nup116-mCh cell line when compared to the GFP-Orf6/Gle2-mCh expressing cell line (Figure 3.2C). Overall, these results suggest that when GFP-Orf6 is expressed in *S. cerevisiae*, GFP-Orf6 localizes at the NE, however, GFP-Orf6 shows only partial co-localization with both Nup116-mCh and Gle2-mCh.

3.2.3 Orf6 localization is not affected by depletion of Nup116 or Gle2.

The Nup98/Rae1 complex has been shown to be a major interacting partner of the SARS-CoV-2 Orf6 protein (Gordon *et al*., 2020; Miorin *et al*., 2020; Li *et al*., 2021), and since GFP-Orf6 partially co-localized with both Nup116 and Gle2 in *S. cerevisiae*, we wanted to assess if depletion of either Nup116 or Gle2 would affect Orf6 localization. Previous investigations have revealed that the deletion of

either Nup116 or Gle2 in *S. cerevisiae* causes severe defects in NPC integrity and a block of nuclear transport, and both have been shown to be necessary for normal cell growth (Wente and Blobal 1993; Murphy *et al*., 1996). Therefore, depletion of either Nup116 or Gle2 protein levels was achieved by placing the *NUP116* and *GLE2* genes under the control of a regulatable MET3 promoter (P_{MET3}).

Integration of the P_{MET3} with a tandem HA tag was targeted for insertion in frame with the start codon of either *NUP116* or *GLE2* so that Nup116 and Gle2 protein levels could be assessed using an antibody directed against HA. GFP-Orf6/P_{MET3}-HA-Nup116 and GFP-Orf6/P_{MET3}-HA-Gle2 strains were grown over an 8 h growth period in either minimal media lacking methionine (Met-), to allow for the active expression of Nup116 or Gle2, or they were supplemented with methionine (Met+) to induce the shutoff of the MET3 promoter and deplete levels of either Nup116 or Gle2. Western blot analysis of whole cell lysates collected from GFP-Orf6/P_{MET3}-HA-Nup116 (Figure 3.3B) or GFP-Orf6/P_{MET3}-HA-Gle2 (Figure 3.3D) strains show that both the HA-Nup116 protein and the HA-Gle2 protein can be depleted by 8 h of growth in the shutoff condition (Met+), however, levels of Nup116 and Gle2 are not fully depleted by this time. Notably, the level of GFP-Orf6 protein seems to be reduced in the GFP-Orf6/P_{MET3}-HA-Gle2 strain after 8 h of Gle2 depletion (Figure 3.3D), but levels of GFP-Orf6 remain comparable in the GFP-Orf6/P_{MET3}-HA-Nup116 strain regardless of Nup116 knockdown (Figure 3.3B). GFP-Orf6/P_{MET3}-HA-Nup116 or GFP-Orf6/P_{MET3}-HA-Gle2 strains were further assessed by fluorescent microscopy analysis to visualize GFP-Orf6 localization when Nup116 and Gle2 protein levels were depleted. GFP-

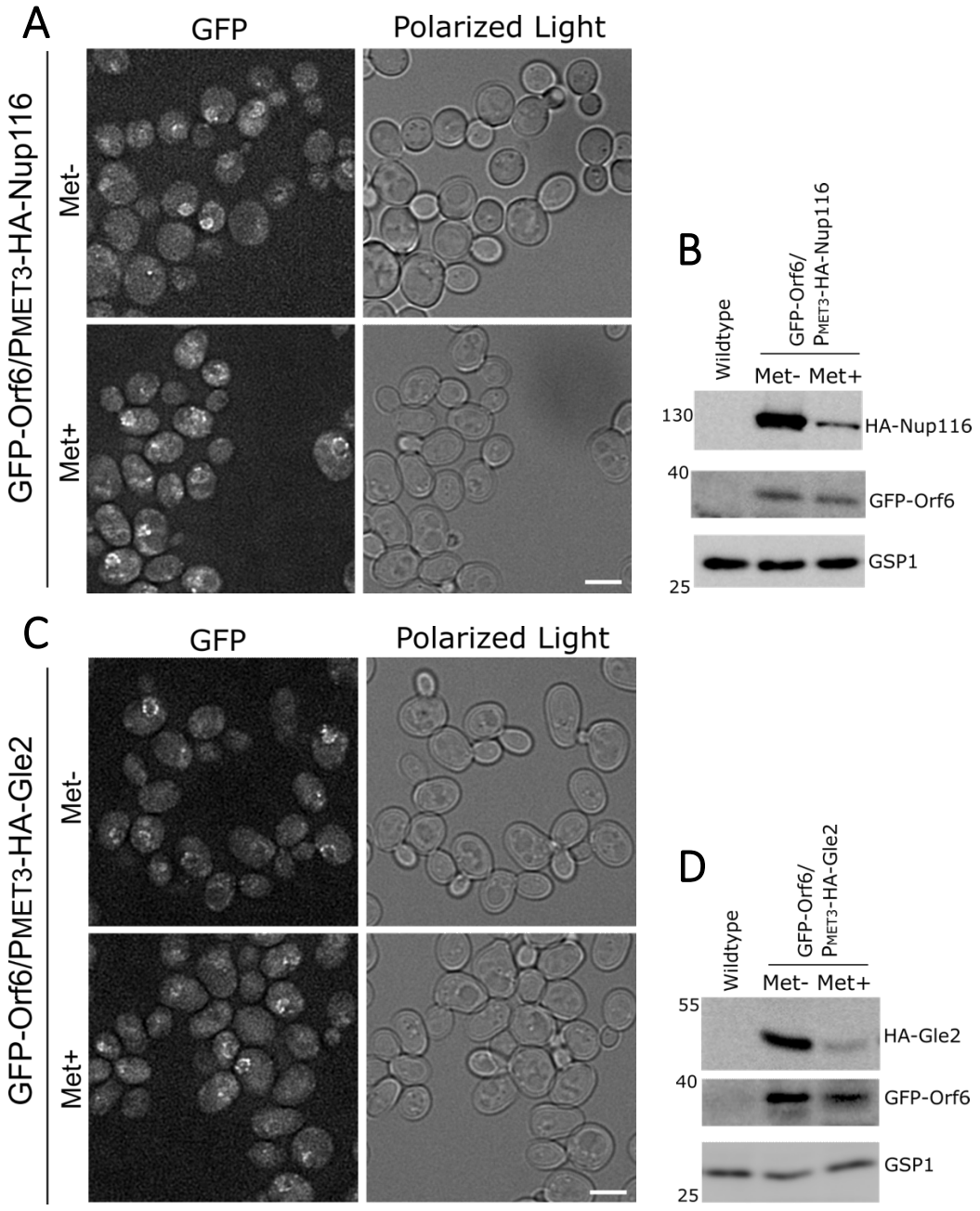

Figure 3.3 Orf6 localization is not affected by depletion of Nup116 or Gle2.
(A) GFP-Orf6/P_{MET3}-HA-Nup116 and **(C)** GFP-Orf6/P_{MET3}-HA-Gle2 strains were grown overnight in medium lacking methionine (Met-). Overnight cultures were diluted into either fresh Met- media or into media supplemented with methionine (Met+) to induce the depletion of Nup116 or Gle2. Cells were grown for 8 h prior to being examined by fluorescence microscopy analysis. Scale bars represent 5 μm. **(B)** and **(D)** Protein depletion in these experiments was confirmed by immunoblot analysis. Whole cell extracts were prepared after 8 h of growth in Met- or Met+ media and analyzed by western blotting using anti-HA, anti-GFP, and anti-GSP1 (load control) antibodies. Molecular mass markers (shown in kDa) are depicted on the left.

Orf6/P_{MET3}-HA-Nup116 (Figure 3.3A) and GFP-Orf6/P_{MET3}-HA-Gle2 (Figure 3.3C) strains were imaged after 8 h of growth in either Met- or Met+ media, and results show that GFP-Orf6 localizes in a similar punctate pattern in both GFP-Orf6/P_{MET3}-HA-Nup116 and GFP-Orf6/P_{MET3}-HA-Gle2 cells, regardless of treatment condition (Figure 3.3A and C). Collectively, these results suggest that the depletion of Nup116 or Gle2 to the levels achieved in this study do not affect the localization of GFP-Orf6 within *S. cerevisiae.*

3.2.4 Orf6 expression does not cause bidirectional nuclear transport defects in *S. cerevisiae.*

Since the SARS-CoV-2 Orf6 protein has been shown to disrupt classical nuclear import in mammalian cells (Miorin *et al*., 2020; Addetia *et al*., 2021), we wanted to examine if Orf6 expression would lead to a similar block of nuclear import in *S. cerevisiae.* Therefore, both WT and GFP-Orf6 expressing strains were transformed with various plasmids containing an NLS-reporter construct to assess if various protein import pathways were affected by the expression of Orf6.

Both WT and GFP-Orf6 expressing strains were transformed with a plasmid to express either a cNLS-GFP or a pho4-NLS-GFP reporter protein, in order to determine if GFP-Orf6 affected the nuclear import of these reporters. Cells were grown to mid-log phase in YPD before being visualized by fluorescent microscopy analysis, and results indicate that the steady state localization of either the cNLS (Figure 3.4A) or the pho4-NLS (Figure 3.4B) reporter protein is not noticeably affected by Orf6 expression, as both WT and GFP-Orf6 expressing cells show

strong nuclear accumulation of both NLS-GFP reporter proteins. Although these results show that Orf6 does not completely inhibit the nuclear import of NLS containing reporter proteins, it does not reveal if the rate of nuclear import is altered between WT and Orf6 expressing cells. Therefore, in order to assess if the relative rate of import is decreased by Orf6 expression, both WT and GFP-Orf6 strains expressing either a cNLS-GFP or a pho4-NLS-GFP reporter protein were treated with 2-deoxyglucose and sodium azide, to force the nucleocytoplasmic equilibration of the NLS-GFP signal.

Sodium azide inhibits ATP production by interfering with oxidative phosphorylation, and 2-deoxyglucose inhibits ATP production by interfering with glycolysis, however, GTP levels are also rapidly decreased upon depletion of ATP. Therefore, the RanGTP gradient is effectively diminished and RanGTP dependent nuclear transport is inhibited, leading to the nucleocytoplasmic equilibration of the NLS-GFP reporter protein (Shulga *et al*., 1996; Schwoebel and Moore, 2002). By temporarily inhibiting the nuclear import of the NLS-GFP reporter protein, re-establishment of the RanGTP gradient can be achieved by addition of glucose, and the relative rates of NLS-GFP nuclear import can be assessed between WT and Orf6 expressing cell lines to determine if Orf6 decreases the relative rate of nuclear import of either the cNLS-GFP or the pho4-NLS-GFP reporter proteins. Therefore cells were grown for 45 min in glucose free synthetic complete media containing 10 mM 2-deoxyglucose and 10 mM sodium azide to induce the nucleocytoplasmic equilibration of the NLS-GFP signal (Shulga *et al.,* 1996), and were then spotted onto an agarose pad containing 2% glucose to induce the nuclear import of the NLS

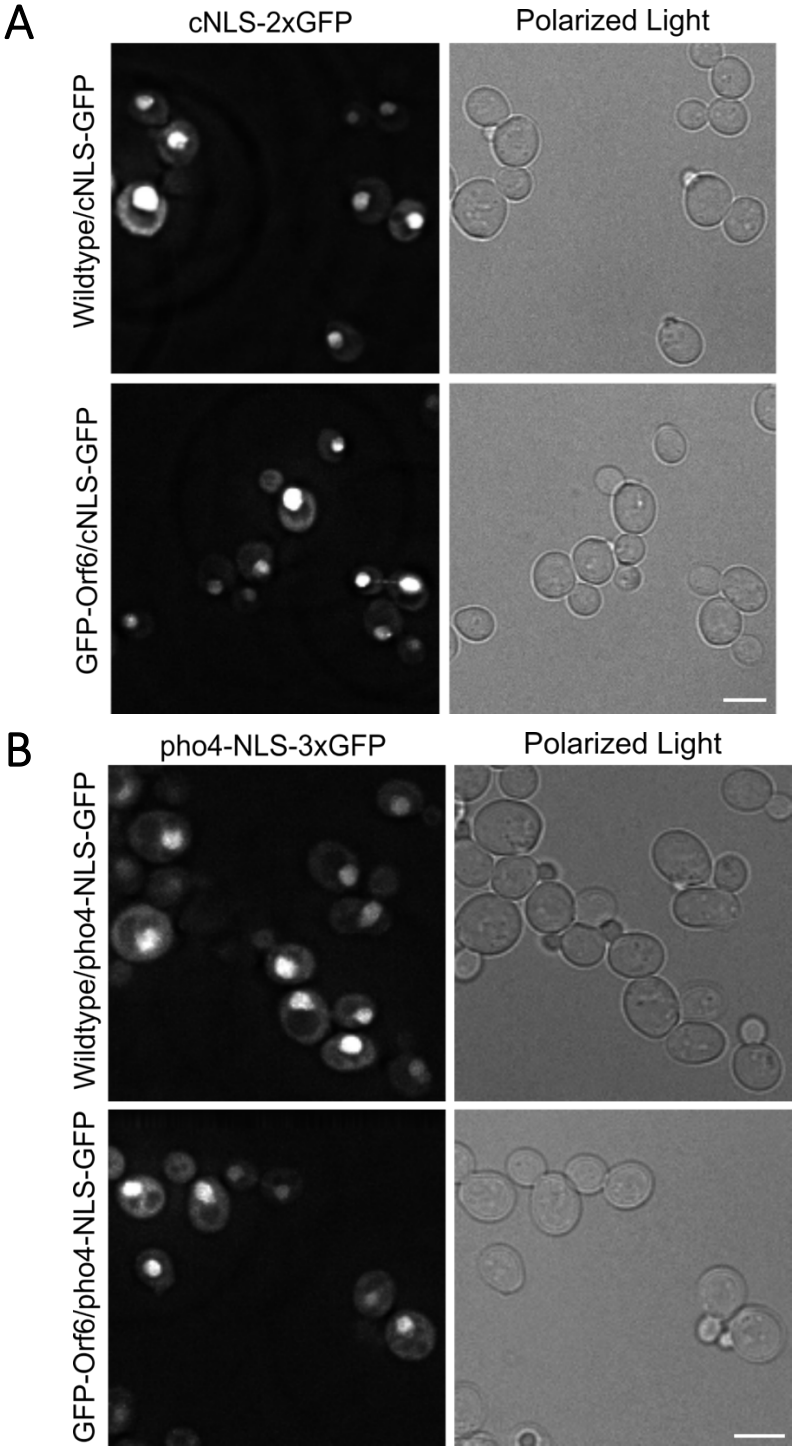

Figure 3.4 Orf6 expression does not affect the steady state localization of cNLS or pho4-NLS reporter proteins.
Wildtype and GFP-Orf6 strains containing a plasmid encoding for a **(A)** cNLS-2xGFP or a **(B)** pho4-NLS-3xGFP reporter protein were grown to early mid log phase in YPD, and the localization of the indicated reporter protein was assessed by fluorescence microscopy analysis. Scale bars represent 5 μm.

reporter protein. Cells were then assessed by fluorescence microscopy every minute for 15 minutes to visualize the nuclear import of the indicated reporter construct. Representative fluorescent microscopy images from WT and GFP-Orf6 strains expressing a cNLS-GFP reporter protein at the start (0 min) and 15 min after removal of sodium azide/2-deoxyglucose and glucose addition, show that the cNLS-GFP reporter protein is distributed throughout the cell at the 0 min timepoint, however, by 15 min the cNLS-GFP signal is strongly accumulated within the nucleus of both WT and GFP-Orf6 expressing strains (Figure 3.5A).

To assess the relative rate of import of both cNLS-GFP (Figure 3.5B) and pho4-NLS-GFP (Figure 3.5C) between WT and GFP-Orf6 expressing cells, fluorescent microscopy images of the above strains were examined each minute after removal of sodium azide/2-deoxyglucose and glucose addition to evaluate the nuclear import of the indicated reporter construct. The same field of cells were followed throughout 15 min, and a cell was scored as having nuclear accumulation of the NLS-GFP reporter protein only if the nuclear signal was brighter than the surrounding cytoplasmic signal and if the cell had a clear nuclear/cytoplasmic boundary visible (Shulga *et al*., 1996). The number of cells with nuclear accumulation of the NLS-GFP reporter protein at each time, is presented as an average percent of the cells counted throughout 2 rounds of each time course (Figure 3.5 B and C). These results indicate that there is no obvious decrease in the relative rate of nuclear import of either the cNLS-GFP or the pho4-NLS-GFP reporter protein in the GFP-Orf6 expressing strain when compared to WT cells (Figure 3.5 B and C).

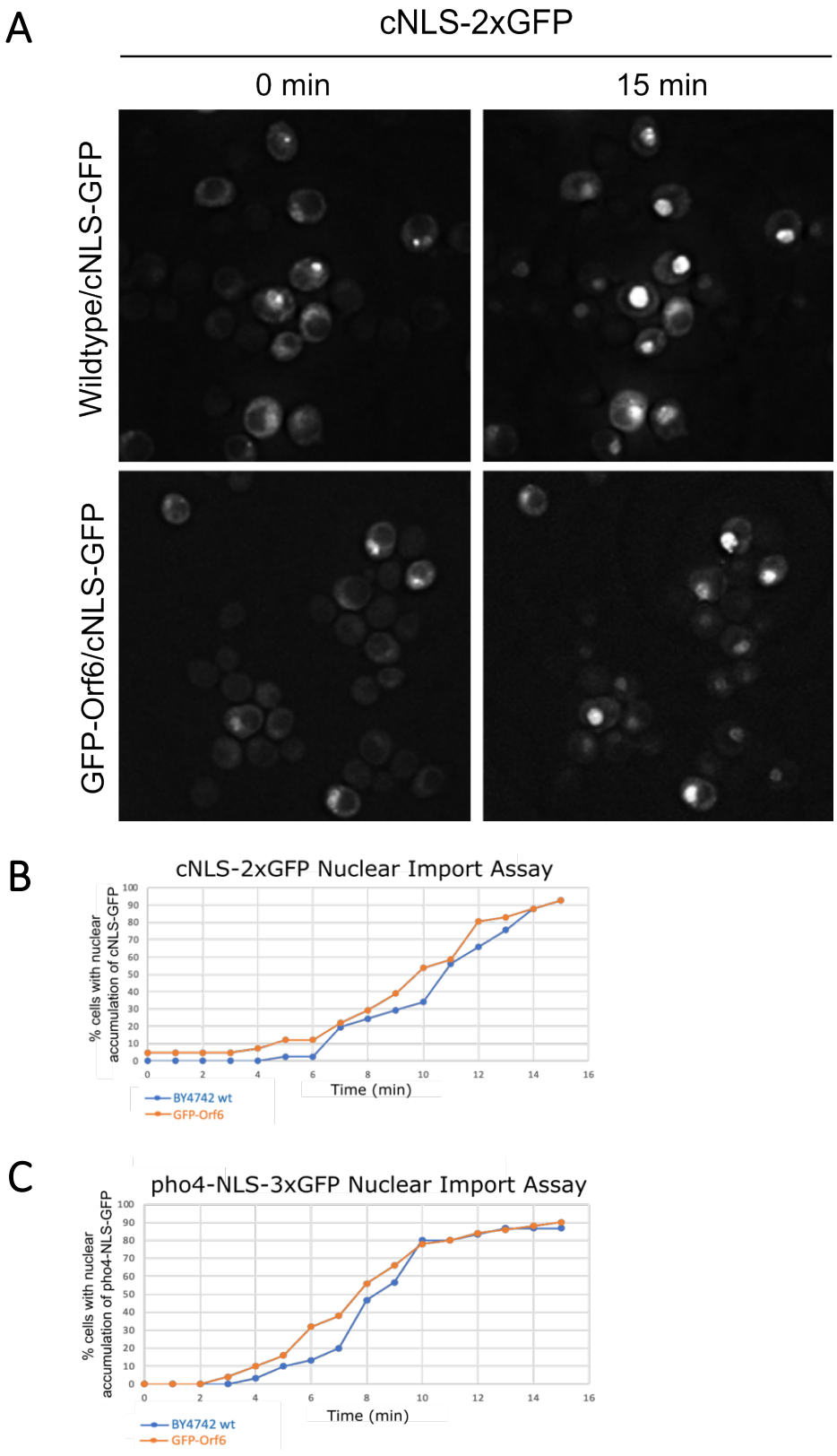

Figure 3.5 Orf6 expression does not cause protein import defects in *S. cerevisiae.*

Figure 3.5 Orf6 expression does not cause protein import defects in *S. cerevisiae.* Wildtype and GFP-Orf6 strains containing a plasmid encoding a cNLS-2xGFP or a pho4-NLS-3xGFP reporter protein were grown to early mid log phase in synthetic complete media. Cells were collected, resuspended in glucose free synthetic complete media containing 10 mM sodium azide and 10 mM 2-deoxyglucose, and incubated for 45 min at 30°C to allow for nucleocytoplasmic equilibration of the NLS-GFP reporter protein. Cells were then spotted onto an agarose pad containing 2% glucose to induce the nuclear accumulation of the NLS-GFP reporter and were examined by fluorescence microscopy. **(A)** Representative fluorescent microscopy images of wildtype and GFP-Orf6 cells expressing a cNLS-2xGFP reporter protein at the start (0 min) and end (15 min) of removal from sodium azide/2-deoxyglucose and addition of glucose. Wildtype and GFP-Orf6 cells expressing either a cNLS-2xGFP reporter protein **(B)** or a pho4-NLS-3xGFP reporter protein **(C)** were counted for nuclear accumulation of the respective NLS-GFP reporter signal throughout 15 min of release from sodium azide/2-deoxyglucose treatment to evaluate the relative rate of protein import between these cell lines. The number of cells with nuclear accumulation of the NLS-GFP reporter protein at each time point is presented as an average percent of cells counted throughout 2 rounds of each time course ($n > 50$ cells).

Since SARS-CoV-2 Orf6 expression has also been shown to cause RNA export defects in mammalian cells though interactions with the Nup98/Rae1 complex (Addetia *et al*., 2021; Hall *et al*., 2022), we wanted to investigate if Orf6 expression would inhibit RNA export in *S. cerevisiae*. To assess this, both WT and GFP-Orf6 expressing strains were subject to FISH analysis to evaluate the cellular distribution of both actin mRNA (ACT1) and poly-A RNA (Figure 3.6). Images of the above cells show that the expression of GFP-Orf6 in *S. cerevisiae* does not lead to visible RNA export defects as there is no noticeable accumulation of either ACT1 mRNA or poly-A RNA within the nucleus of GFP-Orf6 expressing cells when compared to WT cells. Rather, the signal of both ACT1 mRNA and poly-A RNA remains diffusely spread throughout the cytoplasm of both strains, regardless of Orf6 expression (Figure 3.6).

Collectively, this suggests that the levels of Orf6 expression achieved in this study does not lead to obvious bidirectional nuclear transport defects in *S. cerevisiae*, as various protein import pathways and RNA export pathways are not noticeably affected by Orf6 expression.

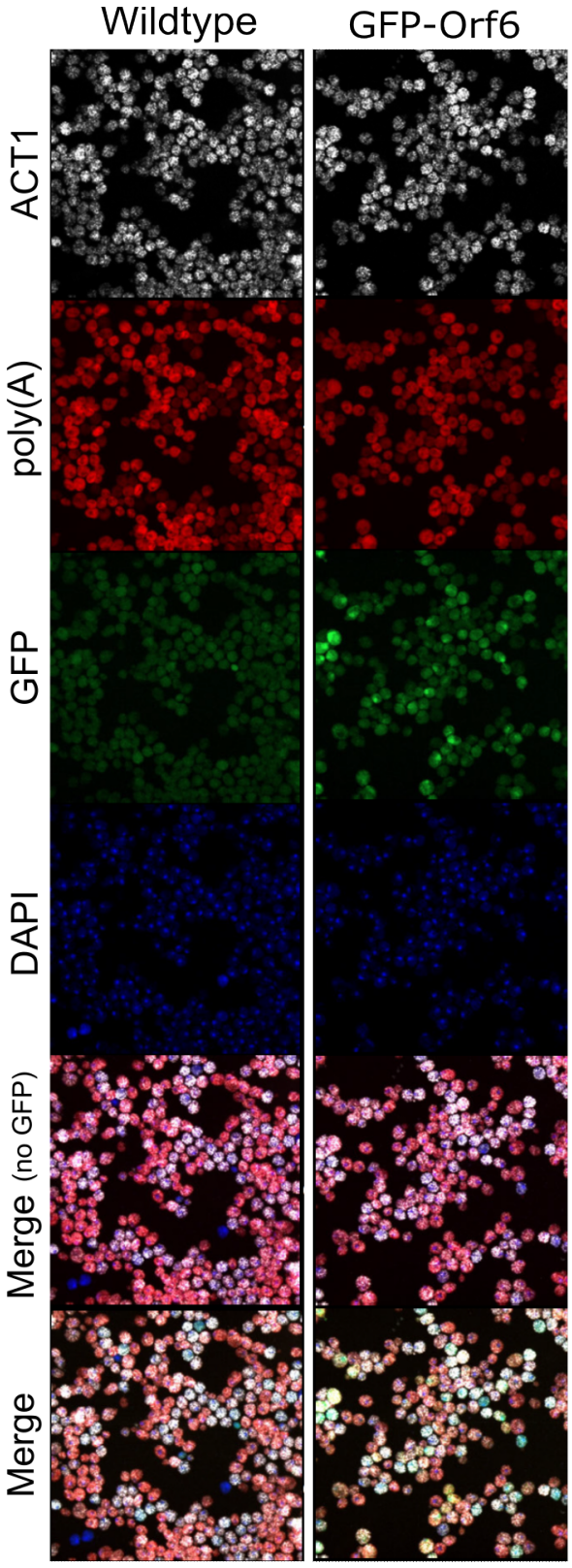

Figure 3.6 (Sandhu, R.) Orf6 expression does not cause RNA export defects in *S. cerevisiae*.

Figure 3.6 (Sandhu, R.) Orf6 expression does not cause RNA export defects in *S. cerevisiae*.
Wildtype and GFP-Orf6 expressing strains were subject to FISH analysis to examine potential mRNA export defects associated with Orf6 expression. GFP-Orf6 (green), ACT1 RNA (grey), poly-A RNA (red), DAPI (blue), and various merged images are shown. This experiment was kindly performed and analyzed by Dr. Rima Sandhu from Dr. Ben Montpetit's laboratory, University of California, Davis.

3.3 Discussion.

S. cerevisiae has been one of the most widely used eukaryotic model organisms to study human biology and disease (Poswal and Saini., 2017). Characterizations of yeast NPC structure and function has advanced the understanding of nuclear transport within mammalian systems, and due to the high conservation of the NPC across all eukaryotes, yeast has remained a highly used model organism for studies on NPC structure and function (Leslie *et al*., 2006; Wente and Route, 2010; Aitchison and Rout, 2012; Ptak and Wozniak, 2014; Kachroo *et al*., 2022).

The human Nup98/Rae1 complex is related to the *S. cerevisiae* Nup116/Gle2 complex, and both have been shown to play important roles in various nuclear import and export pathways (Iovine *et al*., 1995; Murphey at al., 1996; Ren *et al*., 2010; Iwamoto *et al*., 2010). It has been previously suggested that, along with the SARS-CoV-2 Orf6 protein, several other viral proteins contain a Nup98/Rae1 interaction motif which is characterized by a conserved methionine residue surrounded by several acidic amino acid residues (Gordon *et al*., 2020). One of these other viral proteins is the VSV M protein, for which the crystal structure of the interaction between the M protein and the $Nup98_{GLEBS}$/Rae1 complex has been characterized (Quan *et al*., 2014). The conserved methionine residue (M51) within the Nup98/Rae1 interaction motif of the VSV M protein has been shown to interact with several key residues within Rae1, including residues F257, W300, D301, K302, and R305, which make up the hydrophobic pocket of the Nup98/Rae1 complex (Quan *et al*., 2014). Recent investigations into the crystal structure of the SARS-CoV-2 Orf6 protein in complex with $Nup98_{GLEBS}$/Rae1 has also revealed that the conserved methionine

residue (M58) within the Nup98/Rae1 interaction motif of Orf6 forms interactions with the same key residues of Rae1 listed above (Li *et al*., 2022). Mutations in both the M58 residue of SARS-CoV-2 Orf6 or the M51 residue of VSV M have also been shown to significantly impair the ability of these viral proteins to interact with the Nup98/Rae1 complex (Petersen *et al*., 2000; Rajani *et al*., 2012; Miorin *et al*., 2020), suggesting that the interactions formed between the methionine residue and Rae1 are critical for the association of these viral proteins with Nup98/Rae1. Intriguingly, residues F257, W300, D301, K302, and R305 within Rae1 are completely conserved within *S. cerevisiae* Gle2 (Quan *et al*., 2014), which strongly suggests that the SARS-CoV-2 Orf6 protein would likely interact with the Nup116/Gle2 complex in *S. cerevisiae.* Moreover, due to the significant conservation between the nuclear import and export pathways of both *S. cerevisiae* and humans, this ultimately suggests that *S. cerevisiae* could likely be used as a model organism to study the effects of Orf6 on cellular nuclear transport.

SARS-CoV-2 Orf6 can be expressed and localizes at the nuclear envelope of S. cerevisiae.

To assess if *S. cerevisiae* could be used as a model organism to study SARS-CoV-2 Orf6 function, we first had to assess if *S. cerevisiae* could express the Orf6 protein. Western blot analysis indicates that GFP-Orf6 can be expressed (Figure 3.1A) and fluorescent microscopy analysis of GFP-Orf6 shows that Orf6 localizes in punctate foci in *S. cerevisiae,* however, there is heterogeneity in levels of Orf6 seen within the population of GFP-Orf6 expressing cells (Figure 3.1C). Regardless, the localization pattern observed in the above analysis had suggested to us that GFP-

Orf6 localizes to the NPC, due to the striking similarity between the GFP-Orf6 staining pattern and the previously reported localization patterns of various fluorescently tagged Nups (Bucci and Wente, 1997; Lapetina *et al*., 2017).

Since the SARS-CoV-2 Orf6 protein has been shown to interact with the Nup98/Rae1 complex in humans (Miorin *et al*., 2020; Gordon *et al*., 2020), co-localization between GFP-Orf6 and either Nup116-mCh or Gle2-mCh was assessed. Analysis of GFP-Orf6/Nup116-mCh and GFP-Orf6/Gle2-mCh strains show that GFP-Orf6 only partially co-localizes with both Nup116-mCh and Gle2-mCh foci (Figure 3.2C). If GFP-Orf6 foci were not found to be co-localized with either Nup116 or Gle2, GFP-Orf6 was often localized to regions between Nup116 and Gle2 foci, which may suggest that Orf6 can bind regions of the nuclear envelope that are absent of NPCs. Indeed, the SARS-CoV-2 Orf6 protein has been suggested to have membrane binding capacity to do an alpha-helical structure found at its N-terminus (Lee *et al.,* 2021) and may provide explanation as to why GFP-Orf6 is not always found localized to either Nup116 or Gle2 foci in *S. cerevisiae*. Alternatively, since *S. cerevisiae* has been shown to have multiple compositionally distinct populations of NPCs (Lapetina *et al*., 2017; Bensidoun *et al*., 2022), this NPC heterogeneity may provide a reason as to why Orf6 is only partially co-localizing to either Nup116-mCh or Gle2-mCh foci and suggests that Orf6 may be binding to only a subset of NPCs that contain both Nup116 and Gle2. However, it is also possible that only partial co-localization was detected between GFP-Orf6 and Nup116-mCh or Gle2-mCh due to the technical challenges involved with live cell imaging, and the dynamic movement of cellular organelles and structures

during the image acquisition process (Qiu and Yang, 2013). Therefore, slight positional changes of the nucleus, NPCs, or Nups during the time of image acquisition may affect the amount of co-localization detected between GFP-Orf6 and either Nup116-mCh or Gle2-mCh. Regardless, the partial co-localization detected between GFP-Orf6 and either Nup116-mCh or Gle2-mCh suggested to us that GFP-Orf6 is likely interacting with the Nup116/Gle2 complex in yeast.

Analysis of GFP-Orf6/Nup116-mCh and GFP-Orf6/Gle2-mCh strains have also shown that expression of GFP-Orf6 is lower in GFP-Orf6/Gle2-mCh cells (Figure 3.2A) and it was notably more difficult to assess co-localization between GFP-Orf6 and Gle2-mCh when compared to Nup116-mCh (Figure 3.2C). Previous analysis on the regions of Gle2 that interact with the GLEBS motif of Nup116 has indicated that residues close to the C-terminus of Gle2 make extensive interactions with $Nup116_{GLEBS}$ (Quan *et al*., 2014), and therefore, tagging the C-terminus of Gle2 may interfere with the interactions made between Gle2 and Nup116. Consequently, this may hinder the association of GFP-Orf6 at NPCs and may provide reason as to why there are less cells that show GFP-Orf6 localization in punctate foci around the NE in the GFP-Orf6/Gle2-mCh strain when compared to the GFP-Orf6/Nup116-mCh strain (Figure 3.2C). Comparatively, the GLEBS motif of Nup116 is located towards the N-terminus of the Nup116 protein (Quan *et al*., 2014), and therefore, the addition of a C-terminal tag would likely not affect the association of Gle2 with $Nup116_{GLEBS}$ motif. Considering there are more cells within the GFP-Orf6/Nup116-mCh expressing strain that show noticeably higher levels of GFP-Orf6 at the nuclear periphery (Figure 3.2C), this suggests that the

Nup116$_{GLEBS}$/Gle2 interaction is likely not compromised in the GFP-Orf6/Nup116-mCh strain, which may allow for greater binding of GFP-Orf6 to the NPC.

However, since only partial co-localization can be detected between GFP-Orf6 and either Nup116 or Gle2, the analysis of the interaction between GFP-Orf6 and the Nup116/Gle2 complex is difficult to interpret from the above data alone. Further co-immunoprecipitation experiments could be performed in order to determine a physical interaction between GFP-Orf6 and the Nup116/Gle2 complex, which would provide further support that Orf6 is localizing to the Nup116/Gle2 complex in yeast.

Depletion of either Nup116 or Gle2 does not affect GFP-Orf6 association with the nuclear envelope in S. cerevisiae.

The evidence presented above suggests that the SARS-CoV-2 Orf6 protein likely localizes to the NPCs of *S. cerevisiae*, with potential interactions between the Nup116/Gle2 complex. Since previous investigations have shown that the Nup98/Rae1 complex is a major interacting partner of the Orf6 protein in mammalian cells, and that both Orf6 localization and function are affected by the disruption of this interaction (Gordon *et al*., 2020; Miorin *et al*., 2020; Hall *et al*., 2022, Makio *et al.,* in preparation), we wanted to assess if the localization of GFP-Orf6 would be affected by the depletion of either Nup116 or Gle2 in *S. cerevisiae*.

We show here, however, that GFP-Orf6 localization is not affected by either the depletion of Nup116 or Gle2, as GFP-Orf6 can still be found localized in punctate foci at the NE of both control and knockdown cells (Figure 3.3 A and C).

This may suggest that Orf6 can bind low levels of Nup116/Gle2 at the NE after 8 h of depletion, as we do not achieve complete reduction of either Nup116 or Gle2 protein levels by 8 h of knockdown (Figure 3.3 B and D). Conversely, it may also suggest that GFP-Orf6 is binding to a different, yet unknown, molecule at the NE of *S. cerevisiae* and therefore the localization of GFP-Orf6 is unaffected by the depletion of either Nup116 or Gle2. To further characterize GFP-Orf6 interaction with the Nup116/Gle2 complex, GFP-Orf6 could be expressed in a *NUP116 or GLE2* deletion strain to assess Orf6 localization when Nup116 or Gle2 are completely knocked out. Additionally, expression of a GFP-Orf6(M58R) mutant protein in yeast could also be examined to assess if the M58R mutation affects Orf6 localization at NPCs in yeast. Furthermore, it would also be interesting to assess if mutations of the F257, W300, D301, K302, and R305 residues of Gle2 would disrupt Orf6 localization at the NE in *S. cerevisiae*, since these residues are suggested to make critical interactions with the Orf6 M58 residue within human Gle2 counterpart, Rae1 (Li *et al*., 2022).

Interestingly, overall GFP-Orf6 levels are slightly reduced when Gle2 is depleted (Figure 3.3D), but this is not observed when Nup116 is depleted (Figure 3.3B). This would suggest that Gle2 may be required for the stability of GFP-Orf6 in *S. cerevisiae* and provides further support for a potential interaction between GFP-Orf6 and Gle2. Other studies within mammalian model systems have shown that mutations within Rae1 inhibit the interactions between Orf6 and the Nup98/Rae1 complex (Hall *et al*., 2022), and that mutations of the critical M58 residue of Orf6, which make extensive interactions with Rae1, cause an altered

localization Orf6 at the NE (Miorin *et al*., 2020). This would suggest that Rae1 is a major interacting partner of Orf6, and therefore, the reduction of Orf6 upon depletion of Gle2 in *S. cerevisiae* (Figure 3.3D), may provide further support for an important interaction between Gle2 and Orf6 in *S. cerevisiae*. Since we have established some evidence to suggest that GFP-Orf6 localizes at Nup116/Gle2 complexes of *S. cerevisiae*, we hypothesized that the depletion of Nup116 or Gle2 would affect the ability of GFP-Orf6 to interact with yeast NPCs. However, these results ultimately show that depleting Nup116 or Gle2 to the levels achieved in this study, does not noticeably affect the localization GFP-Orf6 at the NE of *S. cerevisiae.*

SARS-CoV-2 Orf6 does not cause bidirectional nuclear transport defects in S. cerevisiae.

The SARS-CoV-2 Orf6 protein has been suggested to inhibit both poly-A RNA export (Addetia *et al*., 2021) and importin-α/β1 mediated cNLS protein import (Miorin *et al*., 2020; Miyamoto *et al*., 2022) within mammalian cells. *S. cerevisiae* contains a homologous protein import pathway, using transport proteins Kap95 and Kap60 to facilitate the nuclear import of cNLS containing protein cargo (Adam, 2009; Chook and Seul, 2010; Oka and Yoneda, 2018). Furthermore, many nuclear export proteins within mammalian cells are related to export proteins within *S. cerevisiae* (Chook and Seul, 2010), and the overall mechanism of mRNA export has been suggested to be conserved across eukaryotes (Stewart, 2019). This ultimately suggested to us, that if Orf6 was able to interact with the *S. cerevisiae* Nup116/Gle2

complex, the expression of Orf6 would also lead to the block of cNLS protein import and poly-A RNA export in yeast. Therefore, we examined GFP-Orf6 expressing *S. cerevisiae* for both protein import, and poly-A RNA export defects.

Specifically, cNLS protein import has been shown to be affected by the expression of Orf6 within mammalian model systems (Miroin *et al*., 2020, Lei *et al*., 2020; Miyamoto *et al*., 2022), therefore, we wanted to investigate if Orf6 expression caused cNLS protein import defects in *S. cerevisiae*. We show here, however, that the steady state localization of the cNLS reporter protein is not affected by Orf6 expression (Figure 3.4A). Therefore, preliminary experiments were conducted to assess the relative rate of nuclear import of the cNLS-GFP reporter protein in WT and GFP-Orf6 expressing cells. Results indicate that there is no obvious difference in the relative rate of nuclear import of the cNLS reporter protein, suggesting that Kap95/Kap60 mediated protein import is not affected by this level of Orf6 expression in *S. cerevisiae* (Figure 3.5 A and B). To confirm these results, an alternative protein import pathway was also examined. The yeast transcription factor, Pho4, has been shown to be imported into the nucleus using the importin-β3 counterpart, Kap121, which facilitates the nuclear import of a diverse set of cargo proteins (Kaffman *et al*., 1998; Chook and Seul, 2011). There is no current evidence to suggest that importin-β3 protein import is affected by Orf6 expression in mammalian systems, and here, we show that the relative rate of nuclear import of the pho4-NLS-GFP reporter construct was not noticeably affected by the expression of Orf6 in *S. cerevisiae* (Figure 3.5C). However, not enough iterations were done to establish significance on the relative rate of nuclear import of either the cNLS-GFP or the pho4-NLS-GFP

reporter proteins in WT compared to GFP-Orf6 expressing S. cerevisiae, and therefore, further experimentation would be necessary to confirm these observations.

Mammalian cells have also been shown to accumulate poly-A RNA within the nucleus when the SARS-CoV-2 Orf6 protein associates with the Nup98/Rae1 complex (Addetia *et al*., 2021), and as such, RNA export defects were also examined in Orf6 expressing *S. cerevisiae.* The localization of both poly-A RNA and actin mRNA were examined in WT and GFP-Orf6 expressing *S. cerevisiae*, and results from FISH analysis show that there are no detectable RNA export defects associated with this level of Orf6 production in *S. cerevisiae* (Figure 3.6).

The results presented above ultimately suggest that there are no detectable nuclear transport defects associated with Orf6 expression in *S. cerevisiae,* however, these results could also suggest that the Orf6 protein is not actually interacting with the Nup116/Gle2 complex in yeast, and therefore, is unable to compete with protein import or RNA export pathways. Alternatively, Orf6 could still be binding to the *S. cerevisiae* Nup116/Gle2 complex but does not function to inhibit bidirectional nuclear transport, indicating that Orf6 is acting in inherently different ways within yeast and mammalian model systems. However, it is also possible that Orf6 is not being expressed at a level sufficient to achieve nuclear transport inhibition in these cell lines, and therefore, we are unable to detect a nuclear transport defect with the levels of Orf6 produced in these strains. Since fluorescent microscopy analysis of GFP-Orf6 expressing strains also indicate cellular heterogeneity in level of GFP-Orf6 detected at the NE of Orf6 expressing cells (Figure 3.1C, 3.2C), this may also impair our ability to observe an overall effect on nuclear transport in these strains. Although

the NOP1 promoter is considered a medium-strength promoter (Hitchcock *et al*., 2005), using a stronger promoter that drives higher levels of transcription, such as the TDH3 promoter (Ziong *et al*., 2018), may potentially reveal a transport defect caused by higher levels of the GFP-Orf6 protein and could be an area for future investigation.

Since there are many benefits to using *S. cerevisiae* as a model organism to study aspects human disease (Mager and Winderickx, 2005; Kachroo *et al*., 2022), and although several lines of evidence had suggested to us that the yeast model system would likely be able to serve as a fascinating alternative to a mammalian model system, the results of our investigation have ultimately revealed that we are unable to detect obvious nuclear transport defects in *S. cerevisiae* that express the SARS-CoV-2 Orf6 protein at the levels achieved in this study.

Chapter IV

SARS-CoV-2 Orf6 requires the Nup98/Rae1 complex to inhibit host bidirectional nuclear transport

4.1 Overview.

The SARS-CoV-2 Orf6 protein has been shown to be a potent inhibitor of the type-1 interferon response (Xia *et al*., 2020). Acting both upstream and downstream of type-1 interferon production, Orf6 has been shown to inhibit the nuclear import of STAT1 and IRF3 (Miorin *et al*,. 2020; Lie *et al*., 2020), which are important transcription factors required for the expression of host genes needed to fight viral infection. Orf6 has also been shown to inhibit the nuclear export of various host RNAs (Addetia *et al*., 2021), including those that encode for antiviral factors which are involved in the suppression of viral replication (Hall *et al*., 2022). Interactions between Orf6 and the Nup98/Rae1 complex (Gordan *et al*., 2020) has been suggested to facilitate the bidirectional nuclear transport defects caused by the Orf6 protein (Miorin *et al*., 2020; Addetia *et al*., 2021), however, the requirement for either Rae1 or Nup98 on Orf6 function has not been fully elucidated. Our analysis here shows that the SARS-CoV-2 Orf6 protein requires the Nup98/Rae1 complex to inhibit bidirectional nuclear transport, and that the depletion of Rae1 restores both STAT1 nuclear import and poly-A RNA export defects in Vero cells that express Orf6. Our results suggest a possible mechanism where Orf6 uses the Nup98/Rae1 complex as a docking site to either directly inhibit the nuclear transport of various cellular cargo, or to inhibit the association of various transport factors with NPCs, effectively blocking the nuclear import and export of various host proteins and RNAs that are needed to combat viral infection.

4.2 Results

4.2.1 shRNA mediated depletion of Nup98 leads to the reduction of multiple nucleoporins at the nuclear envelope.

To investigate if Nup98 is required for Orf6 to inhibit bidirectional nuclear transport, Vero cells stably transfected with a doxycycline inducible shNup98 RNA construct (shNup98) or an shScramble RNA control (shScramble) were characterized to assess the effects of Nup98 depletion on NPC integrity. Previous reports have indicated that levels of multiple other Nups are reduced at the NPCs of cells lacking Nup98 (Wu *et al*., 2001), and consistent with these reports, we show here that shRNA mediated depletion of Nup98 also leads to a reduction of multiple Nups at the NE of Vero cells. Western blot analysis has indicated that induction of shNup98 RNA leads to a reduction of Nup98 protein levels by 96 h, and in addition, levels of other Nups, such as Rae1 and Nup96, are also reduced when Nup98 is depleted (Figure 4.1). Immunofluorescence microscopy analysis has revealed that levels of Rae1 (Figure 4.2A and B), Nup358 (Figure 4.2B), and Nup96 (Figure 4.3A) are diminished at the NE of shNup98 cells treated with doxycycline for 96 h but not in shScramble control cells treated under the same conditions (Figure 4.2, Figure 4.3A). Furthermore, visual analysis of Nup358 (Figure 4.2B) and Nup96 (Figure 4.3A) localization patterns at the NE of Nup98 depleted cells show that NPC density may be reduced when Nup98 is knocked down, as there are areas of the NE that are void of both Nup358 and Nup96 foci.

Since Nup96 is part of the Nup107-160 subcomplex, which is one of the main architectural elements of the NPC and has been shown to be essential for proper NPC

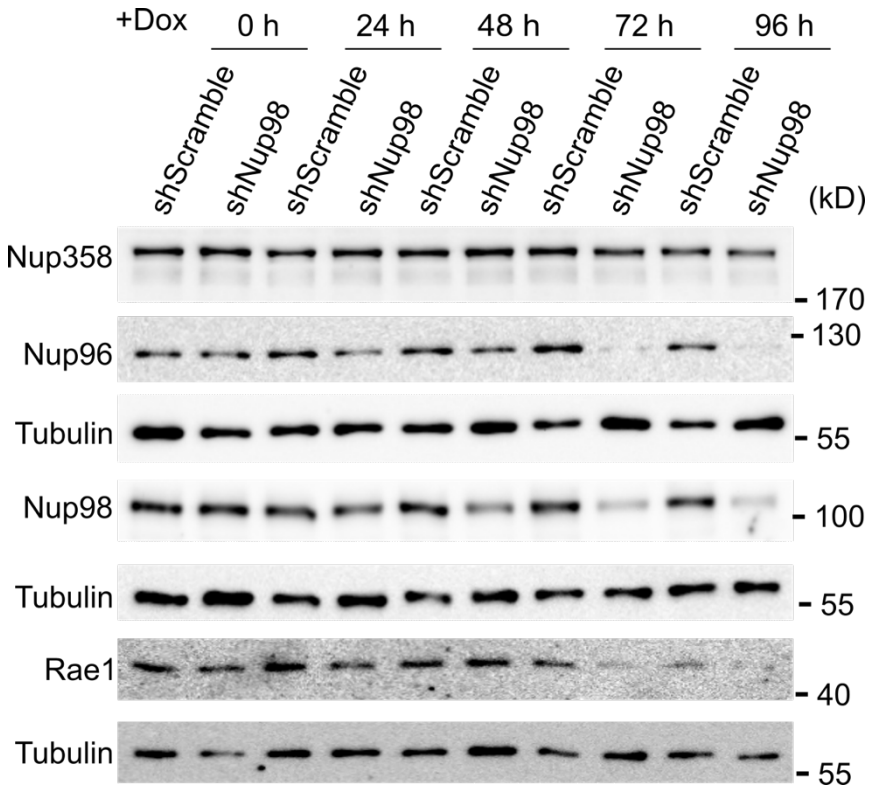

Figure 4.1 Immunoblot analysis following shRNA mediated Nup98 depletion. Vero cells containing doxycycline inducible shRNA constructs (shScramble or shNup98) were treated with doxycycline for the indicated times. Whole cell lysates were prepared and analyzed by western blotting using antibodies directed against Nup98, Rae1, Nup358, Nup96, and tubulin (load control) as indicated to the left of the panels. The positions of molecular mass markers (shown in kDa) are indicated to the right.

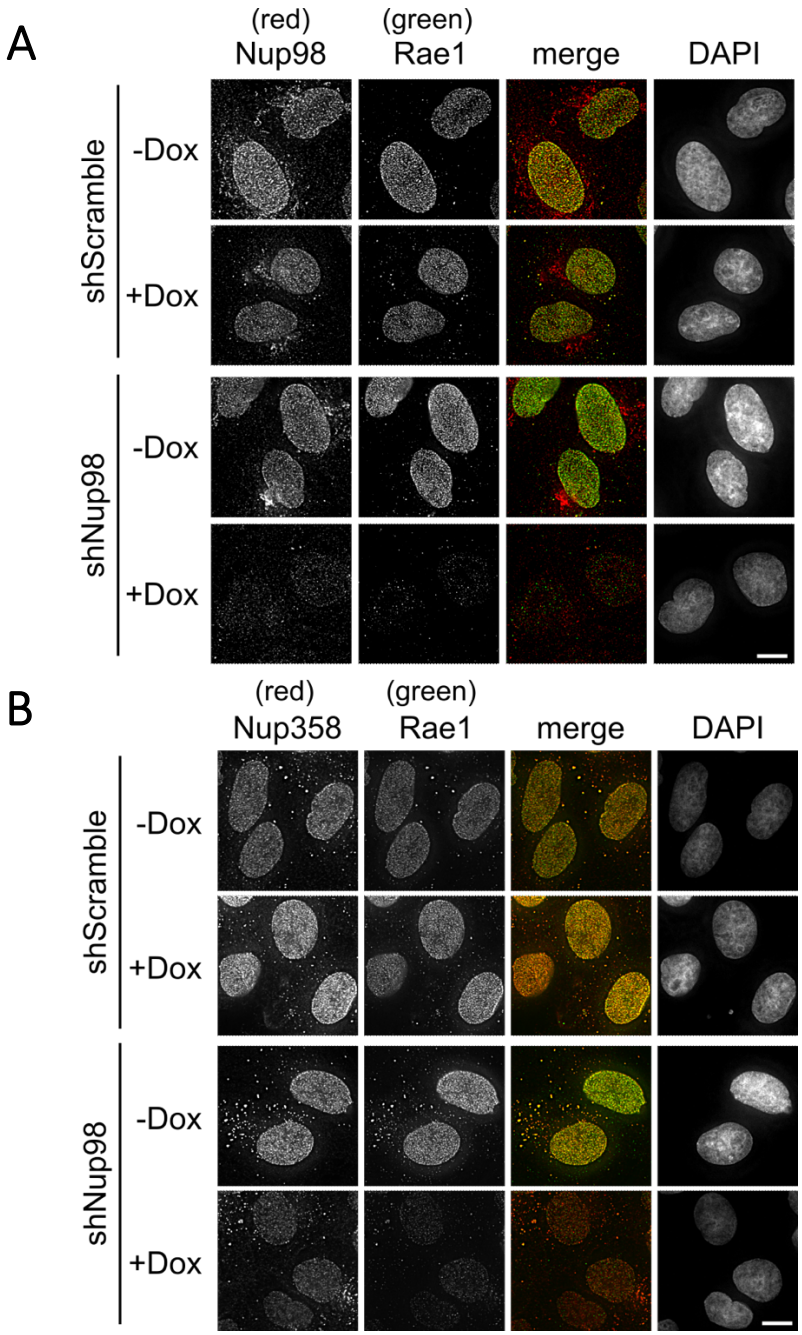

Figure 4.2 Nup98 depletion causes reduction of Rae1 and Nup358 at the nuclear envelope.

Vero cells containing doxycycline inducible shRNA constructs (shScramble or shNup98) were treated with or without doxycycline for 96 h to induce the expression of the indicated shRNA. Cells were examined by indirect immunofluorescence microscopy using either **(A)** anti-Rae1 and anti-Nup98 or **(B)** anti-Rae1 and anti-Nup358 antibodies. The position of the nucleus was detected using DAPI staining. Merged images show Rae1 (green) and Nup98 or Nup358 (red). Scale bars represent 10 μm. Protein depletion in these experiments was confirmed by immunoblot analysis in figure 4.1.

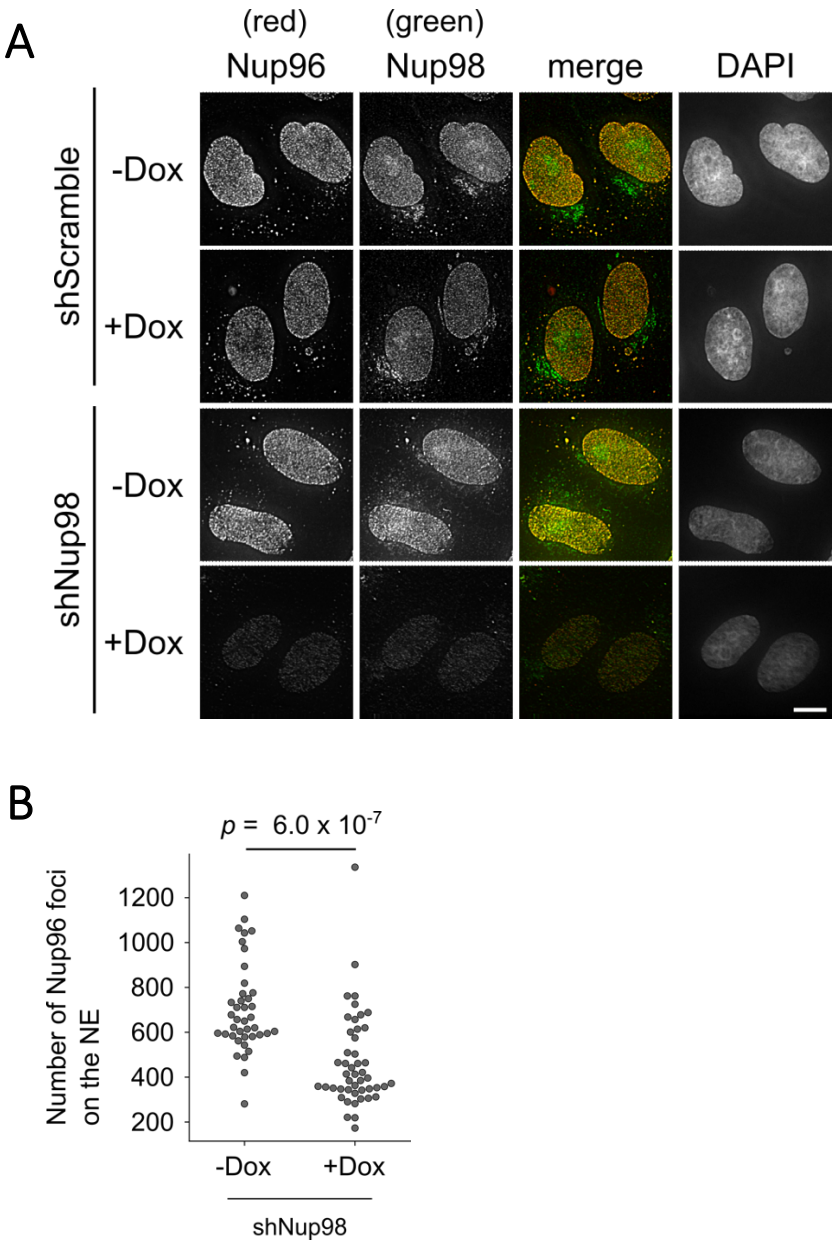

Figure 4.3 Nup98 depletion causes reduction of Nup96 foci at the nuclear envelope.

(A) Vero cells containing doxycycline inducible shRNA constructs (shScramble or shNup98) were treated with or without doxycycline for 96 h to induce the expression of the indicated shRNA. Cells were examined by indirect immunofluorescent microscopy using anti-Nup98 and anti-Nup96 antibodies. The position of the nucleus was detected using DAPI staining. Merged images show Nup98 (green) and Nup96 (red). Protein depletion in these experiments was confirmed by immunoblot analysis in figure 4.1. **(B)** Number of Nup96 foci at the NE of shNup98 cells treated with or without doxycycline for 96 h (shown in panel A) were quantified and plotted as the total number of detected Nup96 foci per cell. Nup96 foci were counted using Imaris software. Significance was determined using a Student's *t*-test.

assembly and function (Harel *et al*., 2003; Krull *et al*., 2004; Kelley *et al*., 2015; Schuller *et al*., 2021), we hypothesized that Nup96 foci detected at the NE would likely represent functional NPCs. Other Nups are reduced at the NPC when Nup98 is depleted (Figure 4.1-4.2), however, the staining intensity of these other Nups when visualized by immunofluorescence microscopy is often variable between cells in the same field, making quantification difficult. Therefore, Nup96 immunostaining was used to assess potential NPC density changes associated with Nup98 depletion, due to the requirement of Nup96 for proper NPC assembly and function and because its staining intensity when visualized by immunofluorescence microscopy analysis was uniform amongst the cells within the population. As such, the number of Nup96 foci at the NE of individual shNup98 cells treated with or without doxycycline were quantified using a spot detection function in Imaris software. The results were plotted as the total number of Nup96 foci detected per nucleus in each treatment condition (Figure 4.3B). Analysis of Nup96 foci reveals a significant decrease of Nup96 foci in Nup98 knockdown cells, suggesting there may be NPC density defects associated with cells depleted of Nup98 (Figure 4.3B).

Analysis of NPCs in Vero cells depleted of Rae1 was also characterized. Induction of shRae1 RNA for 120 h depleted Rae1 protein levels to almost undetectable amounts without affecting levels of other Nups such as Nup358 or Nup98 (Figure 4.4). Immunofluorescence microscopy analysis of Nup98 (Figure 4.5A) and Nup358 (Figure 4.5B) in Rae1-depleted cells show no visual difference in staining intensity or localization pattern when compared to shScramble control cells, even though Rae1 levels are significantly reduced at the NE (Figure 4.5A and B).

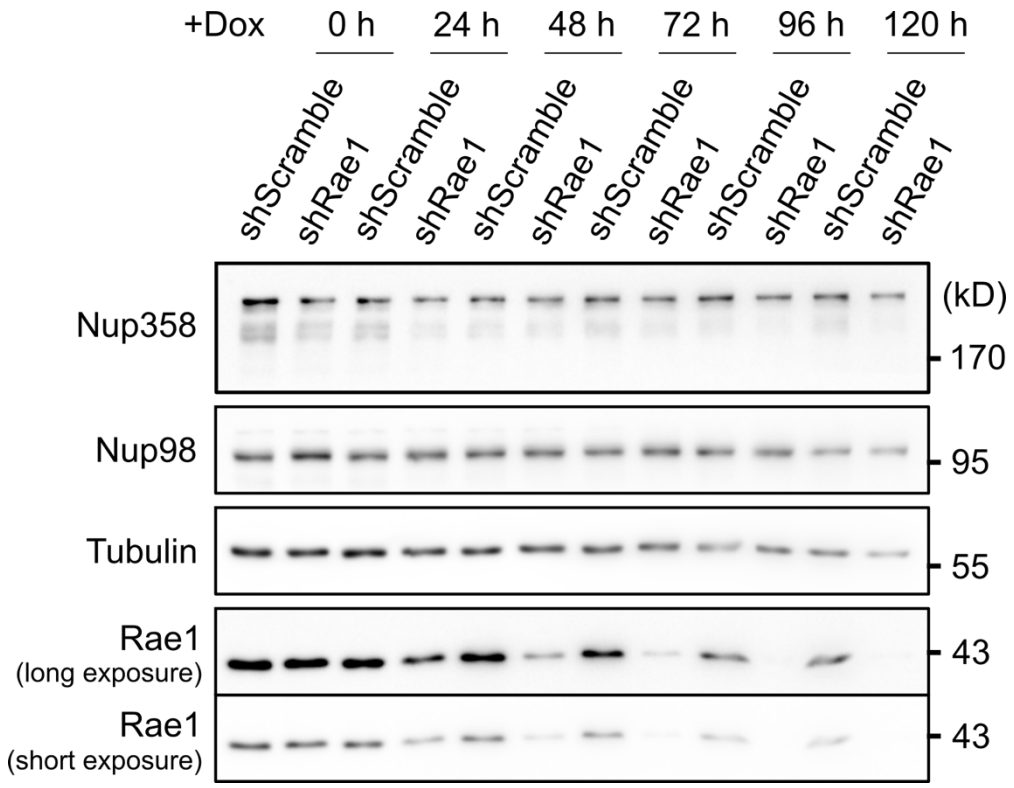

Figure 4.4 (Makio, T.) Immunoblot analysis following shRNA mediated Rae1 depletion.
Vero cells containing doxycycline inducible shRNA constructs (shScramble or shRae1) were treated with doxycycline for the times indicated. Whole cell lysates were prepared and analyzed by western blotting using antibodies directed against Nup98, Rae1, Nup358, and tubulin (load control) as indicated to the left of the panels. The positions of molecular mass markers (shown in kDa) are indicated to the right.

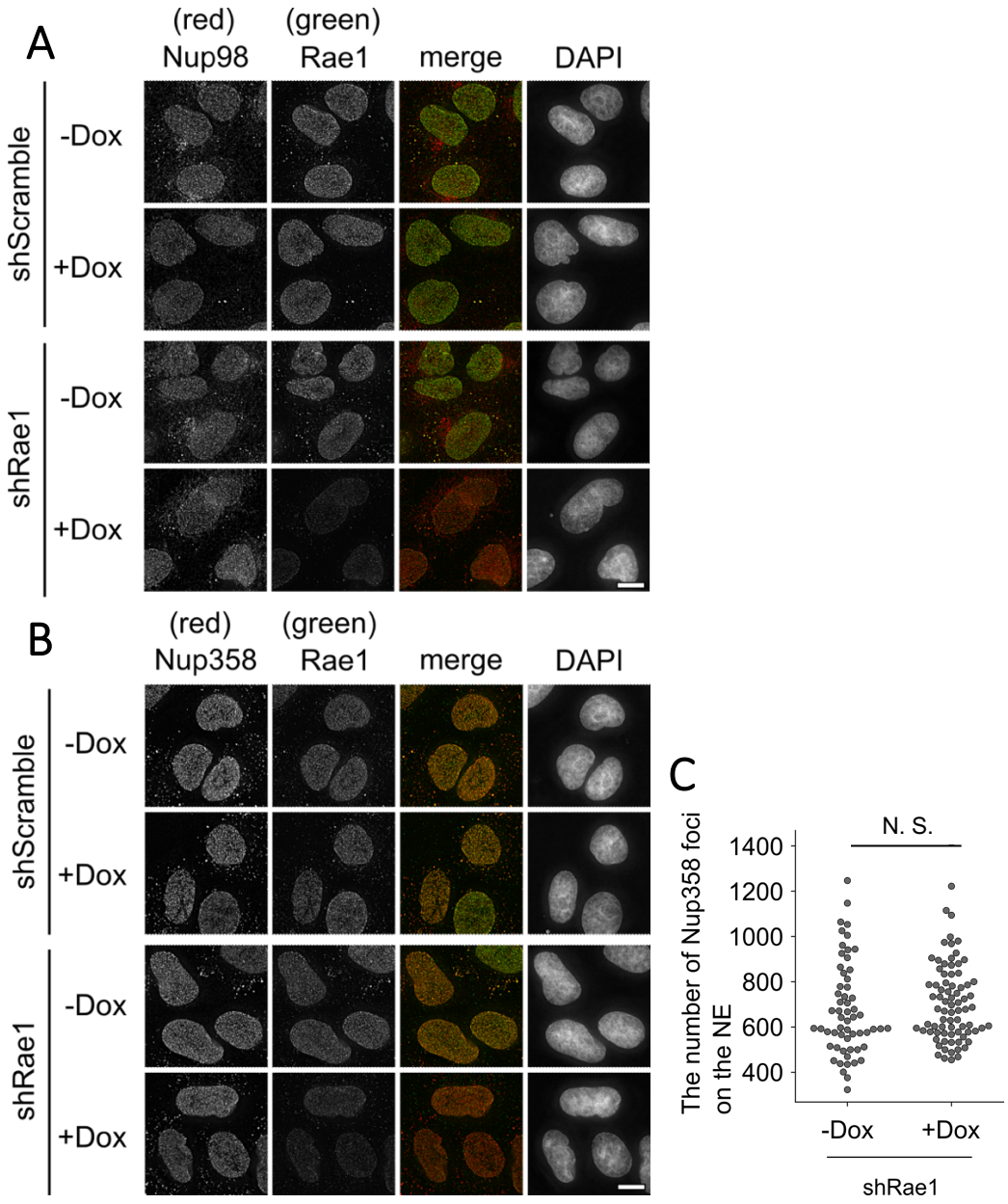

Figure 4.5 (Makio, T.) Rae1 depletion does not cause Nup98 or Nup358 reduction at the nuclear envelope.

Vero cells containing doxycycline inducible shRNA constructs (shScramble or shRae1) were treated with or without doxycycline for 120 h to induce the expression of the indicated shRNA. Cells were examined by indirect immunofluorescence microscopy using either **(A)** anti-Rae1 and anti-Nup98 or **(B)** anti-Rae1 and anti-Nup358 antibodies. The position of the nucleus was detected using DAPI staining. Merged images show Rae1 (green) and Nup98 or Nup358 (red). Scale bars represent 10 μm. Protein depletion in these experiments was confirmed by immunoblot analysis in figure 4.4. **(C)** Number of Nup358 foci at the NE in shRae1 cells treated with or without doxycycline for 120 h (shown in panel B) were quantified and plotted as the total number of detected Nup358 foci per cell. Significance was determined using a Student's *t*-test.

Quantification of Nup358 foci in Rae1 knockdown cells provide support that Rae1 depletion does not lead to NPC density defects, as there is no significant difference in the number of Nup358 foci detected at the NE of Rae1 knockdown cells when compared to cells expressing wildtype levels of Rae1 (Figure 4.5C). Collectively, these results suggest that NPC assembly and function may be affected by Nup98 depletion, but not by Rae1 depletion, in Vero cells.

4.2.2 Depletion of Nup98 leads to growth rate defects in Vero cells.

Due to the observed NPC density defects associated with Nup98 depletion, cell growth and cell viability were assessed in shNup98 and shScramble cells throughout 96 h of doxycycline treatment to evaluate if Nup98 depletion affects growth rate and/or cell viability.

To assess cell growth, Vero cells containing an shNup98 RNA or an shScramble RNA control, were seeded in triplicate and grown in media supplemented with or without doxycycline for 0 h, 24 h, 48 h, 72 h or 96 h to induce the expression of the respective shRNA construct, or not. At the indicated times cells were counted manually and the results were organized in a semi-log plot (Figure 4.6A). Trend lines were included to determine the cell lines and treatment conditions that allow for exponential growth throughout the 96 h time-course. These results show that shScramble control cells grow at an exponential rate throughout 96 h of doxycycline treatment. In contrast, by 72 h, Nup98 knockdown cells begin to show growth rate defects that become more exaggerated by 96 h of depletion (Figure 4.6A).

Cell viability in both shScramble and shNup98 cells was then assessed using a cell cytotoxicity assay kit (Abcam, Cat No. ab112119). This specific cell viability assay is based on the reduction of an oxidized non-fluorescent blue resazurin dye into a red fluorescent resorufin dye by the mitochondrial respiratory chain in live cells, and as such, the fluoresce intensity produced is directly proportional to the number of living cells within the population (Abcam). Vero cells containing doxycycline inducible shScramble and shNup98 RNA constructs were seeded in triplicate, and treated with doxycycline for either 0 h, 24 h, 48 h, 72 h, or 96 h. After 96 h of growth, cell viability was assessed, and the population of viable cells normalized against the scramble control was calculated and plotted (Figure 4.6B). These results show that by 96 h of Nup98 depletion, there is about a 20% decrease in cell viability when compared to the shScramble control cells (Figure 4.6B).

Western blot analysis of shScramble and shNup98 cells treated with doxycycline for either 4 or 14 days has shown that cells expressing shNup98 RNA can grow for extended periods of time while actively depleting Nup98, however, levels of Nup98 by 14 days of depletion are comparable to the levels Nup98 seen at 4 days of depletion (96 h) (Figure 4.16C). This indicates that complete reduction of Nup98 cannot be achieved by the shNup98 RNA construct used in these studies, and that by 96 h hours of knockdown shNup98 cells have reached almost maximum levels of depletion. Together, these results suggest that Nup98 knockdown causes significant growth rate defects in Vero cells by 96 h of depletion, however, shNup98 cells are able to divide and can actively deplete Nup98 over 14 days of growth in doxycycline supplemented media.

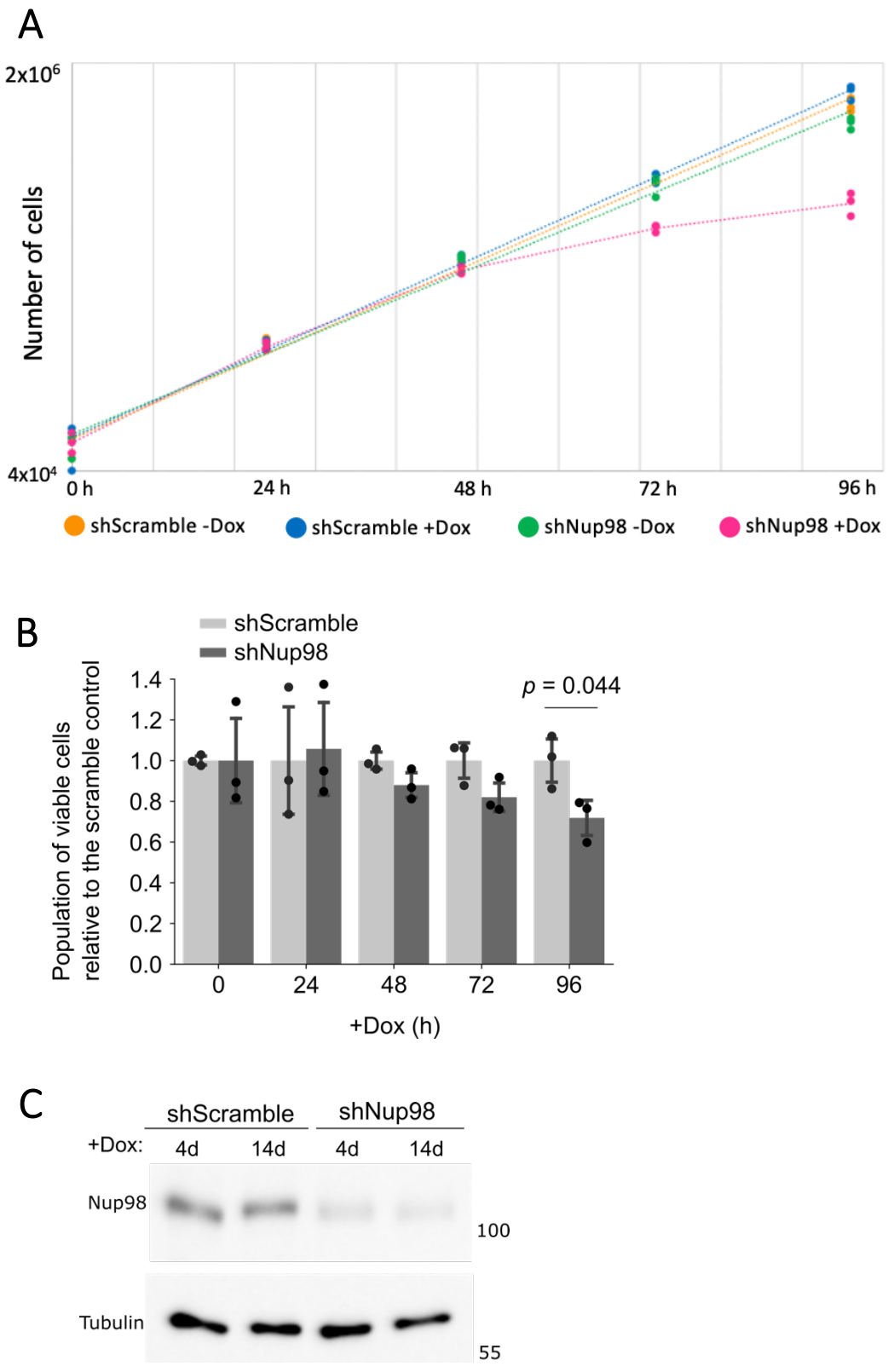

Figure 4.6 Nup98 knockdown causes growth rate defects by 96 h of depletion.

Figure 4.6 Nup98 knockdown causes growth rate defects by 96 h of depletion.
(A) Vero cells containing doxycycline inducible shRNA constructs (shScramble or shNup98), were seeded at the same cell density, and treated with or without doxycycline for 0 h, 24 h, 48 h, 72 h, or 96 h. Cells were trypsinized at the times indicated and fixed in 3.7% formaldehyde. Cells were counted manually using a hemocytometer to determine the number of cells at each time indicated. Cell number was plotted in a semi-log plot and trend lines were included to indicate the cell lines growing at an exponential rate during the 96 h time course. N = 3 biological replicates. **(B)** Vero cells containing doxycycline inducible shRNA constructs (shScramble or shNup98) were seeded at the same density and treated with doxycycline for the indicated times. Cell viability was evaluated after 96 h using a cell viability assay kit to measure the mitochondrial dehydrogenase activity of the cells. The population of viable shNup98 cells normalized against the population of viable scramble control cells was then calculated and plotted. N = 3 biological replicates. Significance was determined using a Student's *t*-test. **(C)** Vero cells containing doxycycline inducible shRNA constructs (shScramble or shNup98), were grown for 4 or 14 days in media containing doxycycline. Whole cell lysates were prepared and analyzed by western blotting using antibodies directed against Nup98 or tubulin (load control) as indicated to the left of the panels. The positions of molecular mass markers (shown in kDa) are indicated to the right.

4.2.3 STAT-1 nuclear import is not affected by Nup98 depletion.

Previous reports have indicated that in cells lacking Nup98, there is an inefficient docking of various nuclear transport factors at the NPC (Wu *et al*., 2001) and impairments in various nuclear import pathways (Wu *et al*., 2001; Hulsmann, 2012). More specifically, it has been suggested that the binding of importin-α and importin-β1 to NPC's is impaired in cells lacking Nup98, and as such, importin-α/β1 mediated nuclear import (i.e., cNLS protein import) is disrupted when compared to control cells (Wu *et al*., 2001). Therefore, to evaluate the potential nuclear import defects associated with Nup98 depletion in Vero cells, STAT1 protein import in shScramble and shNup98 cell lines was analyzed to assess if importin-α /β1 mediated nuclear import is affected by a reduction in Nup98 levels.

To investigate this, shScramble and shNup98 cells were induced, or not, for 96 h to express their respective shRNA constructs and treated with IFN-α for the last 40 min to stimulate the phosphorylation and nuclear import of STAT1. Western blot analysis indicates that Nup98 depletion does not affect the activation of STAT1, as there are comparable levels of phospho-STAT1 (pSTAT1) within the cell lysates of both shScramble and shNup98 cells treated with or without doxycycline (Figure 4.7). Immunofluorescence microscopy analysis has revealed that depletion of Nup98 does not affect pSTAT1 nuclear import, as Nup98 knockdown cells show a similar pSTAT1 signal intensity within the nucleus when compared shScramble control cells (Figure 4.8A). To confirm this observation, the localization of pSTAT1 was quantified by calculating the ratio of the pSTAT1 signal intensities in the nucleus and the cytoplasm of both control and Nup98-depleted cells (Figure 4.8B). These results

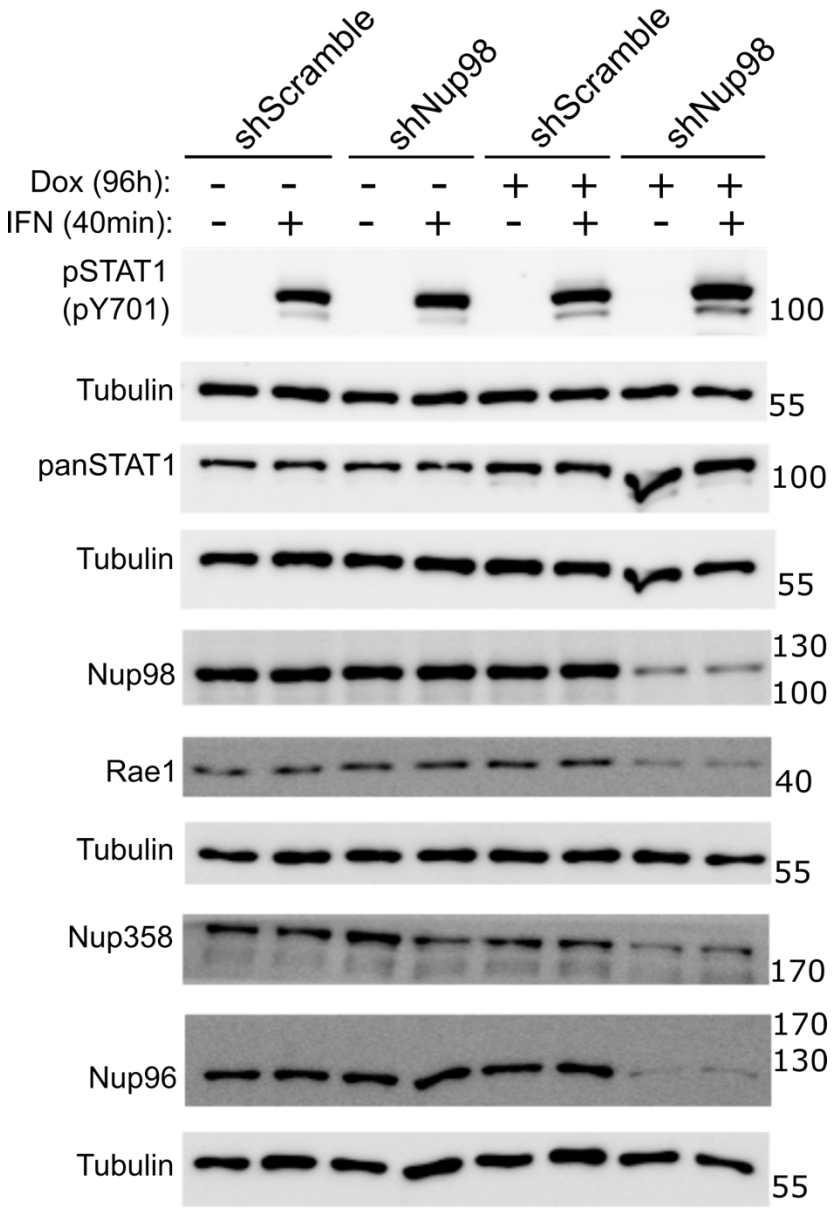

Figure 4.7 Immunoblot analysis following shRNA mediated Nup98 depletion and interferon treatment.
Vero cells containing doxycycline inducible shRNA constructs (shScramble or shNup98) were treated with or without doxycycline for 96 h and were then subject to interferon-α treatment for 40 min to induce the phosphorylation/activation of STAT1. Whole cell lysates were prepared and analyzed by western blotting using antibodies targeted against phospho(pY701)-STAT1, pan-STAT1, Nup98, Rae1, Nup96, Nup358, and tubulin (load control) as indicated to the left of the panels. The positions of molecular mass markers (shown in kDa) are indicated to the right of the panels. Corresponding immunofluorescence images are presented in figure 4.8.

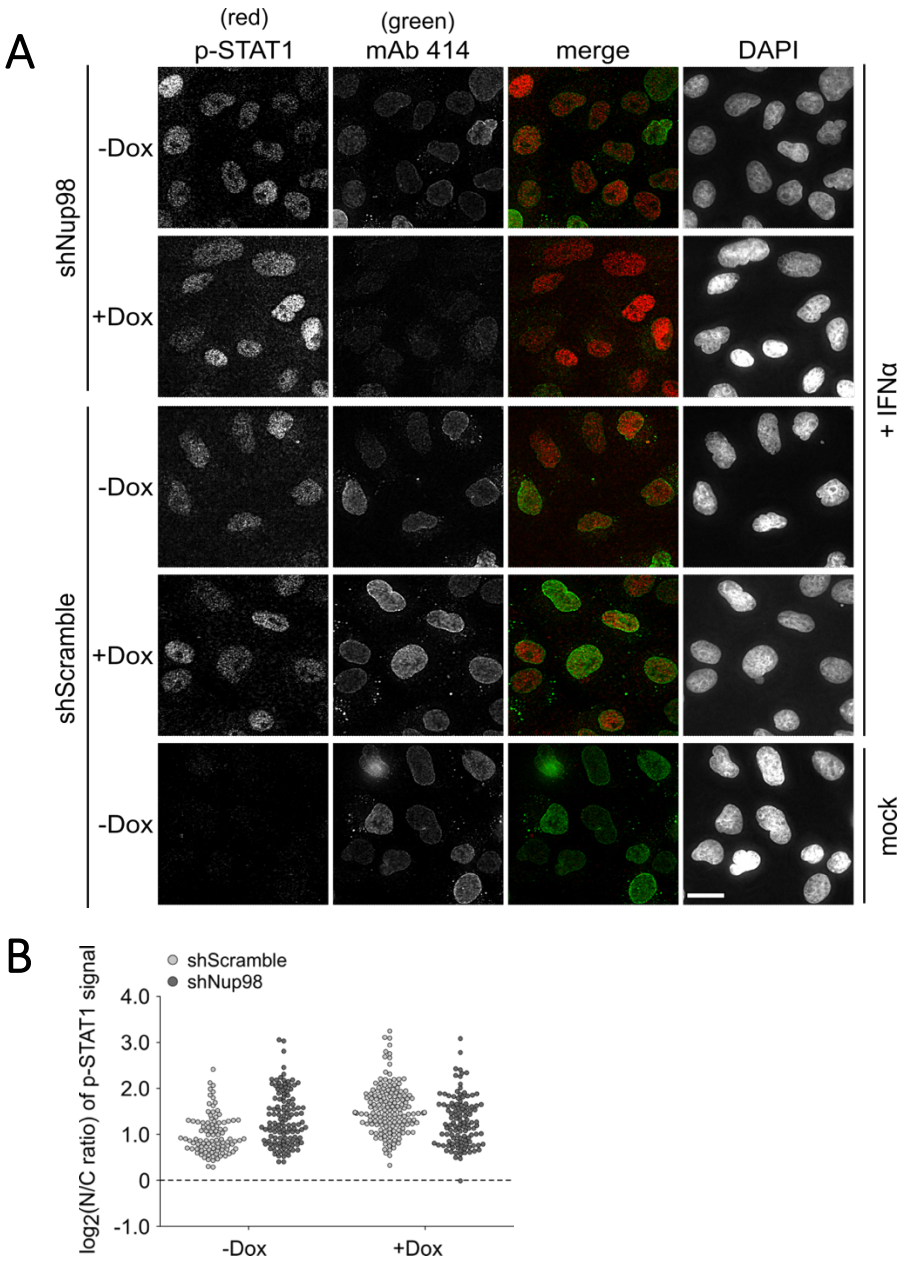

Figure 4.8 Nup98 depletion does not affect STAT1 nuclear import.
(A) Vero cells containing doxycycline inducible shRNA constructs (shScramble or shNup98) were treated with or without doxycycline for 96 h and were subject to interferon-α treatment for 40 min before fixation. Cells were then examined by indirect immunofluorescence microscopy using anti-phospho(pY701)-STAT1 and anti-mAb414 antibodies. The position of the nucleus was detected using DAPI staining. Merged images show phospho-STAT1 (red) and mAb414 (green) staining. Scale bar represents 20 μm. Protein depletion in these experiments was confirmed by immunoblot analysis in figure 4.7. **(B)** The localization of phospho-STAT1 shown in panel (A) was quantified and the ratio of the phospho-STAT1 signal intensities between the nucleus and the cytoplasm were plotted. The dotted line denotes the instances where there is no enrichment of the pSTAT1 signal within the nucleus relative to the cytoplasm.

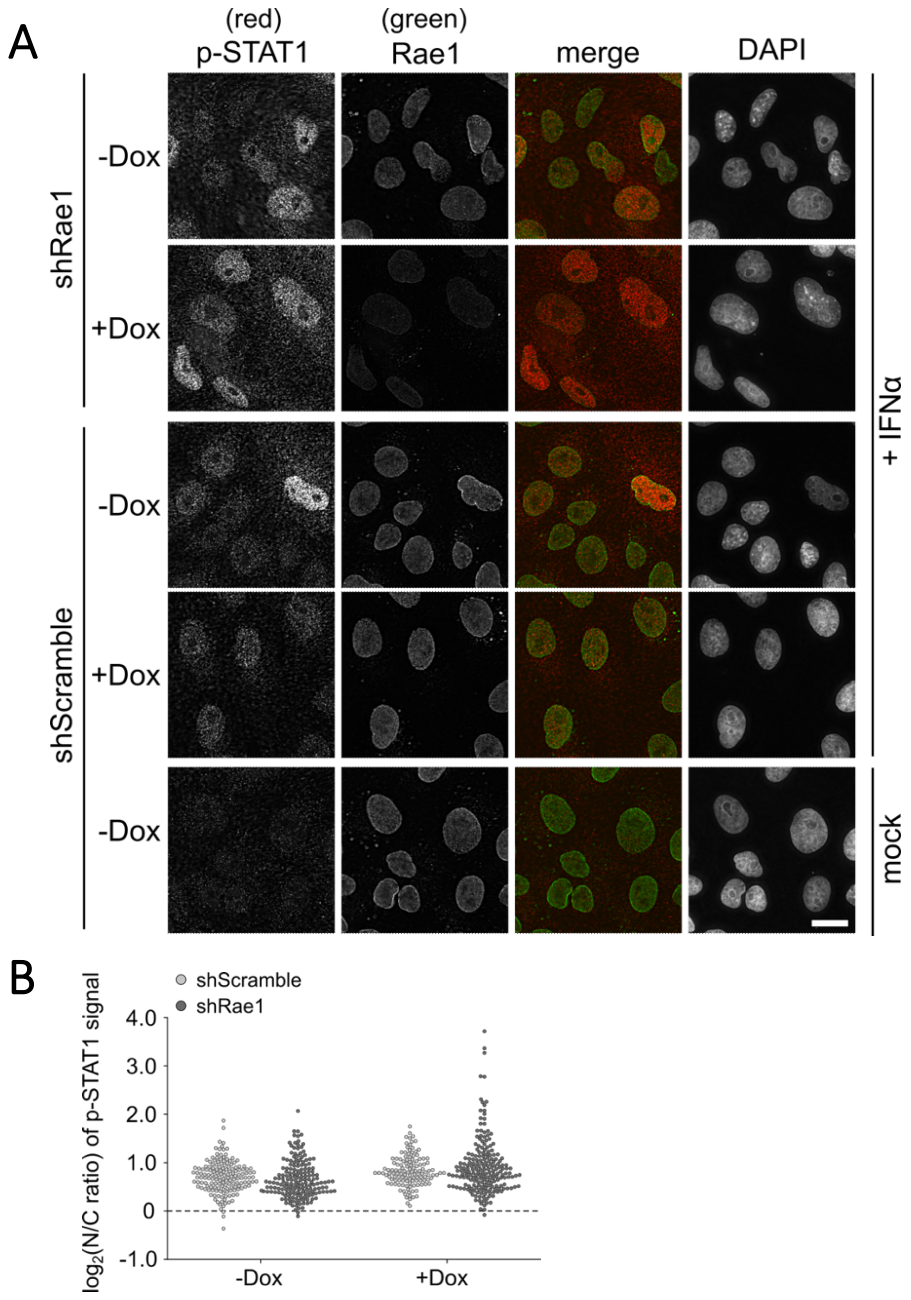

Figure 4.9 (Makio, T.) Rae1 depletion does not affect STAT1 nuclear import.
(A) Vero cells containing doxycycline inducible shRNA constructs (shScramble or shRae1) were treated with or without doxycycline for 120 h and were subject to interferon-α treatment for 40 min before fixation. Cells were then examined by indirect immunofluorescence microscopy using anti-phospho(pY701)-STAT1 and anti-Rae1 antibodies. The position of the nucleus was detected using DAPI staining. Merged images show phospho-STAT1 (red) and Rae1 (green) staining. Scale bar represents 20 μm. **(B)** The localization of phospho-STAT1 shown in panel A was quantified and the ratio of the phospho-STAT1 signal intensities between the nucleus and the cytoplasm were plotted. The dotted line denotes the instances where there is no enrichment of the pSTAT1 signal within the nucleus relative to the cytoplasm.

indicate that Nup98 knockdown cells accumulate pSTAT1 in the nucleus at comparable levels to control cells. A parallel characterization was conducted in shRae1 cells and has indicated that Rae1-depleted cells also accumulate similar levels of pSTAT1 within the nucleus when compared to shScramble control cells (Figure 4.9 A and B). Overall, these results suggest that depletion of either Nup98 or Rae1 does not significantly impair the nuclear import of pSTAT1 in Vero cells stimulated with IFN-α.

4.2.4 Poly-A RNA export is partially affected by Nup98 depletion.

Nup98 has been suggested to function in multiple mRNA export pathways (Powers, 1997) and has also been shown to interact with multiple mRNA export factors including Rae1 (Pritchard *et al*., 1999; Ren *et al*, 2010), NXF1 (Bachi *et al*., 2000; Belvins *et al.*, 2003), and CRM1 (Oka *et al.*, 2010). As such, we wanted to examine if depletion of Nup98 would lead to poly-A RNA export defects in Vero cells.

To determine this, shScramble and shNup98 cells treated with or without doxycycline for 96 h were subject to FISH analysis using an oligo dT probe directed against poly-A RNA (Figure 4.10). These results suggest that the shScramble control cells treated with or without doxycycline and the shNup98 cells treated without doxycycline all show comparable signal intensity of poly-A RNA within the nucleus and the cytoplasm. In contrast, Nup98 depleted cells show an enriched accumulation of poly-A RNA within the nucleus (Figure 4.10). Notably, however, there is still a visible pool of cytoplasmic poly-A RNA within the Nup98-depleted cells, which

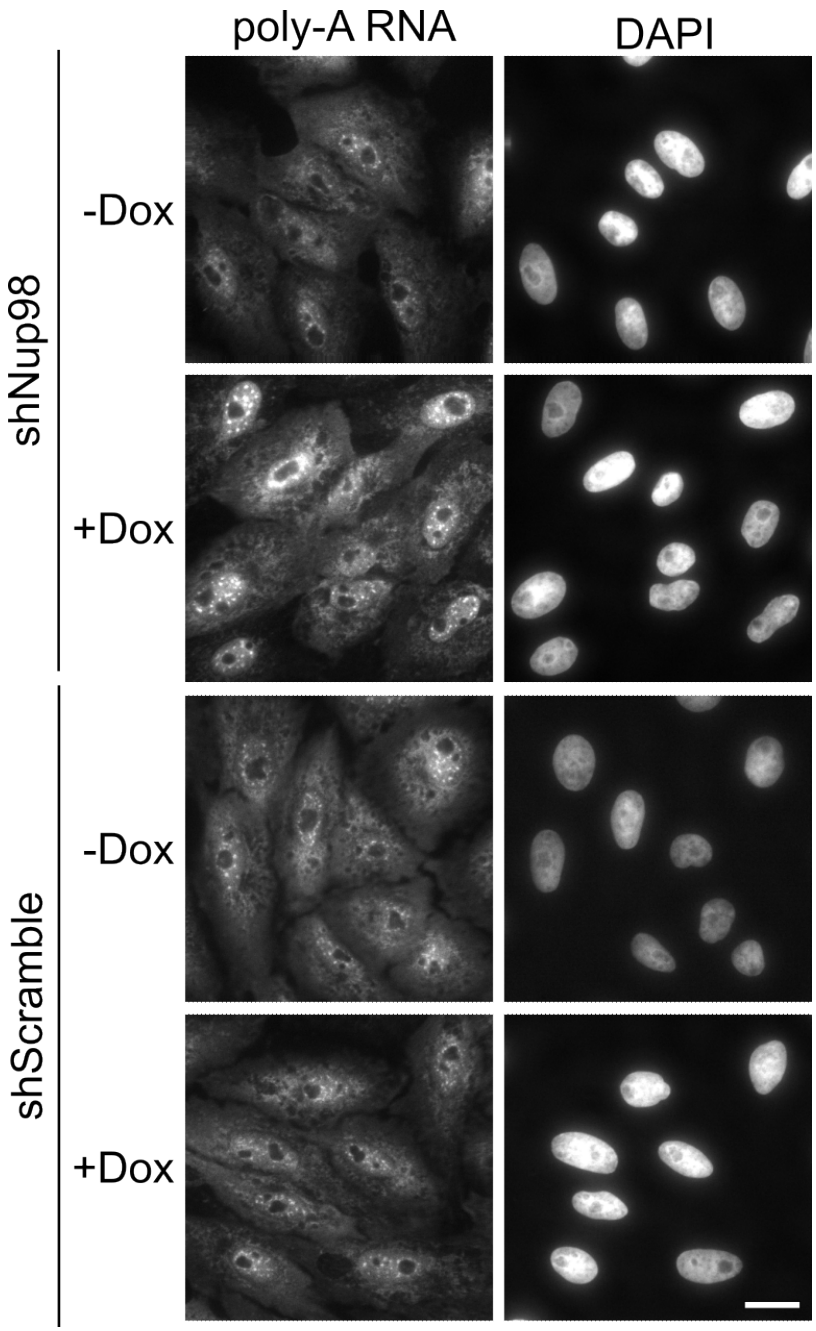

Figure 4.10 Nup98 depletion causes partial poly-A RNA export defects.
Vero cells containing doxycycline inducible shRNA constructs (shScramble or shNup98) were treated with or without doxycycline for 96 h and were subject to fluorescence *in situ* hybridization (FISH) analysis using an oligo dT probe to detect the localization of poly-A mRNA. The position of the nucleus was detected using DAPI staining. Scale bar represents 20 μm. Representative images of poly-A RNA (oligo dT), and the nucleus (DAPI) are shown.

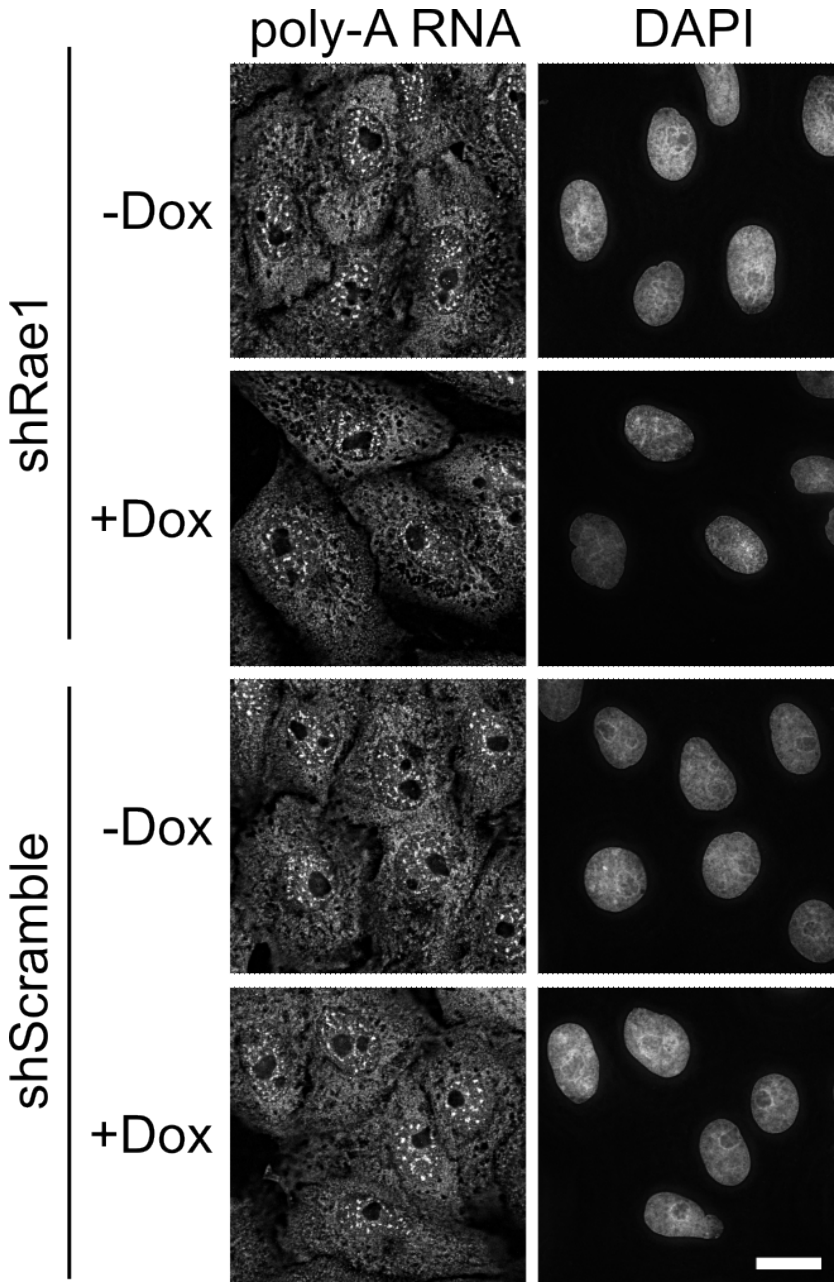

Figure 4.11 (Makio, T.) Rae1 depletion does not affect poly-A RNA nuclear export.
Vero cells containing doxycycline inducible shRNA constructs (shScramble or shRae1) were treated with or without doxycycline for 120 h and were subject to fluorescence *in situ* hybridization (FISH) analysis using an oligo dT probe to detect the localization of poly-A mRNA. The position of the nucleus was detected using DAPI staining. Scale bar represents 20 μm. Representative images of poly-A RNA (oligo dT), and the nucleus (DAPI) are shown.

suggests that poly-A RNA export is still occurring when levels of Nup98 are reduced. Overall, this suggests that poly-A RNA export is only partially affected by Nup98 depletion in Vero cells.

Rae1 has also been implicated in mRNA export (Ren *et al.*, 2010; Faria *et al*., 2005) but its precise role in nuclear export within mammalian cells remains unclear (Xie and Ren, 2019). Therefore, shRae1 cells were also analyzed by FISH analysis to assess potential poly-A RNA export defects associated with Rae1 depletion (Figure 4.11). These results have indicated that both shRae1 cells and shScramble control cells treated with or without doxycycline have comparable levels of poly-A RNA within the nucleus and within the cytoplasm (Figure 4.11) suggesting that depletion of Rae1 does not noticeably affect poly-A RNA export.

Altogether, these results suggest that the shRNA mediated depletion of Nup98, but not Rae1, leads to partial poly-A RNA export defects in Vero cells.

4.2.5 Localization of SARS-CoV-2 Orf6 protein is altered in Nup98 depleted cells.

Previous analysis of the SARS-CoV-2 Orf6 protein in mammalian cells has shown that Orf6 interacts with the Nup98/Rae1 complex (Gordan *et al*., 2020, Miorin *et al*., 2020, Li *et al*., 2022), and as such, we were interested in investigating the localization of Orf6 in Nup98-depleted cells.

Vero cells expressing shNup98 RNA or shScramble RNA for 96 h were transduced with a plasmid encoding Flag-Orf6 for the last 24 h of depletion and were subject to immunofluorescent microscopy analysis to assess Flag-Orf6 localization

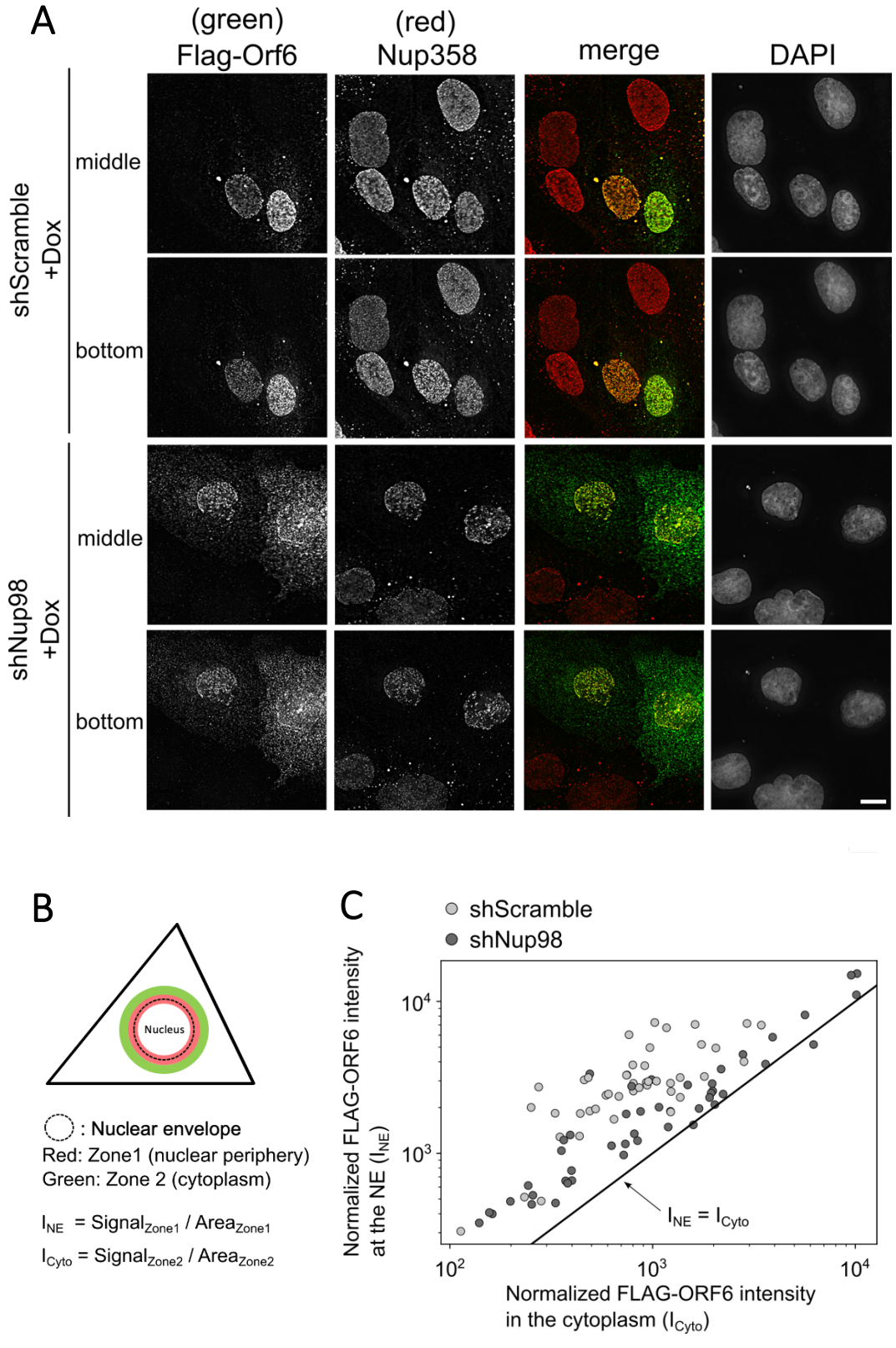

Figure 4.12 Nup98 depletion alters Flag-Orf6 localization at the nuclear envelope.

Figure 4.12 Nup98 depletion alters Flag-Orf6 localization at the nuclear envelope. **(A)** Vero cells containing doxycycline inducible shRNA constructs (shScramble or shNup98) were incubated with or without doxycycline for 96 h and subject to transduction with a plasmid encoding Flag-Orf6 for the last 24 h of incubation. Cells were examined by indirect immunofluorescence microscopy analysis using anti-FLAG and anti-Nup358 antibodies. The position of the nucleus was detected using DAPI staining. Merged images show Flag-Orf6 (green) and antiNup98 or antiNup358 (red). In order assess the colocalization between Flag-Orf6 and Nup358, two different slices from the stacked images (the bottom and the middle sections of the nuclei) are shown. The scale bar indicates 10 μm. **(B)** Accumulation of Flag-Orf6 at the NE was quantified and a schematic of the quantification strategy is depicted. The signal intensities in the region including the nuclear envelope (Zone 1; NE) and the region just outside of Zone 1 (Zone 2; cytoplasm) of cells shown in (A) were measured. **(C)** A scatter plot of the normalized Flag-Orf6 signal intensity at the NE and in the cytoplasm of shScramble and shNup98 cells is presented. The line ($I_{NE} = I_{Cyto}$) denotes the instances where there is no enrichment of Flag-Orf6 signal at the NE relative to the cytoplasm.

localization. Consistent with previous studies on Orf6 localization (Miorin *et al*., 2020), Vero cells expressing shScramble RNA show Flag-Orf6 bound to the NE with colocalization detected between Flag-Orf6 and either Nup98 or Nup358 (Figure 4.12A). Unlike shScramble control cells, shNup98 cells show a more diffuse cellular Flag-Orf6 distribution by 96 h of Nup98 depletion with Flag-Orf6 reduced at the NE and increased in the cytoplasm (Figure 4.12A).

Quantification of the Flag-Orf6 signal at the NE and in cytoplasm was performed to assess changes in levels of Flag-Orf6 association at the NE following Nup98 depletion. A schematic of the quantification strategy is presented in Figure 4.12B indicating areas of the cell where Flag-Orf6 signal intensity was measured. The Flag-Orf6 signal intensities in the region containing the NE (Zone 1; NE) and adjacent to this in the cytoplasm (Zone 2; cytoplasm) were calculated, and the normalized signal intensity of Flag-Orf6 at the NE was then plotted against the normalized signal intensity of Flag-Orf6 in the cytoplasm (Figure 4.12C). Quantification of Flag-Orf6 localization in shScramble control cells versus shNup98 cells shows a decreased signal intensity of Flag-Orf6 at the NE when Nup98 is reduced (Figure 4.12C), suggesting that the localization of Orf6 is altered when Nup98 is depleted.

Flag-Orf6 localization was also assessed in shRae1 cells in a similar manner, to evaluate the requirement of Rae1 for Orf6 accumulation at the NE. Immunofluorescent microscopy analysis revealed that Flag-Orf6 localization is also altered in Rae1 depleted cells (Figure 4.13A) and quantification of the Flag-Orf6 intensity at the NE of shScramble and shRae1 cells has shown that there is a

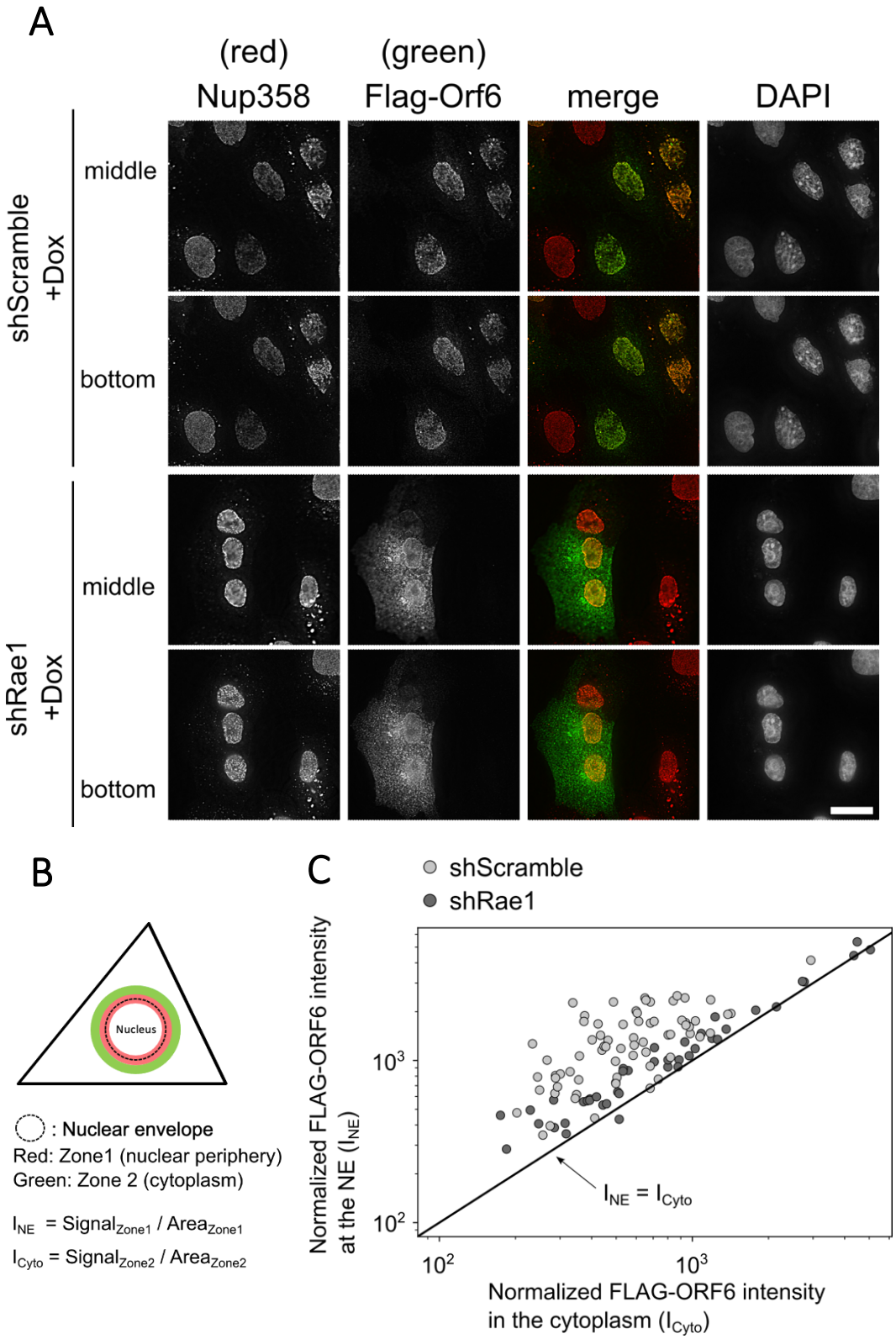

Figure 4.13 (Makio, T.) Rae1 depletion alters Flag-Orf6 localization at the nuclear envelope.

Figure 4.13 (Makio, T.) Rae1 depletion alters Flag-Orf6 localization at the nuclear envelope.

(A) Vero cells containing doxycycline inducible shRNA constructs (shScramble or shRae1) were incubated with or without doxycycline for 120 h and subject to transduction with a plasmid encoding Flag-Orf6 for the last 24 h of incubation. Cells were examined by indirect immunofluorescence microscopy analysis using anti-FLAG and anti-Nup358 antibodies. The position of the nucleus was detected using DAPI staining. Merged images show Flag-Orf6 (green) and antiNup358 (red). In order assess the colocalization between Flag-Orf6 and Nup358, two different slices from the stacked images (the bottom and the middle sections of the nuclei) are shown. The scale bar indicates 10 μm. **(B)** Accumulation of Flag-Orf6 at the NE was quantified and a schematic of the quantification strategy is depicted. The signal intensities in the region including the nuclear envelope (Zone 1; NE) and the region just outside of the Zone 1 (Zone 2; cytoplasm) of cells shown in (A) were measured. **(C)** A scatter plot of the normalized Flag-Orf6 signal intensity at the NE and in the cytoplasm of shScramble and shRae1 cells is presented. The line ($I_{NE} = I_{Cyto}$) denotes the instances where there is no enrichment of Flag-Orf6 signal at the NE relative to the cytoplasm.

decreased intensity of Flag-Orf6 at the NE when Rae1 is depleted (Figure 4.13 B and C). Comparing the quantification results of the shNup98 cells (Figure 4.12C) with that of the shRae1 cells (Figure 4.13C) suggests that Flag-Orf6 localization may be altered more drastically in Rae1 knockdown cells, as there are a greater number of Rae1-depleted cells that show larger reduction of Flag-Orf6 intensity at the NE when compared to Nup98-depleted cells.

Collectively, these results suggest that the depletion of both Nup98 and Rae1 alters Flag-Orf6 localization in Vero cells and reduces the accumulation of Flag-Orf6 at the NE.

4.2.6 Nup98 depletion restores STAT1 nuclear import in Orf6 expressing cells.

SARS-CoV-2 Orf6 has been shown to inhibit the nuclear import of activated STAT1 (Lei *et al*., 2020; Xia *et al*., 2020) through its interactions with the Nup98/Rae1 complex (Miorin *et al*., 2020; Addetia *et al*., 2021). Since pSTAT1 nuclear import was not affected by Nup98 depletion, we wanted to investigate if Nup98 was required for Orf6 to inhibit the nuclear import of pSTAT1 upon interferon induction.

shScramble and shNup98 cells treated with doxycycline for 96 h were transduced with a plasmid encoding Flag-Orf6 for the last 24 h of depletion and were then subjected to IFN-α treatment, or not, for 40 min before being visualized by immunofluorescent microscopy analysis (Figure 4.14A). In shScramble cells treated with IFN-α, the expression of Flag-Orf6 impairs pSTAT1 nuclear import as Flag-Orf6 expressing cells show a diffuse cytoplasmic pSTAT1 signal when compared to non-Flag-Orf6 expressing cells that show an accumulation of pSTAT1 within the nucleus

(Figure 4.14A). In contrast, Nup98 knockdown cells expressing Flag-Orf6 no longer inhibit the nuclear import of pSTAT1 upon IFN-α treatment, as both Flag-Orf6 expressing and non-Flag-Orf6 expressing cells depleted of Nup98 have comparable nuclear accumulation of pSTAT1 (Figure 4.14A). To confirm these results the localization of pSTAT1 in these IFN-α treated cell lines was quantified, and the nuclear accumulation of pSTAT1 in cells expressing Flag-Orf6 or not expressing Flag-Orf6 (bystander cells) was plotted as the ratio between the nuclear and the cytoplasmic signal intensity of pSTAT1 (Figure 4.14B). These results show that Nup98 knockdown cells expressing Flag-Orf6 significantly accumulate greater levels of activated pSTAT1 within the nucleus when compared to Flag-Orf6 expressing scramble control cells (Figure 4.14B), suggesting that Orf6 can no longer inhibit pSTAT1 nuclear import in cells depleted of Nup98.

Consistent with these results, immunofluorescent microscopy analysis of shScramble and shRae1 cells treated with doxycycline for 120 h and IFN-α for 40 min show that Flag-Orf6 expressing scramble control cells inhibit the nuclear accumulation of pSTAT1, while Flag-Orf6 expressing Rae1-depleted cells accumulate activated pSTAT1 within the nucleus (Figure 4.15A). These results were also quantified as described above (Figure 4.15B) and confirmed that Rae1 knockdown cells expressing Flag-Orf6 significantly accumulate higher levels of pSTAT1 within the nucleus when compared to Flag-Orf6 expressing shScramble control cells.

Together these results suggest that Nup98 and Rae1 are required for Orf6 to inhibit STAT1 nuclear import.

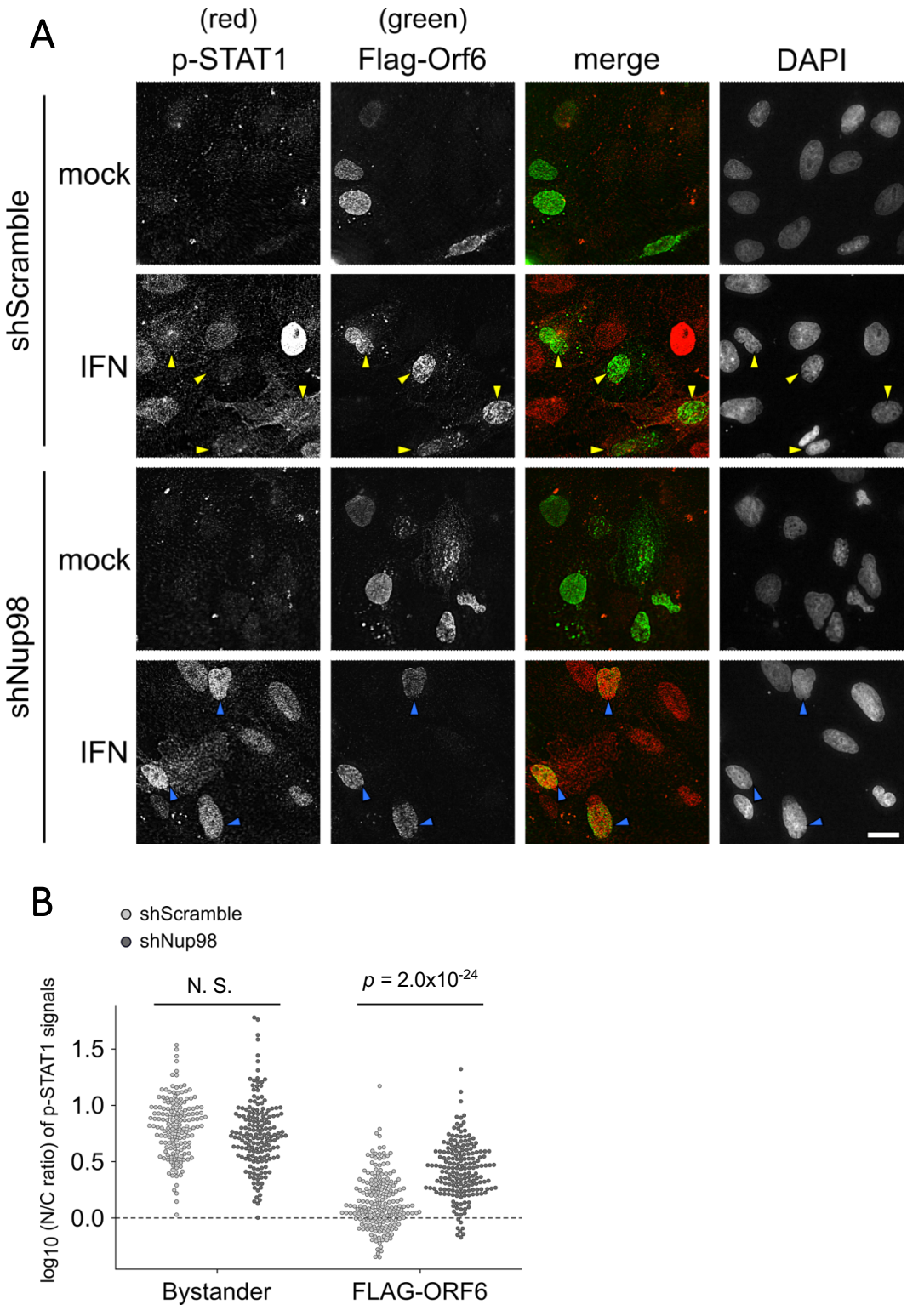

Figure 4.14 Nup98 depletion suppresses the Orf6-mediated block of STAT1 nuclear import.

Figure 4.14 Nup98 depletion suppresses the Orf6-mediated block of STAT1 nuclear import.

(A) Vero cells containing doxycycline inducible shRNA constructs (shScramble or shNup98) were incubated with or without doxycycline for 96 h and subject to interferon-α treatment for 40 min before fixation. Cells were examined by indirect immunofluorescence microscopy analysis using anti-phospho-STAT1 (pSTAT1) and anti-Flag antibodies. The position of the nucleus was detected using DAPI staining. Merged images show Flag-Orf6 (green) and pSTAT1 (red). The cells marked by yellow arrowheads indicate the Orf6-positive cells that failed to accumulate activated pSTAT1 in the nucleus after interferon treatment. The cells marked by blue arrowheads indicate the Orf6-positive cells that accumulated activated pSTAT1 in the nucleus after interferon treatment. The scale bar indicates 20 μm. **(B)** From the images shown in (A), the nuclear accumulation of activated STAT1 after interferon treatment in cells expressing Flag-Orf6 and in bystander cells (not expressing Flag-Orf6) was plotted as the ratio between the nuclear and the cytoplasmic signal intensity of pSTAT1 (N/C ratio). The dotted line denotes the instances where there is no enrichment of the pSTAT1 signal within the nucleus relative to the cytoplasm. Significance was determined using a Welch's ANOVA followed by post-hoc pairwise Welch's *t*-tests with a Bonferroni correction.

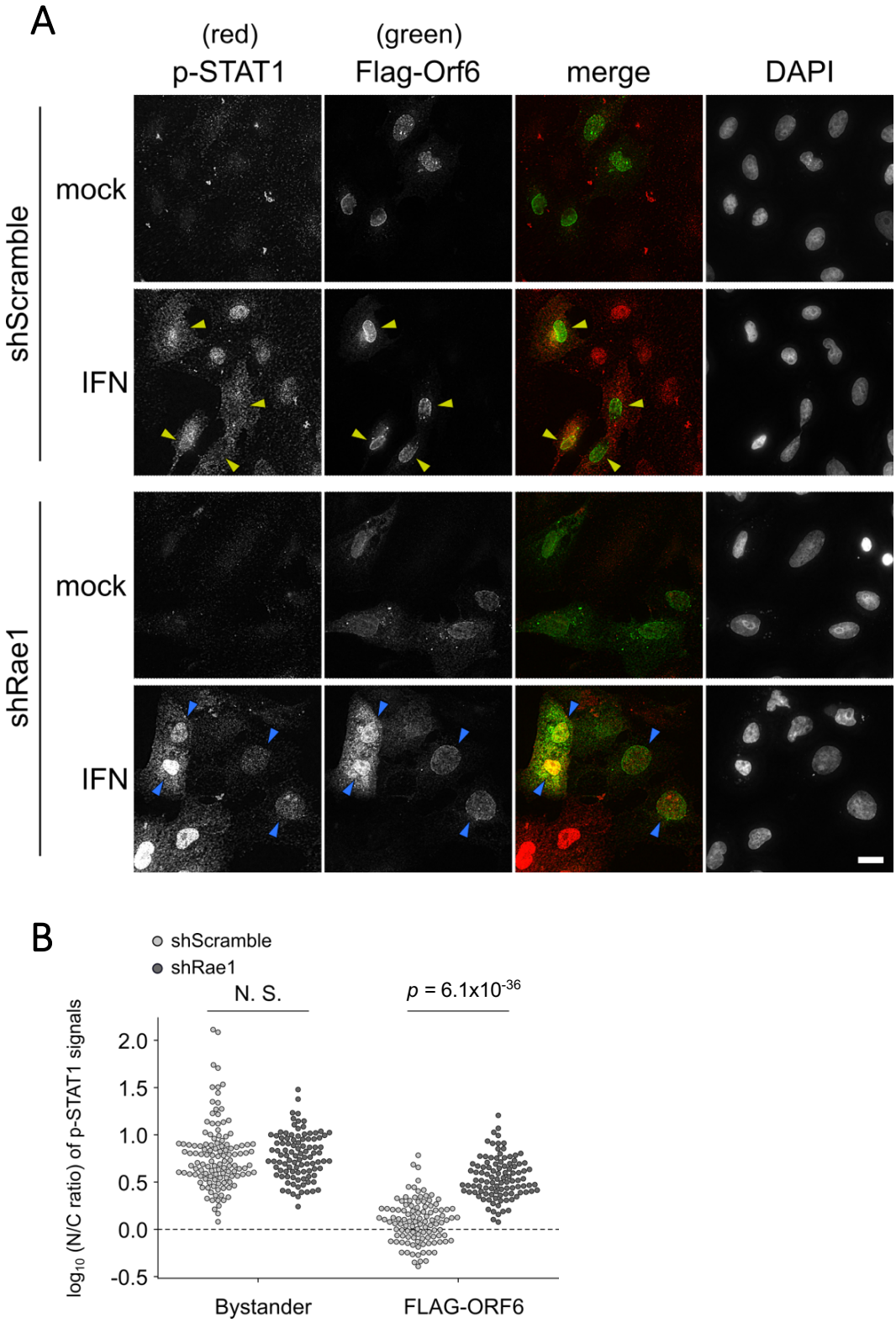

Figure 4.15 (Makio, T.) Rae1 depletion suppresses the Orf6-mediated block of STAT1 nuclear import.

Figure 4.15 (Makio, T.) Rae1 depletion suppresses the Orf6-mediated block of STAT1 nuclear import.
(A) Vero cells containing doxycycline inducible shRNA constructs (shScramble or shRae1) were incubated with or without doxycycline for 120 h and subject to interferon-α treatment for 40 min before fixation. Cells were examined by indirect immunofluorescence microscopy analysis using anti-phospho-STAT1 (pSTAT1) and anti-Flag antibodies. The position of the nucleus was detected using DAPI staining. Merged images show Flag-Orf6 (green) and pSTAT1 (red). The cells marked by yellow arrowheads indicate the Orf6-positive cells that failed to accumulate activated pSTAT1 in the nucleus after interferon treatment. The cells marked by blue arrowheads indicate the Orf6-positive cells that accumulated activated pSTAT1 in the nucleus after interferon treatment. The scale bar indicates 20 μm. **(B)** From the images shown in (A), the nuclear accumulation of activated STAT1 after interferon treatment in cells expressing Flag-Orf6 and in bystander cells (not expressing Flag-Orf6) was plotted as the ratio between the nuclear and the cytoplasmic signal intensity of pSTAT1 (N/C ratio). The dotted line denotes the instances where there is no enrichment of the pSTAT1 signal within the nucleus relative to the cytoplasm. Significance was determined using a Welch's ANOVA followed by post-hoc pairwise Welch's *t*-tests with a Bonferroni correction.

4.2.7 Nup98 depletion does not suppress poly-A RNA export defects caused by Orf6 expression.

Previous investigations have indicated that Orf6 expression causes retention of a broad range of host RNAs within the nucleus (Addetia *et al*., 2021; Hall *et al*., 2022). Since poly-A RNA export was only partially affected by Nup98 reduction, we wanted to investigate how Orf6 expression affected poly-A RNA export in cells depleted of Nup98.

Both shScramble and shNup98 cells treated with doxycycline for 96 h were subject to transduction with a Flag-Orf6 plasmid for the last 24 h of incubation before being analyzed by FISH/IF analysis (Figure 4.16A). These results show that shScramble control cells expressing Flag-Orf6 have greater accumulation of poly-A RNA within the nucleus when compared to shScramble cells not expressing Flag-Orf6, as non-Flag-Orf6 expressing cells show diffuse cellular distribution of poly-A RNA within the nucleus and the cytoplasm while Flag-Orf6 expressing cells have a significant accumulation of poly-A RNA within the nucleus (Figure 4.16A). Flag-Orf6 expressing Nup98-depleted cells also show enhanced accumulation of poly-A RNA within the nucleus, and this level of poly-A RNA accumulation is more exaggerated than the poly-A RNA accumulation caused by Nup98 depletion alone (Figure 4.16A). To confirm these results, the nuclear accumulation of poly-A RNA in cells expressing Flag-Orf6 and in cells not expressing Flag-Orf6 (bystander cells) was quantified and plotted as the ratio between the nuclear and cytoplasmic signal intensity of poly-A RNA (Figure 4.16B). This analysis shows that Nup98 depleted cells and shScramble control cells accumulate comparable levels of poly-A RNA

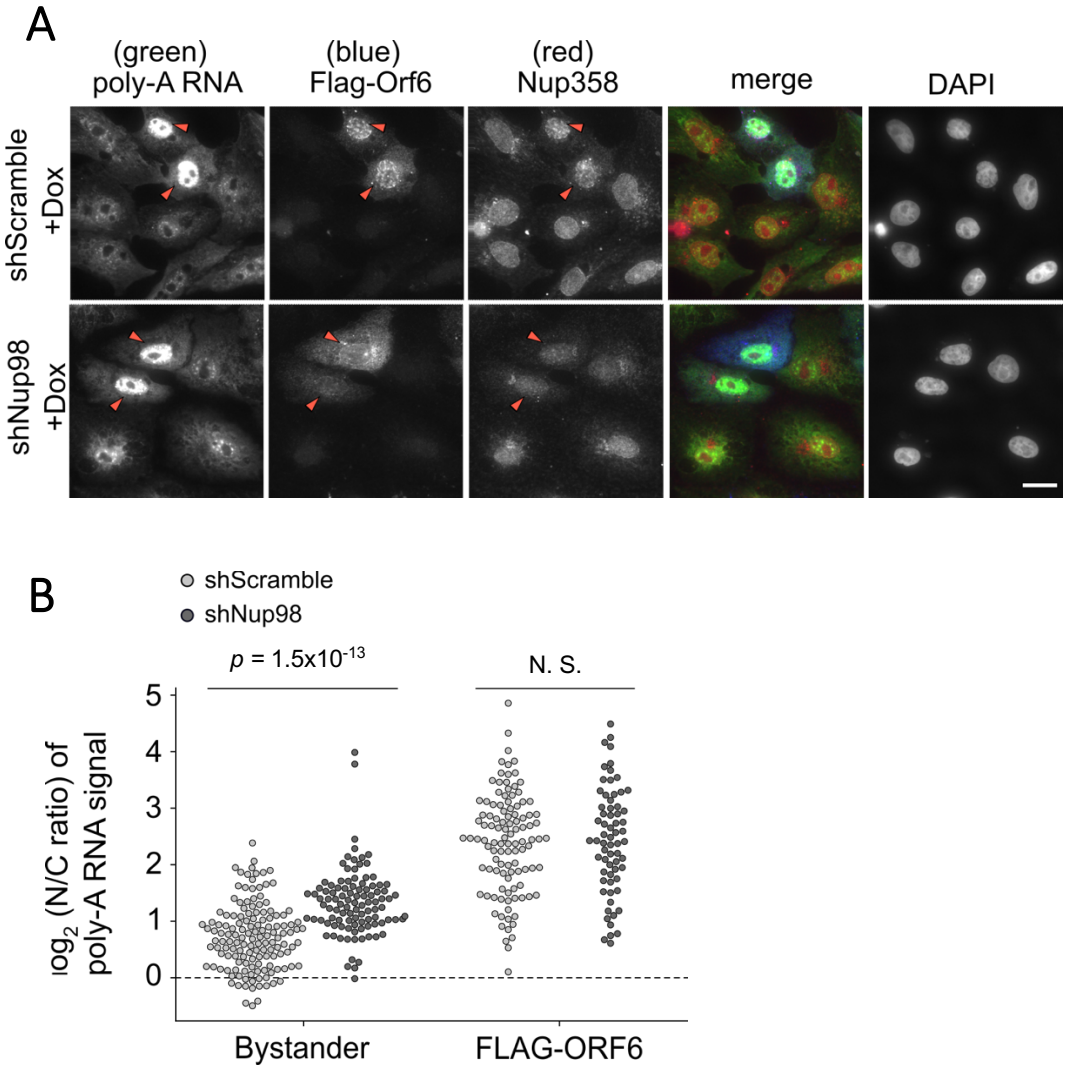

Figure 4.16 Nup98 depletion does not suppress the Orf6 mediated block of poly-A RNA nuclear export.

(A) Vero cells containing doxycycline inducible shRNA constructs (shScramble or shNup98) were incubated with doxycycline for 96 h and transduced with a plasmid encoding Flag-Orf6 for the last 24 h of incubation. Cells were subject to FISH/IF analysis using an oligo dT probe, anti-Flag and anti-Nup98 antibodies. The position of the nucleus was detected using DAPI staining. Merged images show Flag-Orf6 (blue), Nup98 (red) and oligo dT (green) staining. The scale bar indicates 20 μm. **(B)** From the images shown in (A), the nuclear accumulation of poly-A RNA in cells expressing Flag-Orf6 and in bystander cells (not expressing Flag-Orf6) was plotted as the ratio between the nuclear and cytoplasmic signal intensity of poly-A RNA (N/C ratio). The dotted line denotes the instances where there is no enrichment of the poly-A RNA signal within the nucleus relative to the cytoplasm. Significance was determined using a Welch's ANOVA followed by post-hoc pairwise Welch's *t*-tests with a Bonferroni correction.

within the nucleus when expressing Flag-Orf6, and that the overall level of nuclear poly-A RNA accumulation is greater than in cells not expressing Flag-Orf6. This suggests that Flag-Orf6 expression causes RNA export defects in both scramble control and Nup98-depleted cell lines. Additionally, this analysis confirms that Nup98 depletion does cause partial poly-A RNA export defects, as Nup98-depleted bystander cells have a significantly higher accumulation of poly-A RNA within the nucleus when compared to shScramble bystander cells (Figure 4.16B). Overall, these results suggest that Flag-Orf6 expression in Nup98-depleted cells causes poly-A RNA export defects, and that this export defect is more exaggerated than the poly-A RNA export defect caused by Nup98 depletion alone.

To investigate if Orf6 expression triggers similar RNA export defects in Rae1-depleted cells, shScramble and shRae1 cells were examined by FISH/IF analysis after 120 h of doxycycline treatment and 24 h of Flag-Orf6 expression (Figure 4.17A). Results have indicated that shScramble control cells expressing Flag-Orf6 have an accumulation of poly-A RNA within the nucleus, but in contrast, Flag-Orf6 expressing Rae1-depleted cells no longer show a nuclear accumulation poly-A RNA (Figure 4.17A). These Flag-Orf6 expressing Rae1-depleted cells show a comparable poly-A RNA staining pattern when compared to non-Flag-Orf6 expressing Rae1 knockdown cells, suggesting that Orf6 requires Rae1 to inhibit poly-A RNA nuclear export. To confirm the above results, quantification of the poly-A RNA signal within the nucleus and cytoplasm was measured and plotted as described above (Figure 4.17B), and showed that Flag-Orf6 expressing shScramble cells accumulate significantly greater levels of poly-A RNA in the nucleus when compared to Flag-Orf6 expressing Rae1-

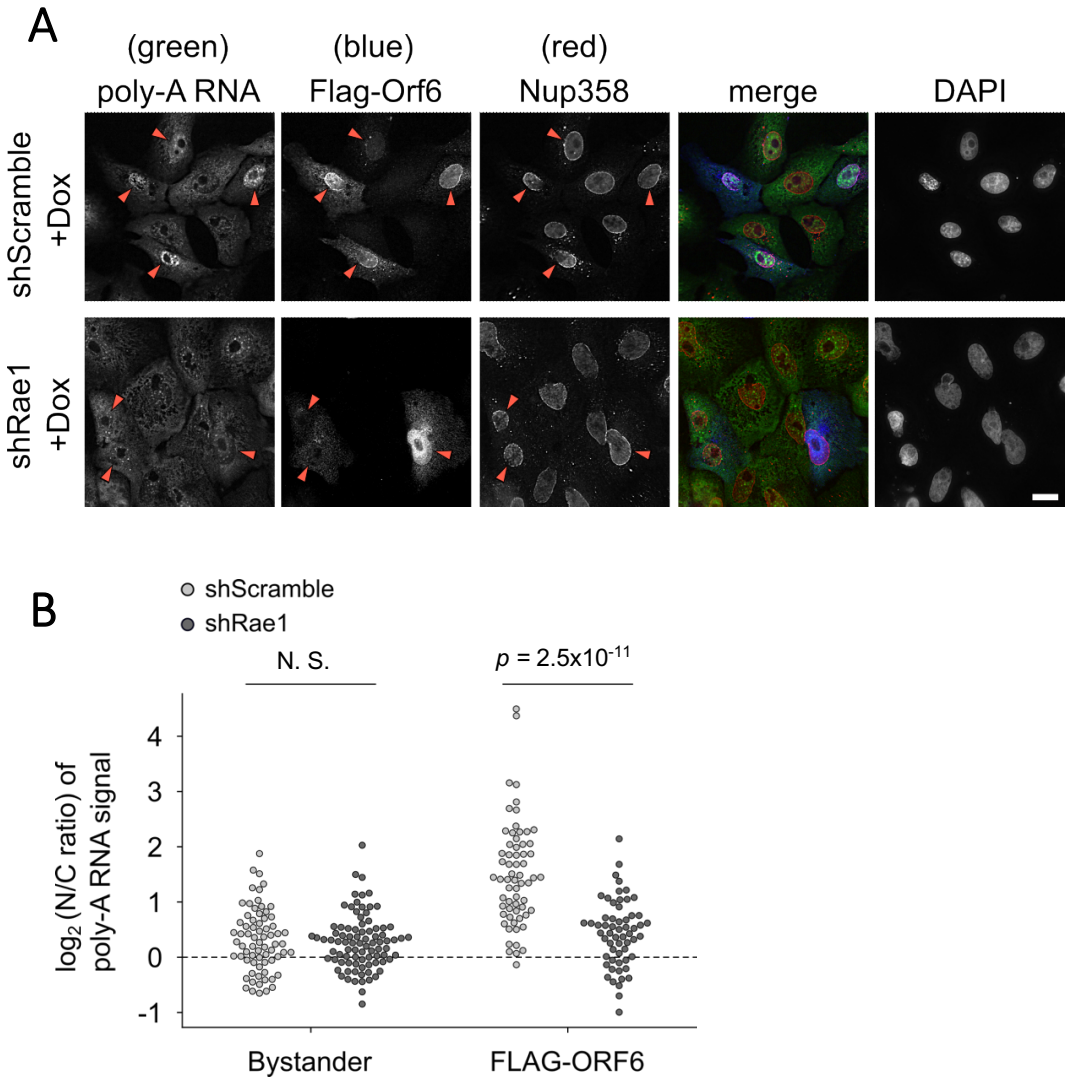

Figure 4.17 (Makio, T.) Rae1 depletion suppresses the Orf6 mediated block of poly-A RNA nuclear export.

(A) Vero cells containing doxycycline inducible shRNA constructs (shScramble or shRae1) were incubated with doxycycline for 120 h and transduced with a plasmid encoding Flag-Orf6 for the last 24 h of incubation. Cells were subject to FISH/IF analysis using an oligo dT probe, anti-Flag and anti-Nup358 antibodies. The position of the nucleus was detected using DAPI staining. Merged images show Flag-Orf6 (blue), Nup358 (red) and oligo dT (green) staining. The scale bar indicates 20 μm. **(B)** From the images shown in (A), the nuclear accumulation of poly-A RNA in cells expressing Flag-Orf6 and in bystander cells (not expressing Flag-Orf6) was plotted as the ratio between the nuclear and cytoplasmic signal intensity of poly-A RNA (N/C ratio). The dotted line denotes the instances where there is no enrichment of the poly-A RNA signal within the nucleus relative to the cytoplasm. Significance was determined using a Welch's ANOVA followed by post-hoc pairwise Welch's *t*-tests with a Bonferroni correction.

depleted cells (Figure 4.17B). Additionally, these results confirm that Rae1 depletion does not cause poly-A RNA export defects on its own, as bystander Rae1 knockdown cells (not expressing Flag-Orf6) show comparable levels of nuclear poly-A RNA when compared to bystander shScramble control cells (Figure 4.17).

Overall, these results suggest that depletion of Nup98 does not overcome the poly-A RNA export defects caused by Orf6 expression, however, these poly-A RNA export defects can be overcome when Rae1 is depleted.

4.2.8 Nup96-V5 can be exogenously expressed and localizes to the nuclear envelope.

Since the knockdown Nup98 leads to the reduction of Nup96 in Vero cells (Figure 4.1, 4.3), shNup98 cells were integrated with a shNup98 RNA resistant Nup96-V5 construct to try and overcome the reduction of Nup96 at the NE of Nup98 knockdown cells.

Nup98 and Nup96 are encoded within a polycistronic mRNA, and are autoproteolytically cleaved after translation (Fontoura *et al*., 1999). The shRNA construct used in this study to target Nup98 RNA was chosen because it caused a robust depletion of Nup98 protein levels, however, this shRNA construct targets an area of the Nup98-Nup96 mRNA that encodes for Nup96 (Figure 4.18A). As such, the exogenous introduction of a Nup96-V5 construct that produces mutant mRNA but codes for a wildtype protein was hypothesized to restore levels of Nup96 at the NE of Nup98-depleted Vero cells, due to the ability of this Nup96-V5 construct to escape silencing by shNup98 RNA. Therefore, both shScramble and shNup98 cells

were subject to reverse-transduction with lentivirus containing the Nup96-V5 construct, and clonal populations of both shScramble and shNup98 cells constitutively expressing Nup96-V5 were isolated and characterized as described below. A schematic of the isolation strategy is depicted in (Figure 4.18B).

shScramble cells and isolated shScramble Nup96-V5 expressing clones (shScramble+Nup96-V5) were subject to 96 h of growth with or without doxycycline before being visualized by immunofluorescent microscopy analysis (Figure 4.19). Visual examination of Nup96 staining pattern at the NE suggests that the expression of Nup96-V5 in shScramble+Nup96-V5 cells does not substantially contribute to the Nup96 signal seen at the nuclear periphery, as the shScramble+Nup96-V5 clones show a similar Nup96 staining intensity and localization pattern when compared to shScramble control cells (Figure 4.19).

This characterization was extended to shNup98 cells, to assess if the expression of the Nup96-V5 construct was resistant to shNup98 RNA mediated knockdown, and to examine if the expression of Nup96-V5 in this cell line is sufficient to increase the number of Nup96 foci found at the NE of Nup98-depleted cells. Immunofluorescent microscopy analysis of shNup98 cells, and isolated shNup98 clones constitutively expressing Nup96-V5 (shNup98+Nup96-V5), was performed after 96 h of treatment with or without doxycycline (Figure 4.20). Consistent with previous results (Figure 4.3), visual analysis of shNup98 cells show a decreased density of Nup96 foci when Nup98 is depleted, with areas of the nuclear periphery that are seemingly void of foci (Figure 4.20). In contrast, the various shNup98+Nup96-V5 clones show slight visual increase of Nup96 foci at the NE when

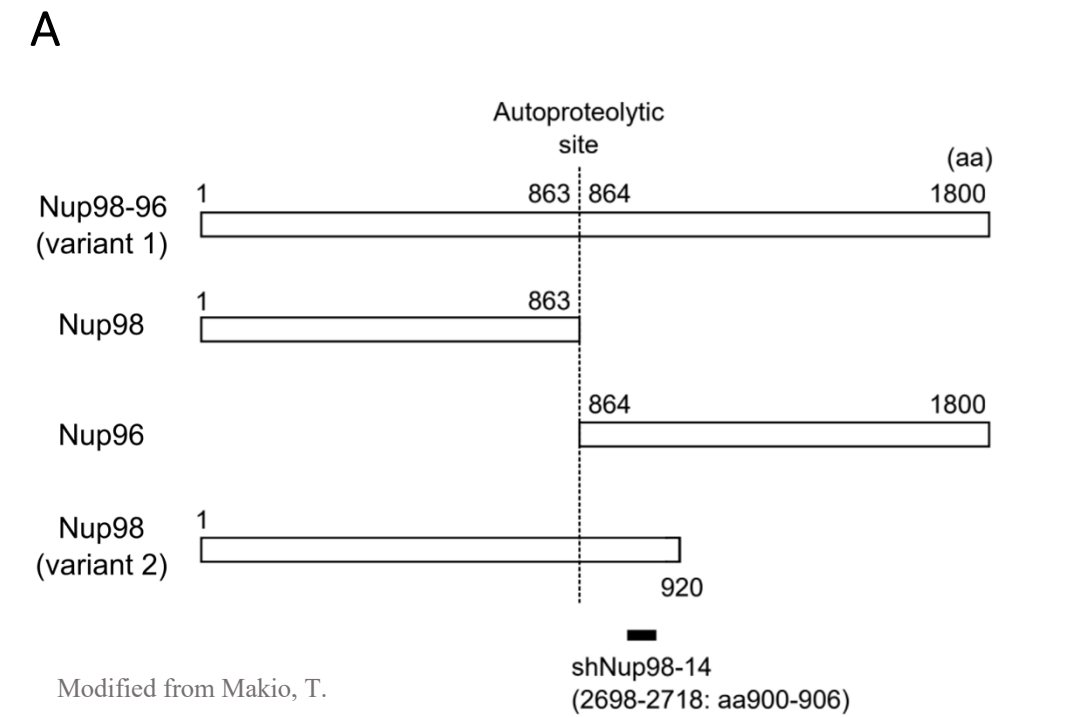

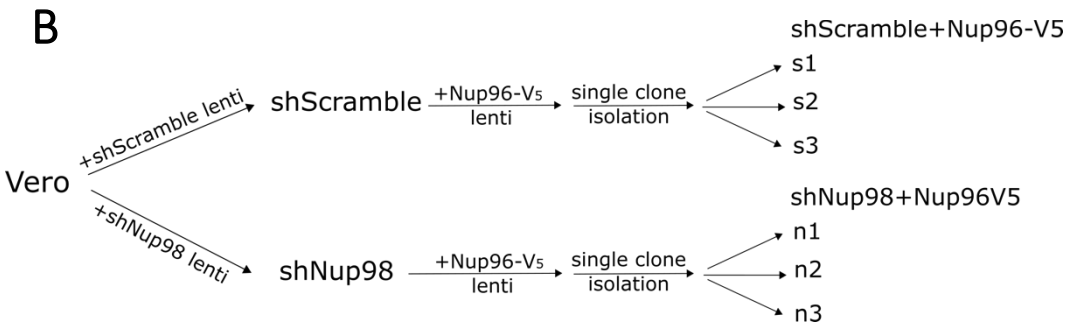

Figure 4.18 Schematic diagrams.
(A) Schematic depicting the two main Nup98 variants produced in mammals. Variant 1: Nup96 and Nup98 are encoded on the same mRNA, generating a Nup98-Nup96 precursor protein that is autoproteolytically cleaved to generate both Nup98 and Nup96. Variant 2: Nup98 is synthesized independently of Nup96 from an alternatively spliced mRNA. shNup98-14 is the shRNA construct used in these studies to deplete Nup98. shNup98-14 is targeted against nucleotides 2698-2718 present in both Nup98 mRNA variants. **(B)** Schematic depiction of the isolation strategy of the clonal populations of shScramble and shNup98 cells expressing an shNup98-14 resistant Nup96-V5 construct.

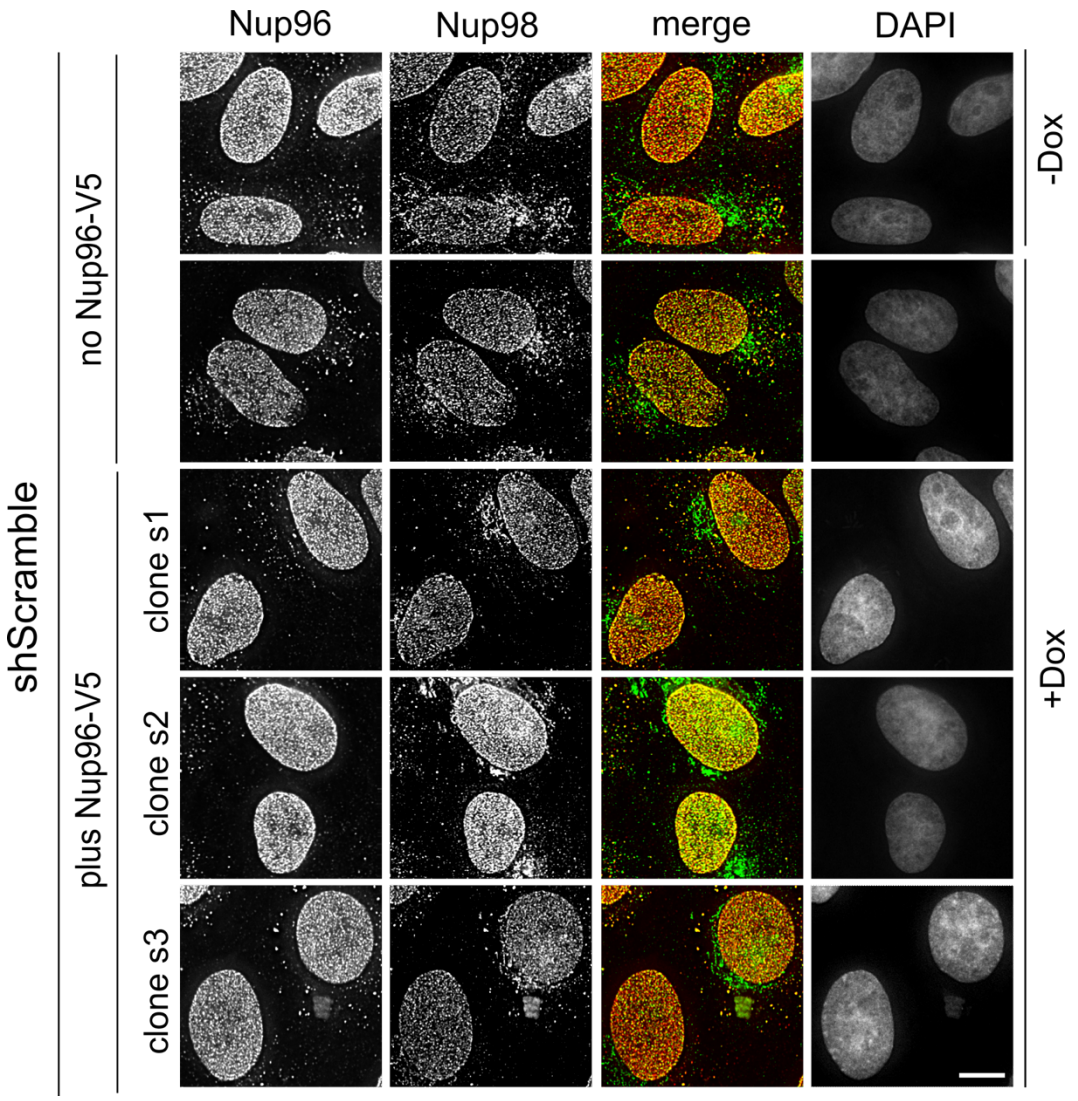

Figure 4.19 Exogenous expression of Nup96-V5 in shScramble cells.
Vero cells containing a doxycycline inducible shScramble RNA construct were stably integrated with a constitutively active Nup96-V5 construct containing a mutated Nup96 mRNA sequence that codes for a wildtype amino acid sequence. shScramble control cells not expressing Nup96-V5, and three clonal populations of shScramble cells expressing Nup96-V5 were treated with or without doxycycline for 96 h. Cells were subject to indirect immunofluorescence microscopy analysis using anti-Nup96 and anti-Nup98 antibodies. The position of the nucleus was detected using DAPI staining. Merged images show Nup96 (red) and Nup98 (green). The scale bar indicates 10 μm. Nup96-V5 expression in these experiments was confirmed by immunoblot analysis in figure 4.21.

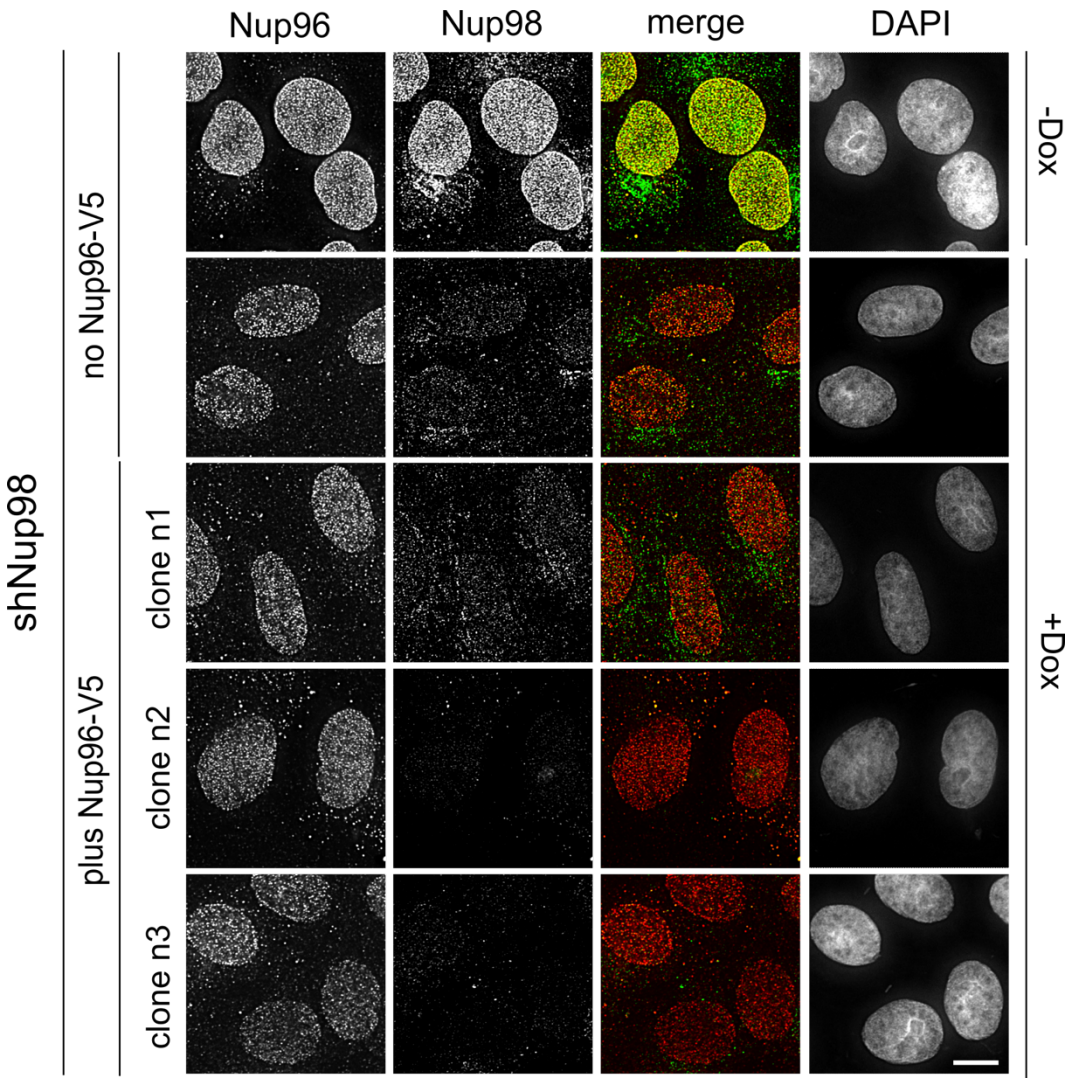

Figure 4.20 Exogenous expression of Nup96-V5 in shNup98 cells.
Vero cells containing a doxycycline inducible shNup98 RNA construct were stably integrated with a constitutively active Nup96-V_5 construct containing a mutated Nup96 mRNA sequence but coding for a wildtype amino acid sequence. shNup98 cells not expressing Nup96-V5, and three clonal populations of shNup98 cells expressing Nup96-V5 were treated with or without doxycycline for 96 h. Cells were subject to indirect immunofluorescence microscopy analysis using anti-Nup96 and anti-Nup98 antibodies. The position of the nucleus was detected using DAPI staining. Merged images show Nup96 (red) and Nup98 (green). The scale bar indicates 10 μm. Nup96-V5 expression in these experiments was confirmed by immunoblot analysis in figure 4.21.

compared to Nup98 depleted cells (Figure 4.20). Furthermore, the expression of Nup96-V5 when Nup98 is depleted seems to partially restore levels of Nup96 associated with Nup98 depletion, as these Nup96-V5 expressing clones do not show as many areas of the NE that are void of Nup96 foci (Figure 4.20).

Western blot analysis of whole cell lysates from shScramble, shScramble+Nup96-V5, shNup98, and shNup98+Nup96-V5 cell lines were examined to assess protein levels before and after doxycycline treatment (Figure 4.21). Results indicate that all shScramble cell lines treated with or without doxycycline produce comparable levels of Nup358, Nup98, Nup96, and Rae1, and that all isolated shScramble+Nup96-V5 clones express similar levels of Nup96-V5 protein (Figure 4.21A). In contrast, all shNup98 cell lines treated with doxycycline show decreased levels of Nup98, Nup96, Nup358, and Rae1 when compared to the no doxycycline treatment condition (Figure 4.21B). The shNup98+Nup96-V5 clones show active expression of Nup96-V5 when treated with or without doxycycline, indicating that the Nup96-V5 construct is resistant to knockdown by shNup98 RNA. The expression level of Nup96-V5 in the three shNup98+Nup96-V5 clones is variable, with clone n3 expressing the highest level of the Nup96-V5 protein (Figure 4.21B). However, regardless of expression level, none of the Nup96-V5 expressing clones restore Nup96 to wildtype levels when Nup98 is being actively depleted (Figure 4.20, 4.21B).

Together, these results suggest that the expression of Nup96-V5 at the levels achieved in this study only partially restores the number Nup96 foci detected at the NE of Nup98 knockdown cells.

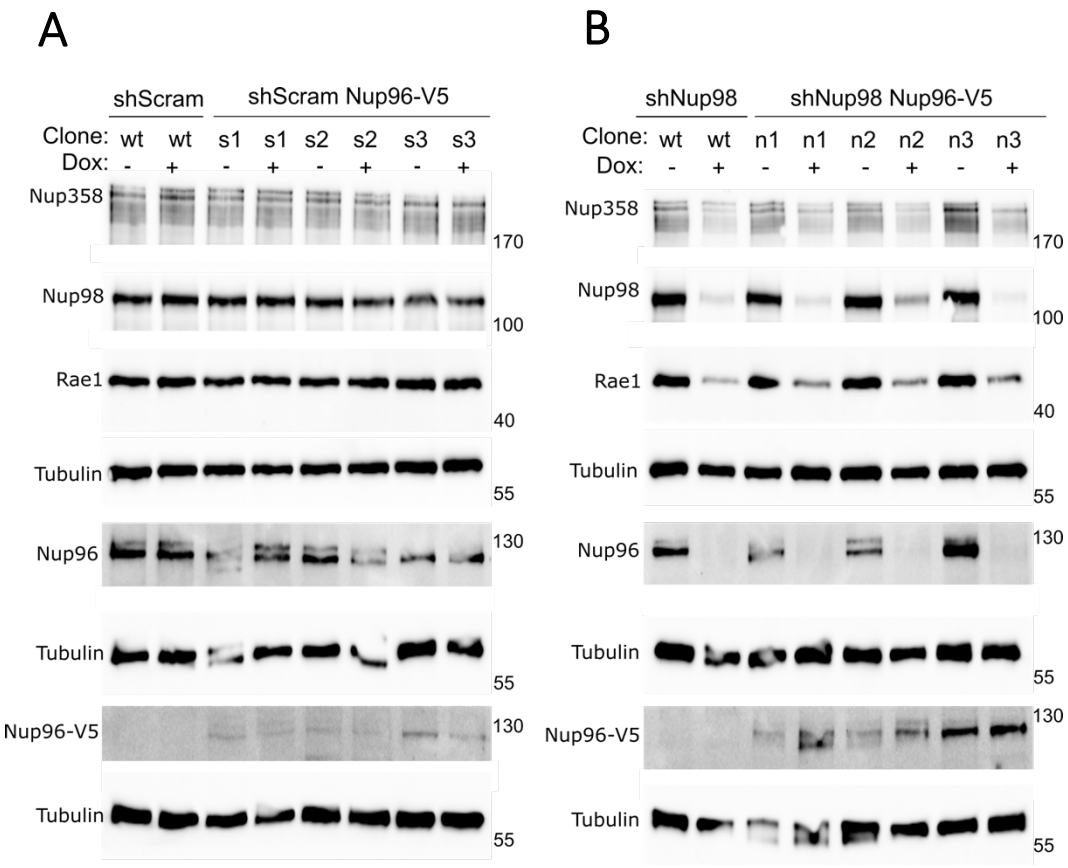

Figure 4.21 Immunoblot analysis of Nup96-V5 expressing clones following shRNA mediated depletion.
Vero cells containing doxycycline inducible shRNA constructs (shScramble **(A)** or shNup98 **(B)**) expressing exogenous Nup96-V5, or not, were treated with or without doxycycline for 96 h. Whole cell lysates were prepared and analyzed by western blotting using anti-Nup98, anti-Rae1, anti-Nup358, anti-Nup96, anti-V5 and anti-Tubulin (load control) antibodies as indicated to the left of the panels. The positions of molecular mass markers (shown in kDa) are indicated to the right. Corresponding immunofluorescence images are presented in figure 4.19 and 4.20.

4.3 Discussion.

SARS-CoV-2, like other viruses, have evolved mechanisms to escape innate immune detection by interfering with host nuclear transport (Miorin *et al.*, 2020; Addetia *et al*., 2021; Quan *et al.,* 2014; Gong *et al*., 2016; Frieman *et al.*, 2007). Interactions between the SARS-CoV-2 Orf6 protein and the Nup98/Rae1 complex has been suggested to inhibit the nuclear import of innate immune stimulated proteins, such as IRF3 and STAT1, which are required to activate an effective innate immune response (Miorin *et al.*, 2020; Lei *et al*., 2020; Xia *et al*., 2020). In addition, Orf6 has also been shown to reduce both the expression (Xia *et al*., 2020; Lei *et al*., 2020) and the nuclear export of host RNAs (Addetia *et al*., 2021; Li *et al*., 2022) that encode for various antiviral factors involved in the suppression of viral replication (Hall *et al*., 2022). Since an optimal innate immune response is critical for viral clearance, Orf6 has become an intriguing target for investigation.

Mutation of a critical methionine residue (M58) in the SARS-CoV-2 Orf6 protein has been shown to reduce its interactions with the Nup98/Rae1 complex (Miorin *et al*., 2020; Hall *et al*., 2022), suppressing the Orf6-mediated block of both STAT1 nuclear import (Miorin *et al*., 2020) and poly-A RNA nuclear export (Addetia *et al*., 2021). This suggests that interactions between Orf6 and the Nup98/Rae1 complex are needed to facilitate the inhibitory functions of Orf6, however, the requirement for Nup98 or Rae1 on Orf6 function has not been fully elucidated. Therefore, in this study, we aim to characterize the Orf6-mediated block of bidirectional nuclear transport within mammalian cells depleted of either Nup98 or Rae1 in order to determine the requirement of Nup98 and Rae1 on Orf6 function.

The shRNA mediated depletion of either Nup98 or Rae1 does not significantly affect bidirectional nuclear transport in Vero cells.

In order to investigate the effect of both Nup98 and Rae1 depletion on Orf6 function, Nup98 and Rae1 depleted cell lines first had to be characterized in order to assess the effects of knockdown on cellular nuclear transport. Since the knockout of either Nup98 or Rae1 has been shown to be embryonically lethal in mouse models (Wu *et al*., 2001; Babu *et al*., 2003) shRNA-mediated knockdown of either Nup98 or Rae1 was employed in this study. We show here that when Vero cells are induced to knockdown Nup98, a complete reduction of Nup98 is not achieved (Figure 4.1, 4.6C), however, levels of Nup98 at the NE are significantly reduced (Figure 4.2). Comparatively, Rae1 is able to be reduced to almost undetectable levels by 120 h of Rae1 depletion (Figure 4.4-4.5).

Previous studies have indicated that levels of other Nups are reduced at the NPC of cells lacking Nup98 (Wu *et al*., 2001), and consistent with these reports, depletion of Nup98 also causes a reduction of Nup358, Nup96, and Rae1 at the NE (Figure 4.2-4.3). Furthermore, the staining pattern of these Nups in immunofluorescent microscopy analysis also suggests that Nup98 depletion my lead to overall NPC density defects in Vero cells, as the NE of Nup98 knockdown cells often show areas that are seemingly void of Nup foci (Figure 4.2-4.3). Since Nup96 is encoded within a polycistronic mRNA with Nup98 (Fontoura *et al*., 1999), many techniques used to deplete Nup98 have also led to the reduction of Nup96 protein levels. Therefore, as expected, levels of Nup96 were also significantly depleted in shNup98 cells treated with doxycycline (Figure 4.1 and 4.3). Since Nup96 has been

shown to play a crucial role in NPC assembly (Krull *et al*., 2004, Schuller *et al*., 2021), the depletion of Nup96 may also explain why there is a reduction of other Nups at the NPC of shNup98 knockdown cells (Figure 4.2B, 4.3). Rae1 levels were also shown to be reduced at the NE when Nup98 was depleted (Figure 4.2), however this was also expected as Nup98 contains a GLEBS motif (Bailer *et al*., 1998; Pritchard *et al*., 1999) that is both necessary and sufficient for Rae1 binding (Ren *et al*., 2010). Yeast studies have indicated that the GLEBS motif of Nup116 (the yeast Nup98 counterpart) is required for Gle2 association at the NE (Ren *et al*., 2010) and provides further evidence for the requirement of Nup98 for Rae1 binding at NPCs. Consistent with these results, recent evidence in mammalian cells has also suggested depletion of Nup98 leads to dislocation of Rae1 at NPCs (Serganov *et al*., 2022), providing further support that the interaction between Rae1 and Nup98 is required for Rae1 localization at the NE. In comparison, Rae1 knockdown does not cause a reduction in levels of other nucleoporins such as Nup358 or Nup98 (Figure 4.4) and does not affect their localization at the NE (Figure 4.5). Therefore, this collectively suggests that Rae1 is likely not required for the efficient assembly of other Nups into mammalian NPCs, however, since the depletion of Nup98 leads to a reduction of various Nups at the NPC, this suggests Nup98 is likely required for proper NPC stability.

Due to the multifaceted nature of the Nup98 protein, the depletion of Nup98 has remained a challenge within mammalian cells. Nup98 is the only GLFG-repeat nucleoporin in higher eukaryotes (Griffis *et al*., 2003) and has previously been established to have important roles in NPC assembly (Wu *et al*., 2001), protein import into the nucleus (Radu *et al*., 1995; Fontoura *et al*., 2000; Ryan and Wente, 2000), and

RNA export out of the nucleus (Belvins *et al*., 2003; Oka *et al*., 2010, Xie and Ren, 2019). Since the knockout of Nup98 has been suggested to cause lethal effects (Wu *et al*., 2001), potentially owing to the many roles of Nup98 in maintaining proper cellular function, cell growth and cell viability were assessed in Nup98 knockdown cells. When shNup98 cells and shScramble control cells are grown without doxycycline, both cell lines grow at an exponential rate over a 96 h time course (Figure 4.6A). shScramble cells grown in doxycycline also grow at an exponential rate throughout 96 h of induction, however, cells induced to express shNup98 RNA show a significant growth rate defect by 96 h of depletion (Figure 4.6A). Cell viability was also assessed in these cell lines, and paralleling the above results, shNup98 cells showed a significantly decreased cell viability by 96 h of Nup98 depletion when compared to shScramble control cells (Figure 4.6B). This cell viability assay specifically measures the mitochondrial dehydrogenase activity of living cells and is based on the reduction of oxidized non-fluorescent blue resazurin to a red fluorescent resorufin dye, as such, the fluorescence produced is directly proportional to the number of living cells in the population (Abcam). Therefore, the growth rate defect caused by Nup98 depletion is likely to impact the results of the viability assay, and thus, the population of Nup98 knockdown cells by 96 h of depletion are most likely viable cells. Further investigation of shNup98 cells induced to deplete Nup98 for 4 or 14 days has shown that shNup98 cells are able to actively deplete Nup98 over a 14 day growth period, however, the level of Nup98 depleted by day 4 is comparable to the level of Nup98 depleted by day 14, suggesting that the shRNA construct used in these studies to target Nup98 cannot completely deplete Nup98 levels within Vero cells (Figure 4.6C). Overall, these

studies would suggest that the knockdown of Nup98 causes significant growth rate defects in Vero cells, however, cells are able to continue to actively divide for an extended period of time while depleted of Nup98, suggesting that cells likely remain viable when Nup98 is depleted.

Although Vero cells depleted of Nup98 show a reduction of multiple Nups at the NE, we wanted to assess the nuclear import of STAT1 when shNup98 cells were treated with IFN-α (Figure 4.8). Nup98 depletion was confirmed in immunofluorescent microscopy analysis using the mAb414 antibody which detects FG-repeat-containing nucleoporins including Nup358, Nup214, Nup153, and Nup62 (Davis and Blobel, 1987; Mimura *et al*., 2017), and consistent with previously reported results (Wu *et al.,* 2001), Nup98 depleted cells show a reduced mAb414 staining intensity at the nuclear periphery when compared to control cells (Figure 4.8A). This suggests that levels of Nup214, Nup153, and Nup62 may also be affected by Nup98 depletion. Intriguingly though, Nup98 depletion does not affect pSTAT1 nuclear import, as Nup98 knockdown cells show a similar nuclear accumulation of pSTAT1 when compared to cells not depleted of Nup98 (Figure 4.8). Although previous analysis on cells lacking Nup98 has indicated there are importin-α/β1 mediated protein import defects (Wu *et al*., 2001), the depletion of Nup98 to the level achieved in this study did not cause nuclear import defects of the importin- α/β1 cargo pSTAT1. Since a complete depletion of Nup98 was not achieved in these studies, low levels of Nup98 may allow for the continued import of importin-α/β1 cargo, however, these results may additionally suggest an alternative mechanism by which pSTAT1 is imported into the nucleus independent of Nup98 and the importin-α/β1

transport pathway. There is currently no evidence to suggest that Rae1 is involved nuclear import, and consistent with this, the reduction of Rae1 does not affect pSTAT1 nuclear import in Vero cells (Figure 4.9). Since Rae1 levels are robustly depleted after 120 h of knockdown (Figure 4.4), this suggests that Rae1 is likely not specifically involved in the nuclear import of the pSTAT1 protein.

To further investigate potential nuclear transport defects associated with Nup98 or Rae1 depletion, both shNup98 and shRae1 cells were analysed by FISH to visualize the cellular distribution of poly-A RNA. The results of this analysis indicate that Nup98 depletion, but not Rae1 depletion, causes partial poly-A RNA export defects in Vero cells (Figure 4.10-4.11). Nup98 has been suggested to play a role in a mRNA export (Powers *et al*., 1997) through interactions with mRNA export factors NXF1:NXT1 (Bachi *et al*., 2000; Belvins *et al*., 2003) and CRM1 (Wu *et al*., 2001; Oka *et al*., 2010). Since the depletion of Nup98 only lead to partial poly-A RNA export defects, it is likely that these export factors can bind to other FG-repeat Nups within the NPC to facilitate the export of poly-A RNA. It should be noted though, that Nup98 reduction also leads to a depletion of Nup358 at the nuclear periphery, and Nup358 depletion has also been shown to cause poly-A RNA export defects in cells (Hamada *et al*., 2011; Forler *et al*., 2004). Additionally, since Nup98 knockdown in Vero cells may lead to reduced NPC density at the NE, it is plausible that these cells experience an overall decrease in rate of RNA export. Therefore, the partial poly-A RNA export defects arising from shNup98 RNA expression could be due to a multitude of reasons, including loss of Nup98 and Nup358 at the nuclear periphery or a kinetic defect in RNA export arising from a reduced number of functional NPCs.

Rae1 has been defined as an mRNA export factor that interacts with Nup98 (Pritchard *et al*., 1999; Ren *et al*., 2010). Rae1 binding to the GLEBS motif of Nup98 creates a hydrophobic mRNA binding groove which has been shown to be capable of interacting with single stranded RNAs (Ren *et al*., 2010), and has been a target of multiple viruses to inhibit host RNA export (Faria *et al*., 2005; Quan *et al*., 2014; Gong *et al*., 2016). Previous studies have suggested that Rae1 may facilitate the interaction of Nup98 with NXF1, the nuclear transport receptor responsible for shuttling the bulk of mRNA across the NE, and therefore plays a role in mammalian mRNA export (Belvins *et al*., 2003). However, the depletion of Rae1 does not cause poly-A RNA export defects in Vero cells (Figure 4.11). Therefore, our results in combination with other reports indicating that Rae1 depletion does not lead to noticeable RNA export defects (Babu *et al*., 2003; Rajani *et al*., 2012), could suggest that Rae1 exports only a small subset of cellular mRNAs, or that Rae1's role in mRNA export may be overcome by redundant cellular export pathways mediated by other nuclear transport factors. Since the role of Rae1 in mRNA export ultimately remains unclear (Xie and Ren, 2019), further investigation into Rae1 is required in order to characterize its precise function in nuclear transport within mammalian cells.

Depletion of Rae1, but not Nup98, completely suppresses the Orf6-mediated block of bidirectional nuclear transport in Vero cells.

Since the depletion of Rae1 or Nup98 did not affect the nuclear import of pSTAT1 and did not largely affect the nuclear export of poly-A RNA, the shNup98

and shRae1 cell lines were further used to characterize the requirement of Nup98 or Rae1 on SARS-CoV-2 Orf6 function.

Previous analysis on the expression of Flag-Orf6, has revealed that Orf6 localizes mainly at the NE with colocalization detected between Flag-Orf6 and Nup98 (Miorin *et al*., 2020). Consistent with these results, shScramble control cells also show an accumulation of Flag-Orf6 at the NE with co-localization detected with both Nup98 and Nup358 foci (Figure 4.12A; Figure 4.13A). However, when cells are induced to knockdown either Nup98 or Rae1, Flag-Orf6 intensity is reduced at the NE and a pool of cytoplasmic Flag-Orf6 can be visualized upon depletion of either Nup98 or Rae1 (Figure 4.12A and C; 4.13A and C). The reduction of Orf6 at the NE of Nup98 depleted cells (Figure 4.12C) is not as substantial as it is in Rae1 depleted cells (Figure 4.13C), and faint Flag-Orf6 staining pattern can still be visualized around the NE of cells depleted of Nup98 (Figure 4.12A). Considering that Rae1 knockdown does not affect Nup98 levels or localization, but still leads to the loss of Orf6 at the nuclear periphery, suggests that Rae1 is required for Orf6 association at the NE and contributes to the localization of Orf6 at NPCs. Since Nup98, or Rae1, are not completely depleted upon expression of shNup98 RNA, Nup98 knockdown cells may still have low levels of functional Nup98/Rae1 complexes at NPCs, and would provide an explanation as to why Flag-Orf6 can still be partially visualized at the NE of Nup98 depleted cells but is drastically reduced at the NE of Rae1 depleted cells. It is plausible that the disruption of the mRNA binding groove formed by the Nup98/Rae1 complex causes Orf6 to dissociate from the NE, and therefore the sole depletion of Nup98 from NPCs may also lead to altered Orf6 localization, however, this phenomenon will likely

not be observed due to Rae1's dependency on Nup98 to bind at NPCs (Ren *et al*., 2010; Funasaka *et al*., 2011, Figure 4.2). Therefore, taken together, these results would suggest that Orf6 requires the Nup98/Rae1 complex to localize at the NE of Vero cells, however, the sole depletion of Rae1 is sufficient to cause mislocalization of the Orf6 protein.

Since the expression of Orf6 has been shown to affect multiple nuclear transport pathways by targeting the Nup98/Rae1 complex, it has been an intriguing area of investigation to assess if SARS-CoV-2 Orf6 acts to generally inhibit nuclear transport, or if Orf6 functions to inhibit specific nuclear transport pathways. One report suggests that Orf6 may act to cross-link FG-Nups within the central channel of the NPC, likely leading to a more general block of nuclear transport (Yoo and Mitchison; 2021), and although further investigations need to be conducted in order to elucidate the precise mechanism of Orf6 function, other bodies of evidence would suggest that Orf6 affects multiple nuclear transport pathways in distinct ways (Miorin *et al*., 2020; Miyamoto *et al*., 2022; Hall *et al*., 2022). This has been highlighted by evidence suggesting that Orf6 inhibits the nuclear import of different importin-α/β1 cargo to varying extents (Miyamoto *et al*., 2022). For example, NF-κB is a cNLS containing cargo that is transported into the nucleus by importin-α/β1 during viral infection (Liang *et al*., 2013). Although NF-κB is imported by importin-α/β1 import pathway, Orf6 expression does not inhibit the nuclear import of NF-kB to the extent that it inhibits the nuclear import of the importin-α/β1 cargo pSTAT1 (Miyamoto *et al*., 2022). This would suggest that Orf6 is likely acting more specifically to inhibit pSTAT1 nuclear import rather than causing a general block to the importin-α/β1

protein import pathway. Indeed, Orf6 has been shown to independently bind to the STAT1 protein (Miyamoto *et al*., 2022), further suggesting that Orf6 likely specifically inhibits the nuclear import of the STAT1 transcription factor. However, immunoprecipitation experiments also reveal that Nup98 interacts less strongly with importin-β1 molecules when Orf6 is expressed (Makio *et al*., in preparation), suggesting that Orf6 could possibly act by generally impairing importin-α/β1 mediated import, while also specifically and robustly inhibiting the nuclear import of other cellular proteins. Moreover, Orf6 has also been shown to differentially affect the export of RNAs, as the nuclear export of various antiviral mRNA has been shown to be inhibited by Orf6 expression while the export other RNAs, such as GAPDH RNA, remains unaffected (Hall *et al*., 2022). Taken together, this suggests that Orf6 likely inhibits the nuclear transport of specific host proteins and RNA, rather than inducing a non-specific nuclear transport block of cellular factors, however, further investigation is required to fully elucidate the mechanism of action behind the SARS-CoV-2 Orf6 protein.

To characterize the requirement of Nup98 or Rae1 on the Orf6-mediated block of nuclear import, both Nup98 and Rae1 knockdown cells were examined after interferon treatment to assess the ability of Orf6 to inhibit pSTAT1 nuclear import. Analysis of both shNup98 and shRae1 cell lines has revealed that Orf6 no longer functions to inhibit the nuclear import of pSTAT1 when either Nup98 or Rae1 are depleted (Figure 4.14; 4.15). Intriguingly, although there are likely still low levels functional Nup98/Rae1 complexes within Nup98-depleted cells capable of interacting with Orf6, this level of Nup98/Rae1 is not sufficient for Orf6 to fully exert its block

on pSTAT1 nuclear import. Since Orf6 has been suggested to specifically bind STAT1 to inhibit its nuclear import (Miyamoto *et al*., 2022), this may suggest that levels of Orf6 at the NPCs of Nup98-depleted cells are too low to cause an inhibitory effect on the nuclear import of STAT1. In the shRae1 cell line, Rae1 levels are almost undetectable after 120 h of Rae1 depletion without effecting levels of Nup98 (Figure 4.4), and since the Orf6-mediated STAT1 nuclear import defect is suppressed by Rae1 depletion alone, this suggests a requirement for Rae1 in facilitating Orf6 function. Taken together, these results ultimately suggest a mechanism whereby Orf6 must interact with the Nup98/Rae1 complex in order to exert an inhibitory function, and therefore, suggests a requirement for both Nup98 and Rae1 on Orf6's ability to perturb host nuclear import.

In addition to protein import, mRNA export defects were assessed in cells expressing Flag-Orf6. Previous reports have indicated that Orf6 expression causes RNA export defects (Addetia *et al*., 2021; Li *et al*., 2022; Hall *et al*., 2022), and consistent with these results, control cells expressing Flag-Orf6 show a significant accumulation of poly-A RNA within the nucleus (Figure 4.14 and Figure 4.15). Interestingly, Nup98-depleted cells show a similar accumulation of poly-A RNA within the nucleus when compared to Flag-Orf6 expressing shScramble control cells (Figure 4.14). This could suggest that the depletion of Nup98 achieved in these studies is not sufficient to suppress the block of RNA export caused by Orf6 expression. In contrast, Orf6 is no longer able inhibit poly-A RNA nuclear export in Rae1 knockdown cells (Figure 4.17), which suggests that Rae1 is required for Orf6 to inhibit host RNA export. However, the overall disruption to the Nup98/Rae1 complex caused

by Rae1 depletion may influence Orf6's ability to inhibit RNA export and cannot be overlooked as the potential underlying cause for the phenotype observed in the Flag-Orf6 expressing Rae1 knockdown cells.

Since the phenotypes associated with Rae1 knockdown cells expressing Orf6 has been largely consistent with Nup98 knockdown cells expressing Orf6, it is curious that the depletion of Rae1, but not Nup98, reverses the Orf6 mediated block of RNA export. Due to an incomplete reduction of Nup98 after 96 h of depletion (Figure 4.1), low levels of Nup98 may be forming functional subcomplexes with Rae1 at the NPC of Nup98 depleted cells, and these functional Nup98/Rae1 complexes likely interact with Orf6. Since Nup98 has been suggested to play important roles in RNA export (Powers *et al*., 1997) through interactions with various RNA export factors such as CRM1 (Oka *et al*., 2010) and NXF1 (Bachi *et al*., 2000; Belvins *et al*, 2003), it is plausible that the association of Orf6 with functional Nup98/Rae1 complexes in Nup98 knockdown cells inhibits the interaction between Nup98 and these other RNA export factors, leading to the accumulation of various RNAs within Orf6 expressing cells that are depleted of Nup98. In this manner, the interaction between Orf6 and the Nup98/Rae1 complex would likely serve as a platform for Orf6 to either directly interact with host factors or to inhibit the interaction of various host transport molecules with the NPC, thereby interfering with cellular nuclear transport. This may provide an explanation as to why Orf6 can no longer function to inhibit poly-A RNA export in Rae1 depleted cells, due to a robust depletion of Rae1 upon shRae1 RNA expression. Therefore, Rae1 depletion within these cells leads to a suppression of Orf6 function as Orf6 can no longer associate with Nup98/Rae1 complexes to subsequently

exert a transport block. However, when Nup98 is reduced to the levels we observe in this study, Orf6 is still able to bind to low levels of Nup98/Rae1 complexes at the NPC and can function in inhibiting host RNA export. However, these results could also point to an important role for Rae1 in facilitating the nuclear transport defects associated with the Orf6 protein.

It is perplexing that depletion of Nup98 reverses the Orf6 mediated block of nuclear import, but not nuclear export. This could provide evidence to suggest that Orf6 functions in a specific manner to inhibit both pSTAT1 import and poly-A RNA export. Alternatively, these results could also suggest that overall levels of Orf6 bound at nuclear pores is an important determinant for its inhibitory functions, and that greater levels of Orf6 are needed at the NPC in order to inhibit protein import. Furthermore, this could also suggest that Nup98 does not function to facilitate the RNA export defects associated with Orf6 expression and therefore, Nup98 knockdown does not affect the nuclear export inhibition caused by Orf6 expression. The requirement for Rae1 on Orf6 function is clearer, as the loss of Rae1 completely abolishes the inhibitory effects of Orf6 restoring both the nuclear import and nuclear export defects associated with Orf6 expression. This implies that Orf6 does require Rae1 for proper function, however the phenotypes observed in Orf6 expressing Rae1 knockdown cells may also be due to the loss of functional Nup98/Rae1 complexes at the NPC, and therefore, these studies ultimately suggest that Orf6 requires interactions with the Nup98/Rae1 complex to inhibit host bidirectional nuclear transport.

While there have been increasing bodies of evidence to suggest Orf6 interacts with the Nup98/Rae1 complex to inhibit host bidirectional nuclear transport (Miorin

et al., 2020; Addetia *et al*., 2020; Li *et al*., 2022; Hall *et al*., 2022), the requirement for either Nup98 or Rae1 on Orf6 function has not been previously investigated before these studies. Although the exact mechanism of Orf6 function has not been fully elucidated here, we provide evidence to suggest that Orf6 function requires Rae1, and that the interaction between Orf6 and the Nup98/Rae1 complex is necessary for Orf6 to block pSTAT1 nuclear import and poly-A RNA export. Furthermore, since the depletion of Nup98 or Rae1 does not inhibit pSTAT1 nuclear import or poly-A RNA nuclear export, the results of this study revel that Orf6 does not target the function of either Nup98 or Rae1 in order to inhibit host bidirectional nuclear transport. Rather, our data would suggest a potential mechanism where the Nup98/Rae1 complex acts as a docking site for Orf6 to bind at a concentration necessary to alter the transport properties of the NPC. In this manner, Orf6 could potentially inhibit aspects of host nuclear transport by altering the hydrophobic FG-Nup interactions within the central channel of the NPC and reducing the movement of NTF-cargo complexes across the NPC. Alternatively, Orf6 could also potentially inhibit the nuclear transport of various host molecules through direct cargo interactions or through direct interactions with various NTFs, ultimately leading to a block in the nuclear transport of specific host molecules. Thus, further detailed investigations need to be employed in order to decipher the full repertoire of host molecules affected by Orf6 expression, and to further elucidate how, mechanistically, Orf6 inhibits bidirectional nuclear transport within host cells through its interactions with the Nup98/Rae1 complex. Overall, these studies provide important insight into the Orf6 mechanism of action, as our results provide evidence that Orf6 function is dependent on the host Nup98/Rae1 complex.

Exogenous expression of Nup96 partially restores Nup96 foci at the nuclear envelope of Nup98 knockdown cells.

Since Nup98 and Nup96 are encoded within the same mRNA (Fontoura *et al*., 1999) the knockdown of Nup98 has remained a challenge within mammalian model systems due to the simultaneous depletion of Nup96 upon expression of interfering RNAs targeted against *NUP98*. Others have reported that Nup98 and Nup96 are generated as a fusion protein, and that the synthesis and autoproteolytic processing of the Nup98-Nup96 precursor is required for proper targeting of Nup96 to the NPC (Fontoura *et al*., 1999; Rosenblum and Blobel, 1999). Rather than a strong nuclear rim staining pattern observed by the expression of a WT Nup98-Nup96 precursor protein, exogenously expressed Nup96 localizes diffusely throughout the cytoplasm (Fontoura *et al*., 1999). It could not be excluded that Nup96 may still be targeted to NPCs however, as there was significant Nup96 protein observed around the nuclear periphery (Fontoura *et al*., 1999). Although this suggests that expression of Nup96 alone may cause an inefficient incorporation of Nup96 into the NPC, there are not many bodies of evidence that examine the exogenous expression of Nup96 in detail. Furthermore, since Nup96 has been shown to have important roles in NPC assembly and function (Harel *et al*., 2003; Krull *et al*., 2004; Kelley *et al*., 2015; Schuller *et al*., 2021), we hypothesized that supplementing Nup98 knockdown cells with exogenous Nup96 may potentially restore levels of other depleted Nups at the NE when Nup98 is knocked down. Therefore, in order to try to overcome some of the defects caused by Nup98 depletion, shScramble and shNup98 cells were integrated with a construct to constitutively express an exogenous Nup96-V5 protein capable of escaping

knockdown by shNup98 RNA (Figure 4.19, 4.20, 4.21) and clonal populations of shScramble+Nup96-V5 and shNup98+Nup96-V5 cells were then isolated and characterized.

Results indicate that shScramble+Nup96-V5 clones express the Nup96-V5 protein at relatively low levels (Figure 4.21A), but don't have a visually noticeable increase in the number of Nup96 foci detected at the NE when compared to shScramble control cells (Figure 4.19). Examination of shNup98+Nup96-V5 clones reveal that these clones are able express the Nup96-V5 protein when cells are induced to knockdown Nup98, indicating that Nup96-V5 can escape silencing by shNup98 RNA (Figure 4.21B). shNup98+Nup96-V5 clone n3 shows the highest level of Nup96-V5 expression when compared to either clones n1 or n2 (Figure 4.21B), however, expression of Nup96-V5 to the levels achieved in these clones is not sufficient to restore wildtype levels of Nup96 when cells are induced to knockdown Nup98, which suggests that the Nup96-V5 protein is not being expressed at levels comparable to the endogenous Nup96 protein (Figure 4.21B). Additionally, expression of Nup96-V5 does not restore levels of other Nups, including Nup358 and Rae1, when Nup98 is depleted (Figure 4.21B). Immunofluorescent microscopy analysis has indicated that the expression of Nup96-V5 in the shNup98+Nup96-V5 clones may partially restore levels of Nup96 at the NE when Nup98 is depleted, as there is a noticeable increase in number of Nup96 foci detected around the NE of various shNup98+Nup96-V5 clones when compared to shNup98 control cells (Figure 4.20). This is exemplified by the observation that Nup98 depleted cells not expressing Nup96-V5 show areas of the NE that are seemingly void of Nup96 foci, however shNup98+Nup96-V5 clones show

reduced areas of the envelope that are void of Nup96 foci (Figure 4.20A). This suggests that Nup96-V5 can likely incorporate into the NE independent of Nup98, implying that Nup96 does not need to be expressed as a polyprotein with Nup98 in order to be targeted to the NE.

Although several rounds of clonal isolation was performed in order to collect cells that express higher levels of the Nup96-V5 protein, we were unsuccessful in generating clonal populations that robustly expressed Nup96-V5. Regardless of expression level though, it is unlikely that the expression of Nup96-V5 in Vero cells will restore Rae1 levels or localization to the NPC when Nup98 is depleted, as Nup98 is the only GLEBS containing nucleoporin in mammals (Griffis *et al*., 2003) and is necessary for the binding of Rae1 to NPCs (Ren *et al*., 2010; Serganov *et al*., 2022). Therefore, the use of this cell line to study the effects of Orf6 expression when Nup98 is reduced will likely not affect the outcome or the interpretation of the results presented in this chapter. Nevertheless, these Nup96-V5 expressing cell lines could potentially be useful in other studies that investigate different aspects of nuclear transport or NPC assembly dynamics. Furthermore, we provide evidence for a system where Nup96 can be partially restored at the NE of Nup98 depleted cells, providing a preliminary strategy to study the effects of Nup98 depletion without complete reduction of Nup96.

Chapter V

Perspectives

5.1 Yeast as a model organism to investigate human biology.

Yeast has been a powerful model organism and has significantly contributed to our understanding of human biology and disease. Yeasts are simple eukaryotic organisms, genetic manipulation is easy, generation times are rapid, the economic burden is much lower than in mammalian systems, and the scientific community has generated a vast network of knowledge and research tools to investigate yeast biology (Mager and Winderickx; 2005; Pesic, 2021; Kachroo *et al*., 2022). The *S. cerevisiae* genome has also been extensively characterized; consisting of 6,275 genes on 16 chromosomes, many yeast genes have been shown to have surprising conservation when compared to the human genome, making *S. cerevisiae* a useful model organism in gene function studies (Liu *et al*., 2017). Additionally, significant efforts from the scientific community have generated libraries of yeast, including extensive gene deletion libraries, inducible depletion libraries, and epitope-tagged fusion libraries, allowing for rapid genetic testing within this organism (Kachroo *et al*., 2022). Although yeasts and humans have been separated by over a billion years of evolution, numerous cellular process and pathways remain conserved between these eukaryotes, and therefore, *S. cerevisiae* has been extensively used as a proxy to explore many aspects of human biological processes (Karathia *et al*., 2011; Aitchison and Rout, 2012).

An interesting area of research has emerged because humans and yeast share several thousands of genes, and although not all genes have functional conservation, many do encode for proteins with comparable function. Therefore, many protein coding human genes can functionally replace their yeast counterpart, which has allowed for the investigation of human protein activity within a simplified, yet related, organismal background. This system has been referred to as “humanized yeast” and

has permitted the study of human gene function within a tractable system (Kachroo *et al*., 2022). Expression of functionally conserved human genes in yeast can enable a detailed exploration of the basic biology underlying human cell functioning and disease, it can serve as a model to rapidly study genetic interactions, and it can also be used to elucidate potential drug targets against various human proteins (Laurent *et al*., 2016; Hamza *et al*., 2020).

Humans and yeast share a remarkable conservation in NPC structure and function. Many human Nups have a counterpart in yeast, and the underlying mechanisms and proteins involved in nuclear transport are well conserved between these eukaryotes. Therefore, for several decades, *S. cerevisiae* has remained an invaluable organism for studies on the nucleus and transport through it (Wente and Rout, 2010; Aitchison and Rout, 2012; Ptak and Wozniak, 2014). As an extension of the humanized yeast approach to study human disease, we hypothesized that the expression of the SARS-CoV-2 Orf6 protein in yeast would elucidate the conserved pathways that are affected by Orf6 expression since Orf6 targets critical residues within the human Nup98/Rae1 complex that are completely conserved within the *S. cerevisiae* Nup116/Gle2 complex. This suggested to us that Orf6 would target the yeast Nup116/Gle2 complex in a similar fashion, and thus, would likely impair conserved nuclear import and export pathways. This would provide a useful tool to rapidly study the nuclear import and export defects associated with the Orf6 protein, due to the availability of many well-established protocols and reagents needed to investigate nuclear transport in yeast (Ptak and Wozniak, 2014; Bensidoun *et al*., 2016). However, in our hands, although the SARS-CoV-2 Orf6 protein could be actively expressed and localized to the NE of *S. cerevisiae,* there were no detectable protein import or RNA

export defects associated with the level of Orf6 expression achieved in these studies. Although this impaired our ability to study the nuclear transport defects caused by Orf6, it provided an interesting insight into the ability of *S. cerevisiae* to express pathogenic viral proteins that cause human disease. Ultimately, this technique may be useful for the study of other viral proteins that affect conserved processes and pathways between humans and yeast, and should not be discarded as a potential tool to study various aspects of human disease caused by viral infection.

Indeed, previous investigations on viral protein expression within yeast has yielded important insights into the mechanisms of viral protein function. Zika virus is a positive sense single-stranded RNA virus that cause severe neurologic disorders and birth defects (Glingston *et al*., 2021). The Zika virus (ZIKV) proteome has been characterized using yeast as a model organism, and investigations into the cellular localization and cytopathic effects of various ZIKV proteins in yeast have provided valuable insights into the function of ZIKV proteins in humans. These studies have ultimately been used as a reference for further studies of viral proteins of interest in mammalian systems, but provides important hints into the molecular mechanisms behind the pathogenic ZIKV proteins that cause neurological disfunction and disease (Li *et al*., 2017; Bukrinsky, 2017; Li *et al*., 2019). Since many viral proteins have been shown to induce cell cycle arrest order to create an environment conducive for viral replication, and because many major cell cycle regulators are conserved across eukaryotes, yeast has been previously utilized as a model organism to study cell cycle regulation defects caused by viral proteins (Glingston *et al*., 2021). For instance, the HIV-1 Vpr protein has been extensively characterized using yeast as a model system and has provided important insight into how Vpr induces cell cycle arrest within

mammalian cells (Zhang *et al*., 1997; Huard *et al*., 2008b). Additionally, the expression of various Zika virus proteins have also been shown to cause cell cycle arrest in yeast (Li *et al*., 2017) which have been further confirmed and characterized in mammalian systems (Liu *et al*., 2018). Since virally induced cell cycle arrest is important to generate conditions favorable for viral replication and propagation, it may be interesting to further investigate potential cell cycle defects caused by SARS-CoV-2 protein expression within yeast. Since the related SARS-CoV-1 proteins, Orf3a, Orf7b and N, have been shown to induce cell cycle arrest in mammalian cells (Su *et al*., 2020), and since there are not extensive investigations into potential cell cycle defects caused by SARS-CoV-2 viral proteins, SARS-COV-2 Orf3a, Orf7b and N expression in yeast may provide insight into potential cell cycle defects caused by these proteins and could be an interesting area for future investigation. Ultimately, by elucidating the conserved factors and pathways that are targeted by SARS-CoV-2 proteins in yeast, potential therapeutic targets for antiviral intervention may be revealed. Importantly, the screening of potential drug compounds can be rapidly investigated using yeast that express viral proteins (Voisset *et al*., 2014), and therefore, expression of SARS-CoV-2 proteins in yeast has the potential to rapidly reveal possible therapeutics that could be effective for treating viral infection in humans.

Synthetic lethality has also been an interesting area of investigation. Synthetic lethality occurs when disruptions to one gene does not cause a lethal phenotype, however the co-occurrence of another genetic disruption results in cell death (Mast *et al*., 2020). At the molecular level, synthetic lethality can reflect redundant pathways within cells, however, synthetic lethality can also extend itself to the synthetic targeting of viruses. Viral induced vulnerabilities occur when viruses hijack host cell machinery

and impair various cellular pathways leading to new host cell vulnerabilities that can be targeted to selectively cripple virally infected cells (Mast *et al*., 2020). Elucidating these viral induced vulnerabilities is important, as these vulnerabilities can be exploited as potential candidates for drug targeting, leading to the development antiviral therapeutics that selectively impair infected cells and leave uninfected cells unperturbed. Yeast has been used extensively as a model organism to study synthetic lethal genetic interactions, and furthermore, using humanized yeast to investigate synthetic lethality has given valuable insights into human cellular pathways and gene function (Kirzinger *et al*., 2019). Although our investigation did not extend to explore viral induced vulnerabilities of the SARS-CoV-2 Orf6 protein, using Orf6 expressing *S. cerevisiae* to study synthetic lethal interactions caused by the deletion of cellular genes while Orf6 is expressed, could potentially further reveal cellular pathways affected by Orf6 expression. However, it can't be ignored that viral proteins also interact with host specific cellular pathways and factors, and therefore, investigations on viral proteins that target mammalian specific pathways may not be fruitful using yeast. Nonetheless, many conserved pathways do exist between these eukaryotes, and since genetic testing in yeast is far more rapid and much more economically feasible than in mammalian systems, synthetic lethal interactions can be quickly elucidated using yeast as a model organism and these viral induced vulnerabilities can then be confirmed and further explored within mammalian systems. Moreover, using *S. cerevisiae* to study synthetic lethality may provide a fascinating alternative for the examination of viral induced vulnerabilities caused by other viral proteins as well, and may present an interesting topic for future investigation.

5.2 The Nup98/Rae1 complex in viral infection.

The Nup98/Rae1 complex is an interferon inducible mRNA export complex that has been shown to be a common target of viruses to inhibit the nuclear transport of essential host molecules needed to fight viral infection. Viruses such as VSV, KSHV, SARS-CoV-1, and SARS-CoV-2, have been shown to use various accessory proteins to bind Nup98 and Rae1 in order to both inhibit the nuclear import of innate immune signalling molecules needed for the transcription of antiviral genes, and to block the export host mRNA required for expression of antiviral proteins (Faria *et al*., 2005; Gong *et al*., 2016; Miorin *et al*., 2020; Li *et al*., 2022). Therefore, targeting the Nup98/Rae1 complex grants viruses the ability to perturb the host innate immune response at various steps within the signalling cascade, allowing for an optimal inhibition of a cellular antiviral response and ongoing viral replication.

Being a GLFG-repeat Nup, Nup98 has been suggested to have important roles in docking and facilitating the transport of protein and RNA across the NPC through its interactions with the nuclear transport factors that bind cellular cargo (Belvins *et al*., 2003; Wu *et al*., 2001; Oka *et al*., 2009; Lau and Webber, 2020). However, many viruses have been shown to interfere with Nup98 function to enhance viral replication. The main virulence factor of Rift Valley fever virus is a non-structural protein called NS and has been shown to bind to Nup98. Depletion of Nup98 inhibits the nuclear import of the NS protein which suggests a critical role for Nup98 in NS nuclear import (Lau and Webber, 2020). Other viruses such as poliovirus and human rhinovirus (HRV), have been shown to directly degrade Nup98 using viral proteases, namely the 2A viral protease ($2A^{pro}$), which has been shown to significantly decrease the nuclear import of host proteins transported by the importin-α/β1 and importin-β2 nuclear import pathways (Yarbrough *et al*., 2014). Viruses such as Mason-Pfizer monkey virus

contain a CTE within their RNA, which is a *cis*-acting RNA sequence that enables unspliced viral RNA export by acting as a binding partner for the RNA export factor NXF1 (Coburn *et al*., 2001). Nup98 has been shown to be able to directly interact with NXF1 and has been further suggested to play a role in the NXF1-mediated export of CTE bearing RNA (Bachi *et al*., 2000). Nup98 has also been shown to interact with the cellular nuclear export factor CRM1 (Oka *et al*., 2009). CRM1 is the major export receptor for cellular protein cargo within the nucleus, but it has also been shown to facilitate the nuclear export of the viral HIV-1 Rev protein (Zolotukhin and Felber, 1999; Hutten and Kehlenback, 2007). Rev is an adaptor protein that binds to a rev response element (RRE) within unspliced HIV-1 viral RNA and is required for its nuclear export (Hammarskjöld *et al*., 1989; Hoffmann *et al*., 2012). Overexpression of the FG-repeat domain of Nup98 results in the down regulation of the expression of HIV-1 RNA typically exported by the viral Rev protein, suggesting a role for Nup98 in the CRM1-mediated export of Rev bound viral RNA (Zolotukhin and Felber, 1999). Therefore, not only does Nup98 have important functions in nuclear transport of host cargo, it also plays critical roles in viral protein import and viral RNA export from the nucleus as well.

Although Rae1's role in nuclear transport is less understood, Rae1 has been suggested to facilitate the interaction of RNA export factors with Nup98, possibility supporting the nuclear export of host RNA through this mechanism (Belvine *et al*., 2003; Xie and Ren, 2019). Although the targeting of Rae1 by the VSV M protein has been shown to inhibit host RNA export (Faira *et al*., 2005; Quan *et al*., 2014), the depletion of Rae1 does not lead to any noticeable RNA export defects on its own (Rajani *et al*., 2012, Figure 4.11), therefore, the role of Rae1 in RNA export remains to be further elucidated (Xie and Ren., 2019). We show in chapter IV that the expression

of Rae1 is critical for the SARS-CoV-2 Orf6 mediated block of bidirectional nuclear transport, as Rae1 depletion abolishes both the STAT1 import defects and poly-A RNA export defects associated with Orf6 expression (Figure 4.15 and 4.17). This suggests that Rae1 is critical for Orf6 function, however, the exact mechanism as to how Orf6 inhibits both protein import and RNA export by targeting the Nup98/Rae1 complex requires further characterization. Regardless, we demonstrate here that Orf6 function requires the Nup98/Rae1 complex, as disruptions to this complex affects Orf6's ability to inhibit nuclear transport. Interestingly, our results suggest that Orf6 is not targeting the function of either Nup98 or Rae1, rather, the Nup98/Rae1 complex is likely acting as a platform for Orf6 to bind in order to subsequently exert an inhibitory effect on host nuclear transport. Since the targeting of the Nup98/Rae1 complex seems to be a common feature among various viral proteins to inhibit an effective innate immune response against viral infection, a focus of future investigation should be directed at how, mechanistically, these viral proteins interfere with nuclear transport by interacting with the Nup98/Rae1 complex. In doing this, potential targets for therapeutic intervention could be discovered, and further insights into the roles of Nup98 and Rae1 during nuclear transport may be revealed.

Interestingly, the targeting of the Nup98/Rae1 complex during the initial stages of viral infection may be beneficial for viruses to swiftly inhibit an immune response to favor early stages of viral replication. The SARS-CoV-1 virus has been suggested to package the Orf6 protein into assembling virions for instant targeting of the innate immune response upon viral entrance (Huang *et al*., 2007), and suggests that the targeting of the Nup98/Rae1 complex during the early stages of infection is beneficial for viral propagation. The SARS-CoV-2 Orf6 protein is suggested to be a more potent inhibitor of the type-1 interferon response when compared to the SARS-CoV-1 Orf6

protein (Kimura *et al*., 2021), and since a deficiency of the innate immune response upon viral infection has been considered a hallmark of the COVID-19 disease, it would be interesting to explore if the SARS-CoV-2 virus also packages Orf6 into assembling virions. Further investigations into the role of Orf6 in innate immune evasion may provide an explanation as to how SARS-CoV-2 infection causes a severely dysregulated immune response and may be an attractive target for therapeutic intervention.

An interesting insight into the pathogenicity of the SARS-CoV-2 Orf6 protein has been revealed by the infection of hamsters with a SARS-CoV-2 virus that contains an *ORF6* deletion. Results show that hamsters infected with the SARS-CoV-2 *ΔORF6* virus have significantly greater weight gain and significantly less viral RNA within the lungs at 5 days post-infection when compared to hamsters infected with WT SARS-CoV-2 virus (Miyamoto *et al*., 2022). Furthermore, when Vero cells are infected with both WT and *ΔORF6* SARS-CoV-2 viruses, viral RNA production and viral titer are not affected, suggesting that the replication of the virus is not affected by *ORF6* deletion (Miyamoto *et al*., 2022). This collectively implies that Orf6 acts as a virulence factor for increased pathogenesis during SARS-CoV-2 infection, and therefore, viral targeting of the Nup98/Rae1 complex leads to a more severe disease outcome by impairing innate immune signalling and reducing the ability of the host to effectively combat viral replication.

Although there has been generation of several successful SARS-CoV-2 vaccines, live attenuated vaccines have not been at the forefront of investigation even though these vaccines have the advantages of a lower economic cost, generation of strong immunogenicity, and the potential for long-lived immunity (Liu *et al*., 2022). Live attenuated vaccines have been considered the most effective vaccines because they simulate a natural infection without the burden of disease (Okamura and Ebina,

2021). In recent studies, a SARS-CoV-2 virus with deletion of various SARS-CoV-2 accessory proteins, including Orf3a, Orf6, Orf7, and Orf8, has been shown to be highly attenuated in hamster models. A single dose vaccination with this live-attenuated SARS-CoV-2 deletion virus protects hamsters against WT virus challenge 28 days post-vaccination (Liu *et al*., 2022), and suggests that a live-attenuated virus lacking various accessory proteins could potentially be a candidate for a vaccine used in humans. Since Orf6 has clearly been shown to be a potent virulence factor for the SARS-CoV-2 virus, further investigation into its mechanism of action by targeting the Nup98/Rae1 complex would provide valuable insight into potential therapeutic targets for not only SARS-CoV-2, but for other viruses that also target the Nup98/Rae1 complex to impair host nuclear transport and successfully evade an immune response.

Undeniable inadequacies in our response to viral epidemics, which has been highlighted by the current COVID-19 pandemic, has exposed a great need to develop broad acting antivirals that can be rapidly distributed in response to viral infection. Ultimately, targeting host processes involved in the propagation of viral replication will allow for the development of drugs less prone to resistance (Lin and Gallay, 2013), however, the elucidation of host pathways usurped by viral proteins is needed to find suitable druggable targets for use as broad-spectrum antivirals. Since many viruses inhibit nuclear transport by targeting the Nup98/Rae1 complex, developing an understanding for how viruses hijack Nup98 and Rae1 to interfere with nuclear transport will be useful to elucidate how, mechanistically, viruses evade the innate immune response by interacting with Nup98/Rae1. Further investigations in this area could provide invaluable knowledge to the scientific community in the hopes of developing potent antivirals that can be rapidly produced and distributed to prevent both the spread and burden of an inevitable future viral outbreak.

References

Adam, Stephen A. 2009. "The Nuclear Transport Machinery in Caenorhabditis Elegans: A Central Role in Morphogenesis." *Seminars in Cell & Developmental Biology* 20(5): 576–81.

Addetia, Amin *et al*. 2021. "SARS-CoV-2 ORF6 Disrupts Bidirectional Nucleocytoplasmic Transport through Interactions with Rae1 and Nup98." *mBio* 12(2): e00065-21. https://doi.org/10 .1128/mBio.00065-21.

Aitchison, John D, and Michael P Rout. 2012. "The Yeast Nuclear Pore Complex and Transport Through It." *Genetics* 190(3): 855–83.

Alber, Frank *et al*. 2007. "The Molecular Architecture of the Nuclear Pore Complex." *Nature* 450(7170): 695–701.

Allen, Nadia P.C., Lan Huang, Al Burlingame, and Michael Rexach. 2001. "Proteomic Analysis of Nucleoporin Interacting Proteins." *Journal of Biological Chemistry* 276(31): 29268–74.

Andersen, Kasper R *et al*. 2013. "Scaffold Nucleoporins Nup188 and Nup192 Share Structural and Functional Properties with Nuclear Transport Receptors." *eLife* 2: e00745.

von Appen, Alexander, and Martin Beck. 2016. "Structure Determination of the Nuclear Pore Complex with Three-Dimensional Cryo Electron Microscopy." *Journal of Molecular Biology* 428(10): 2001–10.

Babu, J. Ramesh *et al*. 2003. "Rae1 Is an Essential Mitotic Checkpoint Regulator That Cooperates with Bub3 to Prevent Chromosome Missegregation." *Journal of Cell Biology* 160(3): 341–53.

Bachi, Angela *et al*. 2000. "The C-Terminal Domain of TAP Interacts with the Nuclear Pore Complex and Promotes Export of Specific CTE-Bearing RNA Substrates." *RNA* 6: 136-58.

Bailer, Susanne M *et al*. 1998. "Nup116p and Nup100p Are Interchangeable through a Conserved Motif Which Constitutes a Docking Site for the MRNA Transport Factor Gle2p." *The EMBO Journal* 17(4): 1107-19.

Baker Brachmann, Carrie *et al*. 1998. "Designer Deletion Strains Derived From Saccharomyces Cerevisiae S288C: A Useful Set of Strains and Plasmids for PCR-Mediated Gene Disruption and Other Applications." *Yeast* 14(2): 115–32.

Bayliss, Richard, Trevor Littlewood, and Murray Stewart. "Structural Basis for the Interaction between FxFG Nucleoporin Repeats and Importin-β in Nuclear Trafficking." *Cell* 102: 99-108.

Beck, Martin, and Ed Hurt. 2017. "The Nuclear Pore Complex: Understanding Its Function through Structural Insight." *Nature Reviews Molecular Cell Biology* 18(2): 73–89. Springer Nature.

Bensidoun, Pierre *et al*. 2022. "Nuclear MRNA Metabolism Drives Selective Basket Assembly on a Subset of Nuclear Pore Complexes in Budding Yeast." *Molecular Cell* 82(20): 3856-3871.e6.

Bensidoun, Pierre, Pascal Raymond, Marlene Oeffinger, and Daniel Zenklusen. 2016. "Imaging Single MRNAs to Study Dynamics of MRNA Export in the Yeast Saccharomyces Cerevisiae." *Methods* 98: 104–14.

Bharathi, Anekella *et al*. 1997. "The Human RAE1 Gene Is a Functional Homologue of Schizosaccharomyces Pombe Rae1 Gene Involved in Nuclear Export of Poly(A)+ RNA." *Gene* 198: 251-58.

Biancalana, Matthew, Eviatar Natan, Michael J. Lenardo, and Alan R. Fersht. 2021. "NF-κB Rel Subunit Exchange on a Physiological Timescale." *Protein Science* 30(9): 1818–32.

Bitplane Scientific Solutions. 2006. "Imaris reference manual". *Bitplane AG, Zürich.* Reference manual V 5.5.0.

Blevins, Melanie B., Ashley M. Smith, Erica M. Phillips, and Maureen A. Powers. 2003. "Complex Formation among the RNA Export Proteins Nup98, Rae1/Gle2, and TAP." *Journal of Biological Chemistry* 278(23): 20979–88.

Bley, Christopher J. *et al*. 2022. "Architecture of the Cytoplasmic Face of the Nuclear Pore." *Science* 376(6598): eabm9129.

Bonne, Gisèle *et al*. 1999. "Mutations in the Gene Encoding Lamin A/C Cause Autosomal Dominant Emery-Dreifuss Muscular Dystrophy." *Nature Genetics* 21(3): 285–88.

Bucci, Mirella, and Susan R. Wente. 1997. "In Vivo Dynamics of Nuclear Pore Complexes in Yeast." *Journal of Cell Biology* 136(6): 1185–99.

Bukrinsky, Michael. 2017. "Yeast Help Identify Cytopathic Factors of Zika Virus." *Cell & Bioscience* 7(1): 12.

Burke, James M, Alison R Gilchrist, Sara L Sawyer, and Roy Parker. 2021. "RNase L Limits Host and Viral Protein Synthesis via Inhibition of MRNA Export." *Science Advances* 7: eabh2479.

Cairo, Lucas V., Christopher Ptak, and Richard W. Wozniak. 2013. "Mitosis-Specific Regulation of Nuclear Transport by the Spindle Assembly Checkpoint Protein Mad1p." *Molecular Cell* 49(1): 109–20.

Capitanio, Juliana S., Ben Montpetit, and Richard W. Wozniak. 2018. "Nucleoplasmic Nup98 Controls Gene Expression by Regulating a DExH/D-Box Protein." *Nucleus* 9(1): 1–8.

Carmody, Sean R., and Susan R. Wente. 2009. "MRNA Nuclear Export at a Glance." *Journal of Cell Science* 122(12): 1933–37.

Carrasco-Hernandez, R, Rodrigo Jácome, Yolanda López Vidal, and Samuel Ponce de León. 2017. "Are RNA Viruses Candidate Agents for the Next Global Pandemic? A Review." *ILAR Journal* 58(3): 343–58.

Cavazza, Tommaso, and Isabelle Vernos. 2016. "The RanGTP Pathway: From Nucleo-Cytoplasmic Transport to Spindle Assembly and Beyond." *Frontiers in Cell and Developmental Biology* 3. http://journal.frontiersin.org/Article/10.3389/fcell.2015.00082/abstract (October 10, 2022).

Chook, Yuh Min, and Günter Blobel. 2001. "Karyopherins and Nuclear Import." *Current Opinion in Structural Biology* 11(6): 703–15.

Chook, Yuh Min, and Katherine E. Süel. 2011. "Nuclear Import by Karyopherin-βs: Recognition and Inhibition." *Biochimica et Biophysica Acta (BBA) - Molecular Cell Research* 1813(9): 1593–1606.

Cingolani, Gino, Carlo Petosa, and Karsten Weis. 1999. "Structure of Importin-β Bound to the IBB Domain of Importin-α." *Nature* 399: 221-29.

Corbett, Anita H., and Pamela A. Silver. 1996. "The NTF2 Gene Encodes an Essential, Highly Conserved Protein That Functions in Nuclear Transport in Vivo." *Journal of Biological Chemistry* 271(31): 18477–84.

Cronshaw, Janet M. *et al*. 2002. "Proteomic Analysis of the Mammalian Nuclear Pore Complex." *Journal of Cell Biology* 158(5): 915–27.

Daniel Gietz, R., and Robin A. Woods. 2002. "Transformation of Yeast by Lithium Acetate/Single-Stranded Carrier DNA/Polyethylene Glycol Method." In *Methods in Enzymology*, Elsevier, 87–96. https://linkinghub.elsevier.com/retrieve/pii/S0076687902509575 (October 4, 2022).

Darnell, James E., lan M. Kerr, and George R. Stark. 1994. "Jak-STAT Pathways and Transcriptional Activation in Response to IFNs and Other Extracellular Signaling Proteins." *Science* 264(5164): 1415–21.

Davis, Laura I, and Gunter Blobel. 1987. "Nuclear Pore Complex Contains a Family of Glycoproteins That Includes P62: Glycosylation through a Previously Unidentified Cellular Pathway" *Proc. Nati. Acad. Sci. USA* 84: 7552-56.

De Vos, Winnok H. *et al*. 2011. "Repetitive Disruptions of the Nuclear Envelope Invoke Temporary Loss of Cellular Compartmentalization in Laminopathies." *Human Molecular Genetics* 20(21): 4175–86.

Delaleau, Mildred, and Katherine Borden. 2015. "Multiple Export Mechanisms for MRNAs." *Cells* 4(3): 452–73.

Diekmann, Yoan, and José B. Pereira-Leal. 2013. "Evolution of Intracellular Compartmentalization." *Biochemical Journal* 449(2): 319–31.

Dultz, Elisa, and Jan Ellenberg. 2010. "Live Imaging of Single Nuclear Pores Reveals Unique Assembly Kinetics and Mechanism in Interphase." *Journal of Cell Biology* 191(1): 15–22.

Enninga, Jost, David E. Levy, Günter Blobel, and Beatriz M. A. Fontoura. 2002. "Role of Nucleoporin Induction in Releasing an MRNA Nuclear Export Block." *Science* 295(5559): 1523–25.

Eriksson, Maria *et al*. 2003. "Recurrent de Novo Point Mutations in Lamin A Cause Hutchinson–Gilford Progeria Syndrome." *Nature* 423(6937): 293–98.

Faria, Paula A. *et al*. 2005. "VSV Disrupts the Rae1/Mrnp41 MRNA Nuclear Export Pathway." *Molecular Cell* 17(1): 93–102.

Fay, Nikta, and Nelly Panté. 2015. "Nuclear Entry of DNA Viruses." *Frontiers in Microbiology* 6:467. doi: 10.3389/fmicb.2015.00467

Feng, Han *et al*. 2020. "Molecular Mechanism Underlying Selective Inhibition of MRNA Nuclear Export by Herpesvirus Protein ORF10." *Proceedings of the National Academy of Sciences* 117(43): 26719–27.

Fontoura, Beatriz, Paula Faria, and Daniel Nussenzveig. 2005. "Viral Interactions with the Nuclear Transport Machinery: Discovering and Disrupting Pathways." *IUBMB Life (International Union of Biochemistry and Molecular Biology: Life)* 57(2): 65–72.

Fontoura, Beatriz M A, Günter Blobel, and Michael J Matunis. 1999. "A Conserved Biogenesis Pathway for Nucleoporins: Proteolytic Processing of a 186-Kilodalton Precursor Generates Nup98 and the Novel Nucleoporin, Nup96." *Journal of Cell Biology* 144(6): 1097-1112.

Fontoura, Beatriz M.A., Günter Blobel, and Nabeel R. Yaseen. 2000. "The Nucleoporin Nup98 Is a Site for GDP/GTP Exchange on Ran and

Termination of Karyopherin B2-Mediated Nuclear Import." *Journal of Biological Chemistry* 275(40): 31289–96.

Forler, Daniel *et al*. 2004. "RanBP2/Nup358 Provides a Major Binding Site for NXF1-P15 Dimers at the Nuclear Pore Complex and Functions in Nuclear MRNA Export." *Molecular and Cellular Biology* 24(3): 1155–67.

Frieman, Matthew *et al*. 2007. "Severe Acute Respiratory Syndrome Coronavirus ORF6 Antagonizes STAT1 Function by Sequestering Nuclear Import Factors on the Rough Endoplasmic Reticulum/Golgi Membrane." *Journal of Virology* 81(18): 9812–24.

Froger, Alexandrine, and James E. Hall. 2007. "Transformation of Plasmid DNA into E. Coli Using the Heat Shock Method." *Journal of Visualized Experiments* (6): 253.

Fu, Xin-Yuan *et al*. 1990. "ISGF3, the Transcriptional Activator Induced by Interferon a, Consists of Multiple Interacting Polypeptide Chains." *Proc. Natl. Acad. Sci. USA* 87: 8555-59.

Funasaka, Tatsuyoshi *et al*. 2011. "RNA Export Factor RAE1 Contributes to NUP98-HOXA9-Mediated Leukemogenesis." *Cell Cycle* 10(9): 1456–67.

Gao, Xiaopan *et al*. 2022. "Structural Basis for Sarbecovirus ORF6 Mediated Blockage of Nucleocytoplasmic Transport." *Nature Communications* 13(1): 4782.

Ghavami, Ali, Erik van der Giessen, and Patrick R. Onck. 2016. "Energetics of Transport through the Nuclear Pore Complex" ed. Eugene A. Permyakov. *PLOS ONE* 11(2): e0148876.

Giri, Rajanish *et al*. 2021. "Understanding COVID-19 via Comparative Analysis of Dark Proteomes of SARS-CoV-2, Human SARS and Bat SARS-like Coronaviruses." *Cellular and Molecular Life Sciences* 78(4): 1655–88.

Gong, Danyang *et al*. 2016. "A Herpesvirus Protein Selectively Inhibits Cellular MRNA Nuclear Export." *Cell Host and Microbe* 20(5): 642–53.

Gordon, David E. *et al*. 2020. "A SARS-CoV-2 Protein Interaction Map Reveals Targets for Drug Repurposing." *Nature* 583(7816): 459–68.

Görlich, D. *et al*. 1996. "Identification of Different Roles for RanGDP and RanGTP in Nuclear Protein Import." *The EMBO Journal* 15(20): 5584–94.

Griffis, Eric R, Songli Xu, and Maureen A Powers. 2003. "Nup98 Localizes to Both Nuclear and Cytoplasmic Sides of the Nuclear Pore and Binds to Two Distinct Nucleoporin Subcomplexes." *Molecular Biology of the Cell* 14: 600–610.

Hall, Ross *et al*. 2022. "SARS-CoV-2 ORF6 Disrupts Innate Immune Signalling by Inhibiting Cellular MRNA Export." *PLOS Pathogens* 18(8): e1010349.

Hamada, Masakazu *et al*. 2011. "Ran-Dependent Docking of Importin β- to RanBP2/Nup358 Filaments Is Essential for Protein Import and Cell Viability." *Journal of Cell Biology* 194(4): 597–612.

Hammarskjöld, M L *et al*. 1989. "Regulation of Human Immunodeficiency Virus Env Expression by the Rev Gene Product." *Journal of Virology* 63(5): 1959–66.

Hamza, Akil *et al*. 2020. "Cross-Species Complementation of Nonessential Yeast Genes Establishes Platforms for Testing Inhibitors of Human Proteins." *Genetics* 214(3): 735–47.

Hanscho, Michael *et al*. 2012. "Nutritional Requirements of the BY Series of *Saccharomyces Cerevisiae* Strains for Optimum Growth." *FEMS Yeast Research* 12(7): 796–808.

Harel, Amnon *et al*. 2003. "Removal of a Single Pore Subcomplex Results in Vertebrate Nuclei Devoid of Nuclear Pores" *Molecular Cell* 11: 853-64.

Hartenian, Ella *et al*. 2020. "The Molecular Virology of Coronaviruses." *Journal of Biological Chemistry* 295(37): 12910–34.

Heaton, Steven M. 2019. "Harnessing Host–Virus Evolution in Antiviral Therapy and Immunotherapy." *Clinical & Translational Immunology* 8(7). https://onlinelibrary.wiley.com/doi/10.1002/cti2.1067 (October 16, 2022).

Herold, Andrea, Ray Truant, Heather Wiegand, and Bryan R Cullen. 1998. "Determination of the Functional Domain Organization of the Importin-α Nuclear Import Factor." *The Journal of Cell Biology* 143(2): 309-18.

Hetzer, M. W. 2010. "The Nuclear Envelope." *Cold Spring Harbor Perspectives in Biology* 2(3): a000539.

Hieronymus, Haley, and Pamela A. Silver. 2004. "A Systems View of MRNP Biology." *Genes & Development* 18(23): 2845–60.

Hitchcock, Amy L., Jason A. Kahana, and Pamela A. Silver. 2005. "The Uses of Green Fluorescent Protein in Yeasts." In *Methods of Biochemical Analysis* 47: 179–201.

Ho, Jennifer Hei-Ngam, George Kallstrom, and Arlen W. Johnson. 2000. "Nmd3p Is a Crm1p-Dependent Adapter Protein for Nuclear Export of the Large Ribosomal Subunit." *Journal of Cell Biology* 151(5): 1057–66.

Hoffmann, Dirk *et al*. 2012. "Formation of Trans-Activation Competent HIV-1 Rev:RRE Complexes Requires the Recruitment of Multiple Protein Activation Domains" *PLoS ONE* 7(6): e38305.

Hoffmann, Markus *et al*. 2020. "SARS-CoV-2 Cell Entry Depends on ACE2 and TMPRSS2 and Is Blocked by a Clinically Proven Protease Inhibitor." *Cell* 181(2): 271-280.

Huang, Cheng, C. J. Peters, and Shinji Makino. 2007. "Severe Acute Respiratory Syndrome Coronavirus Accessory Protein 6 Is a Virion-Associated Protein and Is Released from 6 Protein-Expressing Cells." *Journal of Virology* 81(10): 5423–26.

Huang, Yufan, Huaiyu Dai, and Ruian Ke. 2019. "Principles of Effective and Robust Innate Immune Response to Viral Infections: A Multiplex Network Analysis." *Frontiers in Immunology* 10: 1736.

Huard, Sylvain *et al*. 2008. "Human Immunodeficiency Virus Type 1 Vpr Induces Cell Cycle G $_2$ Arrest through Srk1/MK2-Mediated Phosphorylation of Cdc25." *Journal of Virology* 82(6): 2904–17.

Hülsmann, Bastian B., Aksana A. Labokha, and Dirk Görlich. 2012. "The Permeability of Reconstituted Nuclear Pores Provides Direct Evidence for the Selective Phase Model." *Cell* 150(4): 738–51.

Hutten, Saskia, and Ralph H. Kehlenbach. 2007. "CRM1-Mediated Nuclear Export: To the Pore and Beyond." *Trends in Cell Biology* 17(4): 193–201.

Iovine, M Kathryn, Janis L Watkins, and Susan R Wente. 1995. "The GLFG Repetitive Region of the Nucleoporin Nupll6p Interacts with Kap95p, an Essential Yeast Nuclear Import Factor." *The Journal of Cell Biology* 131: 15.

Ispolatov, Iaroslav, Martin Ackermann, and Michael Doebeli. 2012. "Division of Labour and the Evolution of Multicellularity." *Proceedings of the Royal Society B: Biological Sciences* 279(1734): 1768–76.

Iwamoto, Masaaki, Haruhiko Asakawa, Yasushi Hiraoka, and Tokuko Haraguchi. 2010. "Nucleoporin Nup98: A Gatekeeper in the Eukaryotic Kingdoms: FG Repeats of the Nucleoporin Nup98." *Genes to Cells* 15(7): 661–69.

Janin, Alexandre *et al*. 2017. "Nuclear Envelopathies: A Complex LINC between Nuclear Envelope and Pathology." *Orphanet Journal of Rare Diseases* 12(1): 147.

Kachroo, Aashiq H., Michelle Vandeloo, Brittany M. Greco, and Mudabir Abdullah. 2022. "Humanized Yeast to Model Human Biology, Disease and Evolution." *Disease Models & Mechanisms* 15(6): dmm049309.

Kaffman, Arie, Nicole Miller Rank, and Erin K. O'Shea. 1998. "Phosphorylation Regulates Association of the Transcription Factor Pho4 with Its Import Receptor Pse1/Kap121." *Genes & Development* 12(17): 2673–83.

Karathia, Hiren, Ester Vilaprinyo, Albert Sorribas, and Rui Alves. 2011. "Saccharomyces Cerevisiae as a Model Organism: A Comparative Study." *PLoS ONE* 6(2): e16015.

Katahira, Jun *et al*. 1999. "The Mex67p-Mediated Nuclear MRNA Export Pathway Is Conserved from Yeast to Human." *The EMBO Journal* 18(9): 2593–2609.

Katta, Santharam S., Christine J. Smoyer, and Sue L. Jaspersen. 2014. "Destination: Inner Nuclear Membrane." *Trends in Cell Biology* 24(4): 221–29.

Kelley, Kotaro, Kevin E. Knockenhauer, Greg Kabachinski, and Thomas U. Schwartz. 2015. "Atomic Structure of the y Complex of the Nuclear Pore." *Nature Structural and Molecular Biology* 22(5): 425–31.

Kim, Seung Joong *et al*. 2018. "Integrative Structure and Functional Anatomy of a Nuclear Pore Complex." *Nature* 555(7697): 475–82.

Kimura, Izumi *et al*. 2021. "Sarbecovirus ORF6 Proteins Hamper Induction of Interferon Signaling." *Cell Reports* 34(13): 108916.

Kimura, Makoto, and Naoko Imamoto. 2014. "Biological Significance of the Importin-β Family-Dependent Nucleocytoplasmic Transport Pathways: Biological Significance of Importin-β Family." *Traffic* 15(7): 727–48.

Kimura, Tominori, Iwao Hashimoto, Takahiro Nagase, and Jun-Ichi Fujisawa. 2004. "CRM1-Dependent, but Not ARE-Mediated, Nuclear Export of *IFN-A1* MRNA." *Journal of Cell Science* 117(11): 2259–70.

King, Nicole. 2004. "The Unicellular Ancestry of Animal Development." *Developmental Cell* 7(3): 313–25.

Kirzinger, Morgan W. B. *et al*. 2019. "Humanized Yeast Genetic Interaction Mapping Predicts Synthetic Lethal Interactions of FBXW7 in Breast Cancer." *BMC Medical Genomics* 12(1): 112.

Knockenhauer, Kevin E., and Thomas U. Schwartz. 2016. "The Nuclear Pore Complex as a Flexible and Dynamic Gate." *Cell* 164(6): 1162–71.

von Kobbe, Cayetano *et al*. 2000. "Vesicular Stomatitis Virus Matrix Protein Inhibits Host Cell Gene Expression by Targeting the Nucleoporin Nup98." *Molecular Cell* 6(5): 1243–52.

Kosugi, Shunichi *et al*. 2009. "Six Classes of Nuclear Localization Signals Specific to Different Binding Grooves of Importin α." *Journal of Biological Chemistry* 284(1): 478–85.

Kosugi, Shunichi, Masako Hasebe, Masaru Tomita, and Hiroshi Yanagawa. 2008. "Nuclear Export Signal Consensus Sequences Defined Using a Localization-Based Yeast Selection System." *Traffic* 9(12): 2053–62.

Krull, Sandra *et al*. 2004. "Nucleoporins as Components of the Nuclear Pore Complex Core Structure and Tpr as the Architectural Element of the Nuclear Basket." *Molecular Biology of the Cell* 15: 4261–77.

Kumar, K. Prasanna *et al*. 2000. "Regulated Nuclear-Cytoplasmic Localization of Interferon Regulatory Factor 3, a Subunit of Double-Stranded RNA-Activated Factor 1." *Molecular and Cellular Biology* 20(11): 4159–68.

Kumar, Swatantra, Rajni Nyodu, Vimal K. Maurya, and Shailendra K. Saxena. 2020. "Morphology, Genome Organization, Replication, and Pathogenesis of Severe Acute Respiratory Syndrome Coronavirus 2 (SARS-CoV-2)." In *Coronavirus Disease 2019 (COVID-19)*, Medical Virology: From Pathogenesis to Disease Control. http://link.springer.com/10.1007/978-981-15-4814-7_3 (October 16, 2022).

Kutay, Ulrike, F Ralf Bischoff, Susanne Kostka, and Regine Kraft. 1997. "Export of Importin-α from the Nucleus Is Mediated by a Specific Nuclear Transport Factor." *Cell* 90: 1061-71.

Lange, Allison *et al*. 2007. "Classical Nuclear Localization Signals: Definition, Function, and Interaction with Importin α." *Journal of Biological Chemistry* 282(8): 5101–5.

Lange, Allison, Milo B. Fasken, Murray Stewart, and Anita H. Corbett. 2020. "Dissecting the Roles of Cse1 and Nup2 in Classical NLS-cargo Release in Vivo." *Traffic* 21(10): 622–35.

Lapetina, Diego L., Christopher Ptak, Ulyss K. Roesner, and Richard W. Wozniak. 2017. "Yeast Silencing Factor Sir4 and a Subset of Nucleoporins Form a Complex Distinct from Nuclear Pore Complexes." *Journal of Cell Biology* 216(10): 3145–59.

Lari, Azra *et al*. 2019. "A Nuclear Role for the DEAD-Box Protein Dbp5 in TRNA Export." *eLife* 8: e48410.

Lau, Simone, and Friedemann Weber. 2020. "Nuclear Pore Protein Nup98 Is Involved in Replication of Rift Valley Fever Virus and Nuclear Import of Virulence Factor NSs." *Journal of General Virology* 101(7): 712–16.

Laurell, Eva *et al*. 2011. "Phosphorylation of Nup98 by Multiple Kinases Is Crucial for NPC Disassembly during Mitotic Entry." *Cell* 144(4): 539–50.

Laurent, Jon M., Jonathan H. Young, Aashiq H. Kachroo, and Edward M. Marcotte. 2016. "Efforts to Make and Apply Humanized Yeast." *Briefings in Functional Genomics* 15(2): 155–63.

Lee, Brittany J. *et al*. 2006. "Rules for Nuclear Localization Sequence Recognition by Karyopherinβ2." *Cell* 126(3): 543–58.

Lee, Jin-Gu *et al*. 2021. "Characterization of SARS-CoV-2 Proteins Reveals Orf6 Pathogenicity, Subcellular Localization, Host Interactions and Attenuation by Selinexor." *Cell & Bioscience* 11(1): 58.

Lei, Xiaobo *et al*. 2020. "Activation and Evasion of Type I Interferon Responses by SARS-CoV-2." *Nature Communications* 11(1): 3810.

Leslie, Deena M *et al*. 2004. "Characterization of Karyopherin Cargoes Reveals Unique Mechanisms of Kap121p-Mediated Nuclear Import." *Molecular Cell Biology* 24: 17.

Leslie, Deena M., Benjamin Timney, Michael P. Rout, and John D. Aitchison. 2006. "Studying Nuclear Protein Import in Yeast." *Methods* 39(4): 291–308.

Li, Ge *et al*. 2017. "Characterization of Cytopathic Factors through Genome-Wide Analysis of the Zika Viral Proteins in Fission Yeast." *Proceedings of the National Academy of Sciences* 114(3): E376-E385.

Li, Ge, *et al*. 2019. "The Roles of PrM-E Proteins in Historical and Epidemic Zika Virus-Mediated Infection and Neurocytotoxicity." *Viruses* 11(2): 157.

Li, Tinghan *et al*. 2022. "Molecular Mechanism of SARS-CoVs Orf6 Targeting the Rae1–Nup98 Complex to Compete With MRNA Nuclear Export." *Frontiers in Molecular Biosciences* 8.

Liang, Peizhou *et al*. 2013. "KPNB1 , XPO7 and IPO8 Mediate the Translocation OfNF-KB/P65 into the Nucleus" *Traffic* 14: 1132-43.

Light, William H. *et al*. 2013. "A Conserved Role for Human Nup98 in Altering Chromatin Structure and Promoting Epigenetic Transcriptional Memory" ed. Tom Misteli. *PLoS Biology* 11(3): e1001524.

Lin, Daniel H., and André Hoelz. 2019. "The Structure of the Nuclear Pore Complex (An Update)." *Annual Review of Biochemistry* 88(1): 725–83.

Liu, Jun *et al*. 2018. "Zika Virus Envelope Protein Induces G2/M Cell Cycle Arrest and Apoptosis via an Intrinsic Cell Death Signaling Pathway in

Neuroendocrine PC12 Cells." *International Journal of Biological Sciences* 14(9): 1099–1108.

Liu, Wei *et al*. 2017. "From Saccharomyces Cerevisiae to Human: The Important Gene Co-Expression Modules." *Biomedical Reports* 7(2): 153–58.

Liu, Yang *et al*. 2022. "A Live-Attenuated SARS-CoV-2 Vaccine Candidate with Accessory Protein Deletions." *Nature Communications* 13(1): 4337.

Lott, Kaylen, and Gino Cingolani. 2011. "The Importin β Binding Domain as a Master Regulator of Nucleocytoplasmic Transport." *Biochimica et Biophysica Acta (BBA) - Molecular Cell Research* 1813(9): 1578–92.

Lu, Juane *et al*. 2021. "Types of Nuclear Localization Signals and Mechanisms of Protein Import into the Nucleus." *Cell Communication and Signaling* 19(1): 60.

Lui, Ki and Ying Huang. 2009. "RanGTPase: A Key Regulator of Nucleocytoplasmic Trafficking." *Molecular and Cellular Pharmacology* 1(3): 148–56.

Lusk, C Patrick, and Megan C King. 2017. "The Nucleus: Keeping It Together by Keeping It Apart." *Current Opinion in Cell Biology* 44: 44–50.

Macara, Ian G. 2001. "Transport into and out of the Nucleus." *Microbiology and Molecular Biology Reviews* 65(4): 570–94.

Mager, Willem H., and Joris Winderickx. 2005. "Yeast as a Model for Medical and Medicinal Research." *Trends in Pharmacological Sciences* 26(5): 265–73.

Maciejowski, John, and Emily M. Hatch. 2020. "Nuclear Membrane Rupture and Its Consequences." *Annual Review of Cell and Developmental Biology* 36(1): 85–114.

Mahajan, Rohit *et al*. 1997. "A Small Ubiquitin-Related Polypeptide Involved in Targeting RanGAP1 to Nuclear Pore Complex Protein RanBP2." *Cell* 88(1): 97–107.

Makio, Tadashi *et al*. 2009. "The Nucleoporins Nup170p and Nup157p Are Essential for Nuclear Pore Complex Assembly." *Journal of Cell Biology* 185(3): 459–73.

Malone, Brandon, Nadya Urakova, Eric J. Snijder, and Elizabeth A. Campbell. 2022. "Structures and Functions of Coronavirus Replication–Transcription Complexes and Their Relevance for SARS-CoV-2 Drug Design." *Nature Reviews Molecular Cell Biology* 23(1): 21–39. Springer Nature.

Mast, Fred D. *et al*. 2020. "Crippling Life Support for SARS-CoV-2 and Other Viruses through Synthetic Lethality." *Journal of Cell Biology* 219(10): e202006159.

Mehlin, Hans, Bertil Daneholt, and Ulf Skoglund. 1992. “Translocation of a Specific Premessenger Ribonucleoprotein Particle through the Nuclear Pore Studied with Electron Microscope Tomography.” *Cell* 69(4): 605–13.

Mimura, Yasuhiro *et al*. 2017. “A Statistical Image Analysis Framework for Pore-Free Islands Derived from Heterogeneity Distribution of Nuclear Pore Complexes.” *Scientific Reports* 7: 16315.

Min, Yuan-Qin *et al*. 2021. “Immune Evasion of SARS-CoV-2 from Interferon Antiviral System.” *Computational and Structural Biotechnology Journal* 19: 4217–25.

Miorin, Lisa *et al*. 2020. “SARS-CoV-2 Orf6 Hijacks Nup98 to Block STAT Nuclear Import and Antagonize Interferon Signaling.” *PNAS* 117(45): 28344-54.

Mitchell, Jana M. *et al*. 2010. “Pom121 Links Two Essential Subcomplexes of the Nuclear Pore Complex Core to the Membrane.” *Journal of Cell Biology* 191(3): 505–21.

Miyamoto, Yoichi *et al*. 2022. “SARS-CoV-2 ORF6 Disrupts Nucleocytoplasmic Trafficking to Advance Viral Replication.” *Communications Biology* 5(1): 483.

von Moeller, Holger, Claire Basquin, and Elena Conti. 2009. “The MRNA Export Protein DBP5 Binds RNA and the Cytoplasmic Nucleoporin NUP214 in a Mutually Exclusive Manner.” *Nature Structural & Molecular Biology* 16(3): 247–54.

Montpetit, Ben *et al*. 2011. “A Conserved Mechanism of DEAD-Box ATPase Activation by Nucleoporins and InsP6 in MRNA Export.” *Nature* 472(7342): 238–42.

Moroianu, Junona, Gunter Blobel, and Aurelian Radu. 1997. “RanGTP-Mediated Nuclear Export of Karyopherin-α Involves Its Interaction with the Nucleoporin Nup153.” *Proc. Natl. Acad. Sci. USA*: 94: 9699-9704.

Murphy, Robert, Janis L Watkins, and Susan R Wente. 1996. “*GLE2*, a *Saccharomyces Cerevisiae* Homologue of the *Schizosaccharomyces Pombe* Export Factor *RAE1*, Is Required for Nuclear Pore Complex Structure and Function” *Molecular Biology of the Cell* 7: 1921-37.

Naim, Bracha *et al*. 2009. “Cargo Surface Hydrophobicity Is Sufficient to Overcome the Nuclear Pore Complex Selectivity Barrier.” *The EMBO Journal* 28(18): 2697–2705.

Napetschnig, Johanna *et al*. 2009. “Structural and Functional Analysis of the Interaction between the Nucleoporin Nup214 and the DEAD-Box Helicase Ddx19.” *Proceedings of the National Academy of Sciences* 106(9): 3089–94.

Nardozzi, Jonathan *et al*. 2010. "Molecular Basis for the Recognition of Phosphorylated STAT1 by Importin A5." *Journal of Molecular Biology* 402(1): 83–100.

Nemergut, Michael E. *et al*. 2001. "Chromatin Docking and Exchange Activity Enhancement of RCC1 by Histones H2A and H2B." *Science* 292(5521): 1540–43.

Neumann, Nadja, Daniel Lundin, and Anthony M. Poole. 2010. "Comparative Genomic Evidence for a Complete Nuclear Pore Complex in the Last Eukaryotic Common Ancestor" ed. Cecile Fairhead. *PLoS ONE* 5(10): e13241.

Newton, Amy H., Amber Cardani, and Thomas J. Braciale. 2016. "The Host Immune Response in Respiratory Virus Infection: Balancing Virus Clearance and Immunopathology." *Seminars in Immunopathology* 38(4): 471–82.

Nguyen, Kevin T, Michael P Holloway, and Rachel A Altura. 2012. "The CRM1 Nuclear Export Protein in Normal Development and Disease." *Int J Biochem Mol Biol* 3(2): 137-51.

Nilsen, Timothy W., and Brenton R. Graveley. 2010. "Expansion of the Eukaryotic Proteome by Alternative Splicing." *Nature* 463(7280): 457–63.

Ogawa, Yutaka, Yoichi Miyamoto, Masahiro Oka, and Yoshihiro Yoneda. 2012. "The Interaction Between Importin-α and Nup153 Promotes Importin-α/β-Mediated Nuclear Import: Importin α Promotes Classical Nuclear Import." *Traffic* 13(7): 934–46.

Oka, Masahiro *et al*. 2010. "The Mobile FG Nucleoporin Nup98 Is a Cofactor for Crm1-Dependent Protein Export." *Molecular Biology of the Cell* 21: 1885–96.

Oka, Masahiro, and Yoshihiro Yoneda. 2018. "Importin α: Functions as a Nuclear Transport Factor and Beyond." *Proceedings of the Japan Academy, Series B* 94(7): 259–74.

Okamura, Shinya, and Hirotaka Ebina. 2021. "Could Live Attenuated Vaccines Better Control COVID-19?" *Vaccine* 39(39): 5719–26.

Oldrini, Barbara *et al*. 2017. "EGFR Feedback-Inhibition by Ran-Binding Protein 6 Is Disrupted in Cancer." *Nature Communications* 8(1): 2035.

Pal, Mahendra, Gemechu Berhanu, Chaltu Desalegn, and Venkataramana Kandi. 2020. "Severe Acute Respiratory Syndrome Coronavirus-2 (SARS-CoV-2): An Update." *Cureus* 12(3): e7423.

Pesic, Dusan. 2021. "Why Is Yeast Such a Widely Used Eukaryotic Model Organism? A Literature Review." *Undergraduate Research in Natural and Clinical Science and Technology (URNCST) Journal* 5(9): 1–6.

Petersen, Jeannine M. *et al*. 2000. "The Matrix Protein of Vesicular Stomatitis Virus Inhibits Nucleocytoplasmic Transport When It Is in the Nucleus and Associated with Nuclear Pore Complexes." *Molecular and Cellular Biology* 20(22): 8590–8601.

Poswal, Ashu M., and Adesh K. Saini. 2017. "Yeast as a Model System to Study Human Diseases." In *Metabolic Engineering for Bioactive Compounds*, Springer Singapore, 209–20. http://link.springer.com/10.1007/978-981-10-5511-9_10 (September 19, 2022).

Powers, Maureen A, Douglass J Forbes, James E Dahlberg, and Elsebet Lund. 1997. "The Vertebrate GLFG Nucleoporin, Nup98, Is an Essential Component of Multiple RNA Export Pathways." *The Journal of Cell Biology* 136(2): 241-250.

Pritchard, Colin E.J., Maarten Fornerod, Lawryn H. Kasper, and Jan M.A. Van Deursen. 2000. "RAE1 Is a Shuttling mRNA Export Factor That Binds to a GLEBS-like NUP98 Motif at the Nuclear Pore Complex through Multiple Domains." *Journal of Cell Biology* 145(2): 237–53.

Ptak, Christopher, and Richard W. Wozniak. 2014. "Assessing Regulated Nuclear Transport in Saccharomyces Cerevisiae." *Methods in Cell Biology* 122: 311-330.

Pumroy, Ruth A., and Gino Cingolani. 2015. "Diversification of Importin-α Isoforms in Cellular Trafficking and Disease States." *Biochemical Journal* 466(1): 13–28.

Qiu, M., and G. Yang. 2013. "Drift correction for fluorescence live cell imaging through correlated motion identification," *2013 IEEE 10th International Symposium on Biomedical Imaging*. 452-455.

Quan, Beili, Hyuk Soo Seo, Günter Blobel, and Yi Ren. 2014. "Vesiculoviral Matrix (M) Protein Occupies Nucleic Acid Binding Site at Nucleoporin Pair (Rae1•Nup98)." *Proceedings of the National Academy of Sciences of the United States of America* 111(25): 9127–32.

Quan, Yu *et al*. 2008. "Evolutionary and Transcriptional Analysis of Karyopherin-β Superfamily Proteins" *Molecular & Cellular Proteomics* 7: 1254-69.

Radu, Aurelian, Mary Shannon Moore, and Günter Blobel. 1995. "The Peptide Repeat Domain of Nucleoporin Nup98 Functions as a Docking Site in Transport across the Nuclear Pore Complex." *Cell* 81(2): 215–22.

Radu, Aurellan, Gunter Blobel, and Mary Shannon Mooret. 1995. "Identification of a Protein Complex That Is Required for Nuclear Protein Import and Mediates Docking of Import Substrate to Distinct Nucleoporins." *PNAS USA* 92: 1769-73.

Raices, Marcela, and Maximiliano A. D'Angelo. 2012. "Nuclear Pore Complex Composition: A New Regulator of Tissue-Specific and Developmental Functions." *Nature Reviews Molecular Cell Biology* 13(11): 687–99.

Rajani, Karishma R. *et al*. 2012. "Complexes of Vesicular Stomatitis Virus Matrix Protein with Host Rae1 and Nup98 Involved in Inhibition of Host Transcription." *PLoS Pathogens* 8(9): e1002929.

Ren, Yi, Hyuk-Soo Seo, Günter Blobel, and André Hoelz. 2010. "Structural and Functional Analysis of the Interaction between the Nucleoporin Nup98 and the MRNA Export Factor Rae1." *Proc Natl Acad Sci USA* 107(23): 10406–11.

Ren, Zhihua *et al*. 2020. "Regulation of MAVS Expression and Signaling Function in the Antiviral Innate Immune Response." *Frontiers in Immunology* 11: 1030.

Ribbeck, K. 1998. "NTF2 Mediates Nuclear Import of Ran." *The EMBO Journal* 17(22): 6587–98.

Ribbeck, K., and Dirk Görlich. 2002. "The Permeability Barrier of Nuclear Pore Complexes Appears to Operate via Hydrophobic Exclusion." *The EMBO Journal* 21(11): 2664–71.

Riera Romo, Mario, Dayana Pérez-Martínez, and Camila Castillo Ferrer. 2016. "Innate Immunity in Vertebrates: An Overview." *Immunology* 148(2): 125–39.

Riojas, Marco A. *et al*. 2020. "A Rare Deletion in SARS-CoV-2 ORF6 Dramatically Alters the Predicted Three-Dimensional Structure of the Resultant Protein." preprint. http://biorxiv.org/lookup/doi/10.1101/2020.06.09.134460

Rodríguez-Navarro, Susana, and Ed Hurt. 2011. "Linking Gene Regulation to MRNA Production and Export." *Current Opinion in Cell Biology* 23(3): 302–9.

Rosenblum, Jonathan S., and Günter Blobel. 1999. "Autoproteolysis in Nucleoporin Biogenesis." *Proceedings of the National Academy of Sciences* 96(20): 11370–75.

Rout, Michael P *et al*. 2000. "The Yeast Nuclear Pore Complex: Composition, Architecture, and Transport Mechanism." *The Journal of Cell Biology* 148(4): 635-51.

Ryan, John A. "Cell Cloning by Serial Dilution in 96 Well Plates." Corning protocol. *Corning Incorporated Life Sciences*.

Ryan, Kathryn J, and Susan R Wente. 2000. "The Nuclear Pore Complex: A Protein Machine Bridging the Nucleus and Cytoplasm." *Current Opinion in Cell Biology* 12: 361–71.

Sahaya Glingston, R *et al*. 2021. "Contribution of Yeast Models to Virus Research." *Applied Microbiology and Biotechnology* 105(12): 4855–78.

Schwoebel, Eric D., Thai H. Ho, and Mary Shannon Moore. 2002. "The Mechanism of Inhibition of Ran-Dependent Nuclear Transport by Cellular ATP Depletion." *Journal of Cell Biology* 157(6): 963–74.

Sakuma, Stephen, and Maximiliano A. D'Angelo. 2017. "The Roles of the Nuclear Pore Complex in Cellular Dysfunction, Aging and Disease." *Seminars in Cell & Developmental Biology* 68: 72–84.

Sandre-Giovannoli, Annachiara De *et al*. 2002. "Homozygous Defects in LMNA, Encoding Lamin A/C Nuclear-Envelope Proteins, Cause Autosomal Recessive Axonal Neuropathy in Human (Charcot-Marie-Tooth Disorder Type 2) and Mouse." *Am. J. Hum. Genet* 70(3): 726-36.

Santos-Rosa, Helena *et al*. 1998. "Nuclear MRNA Export Requires Complex Formation between Mex67p and Mtr2p at the Nuclear Pores." *Molecular and Cellular Biology* 18(11): 6826–38.

Savellini, Gianni Gori, Gabriele Anichini, Claudia Gandolfo, and Maria Grazia Cusi. 2022. "Nucleopore Traffic Is Hindered by SARS-CoV-2 ORF6 Protein to Efficiently Suppress IFN-β and IL-6 Secretion." *Viruses* 14(6): 1273.

Sawicki, Stanley G., Dorothea L. Sawicki, and Stuart G. Siddell. 2007. "A Contemporary View of Coronavirus Transcription." *Journal of Virology* 81(1): 20–29.

Schoggins, John W. 2014. "Interferon-Stimulated Genes: Roles in Viral Pathogenesis." *Current Opinion in Virology* 6: 40–46.

Schuller, Anthony P. *et al*. 2021. "The Cellular Environment Shapes the Nuclear Pore Complex Architecture." *Nature* 598(7882): 667–71.

Selezneva, Anna, Alasdair J. Gibb, and Dean Willis. 2022. "The Nuclear Envelope as a Regulator of Immune Cell Function." *Frontiers in Immunology* 13: 840069.

Sen, Rwik *et al*. 2019. "Distinct Functions of the Cap-Binding Complex in Stimulation of Nuclear MRNA Export." *Molecular and Cellular Biology* 39(8): e00540-18.

Serganov, Artem A. *et al*. 2022. "Proteomic Elucidation of the Targets and Primary Functions of the Picornavirus 2A Protease." *Journal of Biological Chemistry* 298(6): 101882.

Serpeloni, Mariana *et al*. 2011. "Comparative Genomics of Proteins Involved in RNA Nucleocytoplasmic Export." *BMC Evolutionary Biology* 11(1): 7.

Shen, Qi *et al*. 2021. "Nuclear Import of HIV-1." *Viruses* 13(11): 2242.

Shen, Qingtang, Yifan E. Wang, and Alexander F. Palazzo. 2021. "Crosstalk between Nucleocytoplasmic Trafficking and the Innate Immune Response to Viral Infection." *Journal of Biological Chemistry* 297(1): 100856.

Shulga, N *et al*. 1996. "In Vivo Nuclear Transport Kinetics in Saccharomyces Cerevisiae: A Role for Heat Shock Protein 70 during Targeting and Translocation." *Journal of Cell Biology* 135(2): 329–39.

Sikorski, Robert S, and Philip Hieter. 1989. "A System of Shuttle Vectors and Yeast Host Strains Designed for Efficient Manipulation of DNA in Saccharomyces Ceratisiae." *Genetics* 122: 19-27.

Smulevitch, Sergey *et al*. 2005. "Structural and Functional Analysis of the RNA Transport Element, a Member of an Extensive Family Present in the Mouse Genome." *Journal of Virology* 79(4): 2356–65.

Somech, Raz *et al*. 2005. "Nuclear Envelopathies—Raising the Nuclear Veil." *Pediatric Research* 57(5 Part 2): 8R-15R.

Speckman, Rebecca A. *et al*. 2000. "Mutational and Haplotype Analyses of Families with Familial Partial Lipodystrophy (Dunnigan Variety) Reveal Recurrent Missense Mutations in the Globular C-Terminal Domain of Lamin A/C." *The American Journal of Human Genetics* 66(4): 1192–98.

Stade, Katrin, Charleen S. Ford, Christine Guthrie, and Karsten Weis. 1997. "Exportin 1 (Crm1p) Is an Essential Nuclear Export Factor." *Cell* 90(6): 1041–50.

Stancheva, Irina, and Eric C. Schirmer. 2014. "Nuclear Envelope: Connecting Structural Genome Organization to Regulation of Gene Expression." *Cancer Biology and the Nuclear Envelope*, Advances in Experimental Medicine and Biology 773: 209-244.

Stavru, Fabrizia *et al*. 2006. "NDC1: A Crucial Membrane-Integral Nucleoporin of Metazoan Nuclear Pore Complexes." *Journal of Cell Biology* 173(4): 509–19.

Stelter, Philipp, Ruth Kunze, Jessica Fischer, and Ed Hurt. 2011. "Probing the Nucleoporin FG Repeat Network Defines Structural and Functional Features of the Nuclear Pore Complex." *Journal of Cell Biology* 195(2): 183–92.

Stewart, Murray. 2019. "Polyadenylation and Nuclear Export of MRNAs." *Journal of Biological Chemistry* 294(9): 2977–87.

Sträßer, Katja, Jochen Baßler, and Ed Hurt. 2000. "Binding of the Mex67p/Mtr2p Heterodimer to Fxfg, Glfg, and Fg Repeat Nucleoporins Is Essential for Nuclear MRNA Export." *Journal of Cell Biology* 150(4): 695–706.

Strawn, Lisa A., Tianxiang Shen, and Susan R. Wente. 2001. "The GLFG Regions of Nup116p and Nup100p Serve as Binding Sites for Both Kap95p and

Mex67p at the Nuclear Pore Complex." *Journal of Biological Chemistry* 276(9): 6445–52.

Terry, Laura J., and Susan R. Wente. 2007. "Nuclear MRNA Export Requires Specific FG Nucleoporins for Translocation through the Nuclear Pore Complex." *Journal of Cell Biology* 178(7): 1121–32.

Terry, Laura J., and Susan R. Wente. 2009. "Flexible Gates: Dynamic Topologies and Functions for FG Nucleoporins in Nucleocytoplasmic Transport." *Eukaryotic Cell* 8(12): 1814–27.

Tessier, Tanner M., Mackenzie J. Dodge, Martin A. Prusinkiewicz, and Joe S. Mymryk. 2019. "Viral Appropriation: Laying Claim to Host Nuclear Transport Machinery." *Cells* 8(6): 559.

Tetenbaum-Novatt, Jaclyn *et al*. 2012. "Nucleocytoplasmic Transport: A Role for Nonspecific Competition in Karyopherin-Nucleoporin Interactions." *Molecular & Cellular Proteomics* 11(5): 31–46.

Thakar, Ketan *et al*. 2013. "Identification of CRM1-Dependent Nuclear Export Cargos Using Quantitative Mass Spectrometry." *Molecular & Cellular Proteomics* 12(3): 664–78.

Thompson, Mikayla R., John J. Kaminski, Evelyn A. Kurt-Jones, and Katherine A. Fitzgerald. 2011. "Pattern Recognition Receptors and the Innate Immune Response to Viral Infection." *Viruses* 3(6): 920–40.

Traglia, Helen M *et al*. 1996. "Nucleus-Associated Pools of Rnalp, the Saccharomyces Cerevisiae Ran/TC4 GTPase Activating Protein Involved in Nucleus/Cytosol Transit." *Proc. Natl. Acad. Sci. USA*: 93(15): 7667–7672.

Van de Vosse, David W., Yakun Wan, Richard W. Wozniak, and John D. Aitchison. 2011. "Role of the Nuclear Envelope in Genome Organization and Gene Expression." *WIREs Systems Biology and Medicine* 3(2): 147–66.

Voisset, Cécile *et al*. 2014. "A Yeast-Based Assay Identifies Drugs That Interfere with Epstein-Barr Virus Immune Evasion." *Disease Models & Mechanisms* 7(4): 435-44.

Weis, Karsten, Ursula Ryder, and Angus I Lamond. 1996. "The Conserved Amino-Terminal Domain of HSRPIa Is Essential for Nuclear Protein Import." *The EMBO Journal* 15(8): 1818-25.

Wente, S R, and G Blobel. 1994. "NUP145 Encodes a Novel Yeast Glycine-Leucine-Phenylalanine-Glycine (GLFG) Nucleoporin Required for Nuclear Envelope Structure." *Journal of Cell Biology* 125(5): 955–69.

Wente, S. R., and M. P. Rout. 2010. “The Nuclear Pore Complex and Nuclear Transport.” *Cold Spring Harbor Perspectives in Biology* 2(10): a000562.

Wente, S. R., M. P. Rout, and G. Blobel. 1992. “A New Family of Yeast Nuclear Pore Complex Proteins.” *Journal of Cell Biology* 119(4): 705–23.

Wente, Susan R and Günter Blobel. 1993 “A Temperature-Sensitive NUPll6 Null Mutant Forms a Nuclear Envelope Seal over the Yeast Nuclear Pore Complex Thereby Blocking Nucleocytoplasmic Traffic.” *The Journal of Cell Biology* 123(2): 275-84.

Wirthmueller, Lennart, Charlotte Roth, Mark J. Banfield, and Marcel Wiermer. 2013. “Hop-on Hop-off: Importin-α-Guided Tours to the Nucleus in Innate Immune Signaling.” *Frontiers in Plant Science* 4: 149.

Worman, H.J., and Neil Segil. 2013. “Nucleocytoplasmic connections and deafness.” *J Clin Invest.* 123(2):553-5.

Wozniak, Richard W, Michael P Rout, and John D Aitchison. 1998. “Karyopherins and Kissing Cousins.” *Trends in Cell Biology* 8(5): 184–88.

Wu, Winco WH, Ying-Hua B Sun, and Nelly Panté. 2007. “Nuclear Import of Influenza A Viral Ribonucleoprotein Complexes Is Mediated by Two Nuclear Localization Sequences on Viral Nucleoprotein.” *Virology Journal* 4(1): 49.

Wu, Xiaosheng *et al*. 2001. “Disruption of the FG Nucleoporin NUP98 Causes Selective Changes in Nuclear Pore Complex Stoichiometry and Function.” *Proc Natl Acad Sci USA* 89(6): 3191-96.

Xia, Hongjie *et al*. 2020. “Evasion of Type I Interferon by SARS-CoV-2.” *Cell Reports* 33(1): 108234.

Xie, Yihu, and Yi Ren. 2019. “Mechanisms of Nuclear MRNA Export: A Structural Perspective.” *Traffic* 20(11): 829–40.

Xiong, Liang *et al*. 2018. “Condition-Specific Promoter Activities in Saccharomyces Cerevisiae.” *Microbial Cell Factories* 17(1): 58.

Xu, Darui *et al*. 2012. “Sequence and Structural Analyses of Nuclear Export Signals in the NESdb Database” ed. Karsten Weis. *Molecular Biology of the Cell* 23(18): 3677–93.

Yarbrough, Melanie L., Miguel A. Mata, Ramanavelan Sakthivel, and Beatriz M. A. Fontoura. 2014. “Viral Subversion of Nucleocytoplasmic Trafficking: Viral Subversion of Nucleocytoplasmic Trafficking.” *Traffic* 15(2): 127–40.

Yap, Puay Yen, and Dieter Trau. 2019. “Direct yeast cell count at OD600”. *Tip Biosystems.* AN 101.

Yoo, Tae Yeon, and Timothy Mitchison. 2021. “Quantification of Nuclear Transport Inhibition by SARS-CoV-2 ORF6 Using a Broadly Applicable Live-Cell Dose-Response Pipeline”. preprint. http://biorxiv.org/lookup/doi/10.1101/2021.12.10.472151

Zhang, Chengsheng, Colin Rasmussen, and Lung-Ji Chang. 1997. “Cell Cycle Inhibitory Effects of HIV and SIV Vpr and Vpx in the YeastSchizosaccharomyces Pombe.” *Virology* 230(1): 103–12.

Zhang, Ke *et al*. 2021. “Nsp1 Protein of SARS-CoV-2 Disrupts the MRNA Export Machinery to Inhibit Host Gene Expression.” *Science Advances* 7(6): eabe7386.

Zhou, Haixia *et al*. 2010. “The N-Terminal Region of Severe Acute Respiratory Syndrome Coronavirus Protein 6 Induces Membrane Rearrangement and Enhances Virus Replication.” *Journal of Virology* 84(7): 3542–51.

Zhou, Zhuo *et al*. 2021. “Sensing of Cytoplasmic Chromatin by CGAS Activates Innate Immune Response in SARS-CoV-2 Infection.” *Signal Transduction and Targeted Therapy* 6(1): 382.

Zhu, Mingzhu *et al*. 2015. “Bipartite Nuclear Localization Signal Controls Nuclear Import and DNA-Binding Activity of IFN Regulatory Factor 3.” *The Journal of Immunology* 195(1): 289–97.

Zhu, Zhixing *et al*. 2020. “From SARS and MERS to COVID-19: A Brief Summary and Comparison of Severe Acute Respiratory Infections Caused by Three Highly Pathogenic Human Coronaviruses.” *Respiratory Research* 21(1): 224.

Zolotukhin, Andrei S., and Barbara K. Felber. 1999. “Nucleoporins Nup98 and Nup214 Participate in Nuclear Export of Human Immunodeficiency Virus Type 1 Rev.” *Journal of Virology* 73(1): 120–27.

Zuleger, Nikolaj *et al*. 2013. “Specific Nuclear Envelope Transmembrane Proteins Can Promote the Location of Chromosomes to and from the Nuclear Periphery.” *Genome Biology* 14(2): R14

A. Appendix.

A.1 Image J macros.

A.1.1 Image J macro for three channel image preparation.

```
function action (input, output, imagetitle){
  // Creating a merge (color) image and split images of individual channels (in grayscale), and
saving all of them
  open(input + imagetitle);
  dot = lastIndexOf(imagetitle, ".");
  titlebody = substring(imagetitle, 0, dot);
  run("Set Scale...", "distance=0 known=0 unit=pixel");

  Stack.setDisplayMode("grayscale");

  // The signal intensity for each channel will be normalized by the parameters described below

  Stack.setChannel(1);
  // The normalization parameters for the Red channel
  setMinAndMax(100, 1000);

  Stack.setChannel(2);
  // The normalization parameters for the Green channel
  setMinAndMax(100, 1000);

  Stack.setChannel(3);
  // The normalization parameters for the Blue channel
  setMinAndMax(100, 1000);

  Stack.setDisplayMode("composite");

  // Creating the Red + Green merge image and saving it
  Stack.setActiveChannels("110");
  rename("Original");
  run("RGB Color", "slices keep");
  rename("merge");
  saveAs("Tiff", output + "/" + titlebody + "_m.tif");

  // Creating the split images (Red, Green and Blue)
  selectWindow("Original");
  run("Split Channels");

  // Convert the Blue (DAPI) channel into the grayscale image and save it
  selectWindow("C3-Original");
  rename("blue");
  run("Grays");
  run("RGB Color");
  saveAs("Tiff", output + "/" + titlebody + "_b.tif");

  // Convert the Red channel into the grayscale image and save it
  selectWindow("C1-Original");
  rename("red");
  run("Grays");
  run("RGB Color");
```

```
  saveAs("Tiff", output + "/" + titlebody + "_r.tif");

  // Convert the Green channel into the grayscale image and save it
  selectWindow("C2-Original");
  rename("green");
  run("Grays");
  run("RGB Color");
  saveAs("Tiff", output + "/" + titlebody + "_g.tif");

  // Close all the image windows
  while(nImages > 0){
    selectImage(nImages);
    close();
  }
}

// The program starts here
// Selecting the input and the output folders for the image manipulations
input = getDirectory("Input directory");
output = getDirectory("Output directory");

setBatchMode(true);

// Creating the list of image files in the input folder and performing the manipulations
list = getFileList(input);
for (i = 0; i < list.length; i++){
  action(input, output, list[i]);
}

setBatchMode(false);
```

A.1.2 ImageJ macro for quantification of Nup foci at the nuclear envelope.

```
function action(input, output, filename){
  /*
  remove extension (.dv) from the filename
  in order to construct the names of output files (outname + ".tif")
  */
  dot = lastIndexOf(filename, ".");
  outname = substring(filename, 0, dot);
  open(input + filename);
  rename("Original");
  run("Split Channels");

  /*
  Extract and save Red (Nup358) images
  */
  selectWindow("C1-Original");
  run("Find Maxima...", "prominence=2200 strict exclude output=List");
  saveAs("Results", output + outname + ".csv");
  run("Clear Results");

  selectWindow("C1-Original");
  run("Find Maxima...", "prominence=2200 strict exclude output=[Point Selection]");
  run("Flatten");
```

```
  saveAs("Tiff", output + outname + ".tif");

  while (nImages>0) {
    selectImage(nImages);
    close();
  }
}

input = getDirectory("Input directory");
output = getDirectory("Output directory");

setBatchMode(true);
list = getFileList(input);
for (i = 0; i < list.length; i++){
        action(input, output, list[i]);
}
setBatchMode(false);
```

A.2 Python scripts.

A.2.1 Python scripts for analysis of viability assays.

```
# -*- coding: utf-8 -*-
"""
Created on Mon Dec 28 20:44:33 2020

@author: tmaki
"""

import pandas as pd
import numpy as np
import seaborn
import scipy
import matplotlib.pyplot as plt

#a = pd.read_excel('27-7-20 - Cov2 CellLine Test_ver210204.xlsx', sheet_name='long')
intensity_data = pd.read_csv('ViabilityAssay_March42022b Removed time point copy.csv')

# Subtract the intensity values by the blank (no cells)
background = np.mean(intensity_data[intensity_data['CellLine'] == 'Blank']['Intensity'])
intensity_data['CorrBack'] = intensity_data['Intensity'] - background
intensity_for_plot = intensity_data[intensity_data['CellLine'] != 'Blank']

# Normalize the intensity values with the value of +Dox 0h for each CellLine
intensity_grouped = intensity_for_plot.groupby(by='CellLine')
frames = []
for name, intensity_by_cell in intensity_grouped:
    intensity_by_cell['Normalized'] = intensity_by_cell['CorrBack'] /
np.mean(intensity_by_cell[intensity_by_cell['Dox'] == 0]['CorrBack'])
    frames.append(intensity_by_cell)
intensity_for_plot2 = pd.concat(frames)

# Normalize the intensity values with the value of TetshScramble for each time point
intensity_grouped = intensity_for_plot2.groupby(by='Dox')
```

```
frames = []
pvalues = []
for name, intensity_by_time in intensity_grouped:
    intensity_by_time['Normalized1'] = intensity_by_time['Normalized'] /
np.mean(intensity_by_time[intensity_by_time['CellLine'] == 'TetshScramble']['Normalized'])
    frames.append(intensity_by_time)
    stat, pvalue = scipy.stats.ttest_ind(intensity_by_time[intensity_by_time['CellLine']
=='TetshScramble']['Normalized1'],
                                         intensity_by_time[intensity_by_time['CellLine']
=='TetshNup98']['Normalized1'])
    pvalues.append({'Dox': name, 'pvalue': pvalue})
    print('Dox:', name, 'h, t-test p-value:', pvalue)
intensity_for_plot3 = pd.concat(frames)
pvalues_df = pd.DataFrame(pvalues)

# plot bars (barplot) and points (swarmplot)
f, axs = plt.subplots(nrows=1, ncols=1, figsize=(6.0,4.0))
seaborn.barplot(data=intensity_for_plot3, x = 'Dox', y = 'Normalized1', hue = 'CellLine',
dodge=True,
                ci='sd', capsize = 0.1, ax=axs)
seaborn.swarmplot(data=intensity_for_plot3, x = 'Dox', y = 'Normalized1', hue = 'CellLine',
dodge=True,
                  color='black', size=7., ax=axs)
axs.set_ylim((0, 2))
axs.set_xlabel('+ Dox (h)')
axs.set_ylabel('Population of viable cells relative to the scramble control')

pvalues_df.to_csv('ViabilityAssay_03042022_removed_timepoint_Normalize-each-time.csv')
f.savefig('ViabilityAssay_03042022_rempved_timepoint_Normalize-each-time.svg')


# -*- coding: utf-8 -*-
"""
Created on Mon Dec 28 20:44:33 2020

@author: tmaki
"""
import pandas as pd
import numpy as np
import seaborn
import scipy
import matplotlib.pyplot as plt

# S*et al*l the variables

# The column labels in the csv file
label_cellline = 'CellLine'
label_timecourse = 'Dox'
label_intensity = 'Intensity'
# The name of the control cell line
cellline_control = 'TetshScramble'
# The name of the tester cell line
cellline_test = 'TetshNup98'
# The name of the blank wells ("no cell", background)
cellline_blank = 'Blank'
# The file name of the input csv file
```

```
datafile = 'Vibility_Assay_05_March112022 copy.csv'

# Read the data
intensity_data = pd.read_csv(datafile)

# Subtract the intensity values by the blank (no cells)
background = np.mean(intensity_data[intensity_data[label_cellline] ==
cellline_blank][label_intensity])
intensity_data['CorrBack'] = intensity_data[label_intensity] - background
intensity_for_plot = intensity_data[intensity_data[label_cellline] != cellline_blank]

# Normalize the intensity values with the value of +Dox 0h for each CellLine
intensity_grouped = intensity_for_plot.groupby(by=label_cellline)
frames = []
for name, intensity_by_cell in intensity_grouped:
    intensity_by_cell['Normalized'] = intensity_by_cell['CorrBack'] /
np.mean(intensity_by_cell[intensity_by_cell[label_timecourse] == 0]['CorrBack'])
    frames.append(intensity_by_cell)
intensity_for_plot2 = pd.concat(frames)

# Normalize the intensity values with the value of TetshScramble for each time point
intensity_grouped = intensity_for_plot2.groupby(by=label_timecourse)
frames = []
pvalues = []
for name, intensity_by_time in intensity_grouped:
    intensity_by_time['Normalized1'] = intensity_by_time['Normalized'] /
np.mean(intensity_by_time[intensity_by_time[label_cellline] == cellline_control]['Normalized'])
    frames.append(intensity_by_time)
    stat, pvalue = scipy.stats.ttest_ind(intensity_by_time[intensity_by_time[label_cellline]
==cellline_control]['Normalized1'],
                                         intensity_by_time[intensity_by_time[label_cellline]
==cellline_test]['Normalized1'])
    pvalues.append({'Dox': name, 'pvalue': pvalue})
    print('Dox:', name, 'h, t-test p-value:', pvalue)
intensity_for_plot3 = pd.concat(frames)
pvalues_df = pd.DataFrame(pvalues)

# plot bars (barplot) and points (swarmplot)
f, axs = plt.subplots(nrows=1, ncols=1, figsize=(6.0,4.0))
seaborn.barplot(data=intensity_for_plot3, x = label_timecourse, y = 'Normalized1', hue =
label_cellline, dodge=True,
            hue_order = ['TetshScramble', 'TetshNup98'], palette = 'Greys',
            ci='sd', capsize = 0.1, ax=axs)
seaborn.swarmplot(data=intensity_for_plot3, x = label_timecourse, y = 'Normalized1', hue =
label_cellline, dodge=True,
              hue_order = ['TetshScramble', 'TetshNup98'],
              color='black', size=7., ax=axs)
axs.set_ylim((0, 1.4))
axs.set_xlabel('+ Dox (h)')
axs.set_ylabel('Population of viable cells relative to the scramble control')

# Write out the results
# pvalue: [input filename]_pvalue.csv
# plot: [input filename]_plot.svg
filename_period_pos = datafile.rfind('.')
filename_body = datafile[:filename_period_pos]
```

```
output_pvalue = filename_body + '_pvalue.csv'
output_plot = filename_body + '_plot.svg'
pvalues_df.to_csv(output_pvalue)
f.savefig(output_plot)
```

A.2.2 Python scrips for quantification of the nucleocytoplasmic ratio pSTAT-1 in shScramble and shNup98 cells.

```
# -*- coding: utf-8 -*-
"""
Created on Fri Jun 10 12:35:59 2022

@author: tmaki
"""
import numpy as np
import matplotlib.pyplot as plt
from scipy import ndimage
import pandas as pd
import tifffile
import skimage
import seaborn
import glob

def quantify_signal(image, mask):
    # The background was determined by the signal quantitation of the area without cells.
    # signal intensity per pixel
    background = 90.
    output_list = []
    labeled_mask, num_features = ndimage.label(mask)
    for nuc_number in range(1, num_features + 1):
        single_mask = (labeled_mask == nuc_number)
        center_x, center_y = ndimage.center_of_mass(single_mask)

        mask_ne = np.logical_xor(ndimage.binary_dilation(single_mask, iterations = 2),
                                 ndimage.binary_erosion(single_mask, iterations = 2))
        mask_cyto = np.logical_xor(ndimage.binary_dilation(single_mask, iterations = 9),
                                   ndimage.binary_dilation(single_mask, iterations = 3))
        mask_n = ndimage.binary_erosion(single_mask, iterations = 3)

        image_ne = image * mask_ne
        image_cyto = image * mask_cyto
        image_n = image * mask_n

        NE_area = mask_ne.sum() * 1.
        NE_signal = image_ne.sum() * 1.
        NE_intensity = NE_signal / NE_area - background
        Cyto_area = mask_cyto.sum() * 1.
        Cyto_signal = image_cyto.sum() * 1.
        Cyto_intensity = Cyto_signal / Cyto_area  - background
        N_area = mask_n.sum() * 1.
        N_signal = image_n.sum() * 1.
        N_intensity = N_signal / N_area  - background

        Cyto_NE = Cyto_intensity / NE_intensity
        N_Cyto = N_intensity / Cyto_intensity
```

```
            output_single = {
                'Nuc_number': nuc_number,
                'Pos_x': center_x,
                'Pos_y': center_y,
                'NE_area': NE_area,
                'NE_signal': NE_signal,
                'NE_intensity': NE_intensity,
                'Cyto_area': Cyto_area,
                'Cyto_signal': Cyto_signal,
                'Cyto_intensity': Cyto_intensity,
                'N_area': N_area,
                'N_signal': N_signal,
                'N_intensity': N_intensity,
                'Cyto/NE': Cyto_NE,
                'N/Cyto': N_Cyto,
                'log2NC': np.log2(N_Cyto)}
            output_list.append(output_single)

    output_df = pd.DataFrame(output_list)
    return output_df

def create_mask(image):
    image_filtered = ndimage.gaussian_filter(image, 5)
    thresh_otsu = skimage.filters.threshold_otsu(image_filtered)
    mask = image_filtered >= thresh_otsu

    border1 = np.zeros_like(mask)
    border1[:50, :] = 1
    border2 = np.zeros_like(mask)
    border2[-50:, :] = 1
    border3 = np.zeros_like(mask)
    border3[:, :50] = 1
    border4 = np.zeros_like(mask)
    border4[:, -50:] = 1

    good_mask = np.zeros_like(mask)
    labeled_mask, num_features = ndimage.label(mask)
    for number in range(1, num_features + 1):
        single_mask = (labeled_mask == number) * 1
        # masks with small areas do not represent nuclei
        if single_mask.sum() < 1000:
            continue

        # excluding the masks touching the borders
        if (single_mask * border1).sum() > 1:
            continue
        if (single_mask * border2).sum() > 1:
            continue
        if (single_mask * border3).sum() > 1:
            continue
        if (single_mask * border4).sum() > 1:
            continue

        good_mask = good_mask + single_mask
```

```
    return good_mask

filelist = glob.glob('images/Vero*.tif')
quant_summary = []
for inputfile in filelist:
    image_all = tifffile.imread(inputfile)
    image_pSTAT1 = image_all[0]
    image_dapi = image_all[2]
    mask = create_mask(image_dapi)

    quantified_df = quantify_signal(image_pSTAT1, mask)
    quantified_df['Filename'] = inputfile

    quant_summary.append(quantified_df)

quant_summary_df = pd.concat(quant_summary)

quant_summary_df.to_csv('quant_summary.csv')


#!/usr/bin/env python3
# -*- coding: utf-8 -*-
"""
Created on Sat Jun 11 16:26:07 2022

@author: makio
"""
import numpy as np
import matplotlib.pyplot as plt
import pandas as pd
import seaborn
import skimage
import scipy

quant_data = pd.read_csv('quant_summary.csv')

filenames = quant_data['Filename']
features=[]
for index, filename in filenames.iteritems():
    # extracting features from the file name
    # Vero-Rae1KD_Dox-0h_IFN-40min_01_R3D_D3D_CRC-s17.tif
    #      ^^^^^^     ^^           ^^
    #      CellLine   Dox          PicNo
    name_features = filename.split('_')

    knockdown = name_features[0].split('-')[1]
    if knockdown == 'ScrKD':
        cellline = 'Tet-shScramble'
    if knockdown == 'Nup98KD':
        cellline = 'Tet-shNup98'

    dox_time = name_features[1].split('-')[1]
    pic_number = name_features[3]

    feature={'CellLine': cellline,
             'Dox': dox_time,
```

```
            'PicNo': pic_number}
    features.append(feature)
features_df = pd.DataFrame(features)
quant_summary_df = pd.merge(quant_data, features_df, how='left',
                            left_index=True, right_index=True)

wt = 'Tet-shScramble'
kd = 'Tet-shNup98'

quant_nodox = quant_summary_df[quant_summary_df['Dox'] == '0h']
stat_nodox, pvalue_nodox = scipy.stats.ttest_ind(quant_nodox[quant_nodox['CellLine'] ==
kd]['log2NC'],
                                         quant_nodox[quant_nodox['CellLine'] == wt]['log2NC'])

quant_plusdox = quant_summary_df[quant_summary_df['Dox'] == '96h']
stat_plusdox, pvalue_plusdox = scipy.stats.ttest_ind(quant_plusdox[quant_plusdox['CellLine'] ==
kd]['log2NC'],
                                           quant_plusdox[quant_plusdox['CellLine'] == wt]['log2NC'])
print('pvalue (no Dox) = ', pvalue_nodox)
print('pvalue (plus Dox) = ', pvalue_plusdox)

f, axs = plt.subplots(nrows=1, ncols=1, figsize=(6.0,4.0))
seaborn.swarmplot(data = quant_summary_df, y = 'log2NC', x = 'Dox',
                  hue = 'CellLine', dodge = True, hue_order = ['Tet-shScramble', 'Tet-shNup98'],
                  palette = 'Greys', linewidth = 0.5, edgecolor ='0.0', size = 4, ax=axs)
#seaborn.violinplot(data = quant_summary_df, y = 'log2NC', x = 'CellLine',
#                   order = ['Tet-shRae1', 'Tet-shScramble'], ax=axs)

axs.set_ylabel('Log2(N/C ratio) of pY701-STAT1 signal')
axs.set_ylim((-1, 4))
f.savefig('Vero-Rae1KD_IFN_ver220830_reordered.svg')
```

A.2.3 Python scrips for quantification of the nucleocytoplasmic ratio pSTAT-1 in shScramble and shNup98 cells transduced with Flag-Orf6.

```
# -*- coding: utf-8 -*-
"""
Spyder Editor

This is a temporary script file.
"""
import pandas as pd
import numpy as np
import glob

def background_correction(raw_df):
    average_background = np.mean(raw_df[raw_df['Type'] == 'B']['RawIntDen'])
    output_df = raw_df[raw_df['Type'] != 'B']
    output_df['CorrBack'] = output_df['RawIntDen'] - average_background

    return output_df

#filelist = glob.glob("Vero-*.xlsx")
filelist = glob.glob("Vero-*_annotated.csv")
```

```
assembled_data = []
for raw_file in filelist:
#    raw_data = pd.read_excel(raw_file)
    raw_data = pd.read_csv(raw_file)
    raw_df = raw_data[['Type', 'No', 'RawIntDen']]
    corrected_data = background_correction(raw_df)

    cell_type = raw_file.split('_')[1]
    if cell_type == 'Bystander':
        cell_type_name = 'Bystander'
    if cell_type == 'FlagOrf6':
        cell_type_name = 'FLAG-ORF6'
    corrected_data['CellType'] = cell_type_name

    cell_line = raw_file.split('_')[0].split('-')[1]
    if cell_line == 'scram':
        cell_line_name = 'Tet-shScramble'
    if cell_line == 'Nup98KD':
        cell_line_name = 'Tet-shNup98'
    corrected_data['CellLine'] = cell_line_name

    image_number = raw_file.split('_')[2]
    corrected_data['ImageNumber'] = image_number

    assembled_data.append(corrected_data)

assembled_data_df = pd.concat(assembled_data)

assembled_data_df.to_csv('assembled_data_replicate1.csv')

# -*- coding: utf-8 -*-
"""
Created on Mon May  2 10:59:49 2022

@author: tmaki
"""
import pandas as pd
import numpy as np
import seaborn
import scipy
import matplotlib.pyplot as plt
import glob
import statsmodels.api as sm
from statsmodels.formula.api import ols
import pingouin as pg
import scipy.stats as stats

filelist = glob.glob("assembled_data*.csv")

assembled_data = []
replicate_number = 1
for raw_file in filelist:
    intensity_data = pd.read_csv(raw_file)
    intensity_data['Rep'] = replicate_number
    assembled_data.append(intensity_data)
```

```
    replicate_number = replicate_number + 1
intensity_data_df = pd.concat(assembled_data)

intensity_grouped = intensity_data_df.groupby(by=['No', 'CellLine', 'CellType', 'ImageNumber',
'Rep'])
frames = []
for name, intensity_by_cell in intensity_grouped:
    nc_ratio = intensity_by_cell[intensity_by_cell['Type'] == 'N']['CorrBack'].mean() /
intensity_by_cell[intensity_by_cell['Type'] == 'C']['CorrBack'].mean()
    frame = {'No': name[0],
             'CellLine': name[1],
             'CellType': name[2],
             'ImageNumber': name[3],
             'NCRatio': nc_ratio,
             'logNC': np.log10(nc_ratio)}
    frames.append(frame)
intensity_for_plot = pd.DataFrame(frames)

wt = 'Tet-shScramble'
kd = 'Tet-shNup98'

# one-way ANOVA
intensity_for_oneway = intensity_for_plot
intensity_for_oneway['Key'] = intensity_for_oneway['CellType'] + '_x_'
+intensity_for_oneway['CellLine']
print('Homoscedasticity test')
print(pg.homoscedasticity(data=intensity_for_oneway, dv='logNC', group='Key',
method='bartlett'))

#model = ols('logNC ~ C(Key)', data = intensity_for_oneway).fit()
#print('one-way ANOVA')
#print(sm.stats.anova_lm(model, typ=2, robust = 'hc3'))

pg_anova = pg.welch_anova(data = intensity_for_oneway, dv = 'logNC', between = 'Key')
print('one-way Welch\'s ANOVA')
print(pg_anova)

# post-hoc Welch t-test
stat_bystander, pvalue_bystander =
scipy.stats.ttest_ind(intensity_for_plot[(intensity_for_plot['CellLine'] == kd) &
(intensity_for_plot['CellType'] == 'Bystander')]['logNC'],
                      intensity_for_plot[(intensity_for_plot['CellLine'] == wt) &
(intensity_for_plot['CellType'] == 'Bystander')]['logNC'],
                      equal_var=False)
stat_ORF6, pvalue_ORF6 = scipy.stats.ttest_ind(intensity_for_plot[(intensity_for_plot['CellLine']
== kd) & (intensity_for_plot['CellType'] == 'FLAG-ORF6')]['logNC'],
                     intensity_for_plot[(intensity_for_plot['CellLine'] == wt) &
(intensity_for_plot['CellType'] == 'FLAG-ORF6')]['logNC'],
                     equal_var=False)

print('Welch\'s t tests')
print('Bystander: pvalue = ', pvalue_bystander)
print('ORF6-positive: pvalue = ', pvalue_ORF6)
print('p-value with Bonferroni correction')
print(pg.multicomp([pvalue_bystander, pvalue_ORF6], alpha=0.05, method='bonf'))
```

```
#pg_tukey = pg.pairwise_tukey(data = intensity_for_oneway, dv = 'logNC', between = 'Key')
#print('Pariwise Tukey HSD')
#print(pg_tukey)
#pg_games = pg.pairwise_gameshowell(data = intensity_for_oneway, dv = 'logNC', between =
'Key')
#print('Pariwise  Games-Howell test')
#print(pg_games)

# two-way ANOVA
#model = ols('logNC ~ C(CellLine) + C(CellType) +C(CellLine):C(CellType)', data =
intensity_for_plot).fit()
#print('two-way ANOVA')
#print(sm.stats.anova_lm(model, typ=3, robust = 'hc3'))
#res = model.resid

intensity_for_plot.to_csv('intensity_for_plot.csv')

f, axs = plt.subplots(nrows=1, ncols=1, figsize=(6.0,4.0))
#axs.set_yscale('log')
seaborn.swarmplot(data=intensity_for_plot, x = 'CellType', y = 'logNC', hue = 'CellLine',
dodge=True,
                  hue_order = ['Tet-shScramble', 'Tet-shNup98'], palette = 'Greys', size = 3,
                  linewidth = 0.3, edgecolor ='0.0', ax=axs)
#res = model.resid
#sm.qqplot(res, stats.t, fit = True, line = '45', ax = axs[1])
#seaborn.swarmplot(data=intensity_for_plot, x = 'CellType', y = 'logNC', hue = 'CellLine',
dodge=True,
#                  color='black', size=7., ax=axs)
#seaborn.boxplot(data=intensity_for_plot, x = 'CellType', y = 'logNC', hue = 'CellLine',
dodge=True,
#                ax=axs)
#seaborn.violinplot(data=intensity_for_plot, x = 'CellType', y = 'logNC', hue = 'CellLine',
dodge=True,
#                  ax=axs)
axs.set_ylabel('log10 (N/C ratio)')
axs.set_xlabel('')

#f.savefig('analysis_combined_reordered.svg')
```

A.2.4 Python scrips for quantification of Flag-Orf6 at the nuclear envelope.

```
# -*- coding: utf-8 -*-
"""
Created on Fri Jun 10 12:35:59 2022

@author: tmaki
"""
import numpy as np
import matplotlib.pyplot as plt
from scipy import ndimage
import pandas as pd
import tifffile
import skimage
import seaborn
import glob
```

```
import sys
import os

def quantify_NE_and_C(image, mask):
    output_list = []
    labeled_mask, num_features = ndimage.label(mask)
    # num_features should be 1.
    for nuc_number in range(1, num_features + 1):
        single_mask = labeled_mask == nuc_number
        center_x, center_y = ndimage.center_of_mass(single_mask)

        mask_ne = np.logical_xor(ndimage.binary_dilation(single_mask, iterations = 2),
                                 ndimage.binary_erosion(single_mask, iterations = 2))
        mask_cyto = np.logical_xor(ndimage.binary_dilation(single_mask, iterations = 9),
                                   ndimage.binary_dilation(single_mask, iterations = 3))
        mask_n = ndimage.binary_erosion(single_mask, iterations = 5)

        image_ne = image * mask_ne
        image_cyto = image * mask_cyto
        image_n = image * mask_n

        NE_area = mask_ne.sum() * 1.
        NE_signal = image_ne.sum() * 1.
        NE_intensity = NE_signal / NE_area
        Cyto_area = mask_cyto.sum() * 1.
        Cyto_signal = image_cyto.sum() * 1.
        Cyto_intensity = Cyto_signal / Cyto_area
        N_area = mask_n.sum() * 1.
        N_signal = image_n.sum() * 1.
        N_intensity = N_signal / N_area

        Cyto_NE = Cyto_intensity / NE_intensity
        NE_Cyto = NE_intensity / Cyto_intensity

        output_single = {
            'Nuc_number': nuc_number,
            'Pos_x': center_x,
            'Pos_y': center_y,
            'NE_area': NE_area,
            'NE_signal': NE_signal,
            'NE_intensity': NE_intensity,
            'Cyto_area': Cyto_area,
            'Cyto_signal': Cyto_signal,
            'Cyto_intensity': Cyto_intensity,
            'N_area': N_area,
            'N_signal': N_signal,
            'N_intensity': N_intensity,
            'Cyto/NE': Cyto_NE,
            'NE/Cyto': NE_Cyto }
        output_list.append(output_single)

    output_df = pd.DataFrame(output_list)
    return output_df

def create_mask(image):
    image_filtered = ndimage.gaussian_filter(image, 5)
```

```
    thresh_otsu = skimage.filters.threshold_otsu(image_filtered)
    mask = image_filtered >= thresh_otsu

    # The masks (nuclei) located within 10 pixels from borders will be excluded.
    border1 = np.zeros_like(mask)
    border1[:10, :] = 1
    border2 = np.zeros_like(mask)
    border2[-10:, :] = 1
    border3 = np.zeros_like(mask)
    border3[:, :10] = 1
    border4 = np.zeros_like(mask)
    border4[:, -10:] = 1

    good_mask = np.zeros_like(mask)
    labeled_mask, num_features = ndimage.label(mask)
    for number in range(1, num_features + 1):
        single_mask = (labeled_mask == number) * 1

        # masks with small areas do not represent nuclei
        if single_mask.sum() < 1000:
            continue

        # excluding the masks touching the borders
        if (single_mask * border1).sum() > 1:
            continue
        if (single_mask * border2).sum() > 1:
            continue
        if (single_mask * border3).sum() > 1:
            continue
        if (single_mask * border4).sum() > 1:
            continue

        good_mask = good_mask + single_mask

    # num_features should be 1 because there is only one nucleus in each cropped image.
    labeled_mask, num_features = ndimage.label(good_mask)
    if num_features != 1:
        return None

    return good_mask

filelist1 = os.listdir('SingleCells/')
filelist = []
for temp in filelist1:
    if 'tif' in temp:
        temp1 = 'SingleCells' + os.sep + temp
        filelist.append(temp1)

quant_summary = []
for inputfile in filelist:
    image_all = tifffile.imread(inputfile)
    image_ORF6 = image_all[1]
    image_dapi = image_all[2]
    mask = create_mask(image_dapi)
    try:
        shape = mask.shape
```

```
    except (TypeError, AttributeError):
        print('The number of nuclei is not one in the image file:')
        print(' ', inputfile)
        sys.exit()

    quantified_df = quantify_NE_and_C(image_ORF6, mask)
    quantified_df['Filename'] = inputfile

    quant_summary.append(quantified_df)

quant_summary_df = pd.concat(quant_summary)

quant_summary_df.to_csv('quant_summary_perCell.csv')

#!/usr/bin/env python3
# -*- coding: utf-8 -*-
"""
Created on Sat Jun 11 16:26:07 2022

@author: makio
"""
import numpy as np
import matplotlib.pyplot as plt
import pandas as pd
import seaborn
import skimage

quant_data = pd.read_csv('quant_summary_perCell.csv')

filenames = quant_data['Filename']
features=[]
for index, filename in filenames.iteritems():
    name_features = filename.split('_')
    name_feature1 = name_features[0].split('/')
    if name_feature1[1] == 'shScram':
        cellline = 'Tet-shScramble'
    if name_feature1[1] == 'shNup98':
        cellline = 'Tet-shNup98'

    feature={'CellLine': cellline,
             'Rep': name_features[5],
             'PicNo': name_features[4]}
    features.append(feature)
features_df = pd.DataFrame(features)
quant_summary_df = pd.merge(quant_data, features_df, how='left',
                            left_index=True, right_index=True)

# Cut out the bystander (untransfected) cells
# Is this beneficial?
#quant_transfected = quant_summary_df[quant_summary_df['N_intensity'] > 200]

f, axs = plt.subplots(nrows=1, ncols=1, figsize=(6.0,4.0))
seaborn.scatterplot(data = quant_summary_df,
                    y = 'NE_intensity', x = 'Cyto_intensity', hue = 'CellLine',
                    hue_order = ['Tet-shScramble', 'Tet-shNup98'],
                    palette = 'Greys',
```

```
            linewidth = 0.5, edgecolor ='0.0',
            ax=axs)
axs.axline((1000.,1000.), (2000.,2000.), color='k')
axs.set_xscale('log')
axs.set_yscale('log')
#axs.set_xlim((100, 10000))
#axs.set_ylim((100, 10000))
axs.set_ylabel('Normalized FLAG-ORF6 intensity at the NE')
axs.set_xlabel('Normalized FLAG-ORF6 intensityin the cytoplasm')

f.savefig('quant_summary_perCell_ver220830.svg')
```

A.2.5 Python scrips for quantification of the nucleocytoplasmic ratio of poly-A RNA in shScramble and shNup98 cells transduced with Flag-Orf6

```
# -*- coding: utf-8 -*-
"""
Spyder Editor

This is a temporary script file.
"""
import pandas as pd
import numpy as np
import glob
import sys

def background_correction(raw_df):
    length = len(raw_df)
    average_background = np.mean(raw_data.iloc[[-4,-3,-2,-1]]['RawIntDen'])
    output_df = raw_df.drop([length - 4, length - 3, length - 2, length -1])
    output_df['CorrBack'] = output_df['RawIntDen'] - average_background

    return output_df

filelist = glob.glob("Vero-*.csv")
#filelist = ['Vero-Rae1KD_Dox-120h_FLAG-ORF6_OligodT_01_R3D_D3D_CRC-s15B.csv']

assembled_data = []
for raw_file in filelist:
    raw_data = pd.read_csv(raw_file)
    # This program assumes that the last 4 lines are quantification of the background.
    # Plus at least N and C of one cell --> minimum 6 lines per file
    if len(raw_data) < 6:
        print('No sufficient number of data in the file:' + raw_file)
        sys.exit()
    # The total number of lines should be even,
    # since data of N and C (2 lines) are always appeared as a set.
    if (len(raw_data) % 2) == 1:
        print('The number of data in the file is odd.')
        print('Please check the file:' + raw_file)
        sys.exit()
    # Performing background correction. Background data are removed from the table.
    raw_df = raw_data[['RawIntDen']]
    corrected_data = background_correction(raw_df)
```

```
    # Giving identifications of the location of quantification (N or C) and the cell number
    # based on the assumption that:
    # line 1: quantification of N of cell #1
    # line 2: quantification of C of cell #1
    # line 3 and 4: N and C of cell #2, ...
    length = int(len(corrected_data) / 2)
    loc_type = []
    cell_num = []
    for num in range(length):
        loc_type.append('N')
        loc_type.append('C')
        cell_num.append(str(num + 1))
        cell_num.append(str(num + 1))
    corrected_data['Loc'] = loc_type
    corrected_data['No'] = cell_num

    # From the file name, the annotations are extracted.
    # The filename is like:
    # Vero-Rae1KD_Dox-120h_FLAG-ORF6_OligodT_01_R3D_D3D_CRC-s15B.csv
    #      ^^^^^^                      ^^              ^
    #      Cell line                Image number        Cell type(Bystander)

    # The letter just before the letter '.' defines the cell type.
    basename = raw_file.split('.')[0]
    if basename[-1] == 'B':
        cell_type = 'Bystander'
    if basename[-1] == 'F':
        cell_type = 'FLAG-ORF6'
    corrected_data['CellType'] = cell_type

    # The first block of the filename split by the letter '_' is 'Vero-Rae1KD'.
    # The second block of the above string split by the letter '-' is 'Rae1KD' (Cell line).
    cell_line = raw_file.split('_')[0].split('-')[1]

    # modified
    if cell_line == 'Nup98KD':
        cell_line_renamed = 'Tet-shNup98'
    if cell_line == 'ScramKD':
        cell_line_renamed = 'Tet-shScramble'
    corrected_data['CellLine'] = cell_line_renamed

    # The fifth block of the filename split by the letter '_' is '01' (image number).
    image_number = raw_file.split('_')[4]
    corrected_data['ImageNumber'] = image_number

    assembled_data.append(corrected_data)

assembled_data_df = pd.concat(assembled_data)

assembled_data_df.to_csv('assembled_data_220331.csv')
# -*- coding: utf-8 -*-
"""
Created on Mon May  2 10:59:49 2022

@author: tmaki
"""
```

```
import pandas as pd
import numpy as np
import seaborn
import scipy
import matplotlib.pyplot as plt
import statsmodels.api as sm
from statsmodels.formula.api import ols
import pingouin as pg
import scipy.stats as stats

intensity_data_df = pd.read_csv('assembled_data_220331.csv')
intensity_grouped = intensity_data_df.groupby(by=['No', 'CellLine', 'CellType', 'ImageNumber'])
frames = []
for name, intensity_by_cell in intensity_grouped:
   nc_ratio = intensity_by_cell[intensity_by_cell['Loc'] == 'N']['CorrBack'].mean() /
intensity_by_cell[intensity_by_cell['Loc'] == 'C']['CorrBack'].mean()
   frame = {'No': name[0],
         'CellLine': name[1],
         'CellType': name[2],
         'ImageNumber': name[3],
         'NCRatio': nc_ratio,
         'logNC': np.log2(nc_ratio)}
   frames.append(frame)
intensity_for_plot = pd.DataFrame(frames)

wt = 'Tet-shScramble'
kd = 'Tet-shNup98'

# Homoscedasticity test
intensity_for_oneway = intensity_for_plot
intensity_for_oneway['Key'] = intensity_for_oneway['CellType'] + '_x_'
+intensity_for_oneway['CellLine']
print('Homoscedasticity test')
print(pg.homoscedasticity(data=intensity_for_oneway, dv='logNC', group='Key',
method='bartlett'))

#Welch ANOVA
pg_anova = pg.welch_anova(data = intensity_for_oneway, dv = 'logNC', between = 'Key')
print('Welch\'s ANOVA')
print(pg_anova)

# post-hoc Welch t-test
stat_bystander, pvalue_bystander =
scipy.stats.ttest_ind(intensity_for_plot[(intensity_for_plot['CellLine'] == kd) &
(intensity_for_plot['CellType'] == 'Bystander')]['logNC'],
                      intensity_for_plot[(intensity_for_plot['CellLine'] == wt) &
(intensity_for_plot['CellType'] == 'Bystander')]['logNC'])
stat_ORF6, pvalue_ORF6 = scipy.stats.ttest_ind(intensity_for_plot[(intensity_for_plot['CellLine']
== kd) & (intensity_for_plot['CellType'] == 'FLAG-ORF6')]['logNC'],
                      intensity_for_plot[(intensity_for_plot['CellLine'] == wt) &
(intensity_for_plot['CellType'] == 'FLAG-ORF6')]['logNC'])

print('Welch\'s t tests')
print('Bystander: pvalue = ', pvalue_bystander)
print('ORF6-positive: pvalue = ', pvalue_ORF6)
print('p-value with Bonferroni correction')
```

```
print(pg.multicomp([pvalue_bystander, pvalue_ORF6], alpha=0.05, method='bonf'))

#pg_tukey = pg.pairwise_tukey(data = intensity_for_oneway, dv = 'logNC', between = 'Key')
#print('Pariwise Tukey HSD')
#print(pg_tukey)
#pg_games = pg.pairwise_gameshowell(data = intensity_for_oneway, dv = 'logNC', between =
'Key')
#print('Pariwise  Games-Howell test')
#print(pg_games)

# two-way ANOVA
#model = ols('logNC ~ C(CellLine) + C(CellType) +C(CellLine):C(CellType)', data =
intensity_for_plot).fit()
#print('two-way ANOVA')
#print(sm.stats.anova_lm(model, typ=3, robust = 'hc3'))
#res = model.resid

intensity_for_plot.to_csv('intensity_for_plot.csv')

f, axs = plt.subplots(nrows=1, ncols=1, figsize=(6.0,4.0))
#axs.set_yscale('log')
seaborn.swarmplot(data=intensity_for_plot, x = 'CellType', y = 'logNC', hue = 'CellLine',
dodge=True,
              hue_order = ['Tet-shScramble', 'Tet-shNup98'], palette = 'Greys', size=4,
              linewidth = 0.5, edgecolor ='0.0', ax=axs)

#sm.qqplot(res, stats.t, fit = True, line = '45', ax = axs[1])

#seaborn.swarmplot(data=intensity_for_plot, x = 'CellType', y = 'logNC', hue = 'CellLine',
dodge=True,
#               color='black', size=7., ax=axs)
#seaborn.boxplot(data=intensity_for_plot, x = 'CellType', y = 'logNC', hue = 'CellLine',
dodge=True,
#              ax=axs)
#seaborn.violinplot(data=intensity_for_plot, x = 'CellType', y = 'logNC', hue = 'CellLine',
dodge=True,
#               ax=axs)
axs.set_ylabel('log2 (N/C ratio)')
axs.set_xlabel('')

intensity_for_plot.to_csv('analyzed_data_for_plot_220331.csv')
#f.savefig('analysis_FISH_220331_reordered.svg')
```

A.2.6 Python scrips for quantification of Nup foci at the nuclear envelope

```
# -*- coding: utf-8 -*-
"""
Created on Fri Jun 10 12:35:59 2022

@author: tmaki
"""

import numpy as np
import matplotlib.pyplot as plt
from scipy import ndimage
import pandas as pd
```

```
import tifffile
import skimage
import seaborn
import glob
import sys

def NPC_counting(basefilename, NPC_positions, mask, image_Nup98):
    output_list = []
    NPC_list = []
    labeled_mask, num_features = ndimage.label(mask)
    for nuc_number in range(1, num_features + 1):
        single_mask = (labeled_mask == nuc_number)
        center_x, center_y = ndimage.center_of_mass(single_mask)

        mask_area = np.sum(single_mask == True, axis = None)

        NPC_in_mask = NPC_positions[single_mask[NPC_positions['Y'], NPC_positions['X']] > 0]
        NPC_number = len(NPC_in_mask)
        NPC_list.append(NPC_in_mask)

        intensity_Nup98 = np.sum(image_Nup98 * single_mask)
        intensity_Nup98_perArea = intensity_Nup98 * 1. / mask_area

        output_single = {
            'Filename': basefilename,
            'Nuc_number': nuc_number,
            'Nuc_pos_X': center_y,
            'Nuc_pos_Y': center_x,
            'Nuc_Area': mask_area,
            'NPC_number': NPC_number,
            'Intensity_Nup98': intensity_Nup98,
            'Nup98_per_area': intensity_Nup98_perArea }
        output_list.append(output_single)

    output_df = pd.DataFrame(output_list)
    NPC_list_df = pd.concat(NPC_list)

    return output_df, NPC_list_df

def create_mask(mask):

    border1 = np.zeros_like(mask)
    border1[:30, :] = 1
    border2 = np.zeros_like(mask)
    border2[-30:, :] = 1
    border3 = np.zeros_like(mask)
    border3[:, :30] = 1
    border4 = np.zeros_like(mask)
    border4[:, -30:] = 1

    good_mask = np.zeros_like(mask)
    labeled_mask, num_features = ndimage.label(mask)
    for number in range(1, num_features + 1):
        single_mask = (labeled_mask == number) * 1
        # masks with small areas do not represent nuclei
        if single_mask.sum() < 1000:
```

```
            continue

        # excluding the masks touching the borders
        if (single_mask * border1).sum() > 1:
            continue
        if (single_mask * border2).sum() > 1:
            continue
        if (single_mask * border3).sum() > 1:
            continue
        if (single_mask * border4).sum() > 1:
            continue

        good_mask = good_mask + single_mask

    return good_mask

if __name__ == '__main__':
    stagepos_df = pd.read_csv('StagePos.csv')
    quant_summary = []
    for index, imageinfo in stagepos_df.iterrows():
        basefilename = imageinfo['Filename']

        image_Nup98 = tifffile.imread('mask/' + basefilename + '_Nup98.tif')
        mask_orig = tifffile.imread('mask/' + basefilename + '_mask.tif')
        mask = create_mask(mask_orig)

        NPC_position_df = pd.read_excel('data/' + basefilename +'.xls', sheet_name = 'Position',
header = 1)
        stage_x = float(imageinfo['Pos_X'])
        PhysicalSizeX = 0.10841400176286697
        stage_y = float(imageinfo['Pos_Y'])
        PhysicalSizeY = 0.10841400176286697
        stage_z = float(imageinfo['Pos_Z'])
        PhysicalSizeZ=0.20000000298023224
        NPC_position_df['X'] = ((NPC_position_df['Position X'] - stage_x + 0.01) / PhysicalSizeX
).astype(int)
        NPC_position_df['Y'] = (1023.01 - (NPC_position_df['Position Y'] - stage_y) /
PhysicalSizeY ).astype(int)
        NPC_position_df['Z'] = ((NPC_position_df['Position Z'] - stage_z + 0.01) / PhysicalSizeZ
).astype(int)

        quantified_df, NPC_list_df = NPC_counting(basefilename, NPC_position_df, mask,
image_Nup98)
        NPC_list_df.to_csv('data/' + basefilename +'_withinMask.csv')
        quant_summary.append(quantified_df)

        del quantified_df, NPC_list_df

    quant_summary_df = pd.concat(quant_summary)

    quant_summary_df.to_csv('quant_summary.csv')


#!/usr/bin/env python3
# -*- coding: utf-8 -*-
"""
```

```
Created on Sat Jun 11 16:26:07 2022
@author: makio
"""
import numpy as np
import matplotlib.pyplot as plt
import pandas as pd
import seaborn
import scipy
import skimage
import sys
import scipy
import statsmodels.api as sm
import statsmodels.formula.api as smf

quant_data = pd.read_csv('quant_summary.csv')

filenames = quant_data['Filename']
features=[]
for index, filename in filenames.iteritems():
    name_features = filename.split('_')

    name_feature1 = name_features[1]
    if name_feature1 == 'scram':
        cellline = 'Tet-shScramble'
    elif name_feature1 == 'N98':
        cellline = 'Tet-shNup98'
    else:
        cellLine = 'Error'

#    name_feature1 = name_features[0]
#    if name_feature1 == 'scram':
#        cellline = 'Tet-shScramble'
#    elif name_feature1 == 'shNup98':
#        cellline = 'Tet-shNup98'
#    else:
#        cellLine = 'Error'

    name_feature1 = name_features[2]
    if name_feature1 == 'noDox':
        dox = 'noDox'
    elif name_feature1 == 'plusDox':
        dox = 'plusDox'
    else:
        dox = 'Error'

    feature={'CellLine': cellline,
             'Dox': dox,
             'PicNo': name_features[5]}
    features.append(feature)
features_df = pd.DataFrame(features)
quant_summary_df = pd.merge(quant_data, features_df, how='left',
                            left_index=True, right_index=True)
quant_filtered_df = quant_summary_df[ (quant_summary_df['CellLine'] != 'Tet-shNup98') |
                                      (quant_summary_df['Dox'] != 'plusDox') |
                                      (quant_summary_df['Intensity_Nup98'] < 25000000)]
```

```
ttest, pvalue = scipy.stats.ttest_ind(quant_filtered_df[(quant_filtered_df['CellLine'] == 'Tet-
shNup98') &
                                      (quant_filtered_df['Dox'] == 'noDox')]['NPC_number'],
                                quant_filtered_df[(quant_filtered_df['CellLine'] == 'Tet-shNup98') &
                                      (quant_filtered_df['Dox'] == 'plusDox')]['NPC_number'])
print('p-value (shNup98) no Dox vs plus Dox: ', pvalue)

quant_shNup98_df = quant_filtered_df[(quant_summary_df['CellLine'] == 'Tet-shNup98')]

quant_Nup98_depleted_df = quant_filtered_df[(quant_summary_df['CellLine'] == 'Tet-shNup98')
&
                                    (quant_summary_df['Dox'] == 'plusDox')]

f, axs = plt.subplots(nrows=1, ncols=1, figsize=(3.0,4.0))
#seaborn.scatterplot(data = quant_summary_df,
#                x = 'Nuc_Area', y = 'NPC_number', hue = 'Dox', ax=axs)
#seaborn.boxplot(data = quant_filtered_df,
#                hue = 'CellLine', y = 'NPC_number',
#                x = 'Dox', dodge = True, fliersize = 0,
#                ax=axs[0])
seaborn.swarmplot(data = quant_shNup98_df,
            y = 'NPC_number', x ='Dox',
            color = '0.4', size = 5,
            linewidth = 0.5, edgecolor ='0.0',
            ax=axs)
#axs.set_xscale('log')
#axs.set_yscale('log')
#axs.set_xlabel('Nuclear area')
axs.set_ylabel('Number of Nup96 foci per cell')

f.savefig('quant_summary_2208230_reorderd.svg')
```